Copyright is owned by the Author of the thesis. Permission is given for a copy to be downloaded by an individual for the purpose of research and private study only. The thesis may not be reproduced elsewhere without the permission of the Author.

EVAPORATIVE CRYSTALLIZATION OF ALPHA-LACTOSE MONOHYDRATE

A thesis presented in partial fulfilment of the requirements
for the degree of

Doctor of Philosophy

In

Chemical Engineering

at Massey University, Manawatu
New Zealand.

Shailesh Ghanashyam Agrawal

2012

Dedicated to

Rasikbihari....

Abstract

Evaporative crystallization has been used by Fonterra Cooperative Group (New Zealand) for producing lactose. It represents an important step during lactose manufacturing where control over crystal size can be obtained, a critical parameter governing the yield and end use. The art of operating these crystallizers has been developed by observation and not from scientific principles. This project was undertaken to understand the mechanisms controlling the crystal size in evaporative crystallizers.

A review of the existing literature showed that secondary nucleation is the major source of nuclei in industrial crystallizers. Based on the review, attrition, contact and fluid shear induced nucleation were identified as the probable secondary nucleation mechanisms in the studied system. Experimental investigation on each of the three mechanisms was carried out separately on a laboratory scale.

It was found that the crystal size had the most significant effect on attrition, followed by impeller speed, which together implies that the crystal collision energy intensity is the dominant factor producing new fragments. Contact nucleation was also found to be controlled by crystal-impeller collisions. It was found that at the studied supersaturation there exists a minimum kinetic energy of contact below which secondary nucleation would not occur. This threshold value was used as the basis to assess the contribution of various mechanisms at the industrial scale. Shear nucleation was found to be independent of shear above 5000 s^{-1}.

A mathematical model describing the operation of the industrial crystallizer was formulated. Sensitivity analysis was conducted by simulating the model for a range of operational and kinetic parameter values. It was found that the crystal size is affected most by secondary nucleation. The volume weighted mean size approximately halved with a 5.5 times increase in the secondary nucleation rate.

The model was refined to accommodate size dependent growth rate and growth rate dispersion. The kinetic parameters were fitted to match the measured size distribution from the industrial crystallizer. A range of simulations were conducted for various theoretical and empirical models and compared to that of plant measurements. Based on the results it was proposed that the majority of secondary nucleation is expected to occur in the pump and the boiling zone.

Acknowledgement

It's not easy to move to an alien country to do a PhD. So my first thank to New Zealand and its people for making me feel comfortable and for being my home for close to four years. I will then like to thank my main supervisor, Prof. Tony Paterson for giving me the opportunity to work under him. Thanks Tony for showing constant faith in my abilities and being there whenever I needed advice, academic or personal. This PhD would not be possible without your guidance and encouragement.

Big thanks to my co-supervisors: Dr. Jeremy McLeod, Prof. Jim Jones and Prof. John Bronlund. Thanks Jeremy for proposing this PhD and getting me started into Fonterra during your last few days with them. Thanks for attending my weekly meeting from USA and taking a keen interest in the project. Jim, I learnt a lot about technical writing from you. I would be happy if I could become half as good as you. John, thanks for helping me with my model. That one small session with you on Matlab got me going!

My sincere thanks to my mentors at Fonterra: Tony Styles and Raymond Joe. It is not easy to carry out experimental studies in an industrial environment. Raymond, thanks for making sure that I have all the resources to complete my trials at Kapuni. Tony thanks for arranging the work contract with Fonterra for the last six months of the project when I ran out of funding. My special thanks to Karl Goble, who was the go to person during my stay at Kapuni; whether it be collecting data from the plant or for discussing my mathematical model or simply someone to talk to regarding the project. Karl, you have got the most amazing collection of theses and references on crystallization!! Thank you to Sharon, Michelle and all others at the Kapuni site who made my stay there enjoyable.

Financial security is a critical factor for any PhD student. Therefore, I will like to thank the Foundation for Research Science and Technology, Government of New Zealand for providing me with the scholarship to able me to undertake this project. I

would also like to thank Fonterra from the bottom of my heart for sponsoring my conference trips and university fees.

I spent most of my PhD study in Taranaki. So I will like to thank all the people who made my stay enjoyable at Hawera and helped me at some stage or other: The Turuturu cricket team and its members, Chandu Bhana and his family, Daniel Hovell and Jimmy. The cricket matches over the weekend were fun and allowed to take my mind off the PhD for little bit. Chandu, thanks for inviting us to your home and the volleyball games on Mondays. Thank you to Daniel and Jimmy for being great flat mates and providing an environment where I could return to in the evenings and relax. Daniel, I will always remember the round the mountain relay which I ran for your team. It was a great experience! Thanks.

I also need to thank people who helped me during my stay at Massey and in Palmy. First of all I will like to thank the PhD students at SEAT in the sustainable processing cluster: Horng, Ihli, Georg, Konrad, Fitri, for making my PhD experience memorable. My thanks to intern students: Amandine, Amit and Yohannes, for being part of my PhD journey at different stages. Thanks to Ann-Marie, Bruce, Anthony and John for helping me in different ways in my experimental work. Thanks to Gayle and Linda for sorting out all the administrative and financial issues during the length of my PhD.

My sincere thanks to Rajesh for being my first point of contact and helping me settle in New Zealand. Thanks to Mallesh for being a wonderful flatmate during my second term in Palmy. I will also like to thank Nilesh to whom I approached whenever I needed some advice. I will like to express my gratitude towards my friends in the badminton group for all the fun I had while playing with them. Palash, I still hope to beat you some day in singles! Special thanks to Ken Mercer for taking me on the most beautiful journeys and giving me an opportunity to see the real NZ. Ken, I will never forget our three day hiking trip to Nelson Lakes National Park!!

I now like to say thank and pay obeisance to my parents for their constant emotional and spiritual support. I cannot express in words my gratitude towards them for the sacrifices they have made. To my brother Saket, thanks for your belief in me. I also

express gratefulness to all my in-laws, especially parents-in-law for their kind words and love.

My hearty thanks to the most special person who became the part of my life during the latter half of my PhD: my wife Sneha. I need to first say sorry to you that you missed the festivities and occasions which are very special for a newly married Indian girl because I dragged you half away across the world to a completely new country. Thanks for all the love and support. Your smiling face is the biggest energy booster for me!!

Table of Contents

ABSTRACT I

ACKNOWLEDGEMENT III

LIST OF FIGURES XI

CHAPTER 1 PROJECT OVERVIEW 1

CHAPTER 2 CRYSTALLIZATION THEORY 5

2.1 Nucleation 5

2.2 Growth 7

2.3 Lactose 9

2.4 Industrial Crystallizer 10

2.4.1 Forced Circulation Evaporative Crystallizers 14

2.5 Modelling 15

2.5.1 Method of Moments (MOM) 18

2.5.2 Discretization 19

2.6 Conclusions 20

CHAPTER 3 LITERATURE REVIEW ON SECONDARY NUCLEATION 21

3.1 Collision Induced Secondary Nucleation 24

3.1.1 Attrition 24

3.1.2 Contact Nucleation 26

3.2 Shear Secondary Nucleation 29

3.3 Secondary Nucleation Studies on Lactose 33

3.4 Conclusions 35

CHAPTER 4 EXPERIMENTS ON SECONDARY NUCLEATION 37

4.1 Attrition 37

4.1.1 Theory 38

4.1.2 Materials and Methods 43

4.1.3 Results and Discussions 44

4.1.4 Conclusions 51

4.2 Contact Nucleation 52

4.2.1 Theory 52

4.2.2 Crystal-impeller Contacts 53

4.2.3 Crystal-crystal Contacts 55

4.2.4 Experimental 57

4.2.5 Results and Discussions 60

4.2.6 Conclusions 68

4.3 Shear Nucleation 69

4.3.1 Results and Discussions 73

4.3.2 Conclusions 74

CHAPTER 5 MODEL DEVELOPMENT AND SENSITIVITY ANALYSIS 75

5.1 Mathematical Model Development 75

5.1.1 Mass Balance 76

5.1.2 Population Balance 79

5.1.3 Growth and Nucleation Kinetics 81

5.1.4 Lactose Solubility 82

5.1.5 Lactose Mutarotation Kinetics 82

5.2 A Brief Review on Lactose Crystallization Kinetics 83

5.2.1 Growth 83

5.2.2 Secondary Nucleation 84

5.2.3 Primary Nucleation 86

5.3 Simulation and Sensitivity Analysis 87

5.3.1 Effect of Growth Rate 88

5.3.2 Effect of Primary Nucleation 92

5.3.3 Effect of Secondary Nucleation 97

5.3.4 Effect of Evaporation Rate 101

5.3.5 Effect of Residence Time 104
5.3.6 Effect of Temperature 108

5.4 Summary and Conclusions 111

CHAPTER 6 INDUSTRIAL CRYSTALLIZER 113

6.1 Hydrodynamics 113

6.2 Plant Data and Parameter Estimation 119
6.2.1 Sampling and analysis 119
6.2.2 Results 121
6.2.3 MSMPR Analysis 125
6.2.4 Simulation and Parameter Estimation 132

6.3 Simulations using Mechanistic Models for Secondary Nucleation 142
6.3.1 Attrition 142
6.3.2 Contact Nucleation due to Crystal-Impeller Collisions 147
6.3.3 Contact Nucleation due to Crystal-crystal Collisions 151
6.3.4 Plant trials 159

6.4 Conclusions 162

CHAPTER 7 PROJECT REVIEW 163

NOMENCLATURE 167

REFERENCES 171

APPENDIX I I

APPENDIX II V

APPENDIX III VII

APPENDIX IV XVII

List of Figures

Figure 1-1. Framework for describing the crystallizer behaviour. 2

Figure 2-1. Solubility diagram, supersaturation generation and crystallization kinetics [adapted from Mersmann (2001b) and Jones (2002)]. Anti-solvents lower the solubility of the solute. On anti-solvent addition (refered to as dilution in the figure), the excessive solute (defined by the anit-solvent solubility curve) precipitates out. Chemical reaction leading to high concentrations of the new generated species can also trigger precipiation.. 6

Figure 2-2. Nucleation mechanisms [adapted from Randolph & Larson (1988)]. 7

Figure 2-3. Plot of crystal growth rate, G, vs. solution velocity (or slurry mixing) showing the mechanism governing crystal growth (Genck, 2003). 8

Figure 2-4. Effect of agitation speed on lactose growth rate at a supersasturation of 5.23 g per 100 g of water at 30^{o}C (McLeod, 2007). 8

Figure 2-5. α-lactose tomahawk morphology [reproduced from van Kreveld & Michaels (1965)] 9

Figure 2-6. Mean crystal size produced by different industrial crystallizers as a function of residence time and nucleation rate [reproduced from Wöhlk, Hofmann, & de Jong (1991). 11

Figure 2-7. Forced circulation evaporative crystallizer [reproduced from Bennet (2002)] 12

Figure 2-8. DTB crystallizer [reproduced from Bennet (2002)]. 13

Figure 2-9. Fluidized bed crystallizer [reproduced from Bennet (2002)]. 13

Figure 2-10. Feedback interactions between various factors effecting crystallization [adapted from Randolph & Larson (1988)]. 15

Figure 2-11. Semi logarithmic plot of population density versus crystal size for an MSMPR continuous crystallizer. 17

Figure 3-1. Secondary nucleation classifications as applicable to an industrial crystallizer. 24

Figure 3-2. Contact nucleation photomicroscopic cell [reproduced from Garside, et al., (1979)]. 27

Figure 3-3. Growth rate comparison of lactose under different experimental conditions. ▲present data from Shi, et al., (1989) for a photomicroscopic cell, × present data from Shi, et al., (1990) for a CSTR (continuous stirred tank reactor). Temperature ranged from 30-60 ^{o}C. Residence time for CSTR studies varied from 4.6-52 minutes and growth rates determined by MSMPR population balance

technique. In the photomicroscopy study, growth of a population of nuclei was followed in a single experiment for 30-500 minutes, with mean growth rate plotted. 29

Figure 3-4. Secondary nucleation studies on lactose. A: Spontaneous nucleation line/ Supersolubility curve (Hunziker, 1949); B: Solubility curve; C: Forced crystallization (Hunziker, 1949) [refers to the optimum viscosity (a function of temperature) and supersaturation at which the solution was seeded and held under vigorous agitation for 60 minutes]; D:Critical supersaturation for growth (Shi, et al., 1989); E: SNT (Butler, 1998); F: Forced secondary nucleation (Shi, et al., 1989) and G:Nuclei first detection curve (Wong, Bund, Connelly, & Hartel, 2011). 34

Figure 4-1. Different attrition mechanisms [adapted from Barbosa-Cánovas, Ortega-Rivas, Juliano, & Yan (2005)]. 38

Figure 4-2. Effect of different dominant attrition mechanisms on the CSD with time [reproduced from Malave-Lopez & Peleg (1986)]. 39

Figure 4-3. Particle size distributions and difference plots for a range of attrition outcomes. 42

Figure 4-4. Normalized frequency CSD for a single HHH run. The trial name represents high levels of crystal size, impeller speed and concentration. 45

Figure 4-5. Cumulative size distribution at 0 and 60 minutes for selected experimental runs. The legend gives high/low levels of particle size, impeller speed and particle concentration respectively. The data shown is the average of four replicates. 46

Figure 4-6. Differential attrition index (*standard error bars, n=4*) measured between time, *t=0* and *t*. Trial names represent high, medium and low levels of crystal size, impeller speed and concentration 48

Figure 4-7. Importance of seed pretreatment for fines. The beaker on the left contained untreated settled seed crystals and would have led to an over-estimation of secondary nucleation, while that on the right are the washed seeds. 57

Figure 4-8. Secondary nucleation versus time (Supersaturation: 10.7 g of α-LMH per 100 g of water / Seed size: 357 µm / Seed loading: 2% (w/w) / Impeller speed: 550 rpm). S*tandard deviation error bars for 4 replicates are shown.* 61

Figure 4-9. Effect of seed loading on secondary nucleation rate at constant supersaturation (8.4g α –LMH per 100 g water) for different combinations of seed size and impeller speed. S*tandard deviation error bars for 4 replicates are shown.*. 64

Figure 4-10. Effect of seed loading on secondary nucleation from kinetic energy and contact frequency perspective at constant supersaturation (8.4 g of α-LMH per 100 g water). 67

Figure 4-11. Secondary nucleation at constant seed loading of 2% (w/w) at 10.7 and 6.7 s.s. (g α-LMH per 100 g water) from a kinetic energy and frequency of contacts perspective. *Standard deviation error bars based on 4 replicates are shown.* The 8

kinetic energies correspond to the same combinations of impeller speed and crystal size as shown in Figure 4-9. 68

Figure 4-12. Experimental setup for shear secondary nucleation. 72

Figure 4-13. Shear secondary nucleation: Effect of shear rate and supersaturation. The primary nucleation trials contain no immobilized lactose crystals. Supersaturations are g of α-LMH per 100 g of water. 74

Figure 5-1. A generalized schematic of an evaporative crystallizer. 76

Figure 5-2. Growth studies on lactose. 84

Figure 5-3. Secondary nucleation studies on lactose..... 85

Figure 5-4. Lactose primary nucleation rate (McLeod, 2007). 87

Figure 5-5. Effect of growth rate kinetics on a), dissolved lactose; b), supersaturation; c), slurry density; d), crystal concentration; e), mean diameter; f), instantaneous growth rate; and g), coefficient of variation. Solid line represent profiles obtained by using growth parameters of Shi, et al.,(1990) and the broken line uses that of McLeod (2007). 92

Figure 5-6. Effect of primary nucleation rate constant on a),dissolved lactose; b),supersaturation; c), slurry density; d), crystal concentration e), instantaneous primary nucleation rate; f), mean diameter and g), coefficient of variation. 96

Figure 5-7. Effect of secondary nucleation rate constant on a), dissolved lactose; b), supersaturation; c), slurry density; d), crystal concentration; e), instantaneous secondary nucleation rate; f), mean diameter; and g), coefficient of variation. 100

Figure 5-8. Effect of evaporation rate on a), dissolved lactose; b), supersaturation; c), slurry density; d), crystal concentration; e), mean diameter; and f), coefficient of variation. 103

Figure 5-9. Effect of residence time on a), dissolved lactose; b), supersaturation; c), slurry density; d), crystal concentration; e), mean diameter; and f), coefficient of variation. 107

Figure 5-10. Effect of temperature of operation (constant for an evaporative crystallizer) on a), dissolved lactose; b), supersaturation; c), slurry density; d), crystal concentration; e), mean diameter; and f), coefficient of variation. 111

Figure 6-1. Fluid dynamics scale in a crystallizer, x represents crystal (reproduced from Rielly & Marquis (2001)). 114

Figure 6-2. Compartment model for a forced circulation evaporative crystallizer (reproduced from Kramer, et al. (2000)). 115

Figure 6-3. Prediction of the height at which boiling starts inside the calandria tubes of the Kapuni FC evaporative crystallizer. 116

Figure 6-4. Slurry velocity in the boiling zone in the calandria tubes of the Kapuni FC evaporative crystallizer. 116

Figure 6-5. Compartmental model for the Kapuni FC evaporative crystallizer. 117

Figure 6-6. Supersaturation decay transient profile in absence of evaporation i.e. no supersaturation generation, for prediction of $t_{\Delta c,1/2}$. 118

Figure 6-7. Residence time profile of the Kapuni FC evaporative crystallizer during the three sampling trials. 121

Figure 6-8. Dissolved solids profile of the Kapuni FC evaporative crystallizer for the three sampling runs (MA: moisture analyzer and HRM: Handheld refractometer). 122

Figure 6-9. Total solids profile of the Kapuni FC evaporative crystallizer for the three sampling runs (measured using the Metler Toledo moisture analyzer). 122

Figure 6-10. Crystalline solids content profile of the Kapuni FC evaporative crystallizer for the three sampling runs (calculated from mass balance using total solids and dissolved solids). 123

Figure 6-11. Crystal size distribution profile of the Kapuni FC evaporative crystallizer for the three sampling runs a) Trial 1 b) Trial 2 c) Trial 3. 0 minute indicates the .. 124

Figure 6-12. Volume weighted mean diameter profiles of the Kapuni FC evaporative crystallizer for the three sampling runs. 125

Figure 6-13. Population density curve for lactose crystals obtained from the Kapuni FC evaporative crystallizer under steady state. 126

Figure 6-14. Size dependent growth rate fitted to the population density curve in Figure 6-13. 128

Figure 6-15. Size dependent growth rate versus crystal size. Fitted values of the parameters a, c and G_e for the Mydlarz model are 0.0059, 0.0091 and 1.82 μm min^{-1}, respectively. 129

Figure 6-16. Various growth rate dispersion models fitted to plant population density. 131

Figure 6-17. Probability density distribution for various growth rate dispersion models (value of the fitted parameters is listed in Table 6-1). 132

Figure 6-18. Effect of grid size on simulation results. 134

Figure 6-19. Dissolved lactose profile for Kapuni FC evaporative crystallizer for fitted growth, primary nucleation and secondary nucleation rate constants. The broken and continuous lines represent the model prediction during the semi-batch and the continuous mode respectively. 136

Figure 6-20. Total solids profile for Kapuni FC evaporative crystallizer for fitted growth, primary nucleation and secondary nucleation rate constants. The broken and continuous lines represent the model prediction during the semi-batch and the continuous mode respectively. 136

Figure 6-21. Crystal concentration profile for Kapuni FC evaporative crystallizer for fitted growth, primary nucleation and secondary nucleation rate constants. The broken and continuous lines represent the model prediction during the semi-batch and the continuous mode respectively. 137

Figure 6-22. Volume weighted mean diameter profile for Kapuni FC evaporative crystallizer for fitted growth, primary nucleation and secondary nucleation rate constants. The broken and continuous lines represent the model prediction during the semi-batch and the continuous mode respectively. The line through the measured data points is drawn as a visual guide to compare with the model prediction. 137

Figure 6-23. Steady state population density distribution for Kapuni FC evaporative crystallizer predicted by the model using optimized fitted parameters. 138

Figure 6-24. Dry crystal sieve analysis representative of the CSD dynamics of the Kapuni FC evaporative crystallizer. 138

Figure 6-25. Dissolved lactose profile for size independent growth. 139

Figure 6-26. Volume weighted mean diameter profile for size independent growth. 140

Figure 6-27. Population density curve for size independent growth. 140

Figure 6-28. Dissolved lactose profile using method of moments and parameters estimated by SIG (size independent growth). 141

Figure 6-29. Volume weighted mean diameter profile calculated using the method of moments. 142

Figure 6-30. Effect of impeller blade discretization on simulation results. 145

Figure 6-31. Dissolved lactose concentration profile with attrition (calculated by Mersmann model) as the source of secondary nucleation. Markers depict measured values. 146

Figure 6-32. Volume weighted mean diameter profile with attrition (calculated by Mersmann model) as the only source of secondary nucleation. Markers depict measured values. 146

Figure 6-33. Crystals withdrawn from the crystallizer at steady state. 147

Figure 6-34. Secondary nucleation at constant seed loading of 2% (w/w) at 10.7 and 6.7 s.s. (g α-LMH per 100 g water) from a kinetic energy and frequency of contacts perspective. 149

Figure 6-35. Plot of ln of the intercept of the lines fitted in Figure 4-11 versus the ln of the supersaturations to determine K_N and b in Equation 4-12. 149

Figure 6-36. Dissolved lactose concentration profile with crystal-impeller contact nucleation at the operational circulation pump speed as the source of secondary nucleation. Markers depict measured values. 150

Figure 6-37. Volume weighted mean diameter profile with crystal-impeller contact nucleation at the standard operating circulation pump speed as the source of secondary nucleation. Markers depict measured values. 150

Figure 6-38. Solid liquid suspension (redrawn from (Eskin et al., 2004)) 151

Figure 6-39. Variation of flow quality with the tube height in the calandria of the Kapuni FC evaporative crystallizer. 156

Figure 6-40. The refractive index (dissolved solids in wt %) trends for the plant trial conducted at two temperatures. The figure on the left gives trend for the lower and to the right for the higher temperature. 159

Figure 6-41. Observed crystal size distribution during unplanned one off trial. Blue line depicts the CSD with the lower feed concentration. Normal feed resumed around midday. Green and red lines depict CSD after approximately 3 and 4 hours of resumption of normal feed. 161

List of Tables

Table 2-1 *Various Moments of Density Distribution and Mean Crystal Sizes* 19

Table 3-1 *Selected Data from Sung, et al., (1973) showing the Generation of Secondary Nuclei for Magnesium Sulphate at Different Levels of Mixing and Supersaturations.* 30

Table 3-2 *Data from Wang, M.L., et al., (1981) in Terms of Shear Rates at a Constant Absolute Supersaturation for Citric Acid (16.6 gm per 100gm of water)* 32

Table 3-3 *Secondary Nucleation Studies in Literature on Lactose* 35

Table 4-1 *Factors Varied during the Attrition experiments. H = High, M= medium, L =Low* 44

Table 4-2 *Experimental Design Matrix (Size:Speed:Concentration)* 44

Table 4-3 *Comparison of Calculated and Experimental Volumetric Attrition Ratios. To Remove the Effect of Concentration) the Mid Values for the Bands HH*, HL*, LH* and LL* After 60 Minutes are Used*.....50

Table 4-4 *Run Time (t) for Different Trials Conducted for Each Experiment with Two Impeller Speeds of 400 and 550 rpm, and Four Particle Sizes of 106-212, 212-300, 300-425 and 425-600 Microns*.....60

Table 4-5 *Values of Different Parameters for Impeller-Crystal Contact Induced Secondary Nucleation* 62

Table 4-6 *Values of Different Hydrodynamic Parameters for Crystal-Crystal Contact for Different Impeller Speeds.* 62

Table 4-7 *Inter-Particle Mean Space and the Kinetic Energy of Contact for Crystal-Crystal Contacts*.....63

Table 4-8 *Straight Line Fits Through the Data Points of Figure 4-9 And Kinetic Energy of Collisions for Various Combinations of Seed Size and Impeller Speed*.....64

Table 4-9 *Comparison of the Experimental and Theoretical Slopes of the Secondary Nucleation Rate Line*.....66

Table 5-1 *Secondary Nucleation Studies on Lactose*.....86

Table 5-2 *Values and Range of Parameters Studied During Simulation* 88

Table 5-3 *Values of the Crystallizer Outputs at Steady State at the Maximum and Minimum Values of the Various Kinetic and Operation Parameters Simulated*.....112

Table 6-1 *Growth Rate Dispersion Models* 130

Table 6-2 *Kinetic Parameters Estimated from Size Dependent and Size Independent Growth Models* 142

Table 6-3 *Values of Critical Parameters for Crystal-Crystal Contacts in the Circulation Loop Pipe* 155

Table 6-4 *Values of Critical Parameters for Crystal-Crystal Contacts in the Calandria Pipes* 156

List of Equations

Equation 2-1 Population balance equation 16

Equation 2-2 Population balance equation for a batch process 16

Equation 2-3 Population balance equation for a continuous process..... 16

Equation 2-4 Population density for a steady state continuous process 17

Equation 2-5 Nucleation rate calculation for MSMPR crystallizer 17

Equation 2-6 Discretized Method of lines for solving population balance equation... 20

Equation 4-1 Secondary nucleation: empirical model 37

Equation 4-2 Difference function for a frequency distribution..... 40

Equation 4-3 Differential attrition index definition 40

Equation 4-4 Volumetric attrition rate due to impeller-crystal collisions 48

Equation 4-5 Volumetric attrition rate due to crystal-crystal collisions 48

Equation 4-6 Volumetric crystal hold up 49

Equation 4-7 Volumetric attrition rate due to crystal-crystal collisions in terms of crystal size and concentration 49

Equation 4-8 Relationship between target efficiency and crystal size..... 49

Equation 4-9 Volumetric attrition rate in terms of crystal size..... 49

Equation 4-10 Volumetric attrition rate ratio for a given impeller 50

Equation 4-11 Volumetric attrition rate ratio approximation by DAI slope ratio 50

Equation 4-12 Collision secondary nucleation 52

Equation 4-13 Kinetic energy of impeller-crystal collision..... 53

Equation 4-14 Mass of a single crystal 53

Equation 4-15 Crystal-impeller collision velocity 53

Equation 4-16 Kinetic energy of contact for impeller-crystal collisions 54

Equation 4-17 Impeller-crystal collision frequency..... 54

Equation 4-18 Target efficiency as a function of Stokes number 54
Equation 4-19 Stokes number 54
Equation 4-20 Contact nucleation due to impeller-crystal collisions 55
Equation 4-21 Kinetic energy of crystal-crystal collision 55
Equation 4-22 Inter-particle space in a slurry suspension 55
Equation 4-23 Crystal-crystal collision velocity 55
Equation 4-24 Length of smallest eddy 56
Equation 4-25 Energy dissipation rate in an agitated system 56
Equation 4-26 Reynolds number for an agitated system 56
Equation 4-27 Crystal-crystal collision frequency 56
Equation 4-28 Total crystal volume in Malvern presentation unit 58
Equation 4-29 Crystal volume per ml of the sample 59
Equation 4-30 Number of crystals in size bin *(i)* 59
Equation 4-31 Total number of crystals across all size bins 59
Equation 4-32 Theoretical ratio of the slopes of fitted lines in Figure 4-9 65
Equation 4-33 Approximate impeller-crystal collision frequency 66
Equation 4-34 Wall shear stress for a flow through a rough tube 69
Equation 4-35 Shear rate at the wall 69
Equation 4-36 Pressure drop for a flow inside a tube 70
Equation 4-37 Wall shear stress for a flow through a rough tube 70
Equation 4-38 Shear rate at the tube wall in terms of pressure drop across the tube .. 70
Equation 4-39 Pressure drop in a U-tube manometer 70
Equation 5-1 Solute balance over crystallizer 76
Equation 5-2 Semi-batch solute balance 77
Equation 5-3 Dissolved lactose concentration differential for semi-batch mode 77
Equation 5-4 Overall mass balance 77

Equation 5-5 Condition for constant operation. Volumetric rate of feed equal to volumetric rate of water removal 78

Equation 5-6 Dissolved lactose concentration differential for continuous mode 78

Equation 5-7 Mean residence time 78

Equation 5-8 Zeroth moment derivative 79

Equation 5-9 First moment derivative 79

Equation 5-10 Second moment derivative 79

Equation 5-11 Third moment derivative 79

Equation 5-12 Fourth moment derivative 79

Equation 5-13 Coefficient of variation of a size distribution 79

Equation 5-14 Slurry voidage 80

Equation 5-15 Rate of change of slurry voidage 80

Equation 5-16 Volume weighted mean diameter 80

Equation 5-17 Crystal content of the slurry 80

Equation 5-18 Total solids in the slurry 80

Equation 5-19 Slurry density-total solids relationship 81

Equation 5-20 Primary nucleation rate 81

Equation 5-21 Secondary nucleation rate 81

Equation 5-22 Growth rate 81

Equation 5-23 Equilibrium α-lactose solubility 82

Equation 5-24 Correction factor for α-LMH 82

Equation 5-25 Equilibrium lactose solubility 82

Equation 5-26 Total dissolved lactose 82

Equation 5-27 Mutarotation rate constant 83

Equation 5-28 Dissolved α-lactose concentration 83

Equation 5-29 Equilibrium mutarotation rate constant as a function of temperature 83

Equation 5-30 Relationship between residence time and mean particle size 104

Equation 6-1 Converting volumetric distribution to population density distribution 125

Equation 6-2 Size dependent growth rate 127

Equation 6-3 Population density with size dependent growth rate 127

Equation 6-4 Growth rate from population density distribution 129

Equation 6-5 Cumulative size distribution with growth rate distribution 130

Equation 6-6 Converting cumulative number distribution to frequency distribution 131

Equation 6-7 Analytical solution for inverse gamma distribution function 131

Equation 6-8 Secondary nucleation rate due to attrition 143

Equation 6-9 Collision secondary nucleation 143

Equation 6-10 Modified Equation 4-20 for secondary nucleation due impeller-crystal collisions 148

Equation 6-11 Determination of collision nucleation rate constant and supersaturation dependence 148

Equation 6-12 Stokes number 152

Equation 6-13 Particle relaxation time 152

Equation 6-14 Turbulent eddy life time 152

Equation 6-15 Turbulent kinetic energy 153

Equation 6-16 Energy dissipation rate in a pipe flow 153

Equation 6-17 Shear velocity 153

Equation 6-18 Wall shear stress 153

Equation 6-19 Crystal RMS velocity 153

Equation 6-20 Constant in Equation 6-19 153

Equation 6-21 Crystal-crystal collision frequency 154

Equation 6-22 Kinetic energy of crystal-crystal contact 154

Chapter 1 Project Overview

The extraction of lactose from whey and milk permeates is achieved using the processes of concentration and crystallization. These occur together during the evaporative crystallization of lactose manufacturing. Despite being in operation over the last 50 years, the dynamic operation of the lactose evaporative crystallizers still present challenges, particularly around controlling the crystal size distribution (CSD). Crystal size is important for both edible lactose and refined/pharmaceutical manufacture for two reasons; first, the particle size has a large impact on the final yield, as small crystals are difficult to separate and process in the post crystallization unit operations and second, size is the defining parameter used to separate the different specifications of lactose.

Evaporative crystallization is the only unit operation in the manufacturing process of lactose where the crystal size distribution (CSD) can be controlled without the need for secondary classification and/or a mechanical unit operation. The use of milling to achieve the desired CSD impacts on the surface properties of the lactose crystals (an undesirable aspect for some end users); the degree to which this occurs depends largely on the initial particle size. Therefore, a dedicated study aimed at understanding the evaporative crystallization of lactose at industrial scale is warranted.

This project was based at the Kapuni lactose manufacturing facility of Fonterra Co-operative group. The intent was to understand how evaporative crystallizer is operated industrially and examine the impact each operational parameter had on crystallization. The framework for achieving this is described in Figure 1-1.

In order to predict the CSD as a function of operational parameters, a mathematical model of the industrial crystallizer was developed from energy, mass and population balance equations. The population balance equations include the crystal nucleation and the growth terms in their formulation. Lactose crystal growth and primary nucleation have been studied in great detail by McLeod (2007). The hypothesis arose

from McLeod's work that secondary nucleation plays the dominant role in evaporative crystallizers. Therefore, the main objectives of the thesis are:

1. Review: to review the existing literature on secondary nucleation, identifying the various forms and mechanisms of secondary nucleation and their dependence on the hydrodynamics of the industrial evaporative crystallizer.
2. Secondary nucleation science: to conduct experiments to study the individual secondary nucleation mechanisms and correlate the findings to theory. Where necessary this may include developing constitutive relationships to describe the observations.
3. Process modelling and performance: to formulate a mathematical model that describes the operation of the industrial evaporative crystallizer. Using this to perform a sensitivity analysis examining how the operational parameters affect the CSD. This also includes kinetic parameter estimation by fitting of the model results with the data measured from the crystallizer.

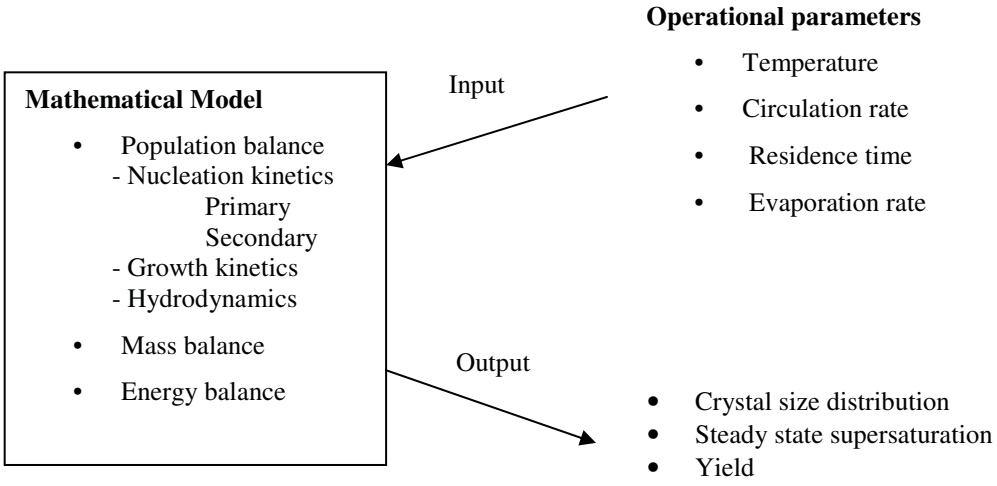


Figure 1-1. Framework for describing the crystallizer behaviour.

The thesis outline is as follows. Chapter 2 describes the crystallization fundamentals including supersaturation, crystallization kinetics, different evaporative crystallizer geometries and population balance equation theory. Chapter 3 covers a detailed qualitative critical review of secondary nucleation, enumerating and distinguishing between the various kinds of secondary nucleation and establishes the limitations of

the current knowledge. Chapter 4 contains laboratory scale experimental studies aimed at separating and developing a fundamental understanding of the secondary nucleation mechanisms for lactose. Chapter 5 deals with the development of the mathematical model describing the actual operation of the industrial crystallizer. A sensitivity analysis of the various operational parameters is also reported, based on the available literature parameters of lactose crystallization kinetics. Chapter 6 deals with the industrial crystallizer analysis and data collection for parameter estimation. Chapter 6 also develops the model from Chapter 5 to incorporate size dependent growth rate as an alternative to growth rate dispersion to match the measured CSD. Simulations using theoretical mechanistic models using parameters estimated in Chapter 4 are also conducted and compared to measured data. Chapter 7 summarizes the outcomes of the research along with the limitations of the findings and lists some possible new research areas.

Chapter 2 Crystallization Theory

A solution in equilibrium with the solid phase is said to be saturated with respect to that solute. This equilibrium state is given by the solubility curve of the solute-solvent combination as a function of temperature. However, a solution can hold more dissolved solute than the equilibrium value. Such a solution is termed a supersautrated solution and the magnitude of the excess dissolved solute is known as the degree of supersaturation. This can be used in place of chemical potential as the fundamental thermodynamic driving force for the crystallization process. Crystallization proceeds by two consecutive supersaturation driven events; (i), nucleation - the generation of new crystals (nuclei); and (ii), growth – where the nuclei formed become larger crystals by subsequent deposition of solute on them.

Ostwald (1897) (cited in Tavare (1995)) introduced the terms *labile* and *metastable*, referring to supersaturations at which spontaneous formation of the solute phase, in the absence of crystallizing material, *will* (in labile) or *will not* (in metastable) occur as shown in Figure 2-1. The width of metastable zone is however variable, influenced by factors like fluid dynamics, rate of supersaturation generation and the presence of dissolved impurities. A more detailed discussion on nucleation follows.

2.1 Nucleation

The various mechanism by which nucleation occurs along with the sub-classifications are shown in Figure 2-2. Nucleation happens via one of two mechanisms, primary or secondary. Primary nucleation occurring directly from a supersaturated solution is either homogeneous or heterogeneous. Primary nucleation occurs readily at high supersaturations (labile zone) and less likely to occur in metastable zone. Homogeneous nucleation occurs directly from solution, whereas heterogeneous nucleation occurs on a foreign surface like dust particles; this reduces the energy required for the creation of nuclei and hence occurs at relatively lower supersaturation, as shown in Figure 2-1. Secondary nucleation involves active participation of the solute crystals already present through various mechanisms shown

in Figure 2-2. It has the lowest energy barrier for nuclei formation and occurs at the lowest supersaturation.

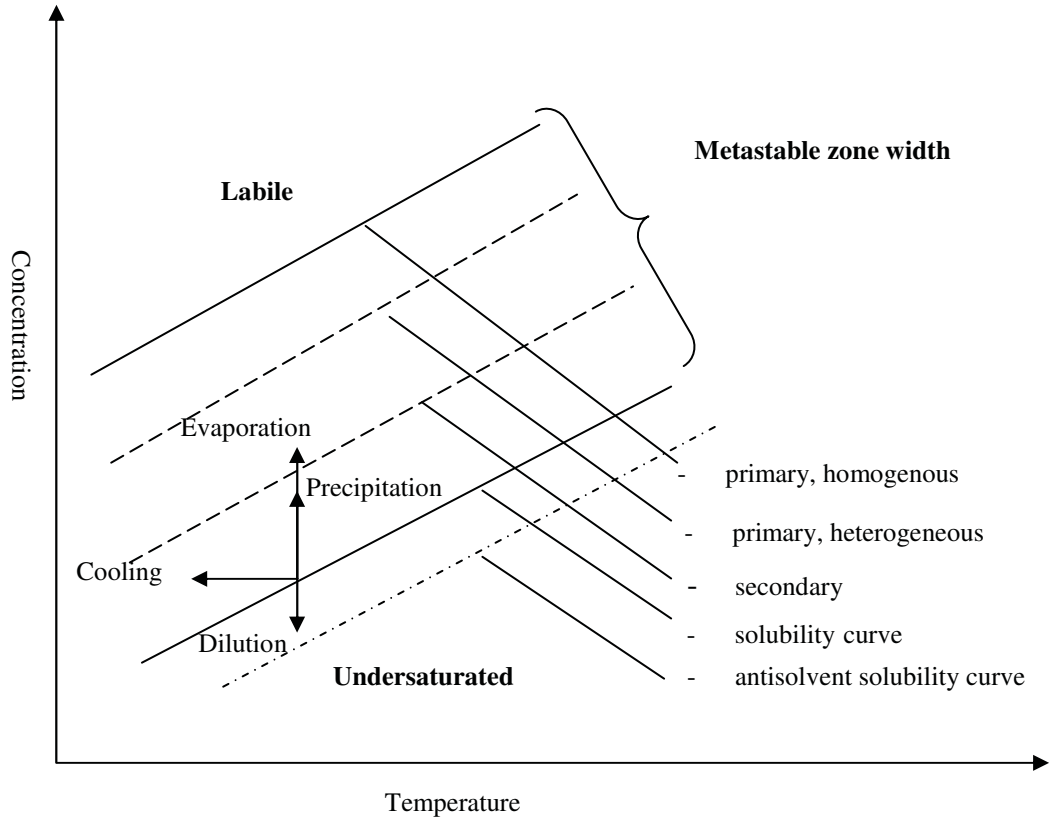


Figure 2-1. Solubility diagram, supersaturation generation and crystallization kinetics [adapted from Mersmann (2001b) and Jones (2002)]. Anti-solvents lower the solubility of the solute. On anti-solvent addition (refered to as dilution in the figure), the excessive solute (defined by the anit-solvent solubility curve) precipitates out. Chemical reaction leading to high concentrations of the new generated species can also trigger precipiation.

Primary nucleation is typically prevailing only during the start up phase of a crystallization process which is not seeded. Once a sufficient number of crystals have formed and supersaturation drops within the metastable regime, secondary nucleation becomes the dominant mechanism for generation of new nuclei. This is the case for many industrial crystallizers, which operate at high crystal loading and supersaturations in the metastable regime. Secondary nucleation is thus, the main focus of this work. A qualitative review on secondary nucleation in general and on lactose in particular is presented in Chapter 3. A quantitative comparison of the available secondary nucleation studies on α-LMH is conducted in Chapter 5.

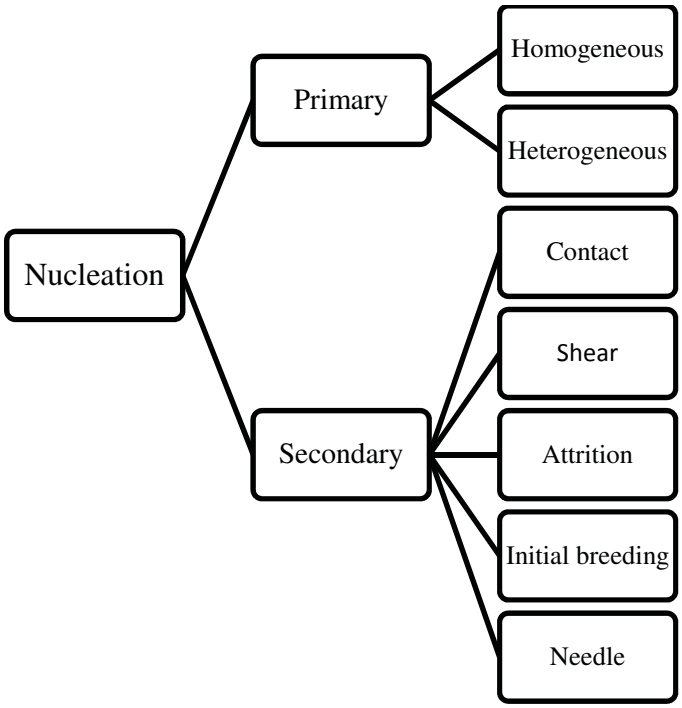


Figure 2-2. Nucleation mechanisms [adapted from Randolph & Larson (1988)].

2.2 Growth

Crystal growth happens by two steps; (i), diffusion of the solute to the crystal surface; followed by (ii), incorporation (surface integration) into the crystal lattice. The crystal growth rate is either diffusion or surface integration controlled. When diffusion is the controlling mechanism, the crystal growth rate increases as the relative velocity between the crystal and the solution in which it is suspended (extent of mixing) increases. This is due to decrease in the diffusion resistance because of thinning of the mass transfer boundary layer. A transition point is reached when it becomes surface integration controlled as shown in Figure 2-3 (Genck, 2003). Thereafter, the growth rate increases very weakly with an increase in the relative velocity because the growth is no longer controlled by the rate of diffusion of solute molecules to the crystal surface but by the rate at which they are incorporated onto the crystal structure. Growth by surface integration steps can be explained by various models namely: continuous growth, birth & spread and screw dislocation (Randolph & Larson, 1988).

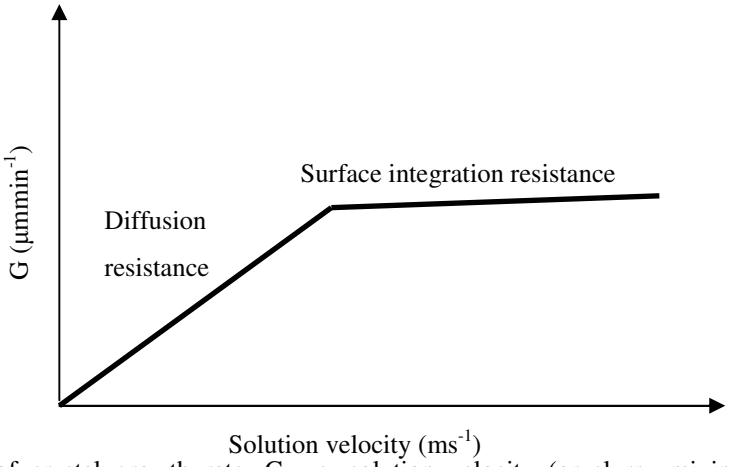


Figure 2-3. Plot of crystal growth rate, G, vs. solution velocity (or slurry mixing) showing the mechanism governing crystal growth (Genck, 2003).

The dependence of growth kinetics on hydrodynamics for lactose can be experimentally proven by the plot of growth rate versus agitation rate shown in Figure 2-4, reproduced from McLeod (2007). The growth rate initially increases as the agitation rate increases and then tends to constant above 300 rpm. This was attributed to a complete suspension of all the seed crystals at an agitation speed of 300 rpm and above. In a well mixed system suspension the lactose growth rate should be constant and dominated by surface integration resistance. A quantitative comparison of α-LMH growth rates reported by various studies is presented in Chapter 5.

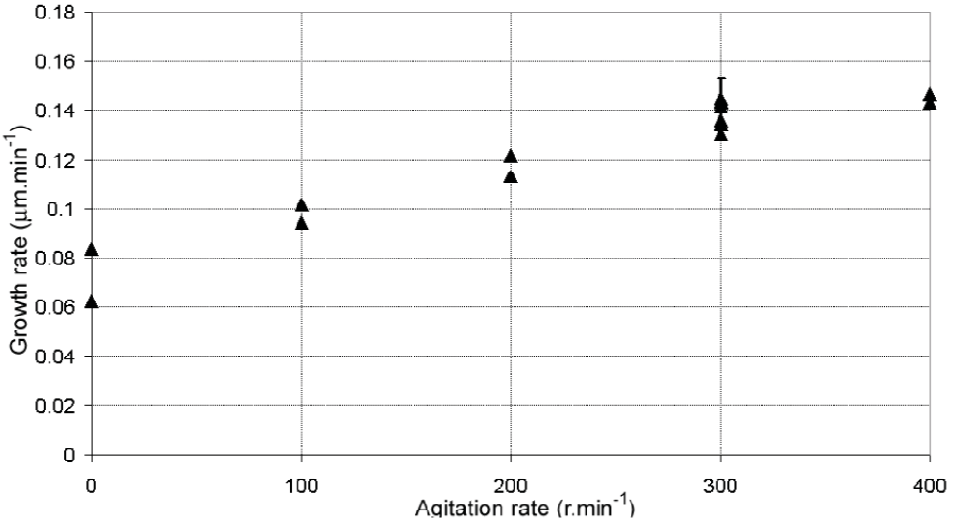


Figure 2-4. Effect of agitation speed on lactose growth rate at a supersasturation of 5.23 g per 100 g of water at 30°C (McLeod, 2007).

2.3 Lactose

Lactose is the major dissolved component of whey, a by-product of cheese manufacturing. Ultrafiltration is used to recover the whey proteins, and the material that passes (permeates) through the membranes is the starting material for lactose crystallisation. Excluding the water fraction, this whey permeate contains approximately 80 percent lactose with the rest being mineral salts and other minor milk components. For alpha-lactose monohydrate production, the whey permeate is concentrated to around 58-75% total solids in a series of evaporation steps, which may include evaporative crystallization. The solution is then cooled to recover more lactose from the mother liquor. The crystals are then separated from the mother liquor by centrifugation and dried.

In solution, lactose is present in two anomeric forms: alpha (α) and beta (β). β-lactose has a greater solubility and sweetness than alpha. The equilibrium ratio between the two forms is affected by temperature (Roetman & Buma, 1974) and pH (Troy & Sharp, 1930). α-Lactose, which is the major form of lactose produced industrially, crystallizes out as a monohydrate and grows with a typical tomahawk shape as shown in Figure 2-5 (van Kreveld & Michaels, 1965). As crystallization proceeds more and more β-lactose converts to α-lactose to maintain the equilibrium. β-lactose crystallizes out only at temperatures greater than 93.5 °C as an uneven sided diamond
.

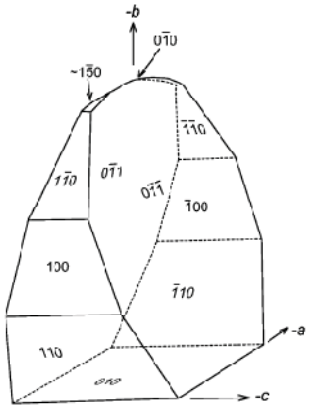


Figure 2-5. α-lactose tomahawk morphology [reproduced from van Kreveld & Michaels (1965)]

The physical, mechanical and thermal properties of α-LMH crystals, lactose solution and slurry are included in Appendix I.

2.4 Industrial Crystallizer

Supersaturation is typically achieved via one of two methods, evaporation or cooling. Cooling exploits the decreased solubility that occurs as the temperature is decreased in systems like lactose solutions. It has the advantage that it only requires the removal of sensible heat. Evaporation is used as a tool to concentrate the solution. Because it can theoreitically occur up to the point where 100% of the solvent is removed, it offers the opportunity for much higher yields than cooling alone. However, since it requires a phase change in the solute, it is a more energy intensive process.

Three widely used continuous crystallizers in industry are; i), Forced Circulation (FC) ii), Draft Tube and Baffled (DTB) iii), Fluidized bed/ Oslo. The mean crystal size that can be obtained from each of these is shown in Figure 2-6. Each of these crystallizers has a slurry suspended in a forced circulation loop, which keeps the supersaturation within the metastable zone, preventing primary nucleation. The circulation ensures uniform distribution of the generated supersaturation and the presence of crystals in the zones of higher supersaturation (boiling zone and feed entry) provides surface for growth which subsequently lowers the solution supersaturation. Additional design features used in the DTB and fluidized bed compared to FC crystallizers results in production of coarser crystals. These are discussed below:

i) A FC crystallizer (Figure 2-7) circulates the entire magma through an external loop using a circulating pump. This results in higher secondary nucleation than the other two designs, reducing the mean size of the particles (200-600 micron).

ii) A DTB uses an annular settling zone (Figure 2-8) from which only the mother liquor, bearing fines, is circulated back along with the fresh feed after passing through a fines destruction loop. The gentle conveying of the suspension, the removal of fine crystals as well as the classifying effect, aid in increasing the crystal size. This makes the DTB crystallizer ideal for the production of medium coarse to coarse crystals (500 -1500 micron).

iii) In the case of a fluidized bed crystallizer there is no circulating agitator, with the energy of the upward flowing fluid used to keep the crystallizer in a fluidized state in the annular space surrounding the downcomer (Figure 2-9). This further reduces the rate of secondary nucleation and results in production of still larger crystals (1000-2000 microns).

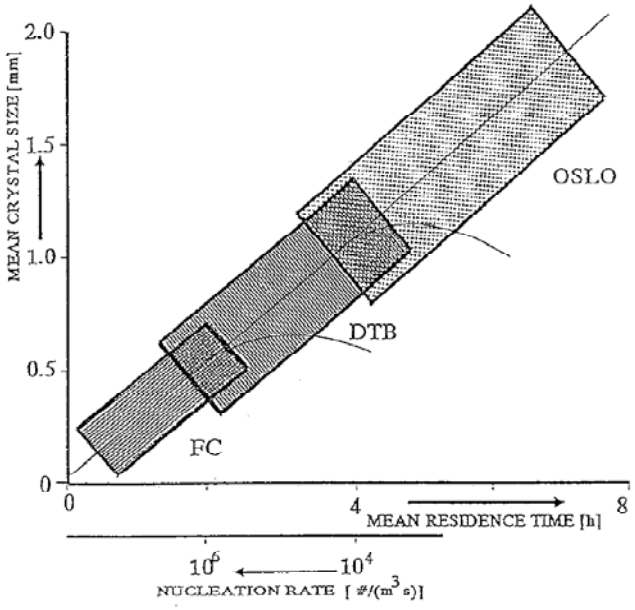


Figure 2-6. Mean crystal size produced by different industrial crystallizers as a function of residence time and nucleation rate [reproduced from Wöhlk, Hofmann, & de Jong (1991).

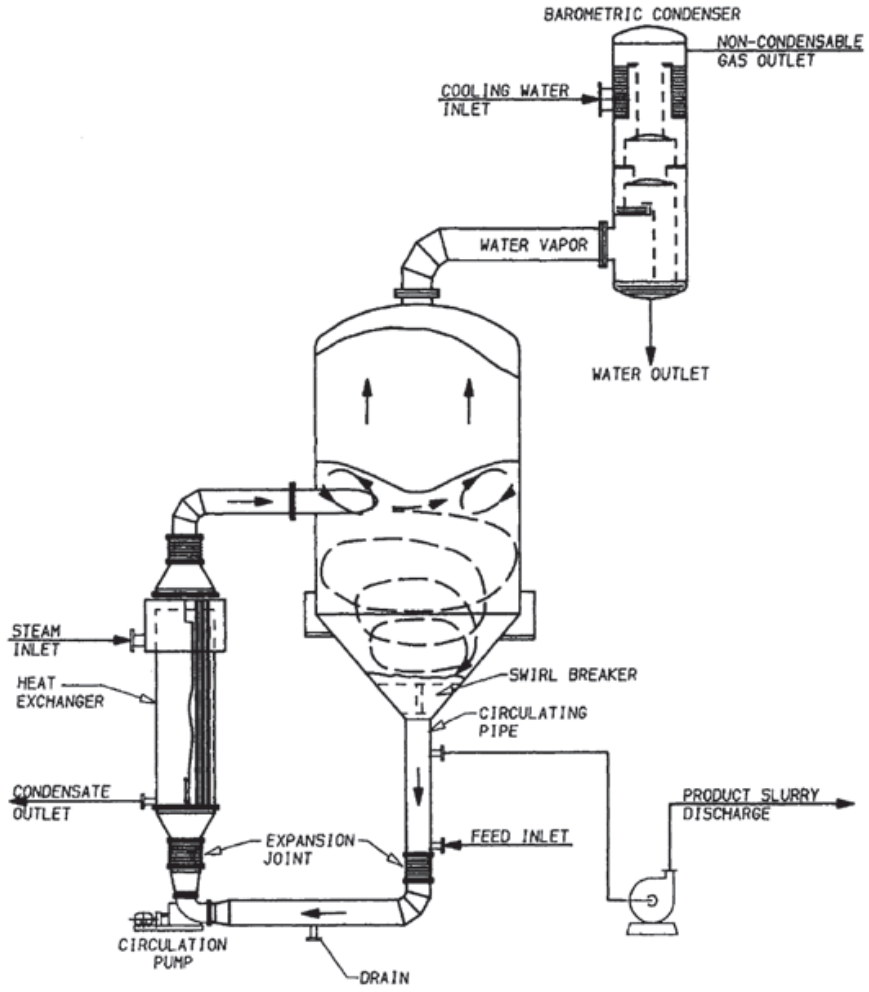


Figure 2-7. Forced circulation evaporative crystallizer [reproduced from Bennet (2002)].

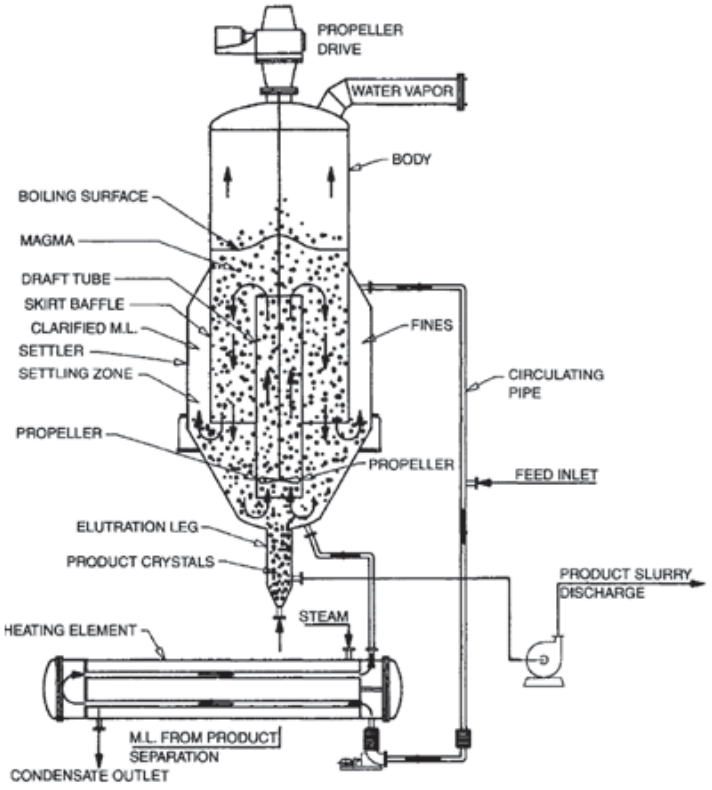


Figure 2-8. DTB crystallizer [reproduced from Bennet (2002)].

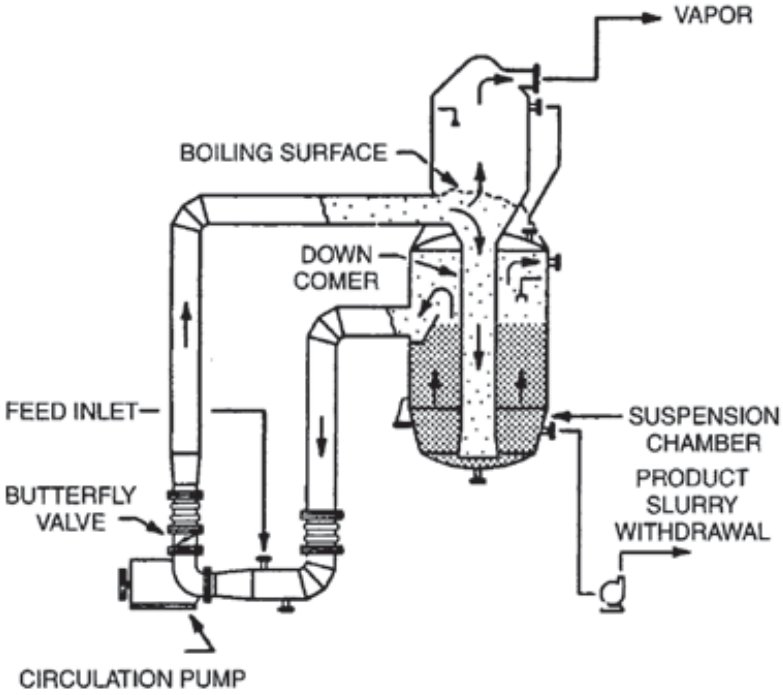


Figure 2-9. Fluidized bed crystallizer [reproduced from Bennet (2002)].

2.4.1 Forced Circulation Evaporative Crystallizers

The industrial unit being studied in this work is a forced circulation crystallizer situated in one of the Fonterra's lactose producing facilities. Selected dimensions and operational parameters of the studied crystallizer are presented in Appendix II. More details cannot be given due to commercially sensitive nature of the information. FC crystallizers are found in sizes ranging from 0.6 m for laboratory equipment up to over 12 m in diameter for industrial applications.

A FC crystallizer consists of two main components:

1. The evaporator cum crystallizer unit
2. The external circulation circuit consisting of the pump and the heat exchanger

The crystallizer consists of a cylindrical vessel with a dished head with a conical base, called the 'separator'. A swirl or vortex breaker is fitted into the conical base. The crystallizer body provides most of the total volume of a FC unit. It is sized to accommodate the boiling zone where supersaturation is realised and provides the majority of the residence time for crystals to grow (Neumann, 2001).

The axial flow pump in the external circulation loop forces the slurry from the separator to the heat exchanger and back to the separator. The slurry gains the energy for solvent vaporization in the heat exchanger with boiling occurring inside the heat exchanger/calandria tubes or in the separator; depending on the design. If the calandria is submerged as shown in the Figure 2-7, the hydrostatic head prevent boiling inside the tubes. The industrial crystallizer under study is a boiling in tube type crystallizer. The forced circulation aids in heat transfer, maintaining a homogenous suspension and effective distribution of the generated supersaturation throughout the crystallizer. This helps in keeping the supersaturation within the metastable zone limit, preventing primary nucleation event. The circulation pump speed needs to be kept at minimum what is hydraulically possible to minimize crystal attrition (Mersmann, 2001b).

Introduction of feed just upstream of the pump, where turbulence is high, helps in effective mixing of the hot concentrated feed. However, the specific power input for FC crystallizer is much larger than for conventional stirred tank crystallizers and this makes them a poor choice for the crystallization of fragile materials (Green, 2002).

2.5 Modelling

The general framework to describe crystallizer behaviour was described in Chapter 1. However, it is not exactly a single direction flow of information from the input parameters to the output results, as shown in Figure 1-1. Feedback interactions occur between the model output (CSD, supersaturation) and the model constituents (mass and population balance) as shown in Figure 2-10, adapted from Randolph & Larson (1988). The hydrodynamics of the system are determined by the operating conditions and play a big role in nucleation kinetics, especially secondary nucleation. Hydrodynamics and its interaction with secondary nucleation are discussed in greater detail in Chapters 4 and 6 which deals with lab scale experiments and industrial crystallizer analysis, respectively.

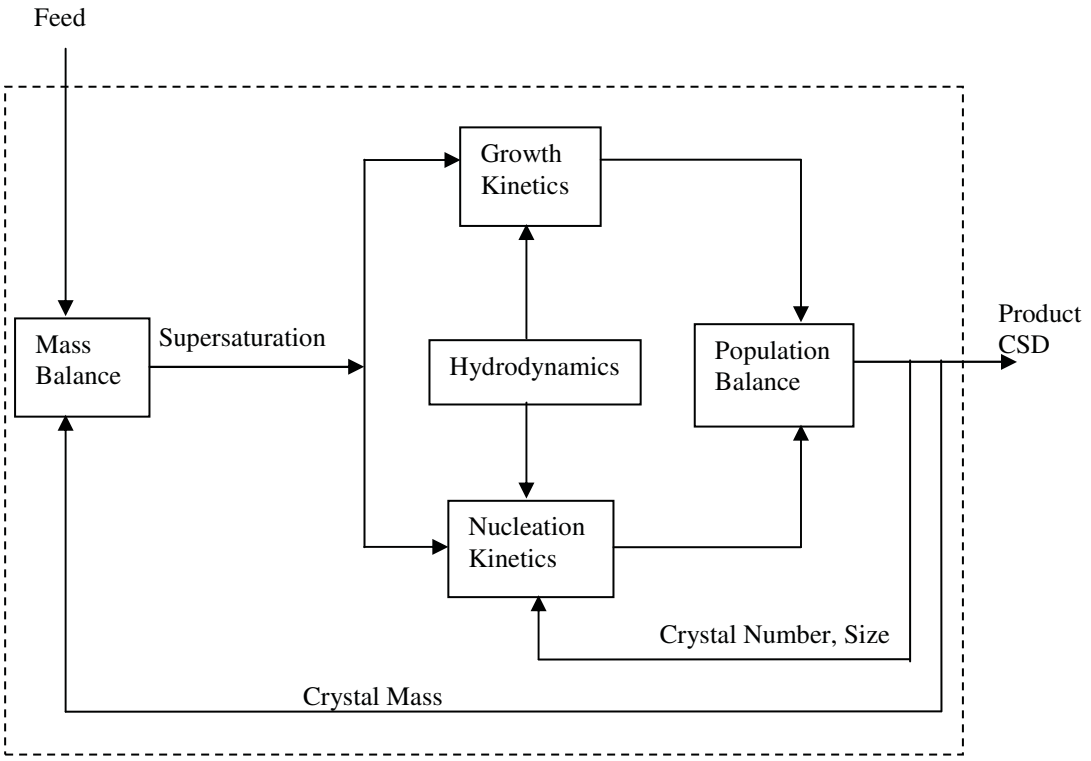


Figure 2-10. Feedback interactions between various factors effecting crystallization [adapted from Randolph & Larson (1988)].

This study aims to model these interactions and to examine the effect of various operating conditions on the crystal size distribution (CSD). The CSD can be modelled using a population balance equation (PBE). PBE deals with the number balance of crystals across both time and size domain. The population balance scheme

for crystallization has been discussed in great detail by Randolph & Larson (1988). A population balance, along with the mass balance, will adequately describe the evaporative crystallization of lactose as developed in Chapter 5. The unsteady state population balance for a continuous constant volume, isothermal, well mixed crystallizer with no agglomeration and breakage is given by

$$\frac{\partial n(L,t)}{\partial t} = -G\frac{\partial n(L,t)}{\partial L} - \frac{n(L,t)}{\tau}.$$

Equation 2-1 Population balance equation

The validity of the above mentioned assumptions for the current system is discussed in Chapter 6. The term on the left hand side (LHS) of Equation 2-1 gives the rate of change of crystal number density where *n(L,t)* is the number density function. *L* and *t* refer to the size and time domain respectively. The first term on the right hand side (RHS) gives the net change in crystal number density due to growth in and out of the size interval *dL*, where *G* [μm min^{-1}] is the size independent growth rate given by *dL/dt*. Size independent growth rate is used in the basic model development in Chapter 5. More complex growth models (size dependent and growth rate dispersion) are discussed in Chapter 6. The second term on the RHS of Equation 2-1 gives the number of crystals within the size interval *dL* that enter and leave the system with the inflow and the outflow of the slurry. The symbol τ is the residence time of the crystallizer [min]. For a batch process ($\tau=\infty$), there is no flux of material entering or leaving the system, so the second term on RHS disappears to give

$$\frac{\partial n(L,t)}{\partial t} = -G\frac{\partial n}{\partial L}.$$

Equation 2-2 Population balance equation for a batch process

For a steady state continuous operation, where the flux of material entering and leaving the system is equal, the term on the LHS of Equation 2-1 disappears to give

$$G\frac{dn}{dL} = -\frac{n}{\tau}.$$

Equation 2-3 Population balance equation for a continuous process

Solving the above equation leads to

$$n\,(L) = \; n_0 \exp\left[-\frac{L}{G\,\tau}\right],$$

Equation 2-4 Population density for a steady state continuous process

where n_0 is the population density of nuclei (zero-size crystal) [# μm^{-1} (kg of slurry)$^{-1}$]. Equation 2-4 is only valid for a mixed suspension mixed product removal (MSMPR) continuous crystallizer. It assumes that the slurry in the crystallizer is well mixed and there is no product classification i.e. no preferential withdrawal of larger crystals occurs. A plot of ln *n* versus *L* (Figure 2-11) gives a straight line with an intercept at *L=0* equal to ln n_0 and a slope of *-1/Gτ*. By knowing the residence time (τ), the linear growth rate of crystals, *G* can be found.

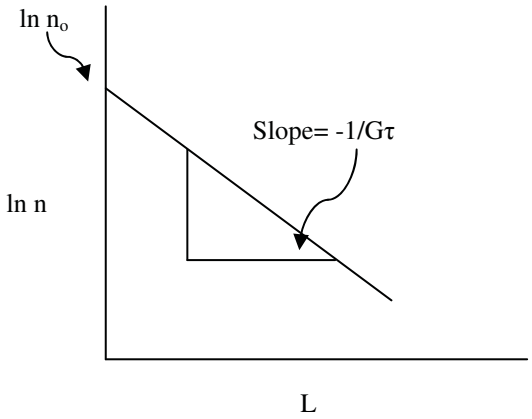


Figure 2-11. Semi logarithmic plot of population density versus crystal size for an MSMPR continuous crystallizer**.**

Knowing the nuclei population density and growth rate, the nucleation rate *B* [# min^{-1} (kg of slurry)$^{-1}$] can be calculated as

$$B = n_o G\,.$$

Equation 2-5 Nucleation rate calculation for MSMPR crystallizer

The above analysis has been used to determine the overall nucleation rate and growth rate for lactose in the past (Griffiths, Paramo, & Merson, 1982; Shi, Liang, & Hartel, 1990). As the MSMPR technique involves crystal slurries, secondary nucleation will preferentially occur and hence the reported nucleation rates will be dominated by secondary nucleation. For implementing the MSMPR analysis, population density distribution is required. However, the most common techniques for CSD measurement (sieve analysis and laser diffraction particle analyzer) yields volumetric

or mass distribution and hence needs to be converted to a population density distribution. The procedure for this is explained in Chapter 6, which deals with the industrial crystallizer analysis. Now the two principle techniques to solve the unsteady state PBE used in this work are discussed.

2.5.1 Method of Moments (MOM)

The various moments of the number density distribution reveal the total number of crystals, surface area and volume of crystals present per unit of slurry suspension. The different moments along with the various mean sizes based on moments are presented in Table 2-1.

The method of moments converts the population balance partial differential equations into a set of ordinary differential equations (ODEs) which can be solved along with the mass and energy balances to adequately describe the crystallizer system. MOM has two disadvantages; (i), a unique CSD cannot be reconstructed from a finite set of moments; and (ii), systems exhibiting size dependent growth rate may not be modelled (Abbas & Romagnoli, 2007). However, for bulk industrial crystallization processes, knowledge of the mean crystal size is often sufficient and a complete CSD is not required. Also, the ease of implementation of MOM has made them a very popular technique to model crystallization systems (Markande, Nezzal, Fitzpatrick, & Aerts, 2009; Tavare & Chivate, 1977; Ward & Yu, 2008). MOM is used in the preliminary crystallizer model development in Chapter 5 of this thesis.

Table 2-1 *Various Moments of Density Distribution and Mean Crystal Sizes*

Moment definitions	Parameter measured	
	General	MSMPR
$m_0 = \int_0^\infty ndL$	Total crystal number per unit slurry suspension $N_T = m_0$	$N_T = n_0 G\tau$
$m_2 = \int_0^\infty L^2 ndL$	Total crystal surface area per unit slurry suspension $A_T = k_a m_2$	$A_T = 2k_a n_o (G\tau)^3$
$m_3 = \int_0^\infty L^3 ndL$	Total crystal volume per unit slurry suspension $\varphi = k_v m_3$	$\varphi = 6k_v n_o (G\tau)^4$

Mean crystal sizes	General	MSMPR
Number weighted L[1,0]	$\frac{m_1}{m_o}$	$G\tau$
Surface area weighted L[3,2]	$\frac{m_3}{m_2}$	$3G\tau$
Volume weighted L[4,3]	$\frac{m_4}{m_3}$	$4G\tau$

k_a and k_v are the area and volume shape factors respectively

2.5.2 Discretization

The disadvantages of MOM are overcome by discretization of the partial differential equation along either the length domain or both the time and length domains. Method of lines (MOL) is a commonly used technique (Abbas & Romagnoli, 2007; Griffin, Mellichamp, & Doherty, 2010; Quintana-Hernández, Bolaños-Reynoso, Miranda-Castro, & Salcedo-Estrada, 2004) for solving the population balance PDEs. In MOL, the PDE is discretized along the linear size domain, resulting in the formation of a set of ODEs which can be solved numerically. The discretization can be done using various finite difference schemes. The following set of ODEs has been derived using a second order finite difference scheme in length as they show less oscillations than

higher order approximation while providing satisfactory numerical efficiency and accuracy (Griffin, et al., 2010).

$$\begin{cases} \dfrac{dn(L_0)}{dL} = \dfrac{-3n(L_0) + 4n(L_1) - n(L_2)}{2\Delta L} + -\dfrac{n(L_0)}{\tau} \\ \dfrac{dn(L_i)}{dL} = \dfrac{n(L_{i+1}) - n(L_{i-1})}{2\Delta L} - \dfrac{n(L_i)}{\tau}, i = 2,3 \dots p-1 \\ \dfrac{dn(L_p)}{dL} = \dfrac{4n(L_p) - 7n(L_{p-1}) + 4n(L_{p-2}) - n(L_{p-3})}{2\Delta L} - \dfrac{n(L_p)}{\tau} \end{cases}$$

Equation 2-6 Discretized Method of lines for solving population balance equation

where, $\Delta L = L_i - L_{i-1}$ and p is the number of discretized intervals and $p+1$ is the number of grid points. The first equation in the set represents the condition where the production of nuclei at the smallest size occurs. No direct nucleation occurs at higher size ranges. The upper boundary condition for the crystal size is chosen such that the number of crystals at that size can be assumed to be zero. It is imperative for the mass balance to hold that the CSD does not outgrow this maximum limit. The upper boundary depends on the various crystallization mechanisms, as well as the residence time for a continuous or batch time for a batch process. It therefore needs to be checked and modified whenever the operational or kinetic parameters of the system change. The MOL is used in Chapter 6 to allow implementation of size dependent growth rate in order to fit the observed CSD from the industrial crystallizer.

2.6 Conclusions

This chapter covers the fundamentals of the crystallization theory. The discussion has been kept to minimum essential as there are numerous handbooks in the literature which provide very elegant studies on each of the topics. However, there has been in general, a scarcity of detailed discussion on secondary nucleation, which plays the dominant role in industrial crystallizers. The next chapter contains a critical literature review of the secondary nucleation phenomenon.

Chapter 3 Literature Review on Secondary Nucleation

In crystallizers with a large number of solute crystals present, the crystal surface area catalyses secondary nucleation, making it the dominant mechanism. While the literature contains a large body of work which attempts to unravel the mysteries of secondary nucleation, there is still ambiguity over its exact mechanism. This chapter considers this research as it relates to crystallization of lactose and other small organic and inorganic compounds.

As discussed in Chapter 2, secondary nuclei originate in the presence of crystal surfaces. The literature supports two possible mechanisms for how this may occur. One proposes that the nuclei originate from the solid crystal and the other that they are formed from the solution layer adjacent to the crystal surface.

Garside, Rusli, & Larson (1979) provided photographic evidence of micro attrition at the surface of a potash alum crystal, which, after it was 'touched' with a rod, produced 5-50 microns fragments. By colliding a PVC rod with a potassium hydrogen phthalate (KAP) crystal and then analyzing the scanning electron microscope (SEM) images collected during the process, Van der Heijden, Elwenspoek, & van der Eerden (1989) demonstrated that secondary nuclei were formed due to attrition of the parent crystal and hence the crystal itself was the source of secondary nuclei.

This mechanism, where secondary nuclei originate from the crystal itself, can also occur by; (i), initial breeding; or (ii), dendritic or needle breeding. Initial breeding is important only in a seeded crystallization process when the fines adhering to the surface of the seed crystals get dislodged, acting as nucleation sites. This can be minimized by pretreating the seed crystals with an appropriate solvent. The number of fines on a seed crystal surface is finite and therefore, initial breeding cannot be a sustained source of nucleation. At high supersaturations, needle or dendritic growth occur over the crystal surface. These then detach from the main crystal due to mechanical forces and grow as independent crystals (Clontz & McCabe, 1971). Due

to the requirements of high supersaturation, needle breeding is unlikely to happen in industrial crystallizers (Myerson & Ginde, 2001). Hence, attrition which involves mechanical removal of material from the crystal surface and is active at lower supersaturations, is only considered in this review. The other possible source, the solution layer adjacent to crystal surface is now discussed.

Friej, Reyhani, & Parkinson (1998) used atomic force microscopy (AFM) to study the impact of sliding a potash alum crystal against a glass slide. They found no evidence of mechanical attrition on the parent crystal and reported generation of numerous secondary nuclei on the glass slide. This supports the presence of an ordered solute layer at the crystal surface as the source of secondary nuclei. Further evidence of solute layer induced secondary nucleation is provided by Qian & Botsaris (1998) who examined the nucleation of a chiral molecule (sodium chlorate). Nucleation was examined under both stagnant and agitated conditions using an immobilized single seed crystal. Once the supersaturation exceeded a certain limit, but still lower than that required for spontaneous primary nucleation, many nuclei of *opposite* chirality to that of the seed were formed. This suggests that the solution around the parent crystal (which contains molecules of both chirality) was the source of secondary nuclei. They also found that at lower supersaturation levels, chirality of the nuclei formed were identical to the seed crystal. This was explained by the conventional secondary nucleation (CSN) mechanism in which seed crystals act as the source of the nuclei either by needle breeding or micro-attrition either due to collision or fluid shear. McBride & Carter (1991) observed that, when a sodium chlorate crystal was subjected to multiple contacts with a magnetic stirrer, thousands of crystals with the *same* chirality as the parent crystal were formed. No damage to the parent crystal was observed suggesting that attrition was not the source of the new nuclei. It was concluded that these nuclei had been incorporated in the parent crystal structure enough to acquire its configuration but were cleaved away from the conformation surface by the stirrer contacts. Further proof of contact nuclei carrying crystallographic information from the parent crystal is provided by Friej, et al., (1998), Reyhani & Parkinson (1996), and Reyhani, Freij, & Parkinson (1999). A strong connection was found between the morphology of the secondary nuclei formed and the face of the parent crystal contacted with a glass slide. They observed the

growth of secondary contact nuclei using an atomic force microscope. The movement and growth of the steps on the baby crystal surface was similar to that of the parent crystal. Elankovan & Berglund (1987) reported generation of two crystal forms of dextrose (alpha-monohydrate and alpha anhydrous) from the contact of a parent crystal of only one form (alpha anhydrous). This again suggests that the layer near the growing crystal is the origin of secondary nuclei as it would contain both conformers.

Nuclei need to attain a critical size to be stable and to grow; below this they quickly dissociate back into the solution. How crystals reach this critical size in the boundary layer surrounding the crystal can be understood by the Embryo Coagulation Secondary Nucleation (ECSN) theory (Qian & Botsaris, 1997). According to ECSN, the solute clusters, which are also called embryos present in a supersaturated solution (as predicted by classical nucleation theory), are attracted by the van der Waals force of the seed crystal. The high concentration of these embryos in the vicinity of crystals results in their rapid coagulation, leading to formation of nuclei greater than the critical size. A collision impact or fluid shear forces can then dislodge these nuclei to the bulk where they can grow as independent crystals. In order to distinguish this from attrition (physical removal of solid material from the crystal surface) due to collision, secondary nucleation by solute layer removal by collision impact will hereafter be referred to as contact nucleation. Tai, Wu, & Rousseau (1992) argued that fluid shear and contact acted similarly in removing the clusters off the surface of the crystal. A contact is, however, more effective than fluid shear in producing secondary nuclei because the impact force gives a larger disturbance to the adsorbed layer of the solute that has not yet become crystalline. Contact nucleation occurs at lower energy levels than those required for attrition and is the most important source of nuclei in a mixed suspension (Randolph & Larson, 1988).

Based on the above discussions, a mechanistic classification of secondary nucleation mechanisms occurring in industrial crystallizers is proposed in Figure 3-1. There are two main sources, collision and fluid shear; and two main mechanisms, attrition and solute layer removal. Collisions primarily occur either between crystal-impeller or between crystal-crystal. Due to significantly lower velocities of crystal-crystal

collision compared to crystal-impeller contacts (Bennett, Fiedelman, & Randolph, 1973), solute layer removal can be concluded to be the only viable mechanism for crystal-crystal collisions. Next the specific mechanisms of collision and shear induced secondary nucleation are discussed.

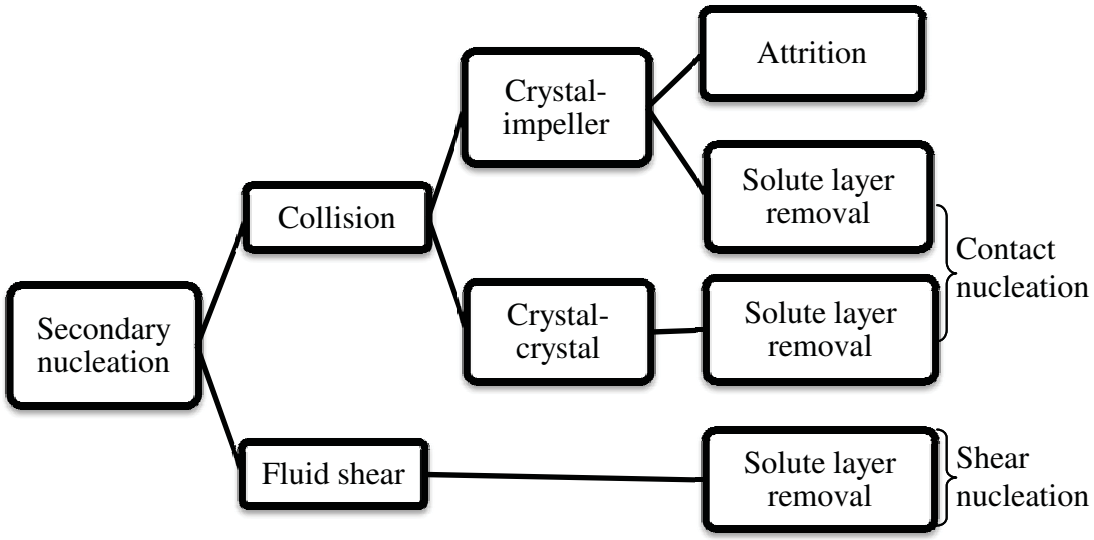


Figure 3-1. Secondary nucleation classifications as applicable to an industrial crystallizer.

3.1 Collision Induced Secondary Nucleation

Collision nucleation occurs either by the removal of some pre-ordered solute layer near the crystal surface, called as contact nucleation, or by attrition at the crystal surface. Since both mechanisms can occur simultaneously in a stirred crystallizer, it is difficult to distinguish them, but based on the experimental conditions and methodology, the relative dominance of one mechanism over the other can be gauged. The following two subsections discuss the experimental methods researchers employ to study these two collision induced mechanisms, starting with attrition.

3.1.1 Attrition

Attrition results in physical damage to the crystal with the fragments from the parent crystal acting as secondary nuclei. Attrition can occur in all industrial crystallization processes due to the presence of high speed moving parts like pumps and stirrers and the fragile nature of many crystalline compounds. It occurs due to high energy

contact of crystals or due to high fluid turbulence (Synowiec, Jones, & Ayazi Shamlou, 1993).

Attrition differs from contact nucleation which is due to the removal of an ordered solute layer from the crystal-solution interface without any apparent damage to the parent crystal. Contact nucleation requires the solution to be supersaturated whereas attrition, being a mechanical process, does not. For studies conducted in non-solvent or saturated solutions and/or involving high energy collisions of brittle compounds, attrition will be the major source of secondary nucleation. The damaged parent crystals, as well as macro attrition fragments (secondary nuclei) are evident immediately after the attrition event because of their larger size than nuclei produced at molecular level due to contact or shear nucleation. In the case of contact nucleation, no apparent damage to crystals occurs and there is a time delay in appearance of the contact nuclei (for nuclei to grow to a detectable size).

Since attrition is a mechanical process, to isolate it from other mechanisms, the studies are conducted in either non-solvents for solutes (Biscans, Guiraud, Laguérie, Massarelli, & Mazzarotta, 1996b; Bravi, Di Cave, Mazzarotta, & Verdone, 2003; Crawley, Gruy, & Cournil, 1996; Synowiec, et al., 1993) or saturated solutions of solute (Biscans, 2004; Biscans, Chemini, Guiraud, & Laguerie, 1996a) or in air (Gahn & Mersmann, 1997). Different techniques have been used to monitor and quantify the attrition phenomenon. These include sieving (Bravi, et al., 2003; Synowiec, et al., 1993), turbidity measurement (Crawley, et al., 1996), laser diffraction (Biscans, et al., 1996b; Dorofeeva, Kol'tsova, & Gordeev, 2006), electrical zone sensing method (Blem & Ramanarayanan, 1987; Garside, et al., 1979), photographic evidence (Biscans, 2004; Garside, et al., 1979; van der Heijden, et al., 1989) and weight loss measurements of individual crystals after impact with a target (Biscans, 2004; Gahn & Mersmann, 1997; Garside, et al., 1979; van der Heijden, et al., 1989).

Attrition fragments can show anomalous growth. This is discussed in detail in a review by Garside & Davey (1980). Garside, et al. (1979) and Rusli, Larson, & Garside (1980) observed that the potash alum microfragments, which were less than 5 micron, did not grow at all. The trend was also reported by Ó Meadhra, Kramer, &

van Rosmalen (1995) for ammonium sulphate fragments. This uncharacteristic growth behaviour exhibited by attrition nuclei has been related to the internal lattice strain incorporated during the attrition process (Bhat, Sherwood, & Shripathi, 1987; Ristic, Sherwood, & Wojciechowski, 1988). Ristic, et al. (1988) studied the Laue diffraction pattern of micro-crystals grown from secondary nuclei to measure the degree of lattice strain. They concluded that the variation in the lattice strain was the major cause of growth rate dispersion (GRD). The GRD concept was introduced to explain the observed distribution of growth rates for crystals under macroscopically similar hydrodynamic and thermodynamic conditions resulting in a broadening of the CSD. The growth rate was found to be inversely proportional to the incorporated strain. The increased strain in the crystal lattice of an attrition fragment increases its solubility, leading to a reduction in the driving force for growth (Gahn & Mersmann, 1999b) or even dissolution (Virone, ter Horst, Kramer, & Jansens, 2005). More specific details on attrition are covered in the next chapter.

3.1.2 Contact Nucleation

Contact nucleation studies involve contacting a crystal with a solid material like a glass rod/ slide and then monitoring the growth of the secondary nuclei formed. A commonly used experimental set up for studying contact nucleation is the photomicroscopic nucleation cell designed by Garside, et al. (1979), shown in Figure 3-2. In the work of Garside, et al. (1979), the seed crystal (2) glued to the support rod (4) was brought into contact with the glass rod by rotating the contact rod (3) about its axis. The temperature was regulated using a continuous water flow at the desired temperature through the lower chamber (6). Observation of any nuclei produced was then continued over time, using photomicroscopic images. Another approach used by the researchers was to slide a crystal over a cover glass slip (5) to produce secondary nuclei (Elankovan & Berglund, 1987; Reyhani & Parkinson, 1996; Shi, Hartel, & Liang, 1989; Shiau, 2003). Shiau (2003) used a modified version of the cell developed by Garside, et al. (1979) to study contact nucleation of sucrose. The former utilized a continuous flow of the solution through the growth chamber as against to the static conditions used by latter. This helped reduce the diffusion resistance to growth of the nuclei. All of the photomicroscopy studies had the

common problem that the energy of contact in the experiments was not quantified. It can, however, based on the experimental technique be gauged that the energy levels were low, supporting the hypothesis of removal of an ordered solute layer from the crystal surface as the source of secondary nuclei.

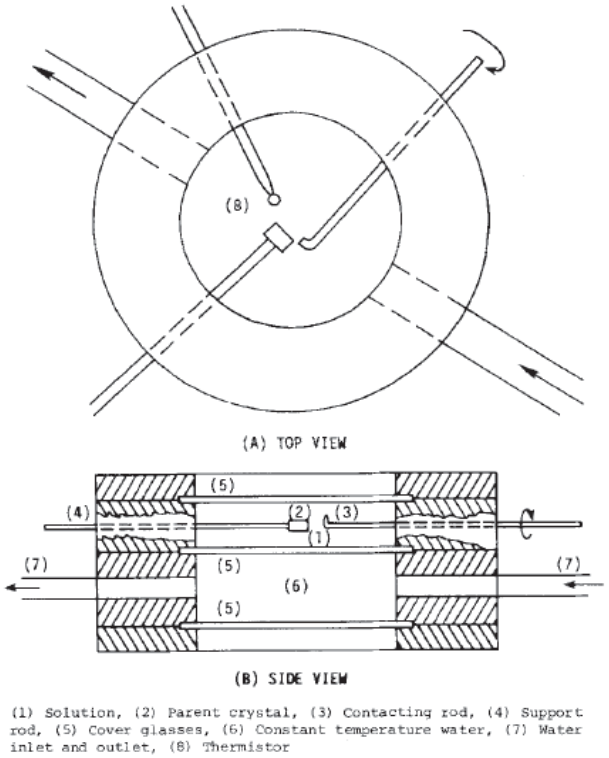


Figure 3-2. Contact nucleation photomicroscopic cell [reproduced from Garside, et al., (1979)].

To overcome the problem of knowing the energy of contact, nucleation can be induced by dropping a rod on the crystal surface from a known height and measuring the generated nuclei using a inline particle counter (Blem & Ramanarayanan, 1987; Garside, et al., 1979). Similarly, Clontz & McCabe (1971), Johnson, Rosseau, & McCabe (1972) and Tai, McCabe, & Rousseau (1975) used a flow system in which the contact nuclei, generated by dropping a known weight, in the form of a rod, were swept down to a growth chamber, allowed to grow and counted. They related the number of nuclei generated to the impact energy of the contact. Another method of quantifying the energy of impact was employed by Kubota & Kubota (1982). They induced multiple contacts between a glass impeller and a seed crystal suspended by a fine nylon thread. The position of collision of the crystal at the impeller was defined

and thus the collision energy was accurately quantified. The collision energy was varied by varying the mass of seed crystal. The next paragraphs discuss the generalized relationships and observations arising from these studies.

A linear relationship was reported between the number of nuclei per collision and the impact energy (Kubota & Kubota, 1982). Johnson, et al. (1972) reported levelling of the number of nuclei generated at contact energies greater than 1.7E-4 J for one set of trials. This indicates towards the scenario where all the clusters at the crystal surface were being dislodged and any further increase in contact energy did not produce any new nuclei. Few of the contact nucleation studies reported generation of attrition fragments (Garside, et al., 1979; van der Heijden, et al., 1989). This might be due to the higher contact energy and the mechanical properties of the contacting surfaces and the crystals used in the trials.

It is difficult to avoid stagnant conditions when using photomicroscopy to examine nucleation. This means, if growth is diffusion controlled, the growth rates will be slow. Liang, Hartel, & Berglund (1987) showed that, when agitated in a suspension crystallizer, the growth rate of sucrose crystals were twice that measured in a photomicroscopic cell. Figure 3-3 compares growth data from Shi, et al., (1989, 1990) for lactose crystals grown in both stagnant and agitated systems; the crystals grow an order of magnitude faster when agitated.

The generated contact nuclei also exhibited distribution in the growth rates or growth rate dispersion (GRD). There are two different theories to model GRD. The random fluctuation (RF) model assumes that the growth rate of individual crystals vary randomly during the course of time. Alternatively, the constant crystal growth (CCG) model suggests that each crystal has a different but a constant growth rate in the same environment (Randolph & Larson, 1988). For lactose, Shi, et al., (1989) reported a CCG model for GRD, although it is not apparent in Figure 3-3 as mean growth rates (at different supersaturations) are plotted. They also reported existence of a critical supersaturation, below which no secondary nucleation was observed. This can be explained by concluding that below the critical supersaturation level, the clusters

cleaved off the crystal surface are not large enough to survive at the bulk supersaturation.

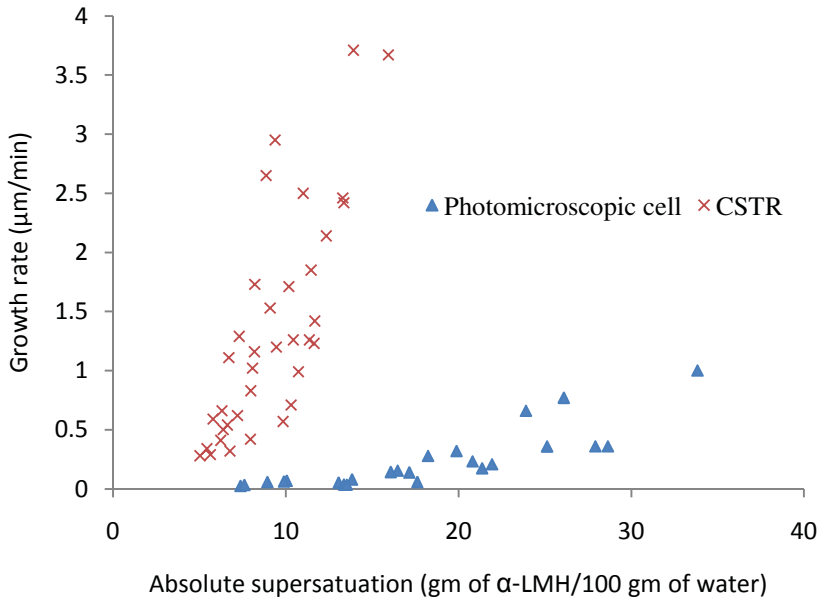


Figure 3-3. Growth rate comparison of lactose under different experimental conditions. ▲present data from Shi, et al., (1989) for a photomicroscopic cell, × present data from Shi, et al., (1990) for a CSTR (continuous stirred tank reactor). Temperature ranged from 30-60 °C. Residence time for CSTR studies varied from 4.6-52 minutes and growth rates determined by MSMPR population balance technique. In the photomicroscopy study, growth of a population of nuclei was followed in a single experiment for 30-500 minutes, with mean growth rate plotted.

3.2 Shear Secondary Nucleation

In addition to the collision induced mechanism discussed in the sections above, fluid shear is also a possible mechanism for secondary nucleation as shown in Figure 3-1. Many different experimental approaches for examining the effect of shear on secondary nucleation are reported in the literature. Wang, J. & Estrin (1996) fixed a crystal to a rod and suspended it in a solution, using an agitator to provide the mechanical shear forces onto the crystal surface. Another technique to impart shear onto an immobilized crystal involved the use of Taylor-Couette system (two concentric cylinders with the inner cylinder being rotated at a controlled speed) (Sung, Estrin, & Youngquist, 1973; Wang, M. L., Huang, & Estrin, 1981; Wang, M. L. & Yang, 1981). A fluid jet was used by Estrin, Wang, & Youngquist (1975), Jagannathan, Sung, Youngquist, & Estrin (1980) and Tai, Tai, & Chang (2009) to generate shear on crystal surfaces. Secondary nuclei in all the above studies were

subjected to higher levels of supersaturation (growth supersaturation) compared to that at which they were produced (generation supersaturation). This was done either by transferring the sheared solution to a separate chamber maintained at a lower temperature (Estrin, et al., 1975; Jagannathan, et al., 1980; Sung, et al., 1973; Wang, J. & Estrin, 1996) or by cooling the generation chamber itself (Wang, M. L., et al., 1981; Wang, M. L. & Yang, 1981). A tubular shear device was employed to study shear nucleation of lysozyme crystals by Tait, White, & Litster (2009). The lysozyme crystals were immobilized by dipping a borosilicate tube in lysozyme solution and allowing the crystals to nucleate and grow on the walls of the tube. A solution was then circulated through the tube, exposing the crystals on the wall to shear.

Table 3-1 shows the results (modified from degrees of sub-cooling to absolute supersaturation) for shear nucleation studies conducted by Sung, et al. (1973). Table 3-2 shows the transformed data from Wang, M. L., et al. (1981) who used a Taylor-Couette system. The rotation speed of the inner cylinder ensured that the flow was turbulent. The actual shear rates were not calculated and results were reported in terms of inner cylinder rotation speed and the distance between the crystal and the inner cylinder. The empirical data was converted to shear rates by the method given by Serra, Colomer, & Casamitjana (1997) for a turbulent Taylor-Couette system. Serra, et al., (1997) used the Taylor-Couette system to study aggregation and breakup of latex particles in a shear flow.

Table 3-1 *Selected Data from Sung, et al., (1973) showing the Generation of Secondary Nuclei for Magnesium Sulphate at Different Levels of Mixing and Supersaturations.*

Run No.	Generation Supersaturation	Growth Supersaturation	No. Of visible nuclei	Crystallization time (minutes)	Rpm
21	8.9	33.8	0	----	1450
22	9.1	33.8	0	----	1880
23	8.9	34.26	2	17	2000
17	8.7	32.8	14	10	2440
8	6.3	32.4	0	----	2000
26	10.43	10.43	0	----	2050

Note: Results have been modified from degrees of sub-cooling to absolute supersaturation. *Supersaturation*: absolute supersaturation (gm per100 gm of water). Distance between the impeller and the seed crystal was constant at 1.8 mm for all runs. *Crystallization time*: time after which nuclei were noticed. Nuclei were visually detected and enumerated. Generation supersaturation refers to the supersaturation at which the crystal was subjected to the fluid shear and growth supersaturation refers to the supersaturation that was subsequently achieved by cooling the sheared fluid.

The following points can be highlighted from the shear nucleation studies in literature:

a) No nucleation was reported in the absence of seed crystal or in the absence of agitation, indicating shear in the vicinity of a crystalline surface is required to initiate the secondary nucleation.

b) Run # 21, 22, 23 and 17 (Table 3-1) were conducted at almost constant generation and growth supersaturations but different rotation speeds. It was only at the rotation speed of 2000 rpm (run # 23) that nuclei appeared, with higher number of nuclei detected at higher rpm (run # 17). This indicates towards the necessity of a critical level of rpm (shear) for nucleation to be initiated. An increase in the number of nuclei with an increase in rotation speed was also reported by Wang, M. L., et al. (1981) (Table 3-2). In run # 8 (Table 3-1), which was conducted at a lower generation but similar growth supersaturation and rpm as run # 23, no nuclei were detected. This showed that a minimum level of generation supersaturation is required for shear secondary nucleation to occur. Run # 26, which was conducted at the highest generation supersaturation but lower growth supersaturation showed no nuclei formation, indicating the need for a higher growth supersaturation for sheared nuclei to survive. In all other shear nucleation studies it was reported that for the sheared nuclei to be detected, they needed to be exposed to much higher supersaturations than what they were generated at.

c) In cases where the sheared fluid was not exposed to higher supersaturation, shear formed nuclei were either not detected or required long time to grow to a detectable size. Tait, et al. (2009) failed to detect any significant shear nucleation compared to primary nucleation for their system and did not use a higher supersaturation for growth. Tai, C. Y., et al. (2009) did not use a higher growth supersaturation, but waited 'several' hours before counting the number of nuclei.

d) All studies were empirical and system specific. Shear rates were varied by either changing the rotation speed or the distance between the immobilized seed and the impeller/ fluid jet/inner cylinder of the Taylor-Coutte system. The shear generated using impellers and jets will vary greatly across the crystal surface. Although the

Taylor-Coutte system would have generated a more uniform shear, actual shear rates were not reported.

Table 3-2 *Data from Wang, M.L., et al., (1981) in Terms of Shear Rates at a Constant Absolute Supersaturation for Citric Acid (16.6 gm per 100gm of water)*

Rotation speed of the cylinder (rpm)	Angular velocity (s^{-1})	Mean fluid velocity ($m\ s^{-1}$)	Specific energy dissipation rate ($m^2\ s^{-3}$)	Shear rate (s^{-1})	Shear stress ($N\ m^{-2}$)	No. Of nuclei observed
480	50.2	0.55	5.8	2407	2.4	4
600	62.8	0.69	11.3	3365	3.4	11
810	84.8	0.94	27.9	5278	5.3	20
980	102.7	1.13	49.3	7024	7.0	23
1160	121.4	1.34	81.8	9046	9.0	26
1660	173.7	1.93	239.8	15486	15.5	25
2100	219.8	2.44	485.5	22035	22.0	28

High levels of shear will be present in industrial crystallizers; for example at the discharge streams of impellers (Rielly & Marquis, 2001), in the boundary layer flow over rotating impellers (Cherry & Papoutsakis, 1986) and during bubble rupture in evaporative crystallizers. However, for shear nucleation to be dominant in industrial crystallizers this will need to be combined with high supersaturation for sustained periods. One area where both high shear and high supersaturation could occur is during the boiling process in an evaporative crystallizer. This process involves constant bubble generation and rupture at the liquid-vapour interface. The shear stresses during the bubble rupture process predicted by Chalmers & Bavarian (1991) and Cherry & Hulle (1992) are in the range of 200-300 $N.m^{-2}$ and 95 $N.m^{-2}$, respectively. These values are an order of magnitude higher than those shown in Table 3-2 to be required for shear nucleation. Combined with the higher supersaturation at the interface layer due to evaporation, bubble rupture could initiate shear induced secondary nucleation.

The effect of bubbling on secondary nucleation is not well reported in the literature, although there are studies on the effect bubbling has on primary nucleation. Wohlgemuth, Kordylla, Ruether, & Schembecker (2009) reported a reduction in the metastable zone, with the bubble surface acting as the foreign body promoting heterogeneous nucleation. Qian & Botsaris (1996) used air bubbling at atmospheric

pressure to successfully simulate the crystal size distribution (CSD) cycling in a vacuum evaporative crystallizer. Bubbling produced a foam layer similar to that in industrial crystallizers, in which high supersaturation is generated. This localized high supersaturation generation was attributed to the sub-cooling and high solute concentration, due to water evaporation at the bubble liquid interface. The CSD cycling was shown to be a result of the fluctuations of supersaturation in this evaporative foam layer. Botsaris, Qian, & Barrett (1999) used bubbling to induce multiple primary nucleation events during chiral crystallization studies, and reported the initiation of nucleation at much lower supersaturation when bubbling was applied to the solution. Therefore, the effect of bubble rupture in the boiling zone on secondary nucleation cannot be ruled out and requires investigation. Having considered the generalized theory on various secondary nucleation mechanisms, secondary nucleation studies on lactose along with their limitations are now discussed.

3.3 Secondary Nucleation Studies on Lactose

Industrial crystallizers need to be operated at a supersaturation that maintains a balance between growth rate and nucleation rate. Excessive supersaturation will result in excessive nucleation and a too low supersaturation can slow the growth and nucleation rates by too much. Low supersaturation also creates a need for long residence times, adding to the capital costs of the equipment. Thus, a good knowledge of the supersaturation at which secondary nucleation is initiated is essential. However, the literature reports varying results for such levels of supersaturation for secondary nucleation initiation for lactose as shown in Figure 3-4. The differences can be attributed to the differing experimental conditions, such as lactose purity level, mechanical agitation conditions, methods of detecting the onset of nucleation and the time frame of the experiments which are elaborated in Table 3-3. These studies show that the supersaturation curve for secondary nucleation initiation, cannot at this stage, be universally defined until further research sheds light on the magnitude of the contributing mechanisms.

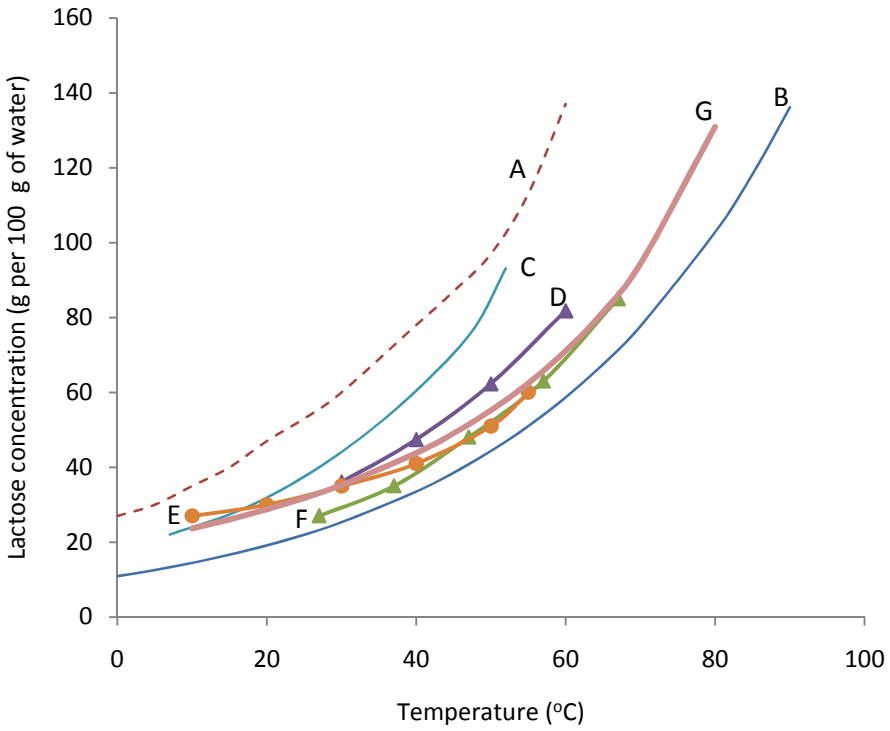


Figure 3-4. Secondary nucleation studies on lactose. A: Spontaneous nucleation line/ Supersolubility curve (Hunziker, 1949); B: Solubility curve; C: Forced crystallization (Hunziker, 1949) [refers to the optimum viscosity (a function of temperature) and supersaturation at which the solution was seeded and held under vigorous agitation for 60 minutes]; D:Critical supersaturation for growth (Shi, et al., 1989); E: SNT (Butler, 1998); F: Forced secondary nucleation (Shi, et al., 1989) and G:Nuclei first detection curve (Wong, Bund, Connelly, & Hartel, 2011).

The curves E, F and G in Figure 3-4 give the critical supersaturations below which no secondary nucleation occurred in the given study. However, operation at such low levels of supersaturation will make the process costly (long residence times are needed to achieve the required crystal growth). Also, some nucleation is necessary to replenish the crystals removed from the crystallizer; therefore a higher supersaturation is desirable at which some secondary nucleation occurs. Wong, et al. (2011) proposed 1% transmittance reduction of the solution as such a higher limit (supersaturation at which the transmittance of the solution reduce by 1% due to secondary nucleation) for lactose. Such a limit however is affected by the agitation levels and thus can be system specific.

Table 3-3 *Secondary Nucleation Studies in Literature on Lactose*

Reference	Comment	Seeding	Agitation	Detection technique	Time frame
(Wong, et al., 2011)	Reported the supersaturation at which the first nuclei were detected along with those at which the transmittance of the solution decreased by 1% and 1.5% due to nucleation.	0.1 g in ≈ 230 ml lactose solution	3 bladed, 2.5 cm marine propeller; 943, 1674 and 2512 rpm	Microscopy and spectroscopy	40 minutes
(Shi, et al., 1989)	Determined the critical supersaturation for generation as well as growth of secondary contact nuclei.	Single crystal	Growth observed under stationary conditions	Photo-microscopy	30-500 minutes
(Butler, 1998)	Introduced the concept of Secondary Nucleation Threshold: supersaturation below which no secondary nucleation is expected to occur	Two seed crystals	Shaking at 200 rpm	Visual	30-700 minutes
(Kauter, 2003)	Determined SNT of lactose water system in presence of impurities	Two seed crystals	600 rpm by magnetic stirrer	Visual	

3.4 Conclusions

This chapter specifically focuses on a qualitative review of secondary nucleation, reviewing the various reported mechanisms. The major mechanisms relevant to the studied industrial system were identified: collision and shear. Collision nucleation

occurs either by attrition or removal of a solute cluster layer at the crystal solution interface, referred to as contact nucleation. Contact nucleation is identified to be the most important source of secondary nuclei. This is due to the lower energy levels required for generation of secondary nuclei by this mechanism, compared to attrition. Shear nucleation requires sustained levels of high shear and supersaturation to contribute substantially to overall secondary nucleation and is therefore generally neglected. The generated secondary nuclei are reported to show anomalous growth behaviour like non-growth, dissolution and growth rate dispersion. The next chapter enumerates the experimental efforts that were directed toward separating the different secondary nucleation mechanisms of alpha lactose monohydrate.

Chapter 4 Experiments on Secondary Nucleation

Secondary nucleation is commonly expressed as an empirical function of agitation level, suspension density and supersaturation as (Myerson & Ginde, 2001)

$$B_N = k_{n,s} N_i^j M_T^k \sigma^b \ ,$$

Equation 4-1 Secondary nucleation: empirical model

where $k_{n,s}$ is the empirical secondary nucleation rate constant, N_i is the impeller speed [rps or rpm], M_T is the suspension density [(kg of crystal) (kg of suspension)$^{-1}$ or (kg of crystal) (m^3 of suspension)$^{-1}$], σ is the supersaturation and j, k, and b are empirical constants. Researchers have tended to lump all secondary nucleation mechanisms discussed in previous chapter together in one expression simply because they depend on the energy intensity (stirring) of the system and the supersaturation. These models are very system specific and difficult to transfer beyond the unique environment in which they were developed. This chapter aims at studying the three secondary nucleation mechanisms of attrition, contact nucleation independently and shear induced nucleation as defined in the classification diagram in Figure 3-1, with no interference from the other two.

4.1 Attrition

Attrition is the term used to describe the form of contact nucleation that involves physical damage of crystals and generation of fragment daughter particles, which are the secondary nuclei. The consequences of such contacts are three-fold, in that they may reduce the value of the mass average particle size, change the CSD and modify the particle morphology (Bravi, et al., 2003) . At the industrial scale, attrition is recognized as a major source of secondary nucleation (Biscans, 2004).

This section focuses on attrition and whether it acts as a source of secondary nucleation during lactose crystallization under stirred conditions**.** Attrition occurs either due to crystal-impeller or crystal-crystal collisions. The major parameters affecting attrition in stirred conditions are (Synowiec, et al., 1993) ; (i), stirring intensity; (ii), impact energy; (iii), particle concentration; (iv), target efficiency, i.e., probability of the crystal colliding with the impeller blades; and (v), material

properties of the crystal and the impeller. Trials were conducted at different levels of parameters (i), (ii) and (iii) and their relative contribution to attrition was studied by comparing crystal size distributions (CSDs). However, before the experimental methods are presented the theory of attrition induced secondary nucleation is discussed below. This is an extension of that presented in Chapter 3, which summarizes the ways of measuring attrition and growth behaviour of attrition fragments.

4.1.1 Theory

There are three possible mechanisms in attrition (Figure 4-1); shattering, chipping and abrasion. Shattering, which is also called breakage or fragmentation, occurs when the collision energy is high enough for particle fracture. Abrasion, which is also called erosion occurs when the collision energy is only capable of removing small amounts of material from the surface of the particles (Bemrose & Bridgwater, 1987). Chipping is characterized by partial fracture (Menacho, 1986), which produces fewer but larger particles as compared to that of abrasion. While abrasion can occur at each impact, shattering often requires accumulation of energy from multiple collisions to propagate cracks (Bermingham, Kramer, & van Rosmalen, 1998a). Generally, no single mechanism occurs in isolation and attrition is a combination of the three mechanisms, where one of the mechanisms may dominate.

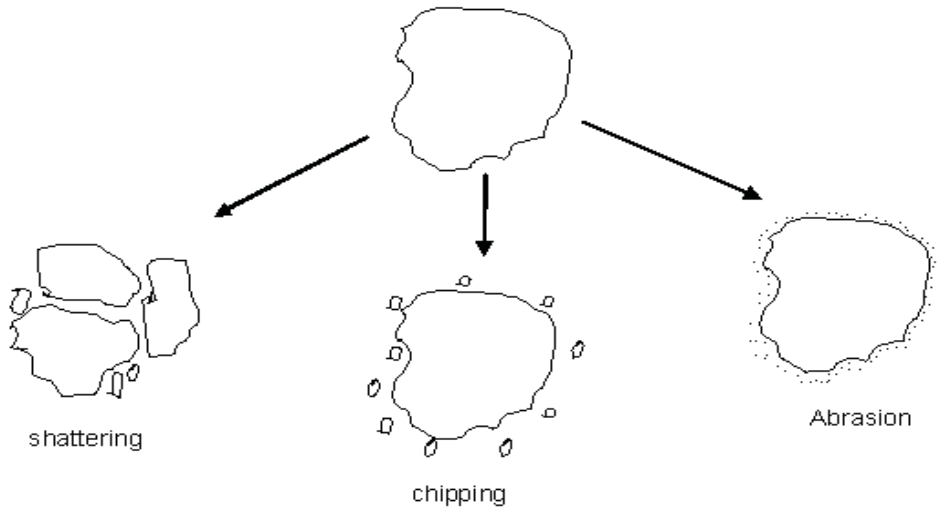


Figure 4-1. Different attrition mechanisms [adapted from Barbosa-Cánovas, Ortega-Rivas, Juliano, & Yan (2005)].

The nature of change in the crystal size distribution indicates which attrition mechanism is occurring, as shown in Figure 4-2. When shattering is dominant there will be a large shift of the CSD main peak towards a smaller size range. When abrasion is dominant, there will be little change in the original mean size and it will lead to a bimodal distribution arising from the generation of fines. Similarly, cumulative size distribution curves can be used to study the attrition behaviour and mechanisms by following the changes in the slope of the original size distribution curve due to generation of new particles and a reduction in size of the original particles (Biscans, et al., 1996b; Bravi, et al., 2003) .

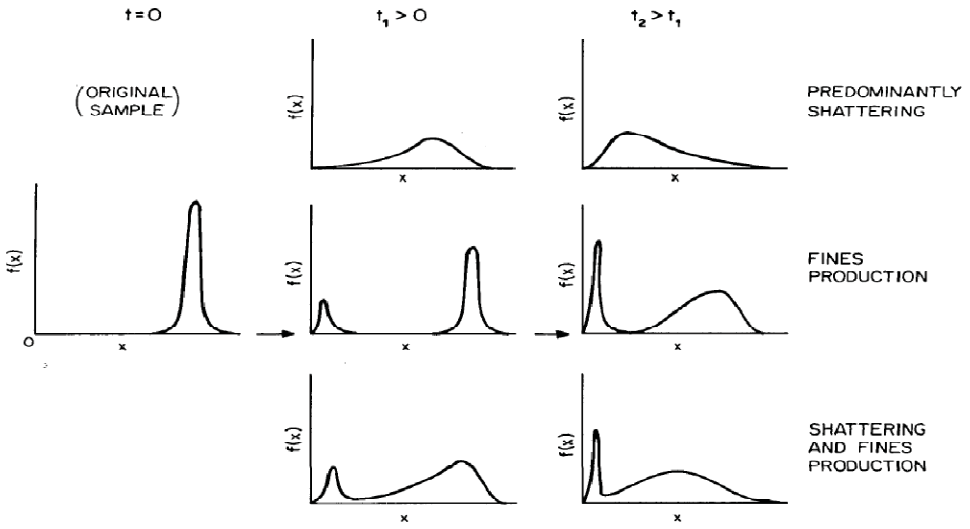


Figure 4-2. Effect of different dominant attrition mechanisms on the CSD with time [reproduced from Malave-Lopez & Peleg (1986)].

Comparing attrition when the independent variables differ by small amounts can be difficult if the CSD changes are minor. A subtle analysis technique is needed. In confronting a similar problem for the agglomeration of milk powder, Williams, Jones, Paterson, & Pearce (2009) proposed a mass-based agglomeration efficiency. This compared the CSDs of the two inlet streams, the recycle powder fines and spray droplets, to the product stream of agglomerated powder. Attrition is the inverse of agglomeration and so a similar approach can be used here to compare two CSDs (e.g.,

between time t=0 and time t within the same experiment). A differential attrition index (DAI) can be defined as the sum of the volume fraction of crystals that appear or disappear within size bins across the distribution divided by 2. This division by two is needed because total volume is conserved. The DAI is obtained by integrating the difference function of the frequency distributions between time, t=0 and t. The difference function is given by

$$df(\log L_i) = nCSD_t(\log L_i) - nCSD_0(\log L_i)$$

Equation 4-2 Difference function for a frequency distribution

where, *nCSD* refers to the normalised crystal size distributions and the log scale is typical for separating the size bins of a power series, e.g., from sieves or laser diffraction. The log scale reflects the way data is gathered by laser diffraction, but also means the index is equally sensitive to changes at either end of the CSD. A negative value for $df(\log L_i)$ indicates a net disappearance of crystals from that size bin. Integrating this difference function and conserving volume gives the differential attrition index (DAI) .

$$DAI = \frac{1}{2}\int_{-\infty}^{\infty} df(\log L_i)\, d\log L_i$$

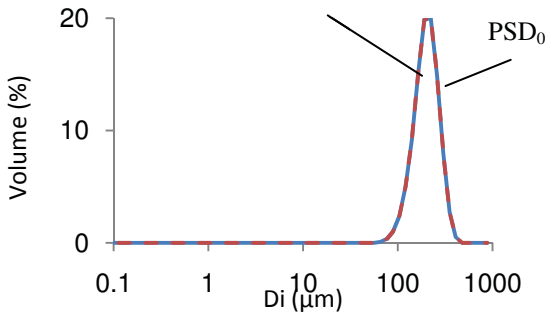
Equation 4-3 Differential attrition index definition

The DAI physically signifies the net relative volumetric movement of crystals from larger to smaller size bins. It must be noted here that removing the sign in Equation 4-3 by using the absolute value, makes the DAI insensitive to agglomeration or attrition. However, the nature of the experiments and the interrogation of the data mean that only size reduction is occurring and therefore the DAI is a measure of attrition.

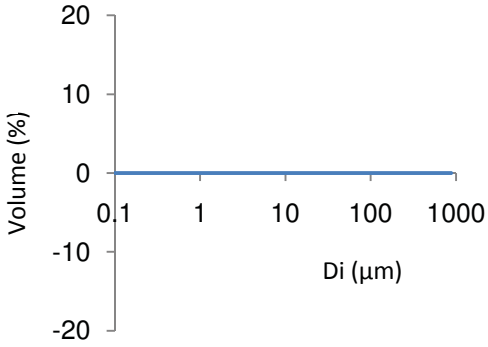
The difference plot can provide information such as no attrition, complete attrition or the occurrence of some attrition, depending upon the shape of the plot.

- If no attrition occurs (Figure 4-3a), the difference plot will be a flat line at 0 (Figure 4-3b) and DAI = 0.

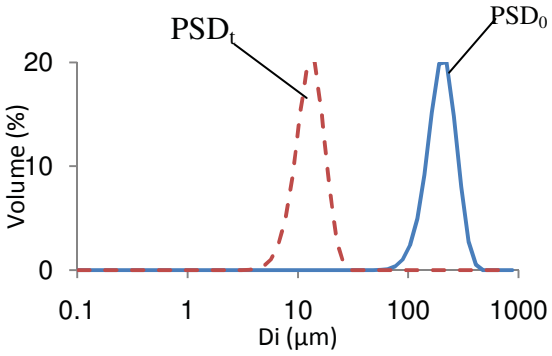
- If complete attrition occurs, the CSDs of the product and the parent crystals do not overlap (Figure 4-3c). The difference plot (Figure 4-3d) contains a positive part exactly identical to the new particle size distribution and a negative part identical to the initial size distribution. Thus, DAI = 1. Two points arise; (i), the DAI cannot exceed 1 and so is not a useful measure when a high degree of attrition occurs; and (ii), complete attrition can still occur with DAI < 1. This implies that size reduction of all parent particles occurs, but that the parent and the product distributions overlap (Figure 4-3e and Figure 4-3f). This latter point is important, because the DAI is an index of the movement of the size distributions, not a direct measure of the quantity of particles that have experienced size reduction.
- If some attrition occurs, the CSDs overlap and 0 < DAI < 1 (Figure 4-3g and Figure 4-3h).



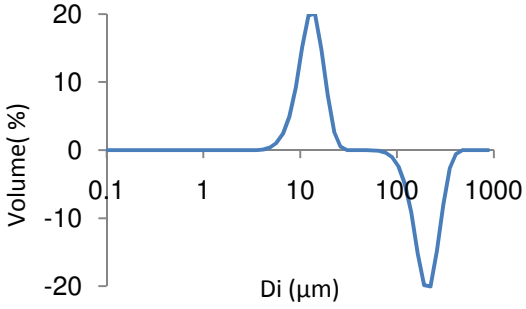
a) PSD for no attrition.



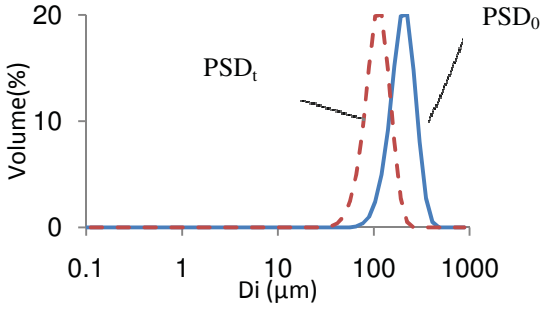
b) Difference plot, g(log D_i), for no attrition. DAI=0



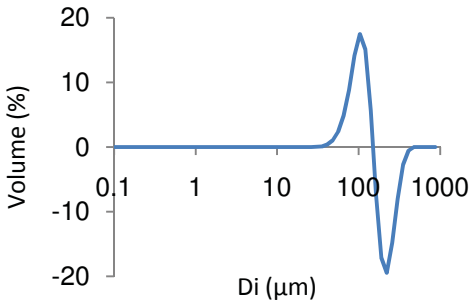
c) PSD for complete attrition.



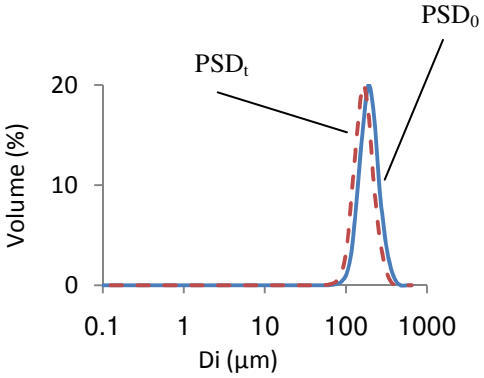
d) Difference plot, g(log D_i), for complete attrition. DAI=1



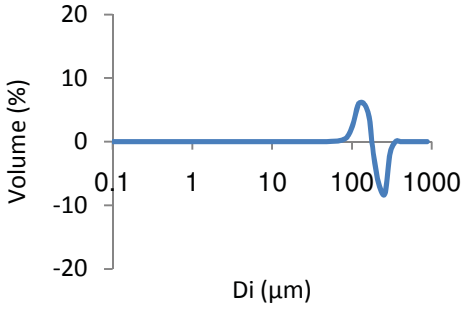
e) PSD for complete attrition.



f) Difference plot, g(log D_i), for complete attrition. DAI ≤1



g) PSD at time t=0 and t after stirring.



h) Difference plot, g(log D_i), for partial attrition. 0<DAI<1

Figure 4-3. Particle size distributions and difference plots for a range of attrition outcomes.

4.1.2 Materials and Methods

Attrition experiments were carried out in the stirred cell *(called the small volume sample presentation unit)* of the Malvern Mastersizer 2000 S. An active beam length of 2.4 mm and a 300 RF lens was used, which can measure sizes between 0.05 – 900 µm. The experimental approach provides an online particle size measurement which prevents experimental losses and errors during filtration, drying, weighing and sieving. These steps are required when sieving is used for size analysis of attrition fragments. The technique also helps to accurately quantify particles in the very small range (<10 µm).

In order to decouple the hydrodynamics affects from supersaturation, non-solvent media for the solute are used to study attrition during crystallization (Biscans, et al., 1996b; Bravi, et al., 2003). This is essential since in the presence of supersaturation other secondary nucleation modes, like contact nucleation and phenomena such as primary nucleation, agglomeration and growth can become active. In this study, Methanol was used as the non-solvent media. However, when methanol contains less than 2% (w/w) moisture, it removes the water of crystallization from alpha-lactose monohydrate crystals to form stable anhydrous alpha-lactose (Lim & Nickerson, 1973). Because this could adversely affect the crystal morphology and its susceptibility to attrition, 5% w/w of water was added. This methanol (95% w/w) was then saturated with excess lactose monohydrate crystals by stirring overnight at 25 ^{o}C. The resultant solution was filtered through a Whatman Filter 113 before use.

Lactose crystals were sieved into ranges of 250 – 300 µm and 150 – 180 µm. They were then washed with distilled water for 10-15 seconds and rinsed immediately with the saturated methanol solution to prevent any further dissolution of crystals. Washing of the crystals was necessary to eliminate the fines adhering to the crystal surfaces, which can lead to errors in the results.

For each trial, 100 ml of saturated 95% (w/w) methanol solution was placed into the cell of the Mastersizer. After setting the propeller to the desired speed, alignment and background measurements were taken. Washed crystals were then added and the Malvern was set to take readings every two minutes.

Each condition was replicated four times. The DAI was calculated for each trial and the averages of these replicates are presented as the results with the standard error reported as error bars. The operating conditions used to investigate the attrition in lactose monohydrate crystals were: concentration of lactose crystals (0.20%, 0.40% and 0.60% w/w), time of stirring (0 – 60 minutes), stirring rate (2000 and 3000 rpm) and size of parent crystals (250-300 µm and 150-180µm) as shown in Table 4-1. Table 4-2 gives the experimental design matrix.

Table 4-1 *Factors Varied during the Attrition experiments. H = High, M= medium, L =Low*

Factor \ Intensity	H	M	L
Size (µm)	250-300	---	150-180
Speed (rpm)	3000	---	2000
Concentration (w/w %)	0.6	0.4	0.2

Table 4-2 *Experimental Design Matrix (Size:Speed:Concentration)*

HHH	HHM	HHL
HLH	HLM	HLL
LHH	LHM	LHL
LLH	LLM	LLL

4.1.3 Results and Discussions

Frequency distributions show how the CSDs change with time. Figure 4-4 shows the initial and final normalized CSDs averaged across four replicates of the HHH runs (high particle size, impeller speed and concentration). The results show a generation of fines and a reduction in the average mass and size of the original particles. The d_{50} of the CSDs between time $t=0$ and t reduced by 15%, where d_{50} is the 50^{th} volume percentile of the cumulative distribution. It is also apparent that the new fragments fall within two size bands, with a peak between 30-60 µm and another between 4-8

µm. Accumulation of fragments into these bands occurred gradually over the entire 60 minute experiment. This banding indicates different mechanisms of origin which will be discussed later.

Cumulative distributions are useful to compare multiple experiments. Figure 4-5 compares the four runs with high crystal concentration (the first column of Table 4-2) between time t=0 and 60 minutes. The degree of attrition can be gauged by the extent of the upward movement of the CSD curves. Here, the order of attrition from maximum to minimum was HHH > HLH > LHH > LLH, where the letters respectively indicate particle size, impeller speed and particle concentration. It is interesting to note that trials with large (HIGH) particle size produced more attrition even though they had fewer particles per unit volume in the system (for the same concentration). This implies that collision frequency is less important than collision success for attrition. Larger particle size clearly affects success. Consider now the impeller which produces more attrition at HIGH speed as it circulates the cell volume past the impeller blades more frequently, resulting in more collisions at greater impact velocity. Combining these factors together, it can be concluded that attrition is strongly dependent on impact energy intensity as manifested in the experimental variables of crystal size and impeller speed.

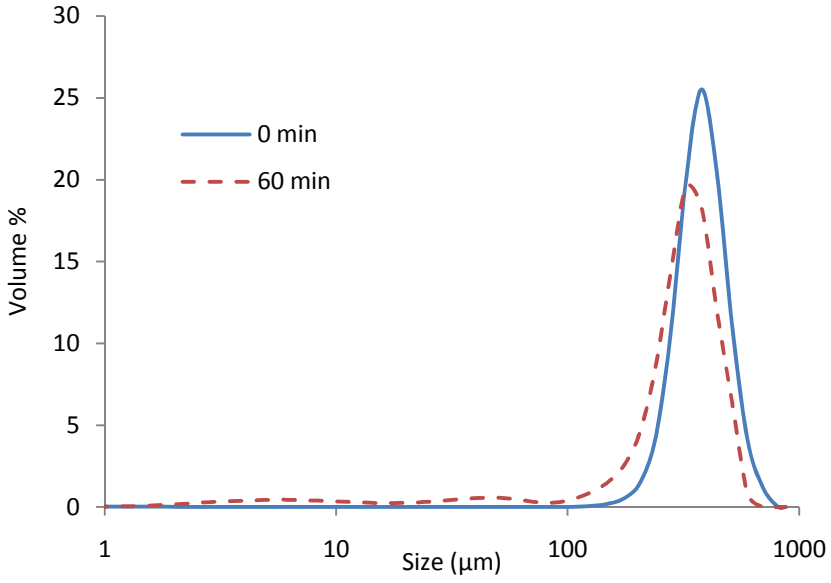


Figure 4-4. Normalized frequency CSD for a single HHH run. The trial name represents high levels of crystal size, impeller speed and concentration.

The three peaks in the frequency distribution for the HHH trial of Figure 4-4 are observed as slope changes in the cumulative plots of Figure 4-5. These three slopes represent the particle size populations of: fines (<10 micron), middle range fragments (10-95 micron) and the larger parent crystals (95-500 micron). A similar trend was found by B. Biscans, et al. (1996b) who deduced the presence of multiple attrition mechanisms working simultaneously. Considering the three mechanisms of abrasion, shattering and chipping: abrasion produces fines (<10 µm), shattering produces fragments covering the whole size range, and chipping is expected to predominately contribute to the middle range fragments. The three slopes in the HHH and HLH trials indicate all of these mechanisms are at play. In contrast, the LHH and LLH trials do not show this variability, where the parent particle size distributions were largely preserved, indicating that with smaller particles, the collision energy intensity was insufficient to cause shattering or chipping. Therefore, in LHH and LLH, abrasion is the dominant mechanism.

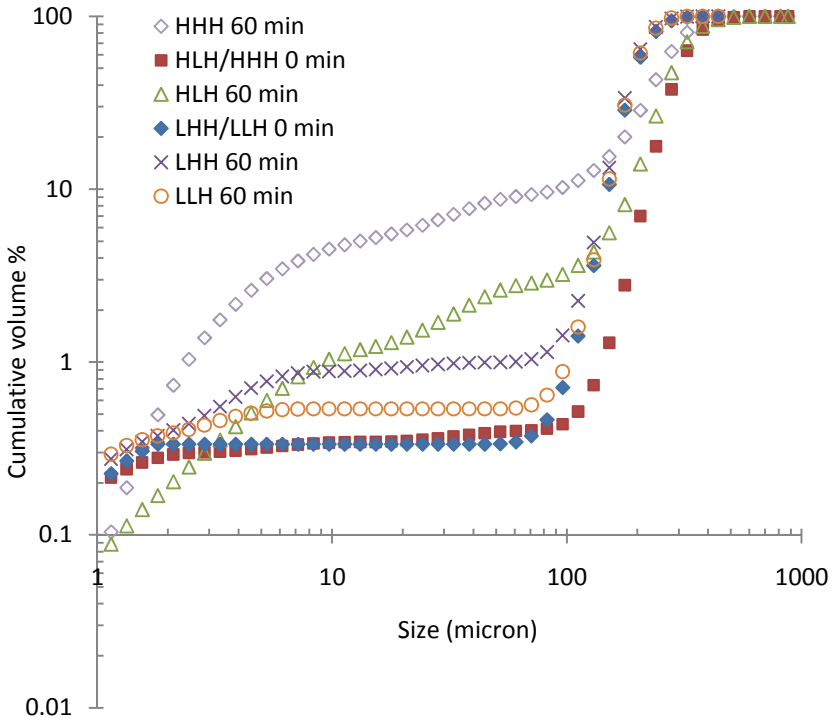


Figure 4-5. Cumulative size distribution at 0 and 60 minutes for selected experimental runs. The legend gives high/low levels of particle size, impeller speed and particle concentration respectively. The data shown is the average of four replicates.

Figure 4-6 present the differential attrition index (DAI) as a function of time. The following observations can be made:

a. DAI increases with time (LL* runs were an exception) showing that lactose undergoes continuous attrition.

b. In the trials exhibiting attrition, the rate of attrition is approximately constant with all indices showing a slight curvature towards the end of 1 hour. This suggests that the attrition rate slows down with time due to decrease in the particle size (which results in lowering of the collision energy and hence the attrition rate). Longer runs are needed to examine this effect in detail. However, straight lines can be fitted through the data with reasonable accuracy for comparison. The magnitude of the rate (i.e., slope) depends on the conditions of the trial.

c. Four clearly identified bands of data were obtained. In order of decreasing attrition rate, these bands are HH*, HL*, LH* and LL*. The * represents crystal concentration, which is the least sensitive variable affecting attrition.

d. Crystal size and impeller speed both markedly affect attrition. For the levels selected, crystal size has the greater influence (because the change in slope is greater between HH* and LH* than between HH* and HL*).

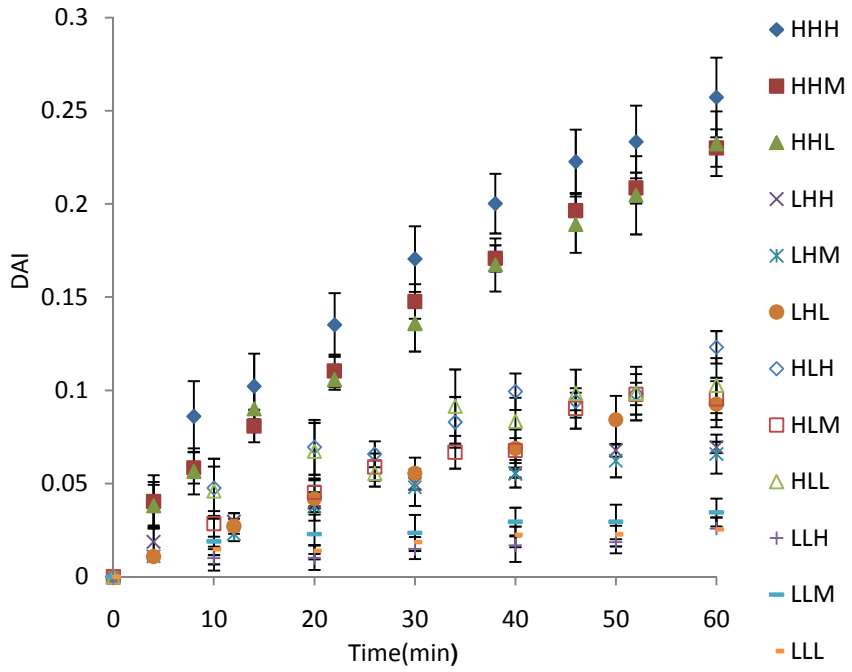


Figure 4-6. Differential attrition index (*standard error bars, n=4*) measured between time, *t=0* and *t*. Trial names represent high, medium and low levels of crystal size, impeller speed and concentration.

As stated above, the observed order of effect on attrition is: crystal size > impeller speed > concentration. These equations can now be qualitatively analyzed. Mersmann, Sangl, Kind, & Pohlisch (1988) used the Hertz-Huber theory which relates stress generation due to collision to the mechanical properties of the materials, to derive a theoretical model for predicting attrition rates in an agitated crystallizer. They proposed the volumetric attrition rate ($\frac{dV_a}{dt(M\alpha)}$), based on crystal volume ($M\alpha$), for impeller-crystal and crystal-crystal impacts as:

$$\left[\frac{dV_a}{dt(M\alpha)}\right]_{i-c} = VAR_{i-c} \propto \eta N_i^{2.2}$$

Equation 4-4 Volumetric attrition rate due to impeller-crystal collisions

$$\left[\frac{dV_a}{dt(M\alpha)}\right]_{c-c} = VAR_{c-c} \propto \alpha\varepsilon^{0.73} d_c^{-0.26}$$

Equation 4-5 Volumetric attrition rate due to crystal-crystal collisions

where, N_i is stirrer speed [rpm], d_c is mean particle size [m], α is the volume of crystals per kg of the slurry [($m^3$of crystal) (kg of slurry)$^{-1}$], η is the impeller target efficiency or probability of collisions resulting in attrition, ε is the specific energy

dissipation rate [m^2 s^{-3}], m is the mass of slurry [kg], V_a is the attrition volume [m^3] and VAR is the volumetric rate of attrition per unit crystal volume [m^3 m^{-3} min^{-1}]. The details of the Hertz-Huber theory is discussed elsewhere in detail (Ploß & Mersmann, 1989).

The volume of crystals per unit of slurry is given by:

$$\alpha \propto n_c d_c^3$$

Equation 4-6 Volumetric crystal hold up

where, n_c is the number concentration [# (kg of slurry)$^{-1}$]. Substituting for α in Equation 4-5 gives

$$VAR_{c-c} \propto n_c \varepsilon^{0.73} d_c^{-2.74}.$$

Equation 4-7 Volumetric attrition rate due to crystal-crystal collisions in terms of crystal size and concentration

The target efficiency for an impeller increases sharply with particle size and for a given impeller can be expressed for a system where the blade dimensions are held constant as (Synowiec, et al., 1993):

$$\eta \propto d_c^2$$

Equation 4-8 Relationship between target efficiency and crystal size

Substituting Equation 4-8 into Equation 4-4 gives the VAR for impeller-crystal collision as:

$$VAR_{i-c} \propto d_c^2 N_i^{2.2}$$

Equation 4-9 Volumetric attrition rate in terms of crystal size

Crystal-crystal impacts (Equation 4-7) are considered negligible because concentration had an insignificant effect on attrition in the experiments reported here. Synowiec, et al., (1993) reported similar observations at low solids concentration (<4 v/v %). Furthermore, viscous drag severely reduces the crystal-crystal contact velocities and the upper limit of such velocities are generally an order of magnitude lower than the corresponding crystal-impeller velocities (Bennett, et al., 1973). Therefore, for the present case only impeller-crystal impacts are analyzed. This is

done comparatively by ratioing the VARs between experiments for impeller-crystal contact as per Equation 4-9.

$$\frac{VAR_1}{VAR_2} = \frac{d_{c,1}^2 N_{i,1}^{2.2}}{d_{c,2}^2 N_{i,2}^{2.2}}$$

Equation 4-10 Volumetric attrition rate ratio for a given impeller

The VAR ratio can be approximated by ratioing the slopes of DAI plots of Figure 4-6.

$$\frac{\frac{d}{dt}(DAI)_1}{\frac{d}{dt}(DAI)_2} \approx \frac{VAR_1}{VAR_2}.$$

Equation 4-11 Volumetric attrition rate ratio approximation by DAI slope ratio

It is only an approximation because VAR and the slope of DAI plot have slightly different definitions. VAR is the volumetric rate at which crystal fragments are removed from parent crystals, whereas the slope of the DAI plot represents the volumetric rate of shift in the PSD. This shift, when DAI <1, cannot account for the volume of all new crystal fragments. However, remarkably, the observed ratios are very close to those expected from the theoretical prediction as listed in Table 4-3. They show the same order of effect on attrition: HH* > HL* > LH* > LL* and that particle size followed by impeller speed most affects the attrition rate.

Table 4-3 *Comparison of Calculated and Experimental Volumetric Attrition Ratios. To Remove the Effect of Concentration) the Mid Values for the Bands HH*, HL*, LH* and LL* After 60 Minutes are Used*

Ratio	Predicted VAR ratio	Ratio of the slopes of DAI plot
HH*/LL*	8.7	8.2
HH*/LH*	3.6	3.3
HH*/HL*	2.4	2.2
HL*/LH*	1.4	1.5

It is important to review the limitations of this study with respect to the role of attrition in providing secondary nuclei. Only a fraction of attrition fragments are reported to grow for certain inorganic compounds (Garside & Davey, 1980; Ó Meadhra, et al., 1995) because of the reasons discussed in Section 3.1. Thus, the

effective nucleation rate will be lower than the attrition rate. The above reported work did not include lactose and, while experimental work is required to validate it, the same trend is expected. Also, these trials were conducted using dilute slurries (0.2-0.6% w/w) which is far from the slurries encountered in industrial crystallizers (>20% w/w). Higher crystal loading have dramatic effects on the fluid viscosity and density and can thus significantly alter the rates due to accompanied changes in hydrodynamics. These limitations make it difficult to directly predict the attrition rates at industrial scale from the results obtained in the present study. These issues will be addressed in the contact nucleation studies in the next section.

4.1.4 Conclusions

This study used a Malvern particle size analyzer as a tool to study attrition of lactose monohydrate crystals under stirred conditions where the variables were particle size, impeller speed and particle concentration. The results show that lactose crystals are susceptible to attrition which occurred steadily over the one hour trials. While particle concentrations were much lower than in industrial crystallizers, they had little effect on attrition. It was thus concluded that crystal-crystal collisions are not a significant source of attrition fragments. Particle size had the most significant effect on attrition, followed by impeller speed, which together implies that the crystal collision energy intensity is the dominant factor producing new fragments. Experimental observations agree closely with theoretical predictions concerning the relative volumetric attrition rates between experiments. In terms of mechanism, the presence of three peaks with the PSDs for large particles at higher speed shows that they underwent shattering, chipping and abrasion, with more attrition at higher impeller speeds. In contrast, the PSDs produced by circulating small particles show that abrasion was the only mechanism.

A quantity called the differential attrition index (DAI) was adapted from agglomeration literature to give a measure of the change in CSD between two times. Tracking across 60 minutes of mixing, the DAI clearly show the difference between experiments. The slope of the DAI data over each experiment provides a measure of the volumetric rate of change of the CSDs. While it is not a direct measure of the

volumetric rate of generation of crystal fragments it does match remarkably well to the predicted values derived from physical principles.

4.2 Contact Nucleation

Contact nucleation is the production of nuclei from the displacement of the ordered solute cluster layer present at the solution-crystal interface as identified in the classification diagram of Figure 3-1. It is the most important source of nuclei in mixed suspensions (Randolph & Larson, 1988). Contact nucleation is not attrition, in that the physical mechanisms of shattering, chipping and abrasion do not occur. Therefore, the original CSDs do not change due to contact nucleation but new nuclei are generated. However, it is possible that some degree of micro-attrition takes place from the crystal surface during the contacts but such a phenomenon will be very difficult to distinguish from pure contact nucleation and hence is considered as a part of contact nucleation in the present study. The trials were conducted in supersaturated lactose solutions and agitation was used to induce collisions in this investigation.

4.2.1 Theory

For lumped secondary nucleation, the approach of Ottens & de Jong (1973) is mechanistic where they express secondary nucleation as a function of kinetic energy of contact of the crystals with the other surface (impeller, parts of crystallizer or other crystals), collision frequency and supersaturation,

$$B_N = K_N E_k f_c \sigma^b,$$

Equation 4-12 Collision secondary nucleation

where

B_N is the nucleation rate [# min^{-1} kg^{-1}]

K_N is the nucleation constant [# J^{-1} (g of solute 100 g^{-1} of the solvent)$^{-b}$] and signifies the number of secondary nuclei generated per unit of contact energy per unit supersaturation.

E_k, the kinetic energy of contact for each collision [J]

f_c is the contact frequency per unit mass of slurry [# min^{-1}(kg of slurry)$^{-1}$]

σ is the absolute supersaturation [(g of solute) (100 g of the solvent)$^{-1}$]

b is an empirical constant

Equation 4-12 can be equally applied to both crystal-crystal and crystal impeller contacts with a few differences. The frequency of crystal-crystal contacts is proportional to the square of the crystal number concentration (ten Cate, Derksen, Kramer, van Rosmalen, & Van den Akker, 2001) as against to a linear relationship for crystal-impeller contacts (Synowiec, et al., 1993). Secondly, crystal-crystal collisions are controlled by the micro-scale hydrodynamics (scale of eddies) whereas the meso-scale hydrodynamics control crystal-impeller collisions (scale of the impeller) (Rielly & Marquis, 2001). From the previous section, crystal-crystal collisions have been discarded as a cause of attrition for lactose. However, a 'low' energy contact can be enough to cleave off clusters near the crystal surface, inducing secondary nucleation. This means it will be essential to study the relationship between kinetic energy and secondary nucleation before discarding the role of crystal-crystal contacts in contact nucleation.

4.2.2 Crystal-impeller Contacts

For crystal-impeller contacts, kinetic energy is defined by

$$E_{k,i-c} = \frac{1}{2} m\, v_{i-c}^2 \,,$$

Equation 4-13 Kinetic energy of impeller-crystal collision

where m is the mass of single crystal which assuming it to be spherical given by

$$m = \frac{1}{6}\pi d_c^3 \rho_c \,,$$

Equation 4-14 Mass of a single crystal

where d_c is the mean crystal diameter [m] and ρ_c is the crystal density [kg m^{-3}]. $v_{i\text{-}c}$ in Equation 4-13 is the impeller-crystal impact velocity and can be substituted by the impeller tip speed given by (Cherry & Papoutsakis, 1986; Ottens & de Jong, 1973)

$$v_{i-c} = \frac{\pi}{60} N_i d_i \,,$$

Equation 4-15 Crystal-impeller collision velocity

where N_i is the impeller speed [min^{-1}], d_i is the impeller diameter [m]. Substituting Equation 4-14 & Equation 4-15 into Equation 4-13 gives the kinetic energy of impeller crystal collisions as

$$E_{k,i-c} = \frac{1}{12}\pi d_c^3 \rho_c \left(\frac{\pi N_i d_i}{60}\right)^2 .$$

Equation 4-16 Kinetic energy of contact for impeller-crystal collisions

The frequency of crystal-impeller contacts per unit mass of slurry can be calculated by

$$f_{c,i-c} = \left(\frac{K_D N_i d_i^3}{V_{sus}}\right) n_c \eta \ ,$$

Equation 4-17 Impeller-crystal collision frequency

where n_c is the crystal number concentration per kg of slurry [# (kg of slurry)$^{-1}$], $K_D N_i d_i^3$ is the volumetric pumping rate of impeller [m^3 min^{-1}], K_D is the discharge coefficient of the impeller, V_{sus} is the volume of slurry suspension present in the crystallizer [m^3] and η is the target efficiency or collision probability. The bracketed term in Equation 4-17 represents the inverse of circulation time [min^{-1}] and is a measure of the frequency of passes a fluid element makes through the impeller zone. Not all the particles entering the impeller zone will collide with the impeller and so a collision probability term is needed, η. This is a function of Stokes number as given by Gahn & Mersmann (1999b)**:**

$$\eta = \left(\frac{\psi}{\psi + 0.32}\right)^{2.1} ,$$

Equation 4-18 Target efficiency as a function of Stokes number

where ψ is the Stokes number defined as

$$\psi = \frac{(\rho_c - \rho_s) v_{rel} d_c^2}{18 \mu_S T_L} \ ,$$

Equation 4-19 Stokes number

where T_L is the target length [m] and is taken as the edge width of impeller blade for the present study, μ_S is the slurry viscosity [kg m^{-1} s^{-1}], $(\rho_c - \rho_s)$ is the density difference between the crystal and the slurry [kg m^{-3}] and v_{rel} is the relative velocity between the crystal and the impeller [m s^{-1}]. It is taken as the impeller tip speed

because the tip speed (the tangential component) is expected to be much larger than the fluid axial velocity (the normal component) for a two bladed impeller circulating in a tank. Substituting Equation 4-16 and Equation 4-17 in Equation 4-12 gives the secondary nucleation due to impeller-crystal impacts as

$$B_{N,i-c} = K_N \frac{1}{12} \pi d_c^3 \rho_c \left(\frac{\pi N_i d_i}{60}\right)^2 \left(\frac{K_D N_i d_i^3}{V_{sus}}\right) \eta n_c \sigma^b \, .$$

Equation 4-20 Contact nucleation due to impeller-crystal collisions

4.2.3 Crystal-crystal Contacts

For crystal-crystal contact, kinetic energy is defined by

$$E_{k,i-c} = \frac{1}{2} m \, v'^2_{c-c} \, .$$

Equation 4-21 Kinetic energy of crystal-crystal collision

The impact velocity ($v'_{c\text{-}c}$) is the root mean square (rms) velocity between the contacting crystals. Cherry & Papoutsakis (1986) suggested that for crystal-crystal collisions the crystal rms velocity can be substituted by eddy velocities of size equivalent to the inter-crystal space estimated by the following relationship (Eskin, Leonenko, & Vinogradov, 2004a)

$$\delta = \left(\left(\frac{\varphi_{lim}}{\varphi}\right)^{\frac{1}{3}} - 1\right) d_c \, ,$$

Equation 4-22 Inter-particle space in a slurry suspension

where φ_{lim} is the limiting (packing) volumetric concentration and d_c is the crystal diameter. Eddy size greater than these will cause group of crystals to move with causing much relative velocities between them reducing chances of collisions.

From Kolmogorov theory (Pope, 2000), the velocity (v_e) and size of smallest eddy (L_e) is given by:

$$v_e = (\varepsilon v_S)^{1/4} = v'_{c-c}$$

Equation 4-23 Crystal-crystal collision velocity

$$L_e = \left(\frac{\upsilon_S^3}{\varepsilon}\right)^{1/4}$$

Equation 4-24 Length of smallest eddy

where, ε is the energy dissipation rate per unit mass of slurry [$m^2\ s^{-3}$], υ_S is the kinematic viscosity of the slurry [$m^2\ s^{-1}$]. The energy dissipation rate in a stirred system can be calculated as

$$\varepsilon = \frac{N_P N_i^3 d_i^5}{V_{sus}},$$

Equation 4-25 Energy dissipation rate in an agitated system

where N_P is the power number and is a function of Reynolds number (Re). The Reynolds number for an agitated system is given by

$$Re = \frac{d_i^2 N_i \rho_S}{\mu_S}\ .$$

Equation 4-26 Reynolds number for an agitated system

The value of power number for a two bladed impeller was estimated, from Nagata (1975) cited in Cherry & Papoutsakis (1986), as 0.4. If $L_e << \delta$, the smallest eddies will viscously dissipate energy in the solution without causing any crystal-crystal collisions. The larger length scale of eddies, called the *inertial subrange*, therefore need to be considered. As the name suggests, these eddies are determined by the inertial effects with negligible viscous effects. The velocity scale of these eddies are dependent on the energy dissipation rate and their length (Pope, 2000):

$$\upsilon_{inertial} = (\varepsilon L_{inertial})^{1/3} = \upsilon_{c-c}\ .$$

As discussed earlier, the eddy lengths of interest should be of the order of inter-crystal distance in the suspension and thus $L_{inertial}$ can be substituted by δ.

The crystal-crystal collision frequency per unit mass as per ten Cate, et al. (2001) is of the order

$$f_{c,c-c} = 4\sqrt{\pi} n_c^2 d_c^2 \sqrt{v'^2_{c-c}}\ \rho_s\ .$$

Equation 4-27 Crystal-crystal collision frequency

4.2.4 Experimental

Secondary nucleation runs were carried out in 1 litre glass vessels (11.5 cm diameter) baffled (width 8% of the beaker diameter) at 180^{o} and covered with lids to reduce evaporation losses and to prevent dust particles from entering. The crystal slurries were stirred using a two bladed (45^{o} blade angle), 5 cm diameter and 1 mm thick impeller. A Phipps and Bird Model 7790-402 four shaft stirrer (Phipps and Bird, Richmond, Virginia, USA) enabled four simultaneous runs to be made. The vessels were submerged in a 30 ^{o}C water bath.

Four parameters were studied: Seed crystal size (106-212, 212-300, 300-425 and 425-600 microns), impeller speed (400 and 550 rpm), absolute supersaturation (6.7, 8.4 and 10.7 g of α-LMH per 100 g of water), and seed loading (2, 5 and 10 % w/w).

Seed crystals were pre-treated to prevent initial breeding caused by the fines adhering to their surface. They were washed with cold RO water for 5-10 seconds with manual shaking to ensure all seeds were in suspension and had been exposed to the wash water. The water was immediately drained off and the seeds rinsed with the same supersaturated lactose solution (prepared in excess) which was used for the experimental runs. The rinsing continued till the rinsed solution was devoid of any observable fines. It typically took 4-5 rinsing steps to achieve this. Figure 4-7 depicts the importance of seed pre-treatment.

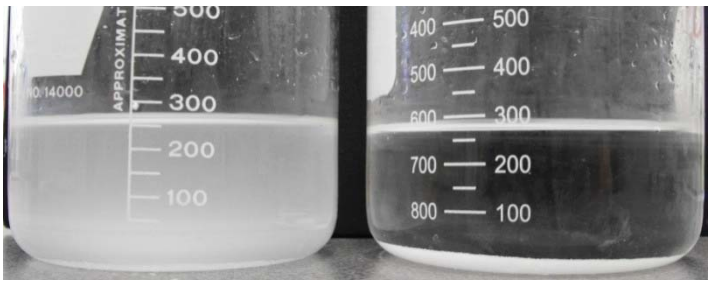


Figure 4-7. Importance of seed pre-treatment for fines. The beaker on the left contained untreated settled seed crystals and would have led to an over-estimation of secondary nucleation, while that on the right are the washed seeds.

The treated crystals were added to the beakers containing supersaturated lactose solution held at 30 ^{o}C in a water bath. The mass of solution and seed crystals were

measured to give the desired seed loading and to obtain a total slurry mass of 300 g. The beakers were then moved to the constant temperature water bath with the multiple impellers and stirring started. The stirring speed was set fast enough to fully suspend the seed crystals.

A handheld digital refractometer was used to measure the dissolved lactose concentration before and after the runs. Due to the nucleation and growth of the crystals, the dissolved lactose concentration dropped over the course of each experiment. The drop in absolute supersaturation was low (6-13% of the initial value) and hence the runs were considered to be carried out at constant supersaturation. The limitation of trying to operate with constant supersaturation meant that runs with higher seed loading needed to be carried out for shorter times. The time of each run is shown in Table 4-4.

Laser diffraction (Malvern Mastersizer Hydro 2000S) was used to quantify the nucleation rate in the same way as Kauter (2003) and Tait, et al. (2009). As the Malvern measures the volume-weighted size distribution it was critical to eliminate the larger seed crystals to correctly enumerate the nuclei formed. To do this, at the end of each run the slurry was filtered through a 36 micron sieve to remove the seeds and allow the nuclei to pass through. Then, known volume of filtrate containing only the secondary nuclei, was introduced to the Malvern cell containing a known volume of dispersing liquid, which was slightly supersaturated lactose solution (1.2g α-LMH per 100 g of water) at the Mastersizer presentation unit temperature of 25-26^{o} C. This allowed the total number of nuclei per ml to be calculated from the particle size distribution (PSD) and the volume concentration (% v/v) readings. Let, Y ml be the volume of dispersant and X ml the volume of sample added, then the total volume in the presentation unit is (X+Y) ml. If z is the reported volumetric concentration (%v/v) by Mastersizer, then the total crystal volume (TCV) in the Malvern presentation unit is

$$TCV = \frac{z(X+Y)}{100} \ .$$

Equation 4-28 Total crystal volume in Malvern presentation unit

And therefore crystal volume per ml of sample (cvm) is

$$cvm = TCV/X\ .$$

Equation 4-29 Crystal volume per ml of the sample

Now, numbers in each size bin (i) of the crystal size distribution (CSD) can be calculated as:

$$n(i) = \frac{(cvm)\frac{V_i}{100}}{\left(\frac{3.14L_i^3 10^{-12}}{6}\right)}\ ,$$

Equation 4-30 Number of crystals in size bin (*i)*

where V_i is the % volume occupied by the size bin (i) in the CSD and L_i is the geometric mean size of the size bin (i) and ($i+1$). The denominator term gives the spherical volume of the single particle of size L_i whereas the numerator gives the total absolute volume occupied by the particles in the size bin (i). 10^{-12} is the conversion factor for the volume in μm^3 to ml. The total number of crystals across all the w bins is given by:

$$N_{tot} = \sum_{i=1}^{w} n(i)\ .$$

Equation 4-31 Total number of crystals across all size bins

Note: (a) All the measurements reported by the Mastersizer are reported for equivalent sphere. The volume concentration reported therefore needs to be multiplied by the volumetric shape factor to arrive at the actual volume concentration of lactose crystals. Shape factor is also required for calculating equivalent volumes of lactose crystals in the individual size bin; the denominator term of Equation 4-30. As the volumetric shape factor needs to be included in both the numerator and the denominator of Equation 4-30, it is not required in the calculation of total number. (b) Size bins of size> 1 μm were taken while calculating the total number of nuclei because the measurements below this size were not consistent. Also 1 μm was used as the size at which nuclei generation occurs in the model (in Chapter 6). The calculated number of nuclei per ml was then divided by the run time to give the nucleation rate in # ml^{-1} min^{-1}. The units can be then converted to # kg^{-1} min^{-1} by

dividing by the slurry density. Four replicates of each condition were performed and the average values along with the standard error bars are reported.

To quantify the contribution of primary nucleation, blank trials in the absence of any crystals were conducted at all supersaturations. Trials were also performed with seed crystals in slightly supersaturated solutions (0.21 g α-LMH per 100 gm of water) to assess the contribution of pure attrition to the overall secondary nucleation. The 'slightly' is a safety precaution to ensure that the solution does not become unsaturated.

Table 4-4 *Run Time (t) for Different Trials Conducted for Each Experiment with Two Impeller Speeds of 400 and 550 rpm, and Four Particle Sizes of 106-212, 212-300, 300-425 and 425-600 Microns*

Supersaturation	Seed loading (% w/w)		
(g α-LMH/100 g water)	2	5	10
6.7	60 min	-	-
8.4	60 min	45 min	30 min
10.7	60 min	-	-

4.2.5 Results and Discussions

The blank runs without crystals did not show any measurable crystals thus ruling out primary nucleation as a contributor to secondary nucleation in other seeded experiments. Similarly no measurable nucleation was observed in the trials with slightly supersaturated seeded solutions thus ruling out attrition as a contributor.

An independent experiment was carried out to monitor the progress of secondary nucleation process with time during the 60 minute batch process. The trials were stopped at 20, 30, 40 and 50 minutes and samples analyzed for the number of nuclei formed. The obscuration levels before 20 minutes were low for accurate enumeration of the number of nuclei. After 20 minutes the number of nuclei increases linearly with time, which suggests that no second generation nuclei were being formed. If this had been the case, the increase would have been exponential. This shows that the secondary nuclei formed were entirely due to the added seed crystals with no

interacting effects of the newly formed nuclei. The nucleation rates can be now related to characteristics like size and number concentration of the added seed crystals.

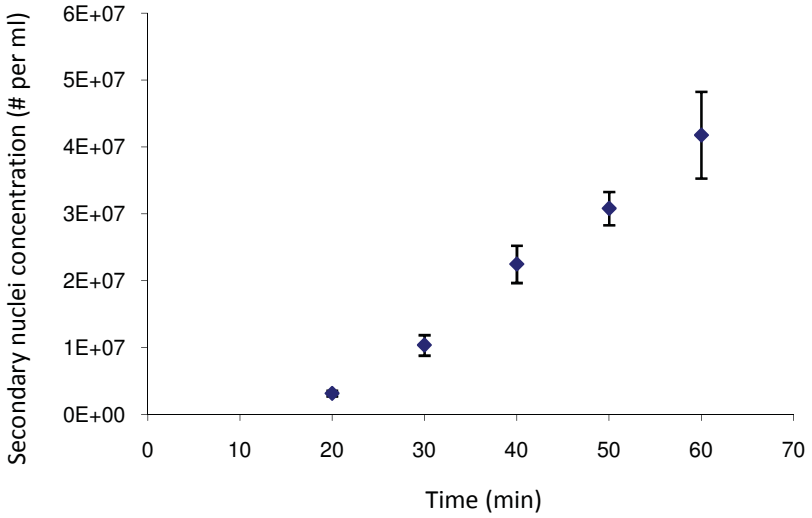


Figure 4-8. Secondary nucleation versus time (Supersaturation: 10.7 g of α-LMH per 100 g of water / Seed size: 357 µm / Seed loading: 2% (w/w) / Impeller speed: 550 rpm). S*tandard deviation error bars for 4 replicates are shown.*

The combination of four particle sizes and two impeller speeds provided eight levels of kinetic energy for impeller-crystal contacts, $E_{k,i\text{-}c}$ and four particles sizes and three seed loadings (by mass) gave twelve levels of seed loading (by number), as is shown in Table 4-5. The physical properties of the slurry, namely, the viscosity and density, depend on the crystal content. Effect of crystal size on viscosity was assumed to be negligible. The calculated values at 2, 5 and 10% w/w seed loading corresponds to 1.4, 3.6 and 7.3% v/v. The calculated densities and viscosities were calculated as 1124, 1134 and 1150 $kg.m^{-3}$ and 0.0013, 0.00138 and 0.00156 Pa.s, respectively at the 2, 5 and 10% w/w seed loadings respectively, using correlations given in Appendix I. The collision probability values in Table 4-5 are reported at the average of these density and viscosity values.

Table 4-5 *Values of Different Parameters for Impeller-Crystal Contact Induced Secondary Nucleation*

Average seed crystal size[a] (μm)	Number concentration of seed crystals for various seed loading [# (kg of slurry)$^{-1}$]			Kinetic energy[b] of contact (J) $E_{k,i\text{-}c}$		Collision probability η	
	2% (w/w)	5% (w/w)	10% (w/w)	400 rpm	550 rpm	400 rpm	550 rpm
150	7.31E6	1.83E7	3.65E7	1.50E-9	2.84E-9	0.28	0.36
252	1.54E6	3.85E6	7.70E6	7.11E-9	1.34E-8	0.55	0.64
357	5.42E5	1.35E6	2.71E6	2.02E-8	3.82E-8	0.73	0.83
505	1.91E5	4.79E5	9.57E5	5.72E-8	1.08E-7	0.84	0.95

Note: [a]log mean of the sieve sizes. [b]calculated for each combination of crystal size and impeller speed using Equation 4-13-Equation 4-14

Table 4-6 gives the hydrodynamic parameters relevant to crystal-crystal collisions in the stirred system. Reynolds number was calculated at the average viscosity and density for the three seed loadings. The smallest eddy size << mean inter-particle distance shown in Table 4-7. Hence the impact velocities of the particles are replaced by the inertial subrange eddy velocities. The calculated kinetic energies of contact for crystal-crystal collisions are shown in Table 4-7.

Table 4-6 *Values of Different Hydrodynamic Parameters for Crystal-Crystal Contact for Different Impeller Speeds.*

Parameter	400 rpm	550 rpm
Re	1.34E4	1.87E4
N_p	0.4	0.4
ε [m^2 s^{-3}]	0.14	0.36
L_e[μm]	61	48
v_e [m s^{-1}]	0.020	0.026

Table 4-7 *Inter-Particle Mean Space and the Kinetic Energy of Contact for Crystal-Crystal Contacts*

Average seed crystal size[a] (μm)	Inter-particle mean space (δ) [μm]			Kinetic energy[b] of contact (J) $E_{k,c\text{-}c}$	
	2% (w/w)	5% (w/w)	10% (w/w)	400 rpm	550 rpm
150	373	235	153	1.9E-12	3.6E-12
252	625	391	256	1.3E-11	2.4E-11
357	885	554	363	4.6E-11	8.7E-11
505	1250	784	513	1.6E-10	3.1E-10

Figure 4-9 shows linear relationships were obtained between the nucleation rate and crystal number concentration at supersaturation of 8.4 g of α-LMH per 100 g water. The slope depended on the seed crystal and the impeller speed. The fact that the relationship is linear suggests that the secondary nucleation is impeller-crystal collision controlled (Equation 4-20) rather than 'crystal-crystal' collision controlled because the latter expects a square relationship between nucleation rate and particle number. This indicates crystal-crystal collisions do not possess sufficient kinetic energy to dislodge the solute clusters from the crystal solution interface in order to generate secondary nuclei. This is supported by the fact that crystal-crystal collision kinetic energies (Table 4-6) are two-three orders of magnitude lower than the kinetic energy of impeller-crystal collisions as shown in Table 4-5. Kinetic energy therefore seems to be the single most important parameter governing contact secondary nucleation. This conclusion is similar to that obtained in the attrition study in the last section. Due to this observation of a linear rather than squared relationship, from here on, only impeller-crystal collisions will be considered.

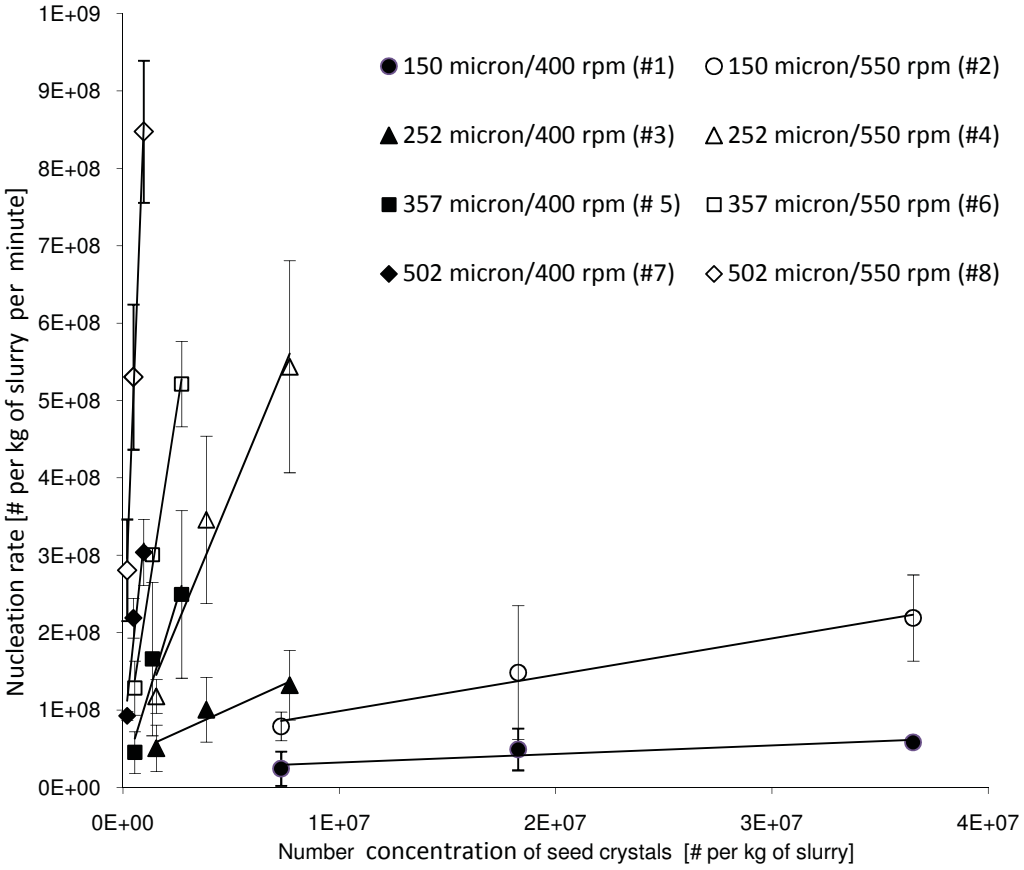


Figure 4-9. Effect of seed loading on secondary nucleation rate at constant supersaturation (8.4g α – LMH per 100 g water) for different combinations of seed size and impeller speed. S*tandard deviation error bars for 4 replicates are shown.*

Table 4-8 *Straight Line Fits Through the Data Points of Figure 4-9 And Kinetic Energy of Collisions for Various Combinations of Seed Size and Impeller Speed*

Trial combination	Slope and intercept of the straight line fitted through the data points		Kinetic energy of impeller-crystal collisions $E_{k,i\text{-}c}$ [J] (Equation 4-16)
	Slope	Intercept	
150 µm/400 rpm (#1)	1.1	2.11E7	1.50E-9
150 µm/550 rpm(# 2)	4.7	5.16E7	2.84E-9
252 µm/400 rpm(# 3)	12.7	3.91E7	7.11E-9
252 µm/550 rpm(# 4)	67	4.18E7	1.34E-8
357 µm/400 rpm(# 5)	91	1.40E7	2.02E-8
357 µm/550 rpm(# 6)	179	4.15E7	3.82E-8
502 µm/400 rpm(# 7)	266	6.09E7	5.72E-8
502 µm/550 rpm(# 8)	732	1.56E8	1.08E-7

The other salient features of Figure 4-9 are:

i) High scatter (evident from the error bars) in experimental data which is typical of nucleation studies.
ii) Nucleation rate increases with an increase in particle size.
iii) Nucleation rate is greater at 550 rpm stirrer speed than at 400 rpm.
iv) Each combination of particle size and impeller speed corresponds to a constant kinetic energy of impeller-crystal collisions. At each constant kinetic energy, the results show that nucleation rate increases with number concentration. More crystals mean more collisions and so, it can be concluded that nucleation increases with an increase in collision frequency.
v) The y intercept value of the lines (when the number concentration of seed crystals is zero) can be regarded as the contribution of primary nucleation to the nucleation rate. Blank trials without crystals concluded that no 'measurable' nucleation was present. However here in the presence of seed crystals it appears that it is necessary to attribute the presence of some nuclei to primary nucleation.
vi) The lowest kinetic energy trial (150 micron/400 rpm) had the lowest nucleation rate despite having the highest crystal number concentration. Any further reduction in kinetic energy will lead to a horizontal line with y = primary nucleation rate, with no effect of the presence of seed crystals. The kinetic energy at 150 micron/400 rpm, 1.50E-9 J, can be regarded as the threshold energy below which no contact secondary nucleation is expected to occur at the studied supersaturation.

The slope of the lines in Figure 4-9 as per Equation 4-20 is given by $K_N E_k \left(\frac{K_D N_i d_i^3}{V_{sus}}\right) \eta \sigma^b$. At the same supersaturation, impeller geometry and suspension volume, the theoretical ratio of the slopes is given by:

$$\frac{E_{k,1}\ \eta_1 N_{i,1}}{E_{k,2}\ \eta_2 N_{i,2}}$$

Equation 4-32 Theoretical ratio of the slopes of fitted lines in Figure 4-9

The ratio of the experimental and theoretical slopes for many of the trial combinations is shown in Table 4-9. It could be seen that the model prediction matches reasonably well with that of experimental considering the large uncertainties associated with nucleation studies.

Table 4-9 *Comparison of the Experimental and Theoretical Slopes of the Secondary Nucleation Rate Line*

Trial numbers	Experimental ratio	Theoretical ratio	% Difference
#8/#4	10.9	11.96	8.8
#7/#3	20.9	12.3	-70
#6/#2	38	31	-22.5
#8/#7	2.8	2.93	4.4
#7/#6	1.5	1.1	-36.4
#8/#2	155.7	100.3	-55.2
#3/#2	2.7	2.78	2.8
#8/#5	8	9.56	16.3
#5/#4	1.4	1.25	12
#7/#5	2.92	3.25	10.2
#4/#3	5.3	3	-76.6

In order to better understand the secondary nucleation mechanism the nucleation rate was normalized by the contact frequency per unit mass of slurry and plotted against the kinetic energy of contacts as shown in Figure 4-10. K_D, d_i and V_{sus} can be assumed constant for the system studied. Thus, for the varied parameters during the trials, contact frequency per unit mass (Equation 4-17) can be approximated by

$$f_{c,i-c} \sim N_i n_c \eta \ .$$

Equation 4-33 Approximate impeller-crystal collision frequency

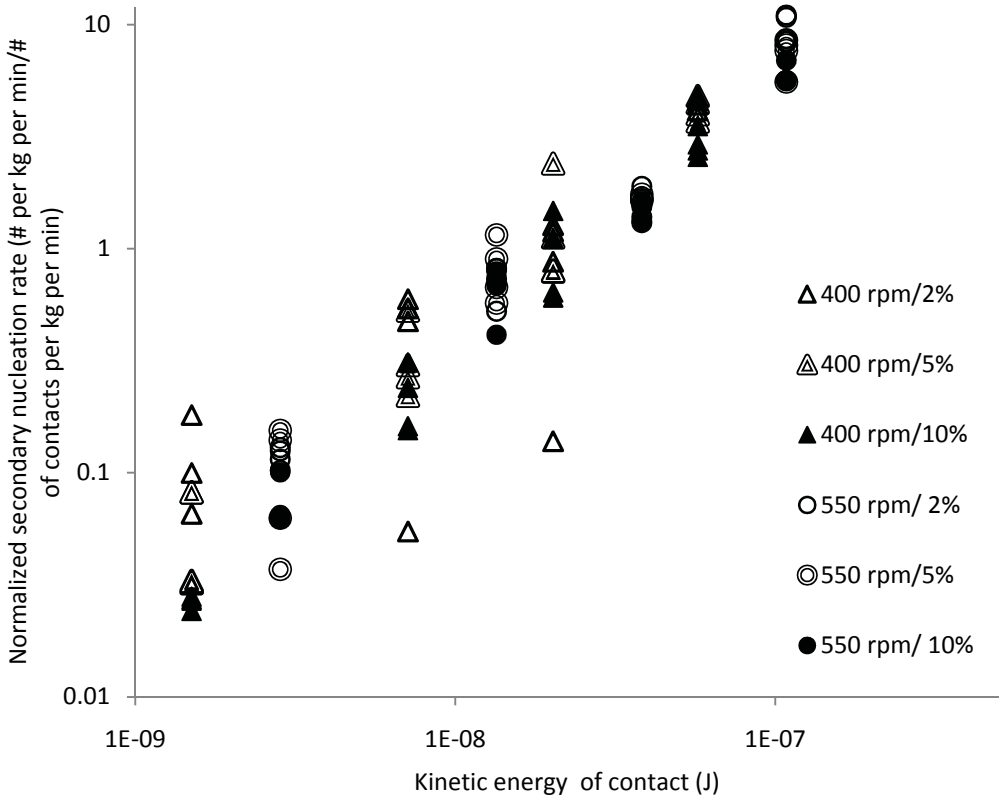


Figure 4-10. Effect of seed loading on secondary nucleation from kinetic energy and contact frequency perspective at constant supersaturation (8.4 g of α-LMH per 100 g water).

When this approach was taken all the lines presented in Figure 4-9 collapsed into a single curve. In Figure 4-9 it is difficult to quantify the effect of each parameter on secondary nucleation. Figure 4-10 presents a single curve for the empirical parameters of suspension density; impeller speed and particle size and shows that secondary nucleation depends on the fundamental parameters of kinetic energy and collision frequency. A curve fitted through the combined data gives a power law exponent of 1.16 (± 0.03 at 95% confidence interval (C.I.)) for kinetic energy. This is close to the value of 1 assumed in the model and that reported by Kubota & Kubota (1982) and Clontz & McCabe (1971).

A similar process of normalization of secondary nucleation rate and plotting against kinetic energy was repeated for data at two other supersaturations as shown in Figure 4-11. The exponential dependence of kinetic energy was 1.14 (±0.056 95% C.I.) and 1.0 (±0.08 95% C.I.) at supersaturation levels of 10.7 and 6.7 g α-LMH per 100 g

water respectively, which are close to the literature value of 1. Further investigation at more supersaturations is needed to comment conclusively on the dependence of the kinetic energy exponent on supersaturation.

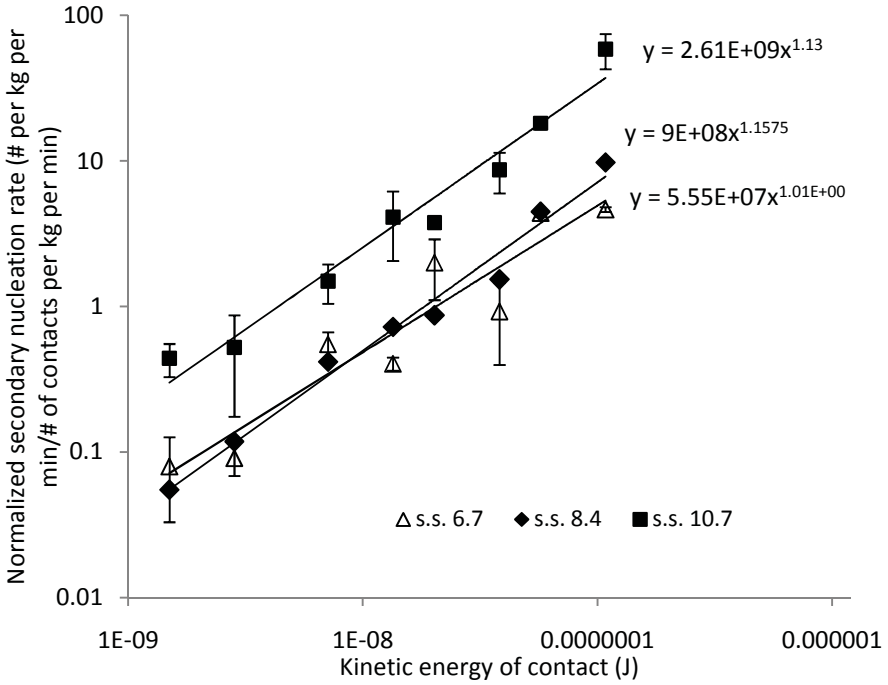


Figure 4-11. Secondary nucleation at constant seed loading of 2% (w/w) at 10.7 and 6.7 s.s. (g α-LMH per 100 g water) from a kinetic energy and frequency of contacts perspective. *Standard deviation error bars based on 4 replicates are shown.* The 8 kinetic energies correspond to the same combinations of impeller speed and crystal size as shown in Figure 4-9.

4.2.6 Conclusions

This study presents secondary nucleation studies on lactose carried out under stirred conditions. The variables investigated were seed loading, seed size, supersaturation and stirrer speed. Secondary nucleation was shown to be dominated by the crystal-impeller contact nucleation. It was found that for the studied supersaturation there exists a minimum kinetic energy below which secondary nucleation is not expected to occur. This has important ramifications in identifying the likely areas in the industrial crystallizer where secondary nuclei generation will occur. The zones where the collision kinetic energy exceeds the threshold value due to hydrodynamic conditions prevailing in them will produce secondary nuclei.

When the nucleation rate was normalized by the contact frequency per unit mass and plotted against the kinetic energy of the contacts, a single curve for the given supersaturation was obtained for all seed loadings, impeller speeds and seed size. The relationship between the kinetic energy and nuclei generation frequency per contact frequency is independent of the mechanism of contacts or scale of operation. This gives a better tool for predicting secondary nucleation rates in industrial crystallizers and is discussed in section 6.3.

4.3 Shear Nucleation

Shear nucleation, as highlighted in the review section, has been studied a number of times as a likely mechanism of secondary nucleation. The experimental methodology to study shear nucleation must ensure that the other two secondary nucleation mechanisms do not occur during the trials i.e. free flowing crystals undergoing collisions should be avoided. Thus, the crystals need to be immobilized. The set up used in the current study was inspired by the one used by Tait, et al. (2009). They immobilized lysozyme crystals inside a borosilicate tube and passed a supersaturated lysozyme solution through the tube subjecting the crystals to fluid shear. The supersaturated solution was circulated through the solution reservoir and the tube circuit for one hour and samples collected for nuclei enumeration every 10 minutes. The wall shear stress for the flow through the tube was calculated by

$$\tau_w = \frac{f \rho_s v_s^2}{2},$$

Equation 4-34 Wall shear stress for a flow through a rough tube

where f is the Fanning friction factor, ρ_s is the density of the solution [kg m^{-3}] and v_s is the velocity through the pipe [ms^{-1}]. By knowing the velocity through the pipe and therefore the Reynolds number, friction factor can be estimated if the pipe roughness ratio is known. The pipe roughness ratio was measured by Tait, et al. (2009) using the methodology proposed by Farshad, Rieke, & Garber (2001). With a known solution viscosity (μ_s), the wall shear stress (τ_w) can be converted to the shear rate (γ) that the immobilized crystals experience, as

$$\gamma = \frac{\tau_w}{\mu_s}.$$

Equation 4-35 Shear rate at the wall

No simple technique exists for direct measurement of pipe roughness ratio and the methodology proposed by Farshad, et al. (2001) requires specialized equipments. In this study, shear rate was expressed in terms of pressure drop across the pipe. The theoretical pressure drop for a flow through a pipe of diameter D [m], length l [m] with velocity v [m s^{-1}] is given by,

$$\Delta P = \frac{2 f v^2 l \rho_s}{D}.$$

Equation 4-36 Pressure drop for a flow inside a tube

The pressure drop term incorporates the friction factor term. On substituting the friction factor term, f from Equation 4-36 in Equation 4-34, wall shear stress can be expressed as a function of pressure drop,

$$\tau_w = \frac{D \Delta P}{4l}.$$

Equation 4-37 Wall shear stress for a flow through a rough tube

Substituting Equation 4-37 in Equation 4-35 leads to the expression of shear rate without the friction factor term,

$$\gamma = \frac{D \Delta P}{4 \mu_s l}.$$

Equation 4-38 Shear rate at the tube wall in terms of pressure drop across the tube

Two pressure taps (in the form of a T-joint) at the either end of the tube were used to measure the pressure drop across the tube containing immobilized lactose crystals. This was achieved using an inverted U-tube manometer as shown in Figure 4-12. The pressure drop in terms of height difference (ΔH) in the two columns of a manometer is given by

$$\Delta P = \rho_s g \Delta H .$$

Equation 4-39 Pressure drop in a U-tube manometer

The crystals were immobilized inside the tube wall by dipping the tube overnight in a concentrated lactose solution (44% w/w). Long connecting tubing was used to dampen the pulses due to the pumping action of a peristaltic pump. The temperature drop in the reservoir temperature due to the long tubing was less than 1 ^{o}C.

Trials were conducted at two different supersaturations (8.4 and 10.7 g of α-LMH per 100 g of water) under various shear rates achieved by changing the flow rates. Before the nucleation trials the tube was flushed thrice with excess supersaturated lactose solution prepared to eliminate any loosely held crystals in the tube. The diameter and the length of the plexi-glass tube used were 6 mm and 25 cm, respectively. The supersaturated lactose solution (400 g) was maintained at 30 ^{o}C by immersing the reservoir beaker in a constant temperature water bath. It was passed through the tube and then circulated back to the reservoir in a closed loop using a peristaltic pump. This was continued for 5 minutes and the heights of the fluid in the two columns of the inverted tube manometer were recorded and pressure drop calculated using Equation 4-39. The sheared solution in the reservoir was then filtered (Watmann No. 113) to remove any crystal which might have detached during the shearing process and incubated under stirring (200 rpm) at 30 ^{o}C for 2 hours. The formed nuclei were then enumerated by the procedure explained in section 4.2.3. The number concentration of the nuclei was then divided by 5 minutes (the circulation time) to give the nucleation rate [# kg^{-1} min^{-1}].

Two sets of blank runs were conducted. In the first, supersaturated lactose solution was directly incubated without passing it through the shearing tube. This quantified nucleation in the absence of shear as well as lactose crystals: two critical requirements for shear secondary nucleation to occur. In the second set, supersaturated solution was sheared in the tubes with no immobilized lactose crystals. These runs helped in quantifying the effect of primary nucleation at the shear rates studied for the secondary nucleation trials. Since the presence of immobilized crystals increase the shear levels due to increased roughness at the tube walls, a smaller tube diameter (5 mm) was used in conjunction with the highest pump speed to reach comparable shear rates for these trials.

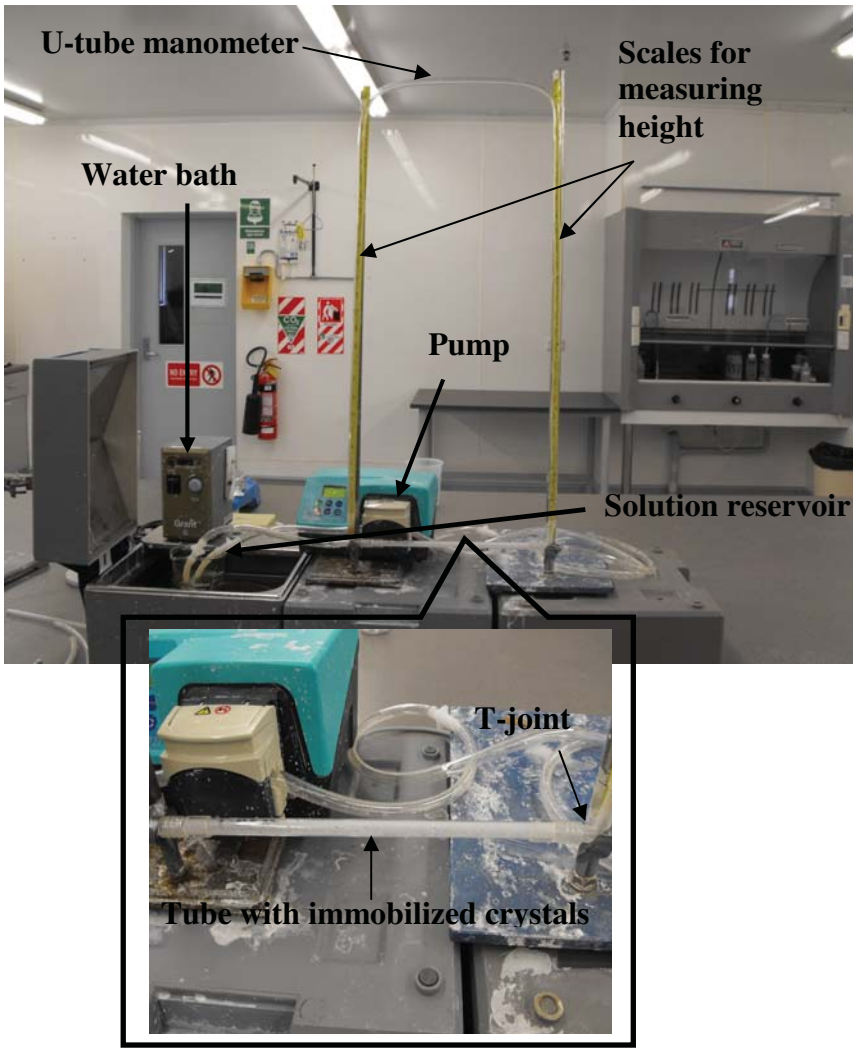


Figure 4-12. Experimental setup for shear secondary nucleation.

The fluid underwent sudden contraction and expansion while entering and leaving the shear tubes through the connecting tubing which was of larger diameter (8 mm) than the shear tubes. The head loss due to these phenomena depends on the ratio of the areas and the fluid velocity through them. The combined head loss (contraction and expansion) for the smaller diameter tube used in the blank runs works out to be 9 cm of lactose solution. For the secondary nucleation trials the maximum head loss was found to be 3 cm of lactose solution. The higher head loss in the blank runs was due to the smaller diameter tube and higher flow rates used.

4.3.1 Results and Discussions

The shear secondary nucleation results are shown in Figure 4-13. The salient observations are highlighted:

i) Higher nucleation rates were obtained at higher supersaturation. This can be explained in two ways. At higher supersaturation the semi-ordered layer at the crystal surface is thicker and hence contains a larger number of solute crystals that are washed away. Secondly, the critical size of nuclei (minimum size below which the nuclei dissolve) decreases with an increase in supersaturation and hence more clusters survive at higher supersaturation leading to higher nucleation rates.

ii) No measurable nucleation was detected at either supersaturation in the first set of blank runs in which the solution was not sheared through the tubes prior to incubation.

iii) Shearing in the presence of crystals induced nucleation at both supersaturations studied. In order to quantify the role of shear induced primary nucleation in the observed nucleation, the second set of blank trials were conducted. In the second set of blank runs, where the solution was passed through the smaller diameter tube with no immobilized crystals, solutions showed detectable levels of primary nucleation at comparable shear rates. The nucleation rates however were an order of magnitude lower than when the crystals were present. This shows that shear induced secondary nucleation was the major contributor to the observed nucleation.

iv) There was no effect of shear at rates greater than 5000 s^{-1}. It can be postulated that above these shear levels all the clusters in the layer at the crystal surface are being washed away, leading to no changes in nucleation rates with shear rates. A drop in the nucleation rates at lower shear rates for supersaturation 10.7 g of α-LMH per 100 g of water is observed. Trials at still lower shear rates were not feasible due to the inability of the experimental set up to measure pressure drops

lower than 4 cm of fluid column. This was because of the significant increase in the pulsations from the peristaltic pump at the lower end of its pumping speed.

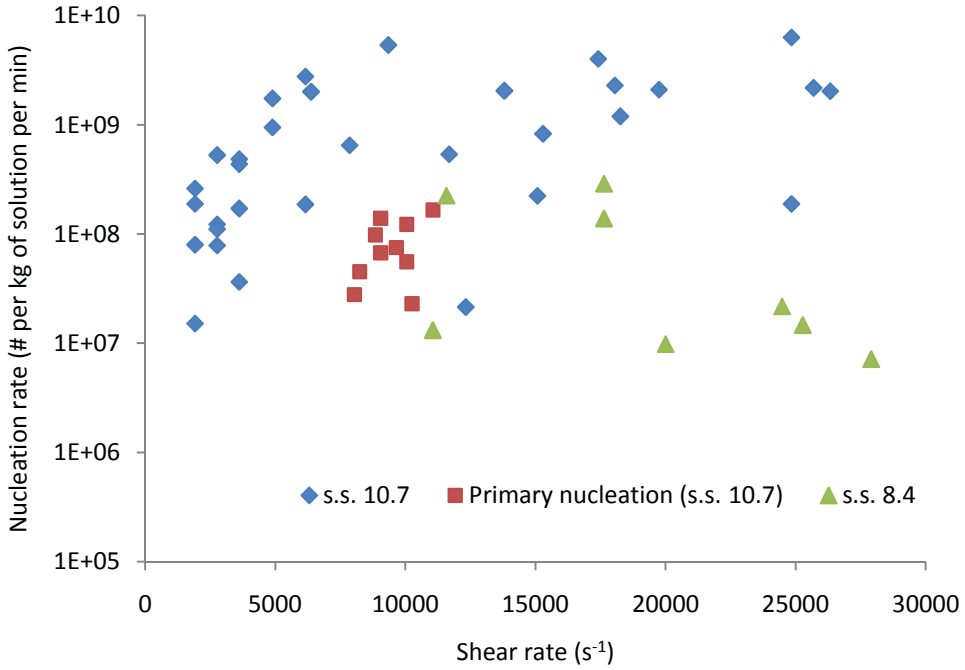


Figure 4-13. Shear secondary nucleation: Effect of shear rate and supersaturation. The primary nucleation trials contain no immobilized lactose crystals. Supersaturation (s.s.) is g of α-LMH per 100 g of water.

4.3.2 Conclusions

This section presents a preliminary work on the shear secondary nucleation of α-LMH. Shear was shown to induce nucleation rates higher than those due to primary nucleation at comparable shear rates. Shear rates above 5000 s^{-1} showed no effect on nucleation rates. Trials need to be conducted at lower shear rates to gain further understanding of the effect of shear on secondary nucleation.

Chapter 5 Model Development and Sensitivity Analysis

This study aims to improve the understanding of how to control the size of lactose crystals produced in an evaporative crystallizer. After experimental investigation of the individual secondary nucleation mechanisms, it is worthwhile to develop a preliminary conceptual mathematical model for the studied evaporative crystallizer. This will assist to better understand the interplay between the various operating parameters and the crystallization kinetics. The main objectives of the chapter are:

i) To develop a mathematical model incorporating the salient operational features of the industrial evaporative crystallizer
ii) To review current literature on lactose crystallization kinetics required for the model
iii) To simulate the developed mathematical model using MATLAB
iv) To perform a sensitivity analysis and determine the most important operational and kinetic parameters controlling the mean particle size.

5.1 Mathematical Model Development

In the development of this model the following assumptions have been made:

i) The crystallizer operates under ideal mixed suspension mixed product removal (MSMPR) conditions. It is well mixed and the temperature, crystal suspension and supersaturation are uniform throughout the crystallizer. The product removal is isokinetic and no classification of the crystals occurs. The validity of these assumptions has been examined in Chapter 6 for the current industrial system.
ii) Lactose crystals are spherical.
iii) No agglomeration or crystal breakage occurs. The attrition study in the previous chapter shows that the lactose crystals are susceptible to attrition. However the parent crystals do not undergo drastic size reduction (maximum reduction of 15% of the d_{50} over the one hour trial period). Therefore size reduction due to attrition is ignored. Secondary nucleation induced by attrition has been lumped in the secondary nucleation term.
iv) Crystals do not show either growth rate dispersion or size dependent growth rate. This is dealt with in detail in the next chapter.

v) The literature kinetic values (nucleation and growth) can be applied to the industrial crystallizer under study i.e. they are scale independent.

vi) The fluctuations and disturbances common during industrial operation are neglected and a smooth steady operation is assumed.

5.1.1 Mass Balance

A schematic representation of an evaporative crystallizer is shown in Figure 5-1. Q [kg min^{-1}], φ [(kg of solution) (kg of slurry)$^{-1}$], C [(kg of dissolved lactose) (kg of crystal free slurry)$^{-1}$] represents the mass flow rate, voidage and dissolved lactose concentration respectively. Subscripts f and o denotes the feed and the discharge streams to and from the crystallizer. M [kg] is the mass of the slurry present in the crystallizer at any given time. k_{evap} [kg min^{-1}] is the evaporation rate.

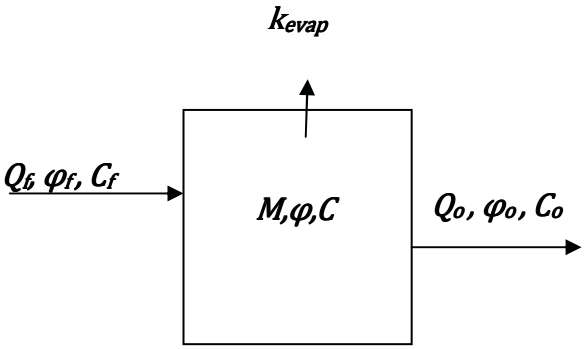


Figure 5-1. A generalized schematic of an evaporative crystallizer.

The overall lactose solute balance in the crystallizer is given by:

$$\frac{d}{dt}[M\varphi C] + \frac{d}{dt}[0.95M(1-\varphi)] = Q_f\varphi_f C_f - Q_o\varphi_o C_o + 0.95Q_f(1-\varphi_f) - 0.95Q_o(1-\varphi_o)$$

Equation 5-1 Solute balance over crystallizer

where, the terms on the left hand side represent the rate of accumulation of the dissolved and crystalline lactose respectively in the crystallizer. The first two terms on the right hand side give the feed and discharge rate of dissolved lactose and the last two terms gives the feed and discharge rate of crystalline lactose. The crystalline

lactose terms need to be multiplied by 0.95; mass fraction of lactose present in α-LMH, to account for the water of crystallization.

The industrial crystallizer being modelled operates in two distinct modes. During the start up, lactose solution is fed into the crystallizer vessel until a targeted volume level is achieved. The steam flow to the calandria (heat exchanger) is then initiated, providing energy to concentrate the solution. The feed flow is controlled to maintain a constant volume in the crystallizer. Fresh lactose solution is thus continuously fed to the crystallizer in order to make up for the reduction in volume due to evaporation. Therefore, the start up phase can be considered as a semi-batch or fed batch mode of operation. This semi-batch concentration process continues till the desired slurry density is achieved. Then the discharge valve is opened and slurry is pumped forward to the next stage in the process. At this point the feed flow is set to maintain a constant level in the crystallizer, allowing for evaporation and the discharge flow. This marks the start of the continuous operation.

Equation 5-1 for a semi-batch system under no discharge ($Q_o = 0$) and crystal free feed ($\varphi_f = 1$) conditions, becomes:

$$\frac{d}{dt}[M\varphi C] + \frac{d}{dt}[0.95M(1-\varphi)] = Q_f C_f$$

Equation 5-2 Semi-batch solute balance

Equation 5-2 on differentiating and rearranging takes the form:

$$\frac{dC}{dt} = \frac{M[0.95 - C]\frac{d\varphi}{dt} - [\varphi C + 0.95(1-\varphi)]\frac{dM}{dt} + Q_f C_f}{M\varphi}$$

Equation 5-3 Dissolved lactose concentration differential for semi-batch mode

Solving Equation 5-3 gives the dissolved lactose concentration profile for the semi-batch process. The rate of change of crystallizer mass during this process is given by Equation 5-4 :

$$\frac{dM}{dt} = Q_i - k_{evap}$$

Equation 5-4 Overall mass balance

The feed rate of solution is not directly measured in the industrial crystallizer under study. However, since the crystallizer is operated at constant volume, the volumetric feed rate is equal to the volumetric rate of water removal as shown in Equation 5-5, where ρ_w is the density of water and ρ_s is the density of feed solution.

$$\frac{Q_i}{\rho_s} = \frac{k_{evap}}{\rho_w}$$

Equation 5-5 Condition for constant volume operation. Volumetric rate of feed equal to volumetric rate of water removal

The evaporator operates as a single effect with no vapour recompression allowing the evaporation rate to be taken as the steam mass flow rate fed to the calandria. The density of the feed lactose solution was estimated at the feed concentration by the relationship given in Appendix I. In the continuous mode, M is a constant as the crystallizer operates at constant volume and density.

For the continuous mode, under the conditions of crystal free feed ($\varphi_f = 1$) and well mixed assumption($C_o = C, \varphi_o = \varphi$), Equation 5-1 on rearrangement becomes:

$$\frac{dC}{dt} = \frac{Q_f}{M}\frac{C_f}{\varphi} - \frac{C}{\tau} - \frac{0.95(1-\varphi)}{\tau\varphi} - \frac{(C-0.95)}{\varphi}\frac{d\varphi}{dt}$$

Equation 5-6 Dissolved lactose concentration differential for continuous mode

where, τ is the mean residence time given by ratio of mass in the crystallizer to the discharge flow rate expressed as:

$$\tau = \frac{M}{Q_o}$$

Equation 5-7 Mean residence time

This leaves φ and $\frac{d\varphi}{dt}$, the slurry voidage terms to be defined. The voidage is defined by the crystal content of the slurry and is therefore governed by the number and size of the crystals present in the slurry. This leads to the population balance equations discussed in next section.

5.1.2 Population Balance

A Method of Moments (MOM) approach can be used to convert the population balance equation (PBE) from a partial differential equation to a number of ordinary differential equations (ODEs) (Randolph & Larson, 1988). The different moments give information such as: number of crystals [0^{th} moment (m_0)]; average length of crystals [1^{st} moment (m_1)]; surface area of crystals [2^{nd} moment (m_2)]; volume of crystals [3^{rd} moment (m_3)].

The zero moment derivative is given by

$$\frac{dm_0}{dt} = B - \frac{m_0}{\tau},$$

Equation 5-8 Zeroth moment derivative

the first moment derivative by

$$\frac{dm_1}{dt} = Gm_0 \ - \frac{m_1}{\tau},$$

Equation 5-9 First moment derivative

the second moment derivative by

$$\frac{dm_2}{dt} = 2Gm_1 - \frac{m_2}{\tau},$$

Equation 5-10 Second moment derivative

the third moment derivative by

$$\frac{dm_3}{dt} = 3Gm_2 - \frac{m_3}{\tau},$$

Equation 5-11 Third moment derivative

and the fourth moment derivative by

$$\frac{dm_4}{dt} = 4Gm_3 - \frac{m_4}{\tau}.$$

Equation 5-12 Fourth moment derivative

Coefficient of variation of a volumetric size distribution is given by

$$CV = (m_3 m_5 / m_4^2 - 1)^{0.5}.$$

Equation 5-13 Coefficient of variation of a size distribution

The coefficient of variation (CV) is a measure of the width of the size distribution. For an ideal MSMPR crystallizer CV is always equal to 0.5 (Randolph & Larson, 1988) .

The second term on the right hand side in the moment equations becomes zero for a semi-batch process as $\tau = \infty$ for $Q_o = 0$ as per Equation 5-7. The slurry voidage (φ) is given by

$$\varphi = 1 - \rho_c m_3 \ .$$

Equation 5-14 Slurry voidage

Differentiating Equation 5-14 gives

$$\frac{d\varphi}{dt} = -\rho_c \frac{dm_3}{dt} .$$

Equation 5-15 Rate of change of slurry voidage

The volume weighted mean diameter D[4,3] as per Randolph & Larson (1988) is given by

$$D[4,3] = \frac{m_4}{m_3} \ .$$

Equation 5-16 Volume weighted mean diameter

The crystal content C_c is calculated as,

$$C_c = m_3 \rho_c \ .$$

Equation 5-17 Crystal content of the slurry

The slurry density is an online measured quantity in the industrial system and is used as a measure of total solids. Total solids can be calculated as

$$TS = \varphi C + 0.95 C_c \ .$$

Equation 5-18 Total solids in the slurry

From an experiment performed in the laboratory, it was found that the density of the slurry remains unchanged irrespective of the state of solute (dissolved or crystalline). The details are given in Appendix I of this chapter. Hence, a relationship between the dissolved solids and the solution density can be used to relate total solids to the slurry

density. Due to a lack of data on lactose solution density at higher concentrations, sucrose solution density data from Bubnik, Kadlec, Urban, & Bruhns (1995) was used to correlate slurry density to total solids at the crystallizer temperature for lactose. The sucrose solution density matched very closely (a maximum error of 1%) with the limited density data available for lactose solutions from Buma (1980).

$$\rho_s = 983.2e^{0.0042(T.S.)}$$

Equation 5-19 Slurry density-total solids relationship

The slurry density in itself does not present a complete picture regarding the crystal yield as it is a function of total solids, which in turn depends on both dissolved as well as crystalline solids. Hence, the crystal concentration needs to be evaluated separately in order to estimate the production rate of crystals.

The PBE scheme discussed above requires growth and nucleation kinetic models which are discussed now.

5.1.3 Growth and Nucleation Kinetics

During the start up process of an evaporative crystallizer, in the absence of any seeding, crystal formation occurs by primary nucleation. After the start up, the system contains a slurry of dissolved and crystalline lactose and operates at a lower supersaturation. During this stage secondary nucleation becomes the dominant mechanism of nucleation. The primary nucleation, secondary nucleation and growth kinetics of α-LMH can be expressed as

$$B_p = k_{n,p}\left(\frac{C_\alpha}{1-C} - C_{\alpha s}\right)^{n_p},$$

Equation 5-20 Primary nucleation rate

$$B = k_{n,s}{C_c}^{j}\left(\frac{C_\alpha}{1-C} - C_{\alpha s}\right)^{b},$$

Equation 5-21 Secondary nucleation rate

$$\& \quad G = k_g\left(\frac{C_\alpha}{1-C} - C_{\alpha s}\right)^{g},$$

Equation 5-22 Growth rate

where B [# min^{-1} (kg of slurry)$^{-1}$] and G [μm min^{-1}] are the nucleation and growth rate, respectively. As secondary nucleation occurs in the presence of solute crystals, the concentration of crystals is included in the rate expression with the order of dependence, j. n_p, b and g represent the order of dependence of primary nucleation, secondary nucleation and growth kinetics, respectively on supersaturation (the bracketed term). $k_{n,p}$, $k_{n,s}$ and k_g are the rate constants. Subscripts, p and s denote primary and secondary nucleation respectively. Lactose crystallization kinetic parameters present in literature are discussed in detail in section 5.2.

5.1.4 Lactose Solubility

The equilibrium α-lactose solubility in the presence of β-lactose is given by Visser (1982) as

$$C_{\alpha s} = \frac{C_{LS} - FK_m(\frac{C}{1-C} - C_{LS})}{1 + K_m},$$

Equation 5-23 Equilibrium α-lactose solubility

where F is a temperature dependent correction factor suggested by Visser (1982) to account for the suppression of solubility of α-lactose in presence of β-lactose. It's dependence on temperature can be given by the following exponential relationship

$$F = 0.0187exp^{0.0236T}.$$

Equation 5-24 Correction factor for α-LMH

C_{LS} is the lactose equilibrium solubility at a given temperature T (McLeod, 2007) can be estimated by

$$C_{LS} = \frac{10.9109exp^{0.02804T}}{100}.$$

Equation 5-25 Equilibrium lactose solubility

5.1.5 Lactose Mutarotation Kinetics

The total lactose concentration (C) is the sum of α and β lactose concentrations,

$$C = C_\alpha + C_\beta.$$

Equation 5-26 Total dissolved lactose

The equilibrium mutarotation rate constant is defined as

$$K_m = \frac{C_\beta}{C_\alpha}.$$

Equation 5-27 Mutarotation rate constant

Combining Equation 5-26 and Equation 5-27, the α-LMH concentration can be calculated from the total lactose concentration by

$$C_\alpha = \frac{C}{(1 + K_m)}.$$

Equation 5-28 Dissolved α-lactose concentration

McLeod (2007) fitted the data by Roetman & Buma (1974) to give the following equation to predict K_m as a function of temperature.

$$K_m = -0.0024T + 1.6353$$

Equation 5-29 Equilibrium mutarotation rate constant as a function of temperature

5.2 A Brief Review on Lactose Crystallization Kinetics

Lactose crystallization kinetic parameters are required to simulate the mathematical model developed in the previous sections. In this section the available growth and nucleation studies on lactose are reviewed. The range of the kinetic parameters used during simulation was then determined.

5.2.1 Growth

There are numerous studies in the literature investigating lactose monohydrate crystal growth rate [(Arellano, Aguilera, & Bouchon, 2004; Butler, 1998; Dincer, Ogden, & Parkinson, 2009b; Griffiths, et al., 1982; Jelen & Coulter, 1973; Lifran, Vu, Durham, Hourigan, & Sleigh, 2007; McLeod, 2007; Shi, et al., 1989; Shi, et al., 1990; Thurlby, 1976)]. Figure 5-2 shows the results from a selection of these studies. For comparisons the units were converted to common units of μmmin^{-1} for growth rate and g of α-LMH per 100 g of water for supersaturation. The growth curves were plotted for the studies in which the growth rate equations were reported directly in the required units. It can be seen that a range of growth rates have been reported for lactose monohydrate. These variations can be attributed to the different experimental approaches used to obtain the results including factors such as the hydrodynamics of

the systems and the purity of lactose solutions used. The growth rates reported by Thurlby (1976) were an order of magnitude higher compared to others at similar supersaturations. The trials were also conducted in a small range, at low levels of supersaturation. In the study of Shi, et al. (1989), experiments were conducted under stagnant conditions. They reported the slowest growth rates of all the studies and are likely to have been diffusion limited. Both of the above growth rate expressions were hence ruled out for simulation. All the other rate curves fall between those proposed by McLeod (2007) and Shi, et al., (1990). The growth rates proposed by these two studies were used during the simulation runs to see the effect of growth kinetics on crystallizer dynamics.

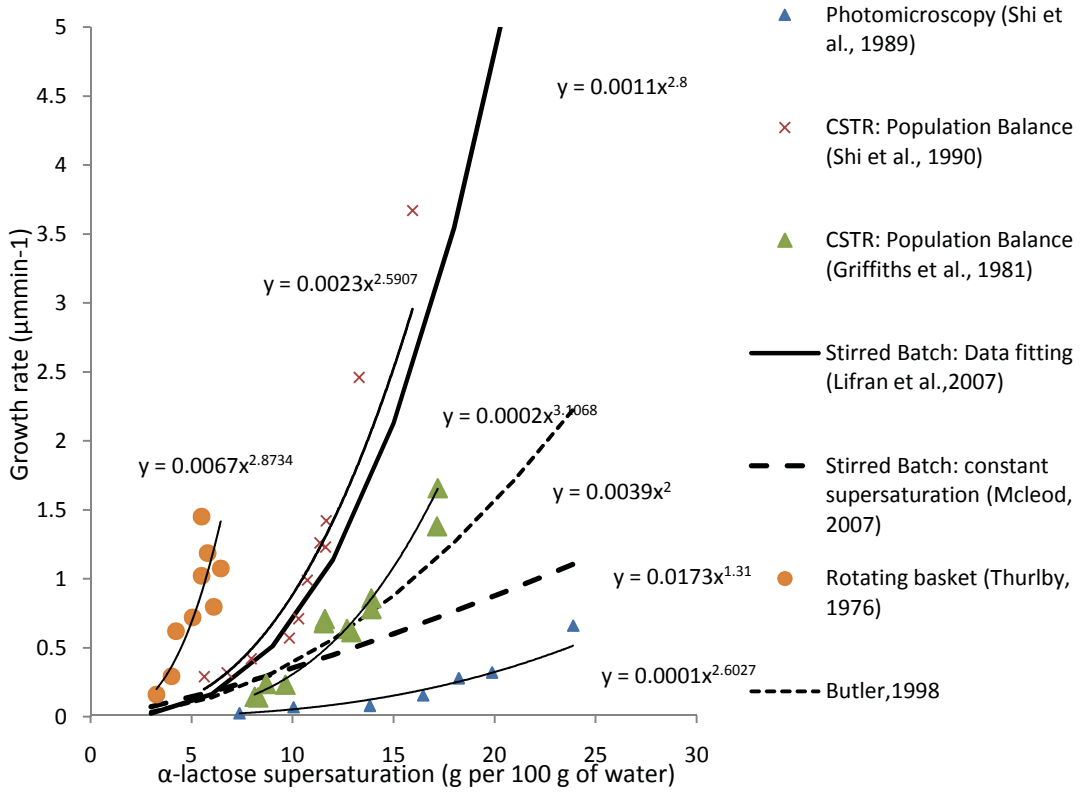


Figure 5-2. Growth studies on lactose.

5.2.2 Secondary Nucleation

Only limited literature exists on the secondary nucleation kinetics of lactose as shown in Figure 5-3. There is a huge variation and scatter in the data presented. This is attributed to the stochastic nature of the nucleation process and the different

experimental and analytical techniques used, as shown in Table 5-1. Since the analysis by Liang, et al., (1991) was the most robust, the value of 1.5 for *b*, calculated in their study, was fixed across all the simulation runs. The high uncertainty in the prediction of secondary nucleation rate was taken into account by altering the rate constant ($k_{n,s}$) value by two orders of magnitude during the simulation runs.

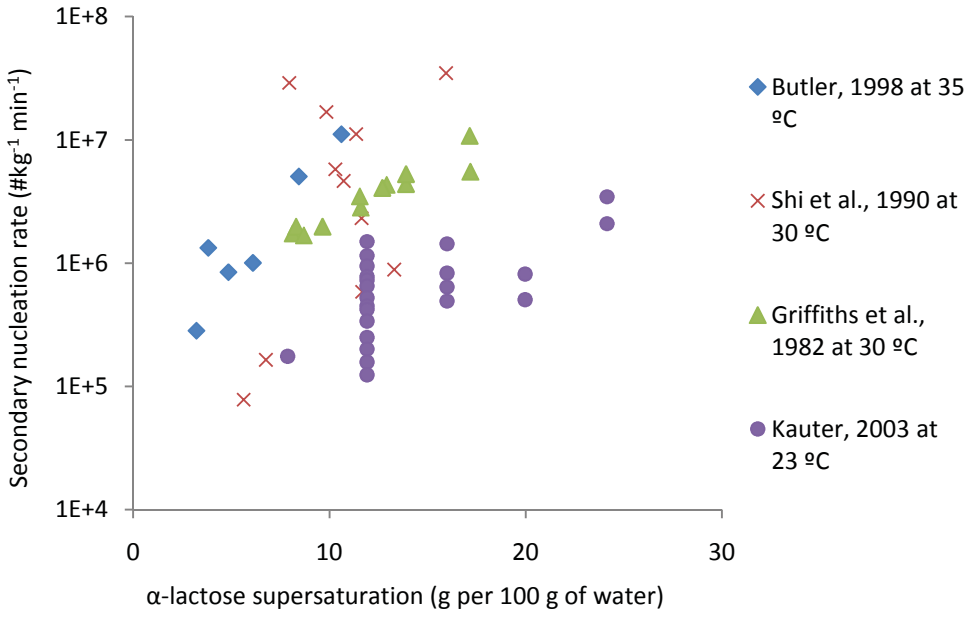


Figure 5-3. Secondary nucleation studies on lactose.

Table 5-1 *Secondary Nucleation Studies on Lactose*

Study	Value of *b* (errors reported at 95% confidence interval limit)	Methodology	Measurement technique
(Kauter, 2003)	1 ± 0.7	Batch stirred system, 5-100 seed crystal, constant supersaturation, generated nuclei enumerated	Laser diffraction
(Griffiths, et al., 1982)	2.33	Continuous stirred system, MSMPR population balance analysis	Sonic sieving
(Shi, et al., 1990)	1.89 ± 0.78	MSMPR analysis, calculated kinetic parameters based on linear extrapolation of the curved MSMPR plot	Electrical sensing zone (Coulter Counter)
(Liang, et al., 1991)	1.2±0.36 - 1.5±0.28	Similar to Shi, et al. (1990), used growth rate dispersion (GRD) models to calculate kinetic parameters from the curved MSMPR plot rather than linear extrapolation, yielded different values depending on the GRD model used	Electrical sensing zone (Coulter Counter)

5.2.3 Primary Nucleation

The data from Mcleod (2007) at 40°C was used (Figure 5-4) to arrive at the primary nucleation expression to be used as the standard reference run for simulations. This work studied primary nucleation of lactose under stirred conditions using spectrophotometer absorbance to follow the degree of nucleation. Due to the system specific nature of nucleation, high inherent uncertainty exists. Hence, simulations at two orders of magnitude variation in $k_{n,p}$ values were conducted to study the effect of primary nucleation, with a fixed value of 2.5 for n_p.

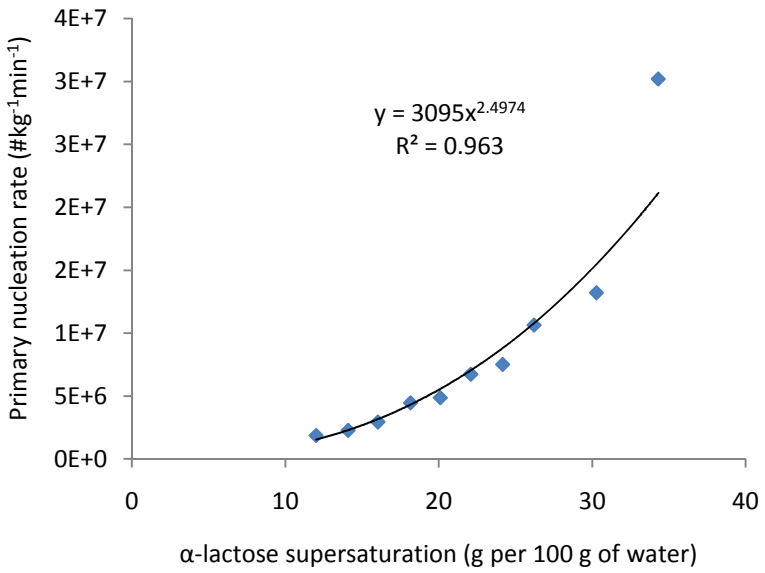


Figure 5-4. Lactose primary nucleation rate (McLeod, 2007).

5.3 Simulation and Sensitivity Analysis

The above differential algebraic equations were solved in MATLAB (R2007) using the *ode45* routine. The semi-batch and continuous mode equations were solved separately with the end conditions of the semi-batch serving as the initial conditions for the continuous mode. As there were no seed crystals, the initial conditions for all the moment equations for the semi-batch mode were set as zero. For the crystallizer mass and dissolved lactose concentration, 14000 kg and 0.55 kg of dissolved lactose per kg of solution respectively were used as the initial conditions. A sensitivity analysis was conducted to find out the effect of parameters on the volume weighted crystal size (D[4,3]), the crystal content and the slurry density. Values of the different parameters used for the sensitivity analysis simulations are shown in Table 5-2.

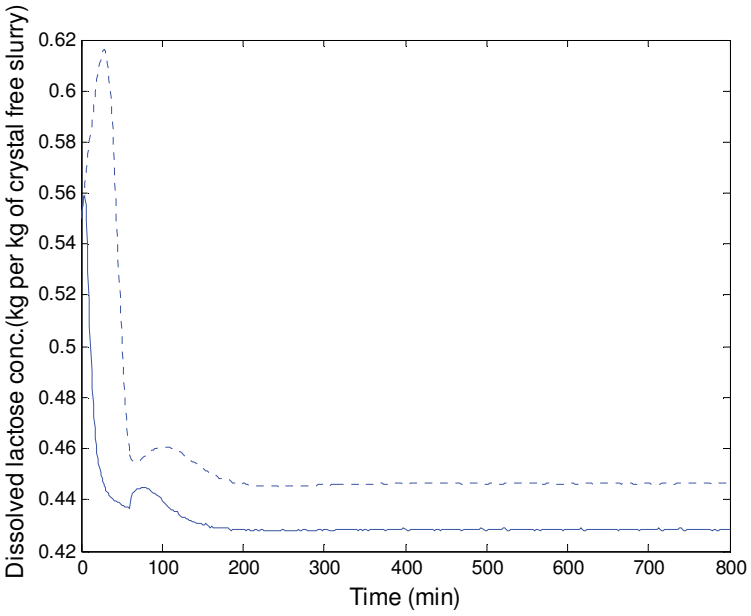
Table 5-2 *Values and Range of Parameters Studied During Simulation*

Parameter	Standard Reference Run Value	Other Values studied	Comment on standard reference run values
b	1.5 (Liang, et al., 1991)	---	Used by Mimouni, Schuck, & Bouhallab (2009); constant across all runs
n_p	2.5	---	From McLeod (2007); constant across all runs
g	1.3 (McLeod, 2007)	2.6 (Shi, et al., 1990)	---
$k_{n,s}$	1.0E10 [# min^{-1} (kg of crystal)$^{-1}$ ((kg of α-LMH) (kg of water)$^{-1}$)$^{-1.5}$] (Mimouni, et al., 2009)	1.0E9-1.0E11	Value was estimated by Mimouni, et al., (2009) by fitting to their experimental data; converted to (per kg of crystal) from (per g of crystal) to match the units used in the current model
$k_{n,p}$	3.1E8 [# min^{-1} (kg of slurry)$^{-1}$((kg of α-LMH) (kg of water)$^{-1}$)$^{-2.5}$] (McLeod, 2007)	3.1E7-3.1E9	Converted to match the supersaturation units used in the model (kg of α-LMH per kg of water)
k_g	7 [μm min^{-1} ((kg of α-LMH) (kg of water)$^{-1}$)$^{-g}$] (McLeod, 2007)	364 (Shi, et al., 1990)	Converted to match the supersaturation units used in the model (kg of α-LMH per kg water)
k_{evap}	70 kg min^{-1}	60-80	Average plant operation value
j	1	---	(Shi, et al., 1990)
τ	55 min	37-90	Average plant operation value
T	T	55-70	Crystallizer operating temperature, set by the quality standards of the end product; constant across all runs; not disclosed as commercially sensitive

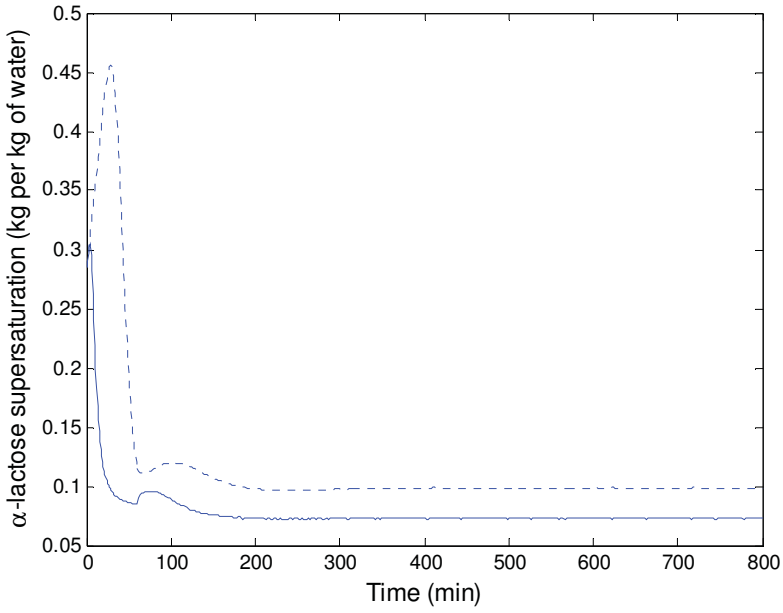
5.3.1 Effect of Growth Rate

The simulation results for the two growth rate equations proposed by McLeod (2007) and Shi, et al., (1990) are shown in Figure 5-5 (a-g). Figure 5-5 (a) & (b) show that the dissolved lactose concentration and supersaturation increases initially as

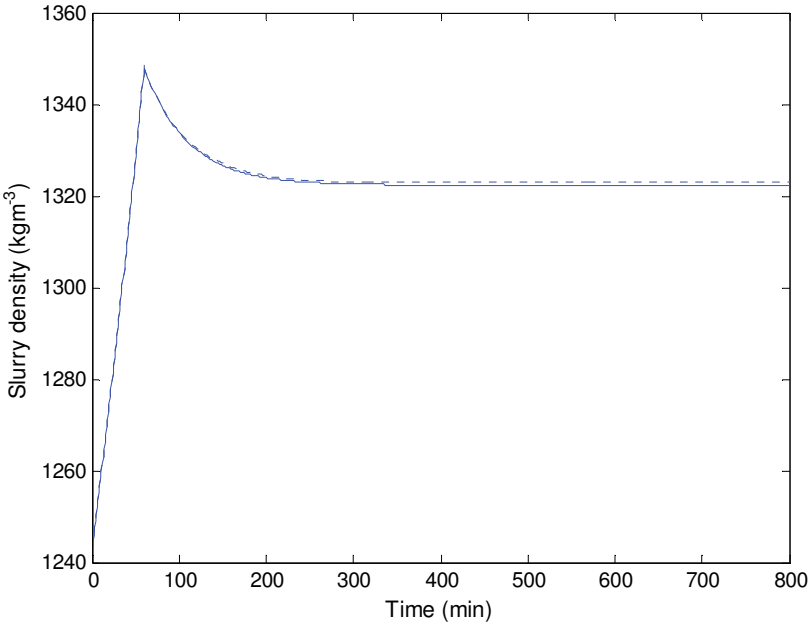
evaporation occurs but drops once nucleation followed by growth begins. The crystallizer gradually reaches a steady state following a transition phase once the continuous operation starts. The slurry density or the total solids remain unchanged in view of constant evaporation rate (Figure 5-5(c)). Higher growth rates result in higher depletion of lactose from the slurry, resulting in higher crystal content (Figure 5-5 (d)). There is only a minor increase of ~10 μm in the particle mean diameter between the fastest (Shi, et al., 1990) and the slowest growth rates (McLeod, 2007) as evident from Figure 5-5(e). The instantaneous growth rate for the two cases is identical at the steady state (Figure 5-5 (f)). The minor increase in the particle size can be explained by a lower secondary nucleation rate at faster growth rate (due to a lower steady state supersaturation level). The faster growth rate resulted in a wider size distribution (greater coefficient of variance values) initially before settling to the theoretical value of 0.5 for an ideal MSMPR (Figure 3-5(g)).



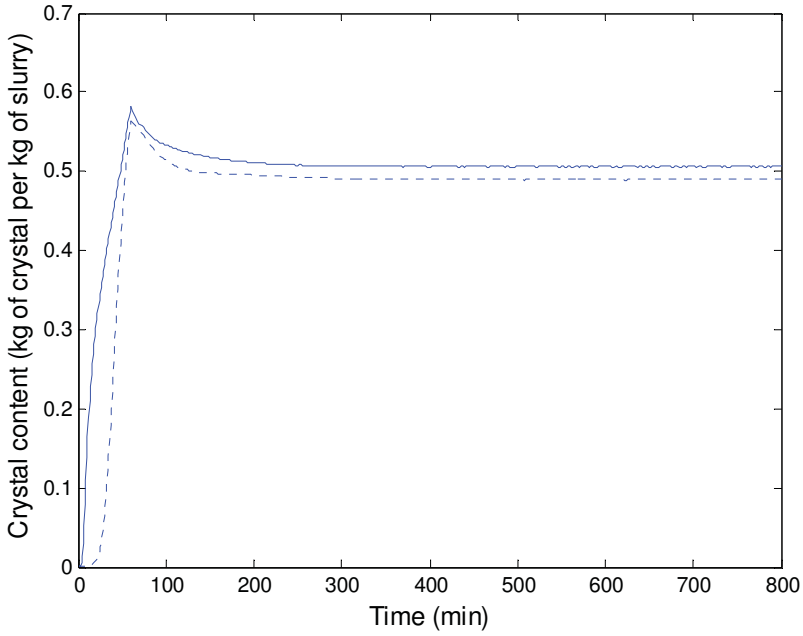
(a)


α-lactose supersaturation (kg per kg of water)
0.5
0.45
0.4
0.35
0.3
0.25
0.2
0.15
0.1
0.05
0
100
200
300
400
500
600
700
800
Time (min)

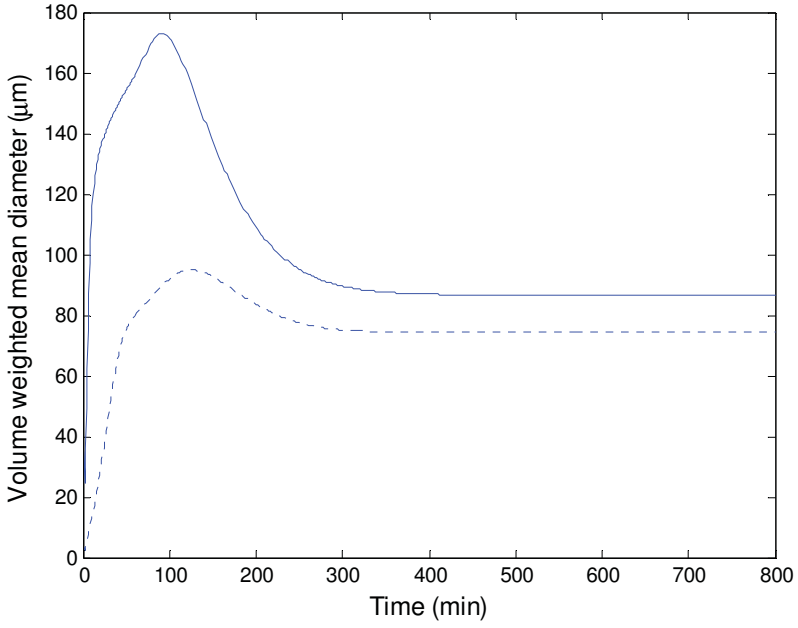
(b)


Slurry density (kgm-3)
1360
1340
1320
1300
1280
1260
1240
0
100
200
300
400
500
600
700
800
Time (min)

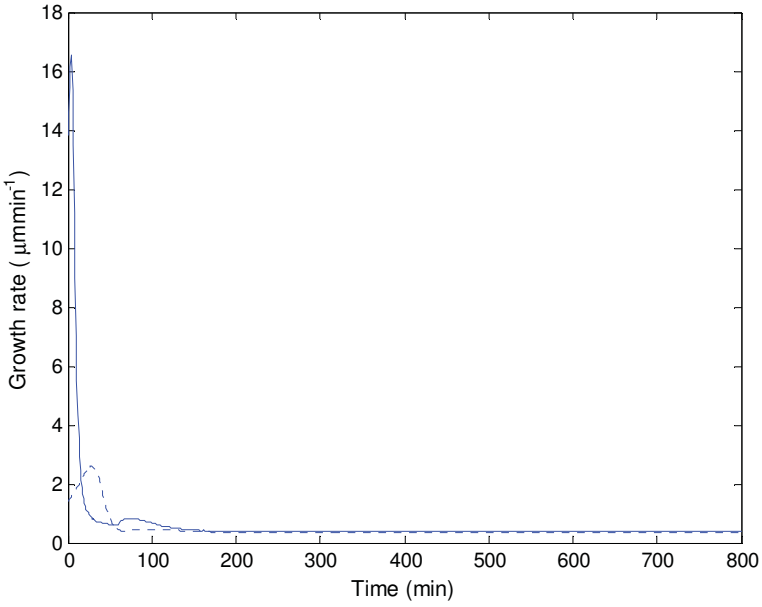
(c)


Crystal content (kg of crystal per kg of slurry)
0.7
0.6
0.5
0.4
0.3
0.2
0.1
0
0
100
200
300
400
500
600
700
800
Time (min)

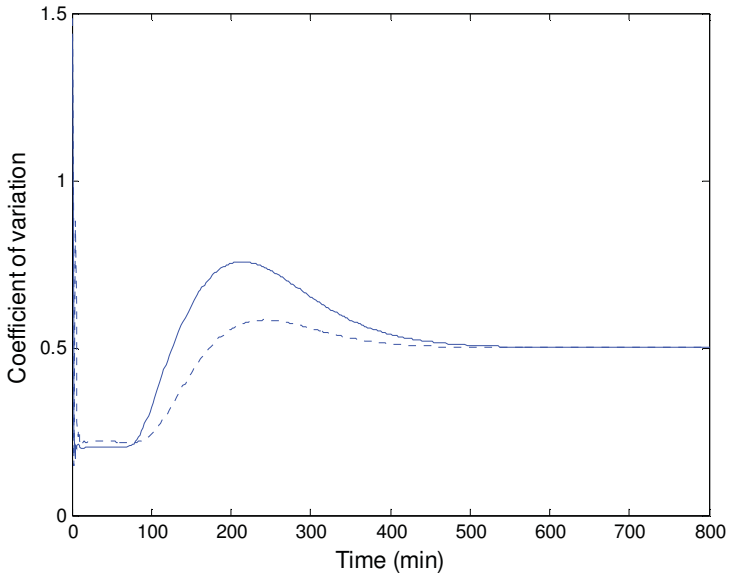
(d)


Volume weighted mean diameter (μm)
180
160
140
120
100
80
60
40
20
0
0
100
200
300
400
500
600
700
800
Time (min)

(e)



(f)



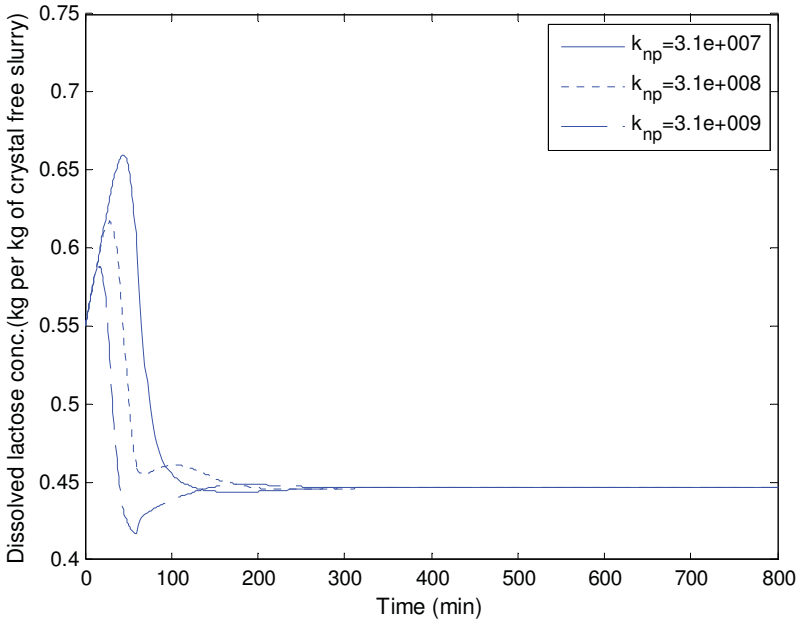
(g)

Figure 5-5. Effect of growth rate kinetics on a), dissolved lactose; b), supersaturation; c), slurry density; d), crystal concentration; e), mean diameter; f), instantaneous growth rate; and g), coefficient of variation. Solid line represent profiles obtained by using growth parameters of Shi, et al.,(1990) and the broken line uses that of McLeod (2007).

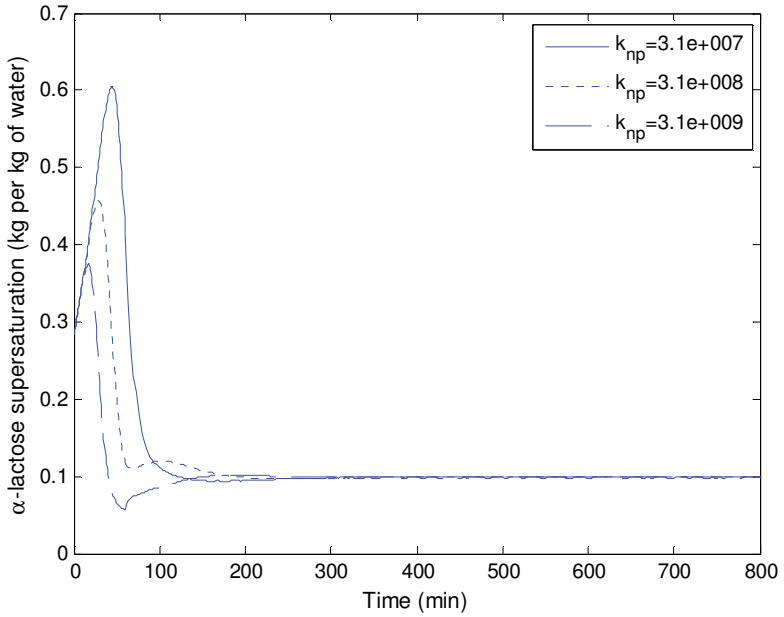
5.3.2 Effect of Primary Nucleation

The model has provision for primary nucleation occurring only during the semi-batch mode. Figure 5-6 (a-g) shows the effect of changing the primary nucleation rate constant from 3.1E7 to 3.1E9 [# min^{-1} (kg of slurry)$^{-1}$((kg of α-LMH) (kg of water)$^{-1}$)$^{-}$

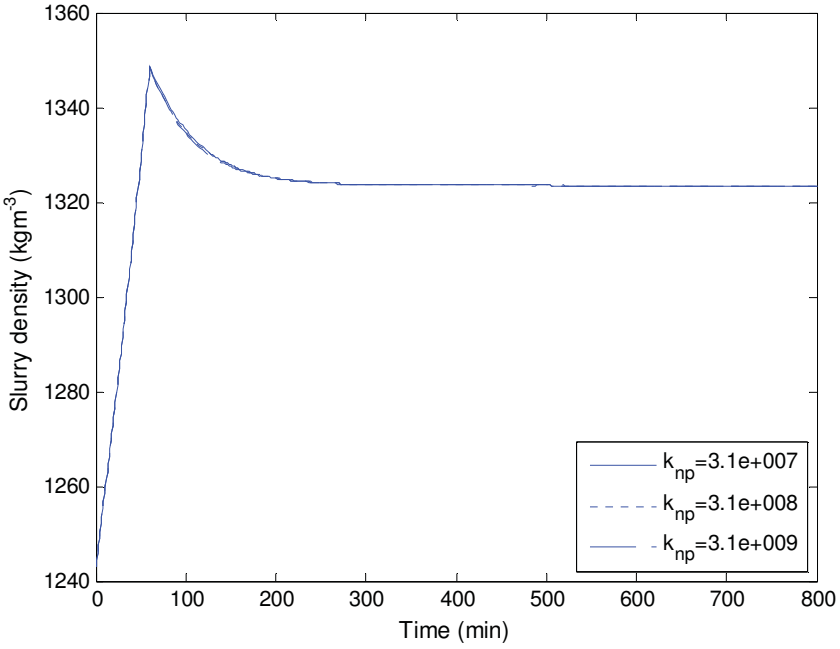
$^{2.5}$]. The increase in lactose concentration and the supersaturation (Figure 5-6 (a) & (b)) during the semi-batch stage is greater at lower primary nucleation rate constant due to the presence of lesser number of nuclei to absorb lactose from the solution. As expected no changes were observed in the slurry density as the evaporation rate remained constant (Figure 5-6(c)). Fewer nuclei results in a lesser depletion of lactose from the solution, resulting lower crystal content (Figure 5-6(d)). Since nucleation rate depends on both, the rate constant and supersaturation, absolute nucleation rate for different rate constants was plotted in Figure 5-6(e). Higher rate constants resulted in higher nucleation rates. This reduced the supersaturation driving force, which in turn reduced the nucleation rate. These opposing factors neutralized each other to an extent, resulting in similar nucleation rate values by the end of semi-batch mode. At lower nucleation rate constants, a lower nucleation rate and higher supersaturation promoted growth, leading to an increase in the mean particle size (Figure 5-6(f)). All the parameters stabilize to a steady constant value after 6 hours, independent of the primary nucleation rate as secondary nucleation takes over as the dominant nuclei source. Hence, primary nucleation rate is not an important factor in controlling the output particle size from the existing crystallizer.



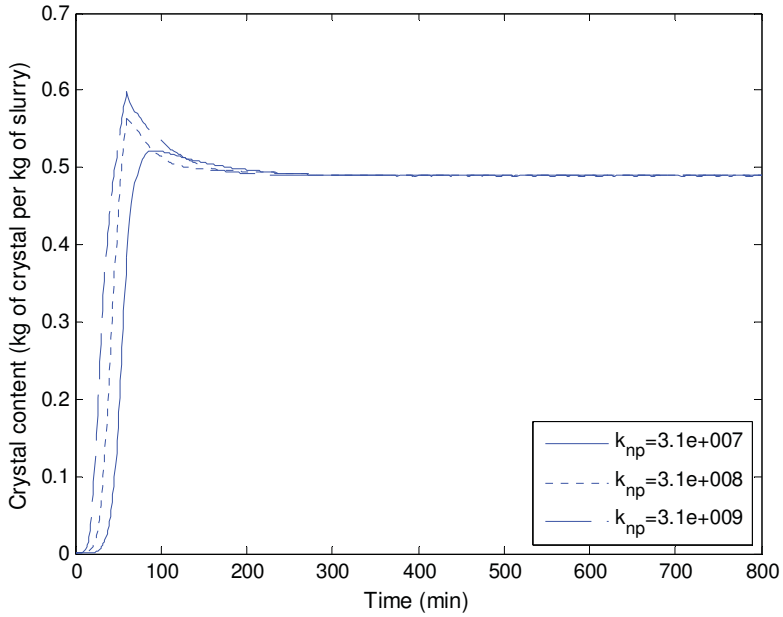
(a)


α-lactose supersaturation (kg per kg of water)
Time (min)
k_np=3.1e+007
k_np=3.1e+008
k_np=3.1e+009

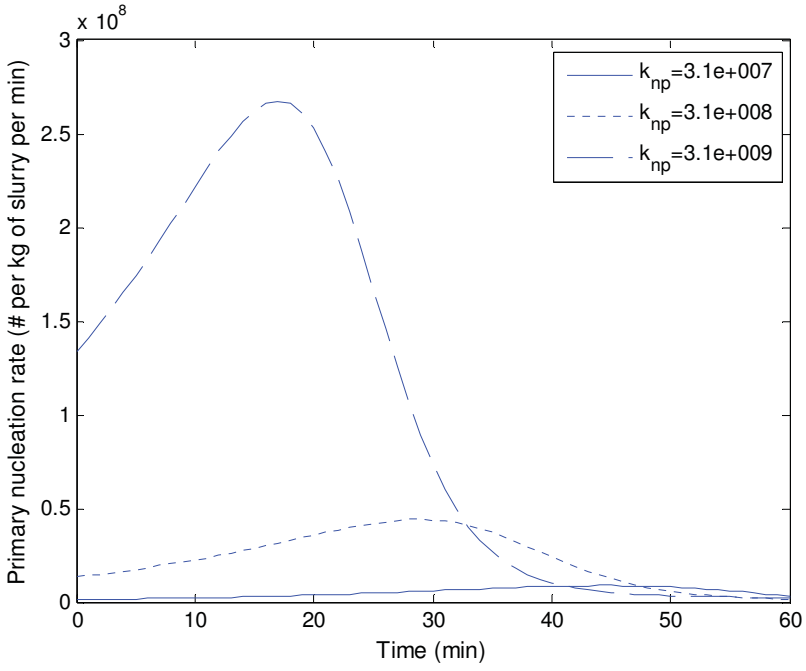
(b)


Slurry density (kgm-3)
Time (min)
k_np=3.1e+007
k_np=3.1e+008
k_np=3.1e+009

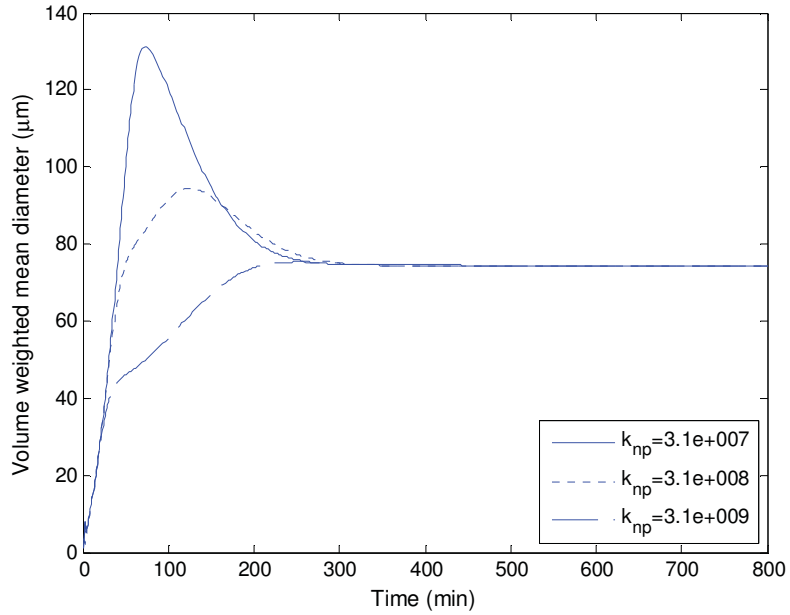
(c)


Crystal content (kg of crystal per kg of slurry)
Time (min)
0.7
0.6
0.5
0.4
0.3
0.2
0.1
0
0
100
200
300
400
500
600
700
800
k_np=3.1e+007
k_np=3.1e+008
k_np=3.1e+009

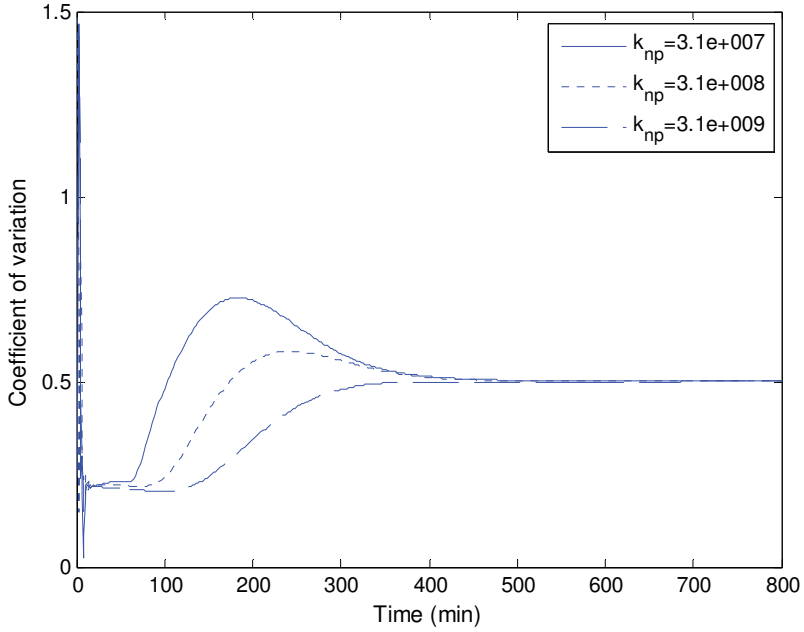
(d)


x 10^8
Primary nucleation rate (# per kg of slurry per min)
Time (min)
3
2.5
2
1.5
1
0.5
0
0
10
20
30
40
50
60
k_np=3.1e+007
k_np=3.1e+008
k_np=3.1e+009

(e)



(f)

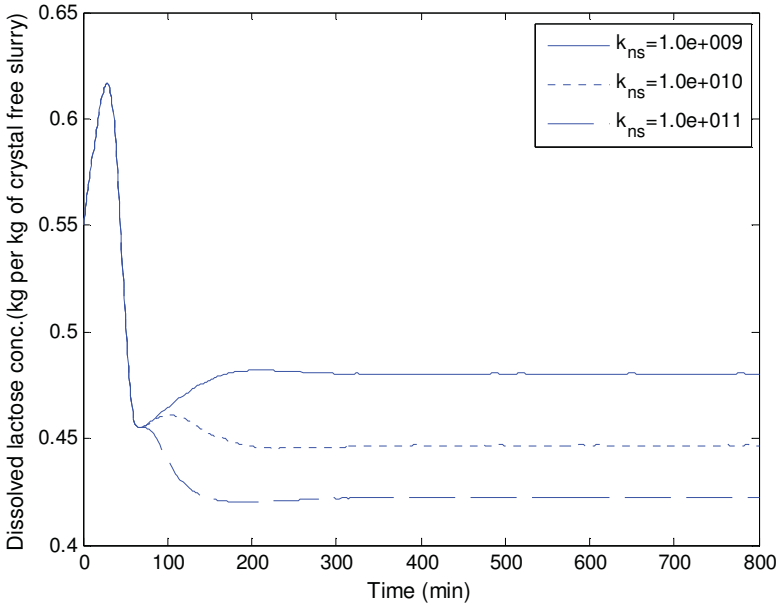


(g)

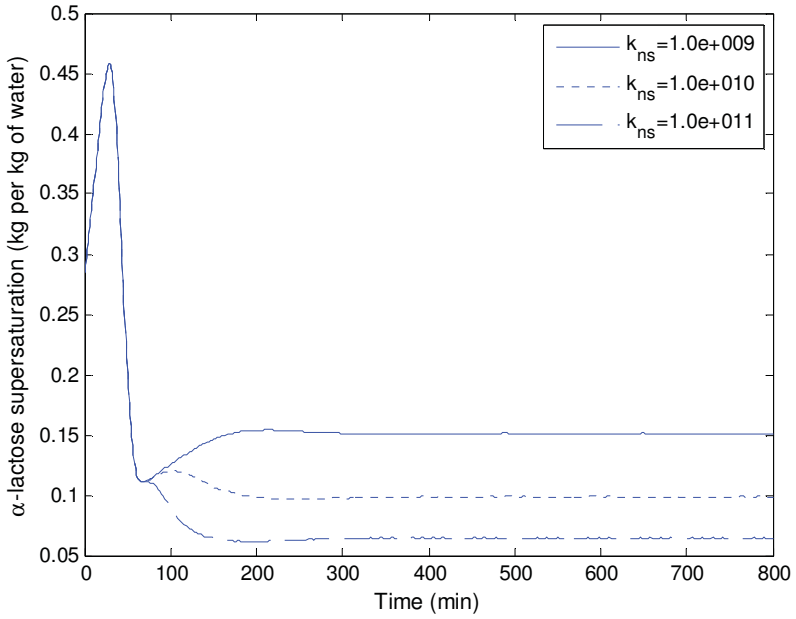
Figure 5-6. Effect of primary nucleation rate constant on a), dissolved lactose; b), supersaturation; c), slurry density; d), crystal concentration e), instantaneous primary nucleation rate; f), mean diameter and g), coefficient of variation.

5.3.3 Effect of Secondary Nucleation

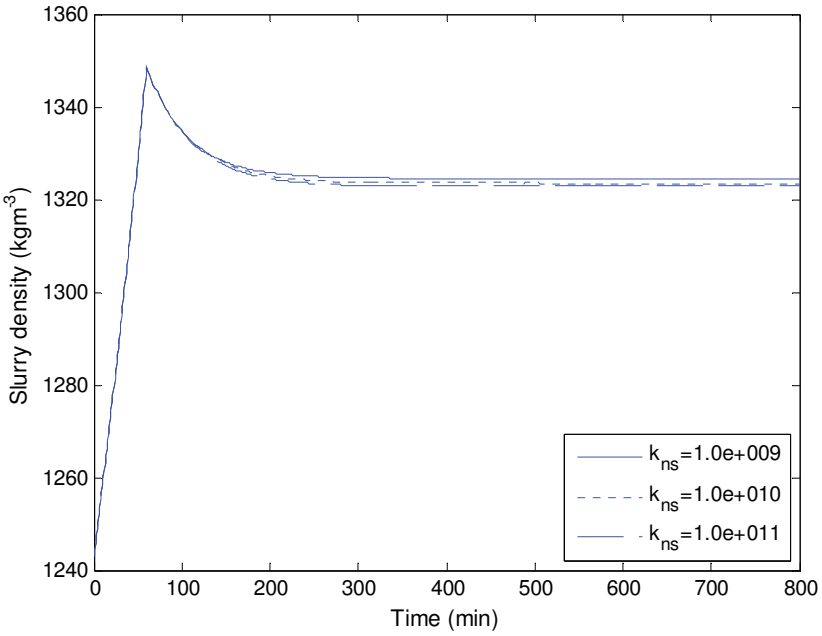
The results in Figure 5-7 show the effect of change in secondary nucleation rate constant. On decreasing the secondary nucleation rate constant, the steady state dissolved lactose concentration (Figure 5-7(a)) and supersaturation (Figure 5-7(b)) increased. The steady state nucleation rate decreased 5.5 times for every order of magnitude decrease in nucleation rate constant, shown in Figure 5-7(e). The particle size roughly doubled for every order of magnitude decrease in the nucleation constant or 5.5 times decrease in nucleation rate (Figure 5-7(f)). This demonstrates that controlling the secondary nucleation rate is the key to controlling the crystal size. One point worth noting in these results is that the crystal content of the slurry (Figure 5-7(d)) is higher at higher nucleation rate constants, because more lactose is removed from solution through nucleation and growth due to the increased crystal surface area created. But the higher lactose recovery at higher nucleation rates is in the form of finer crystals. The difficulties in recovering smaller crystals during downstream processes will largely negate the small advantage of higher lactose recovery and thus it is invariably desired to produce larger crystals by reducing the secondary nucleation rate.



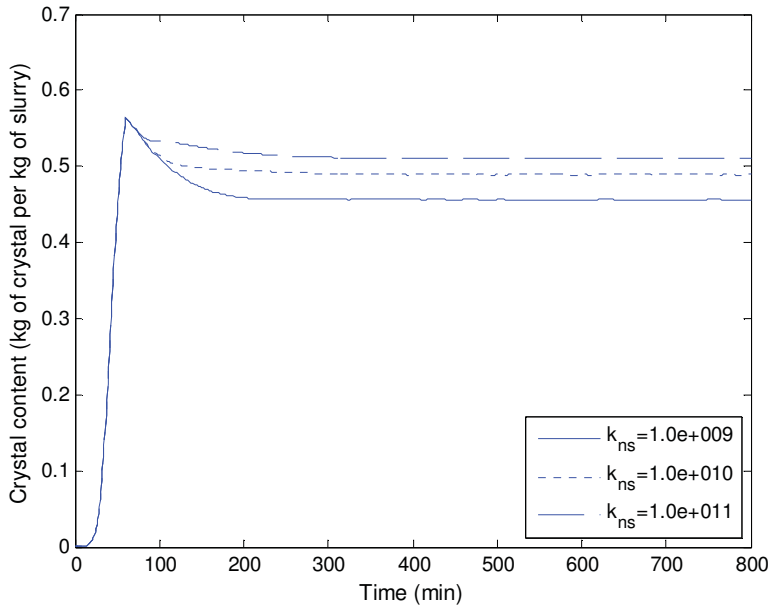
(a)


α-lactose supersaturation (kg per kg of water)
Time (min)
k_ns=1.0e+009
k_ns=1.0e+010
k_ns=1.0e+011

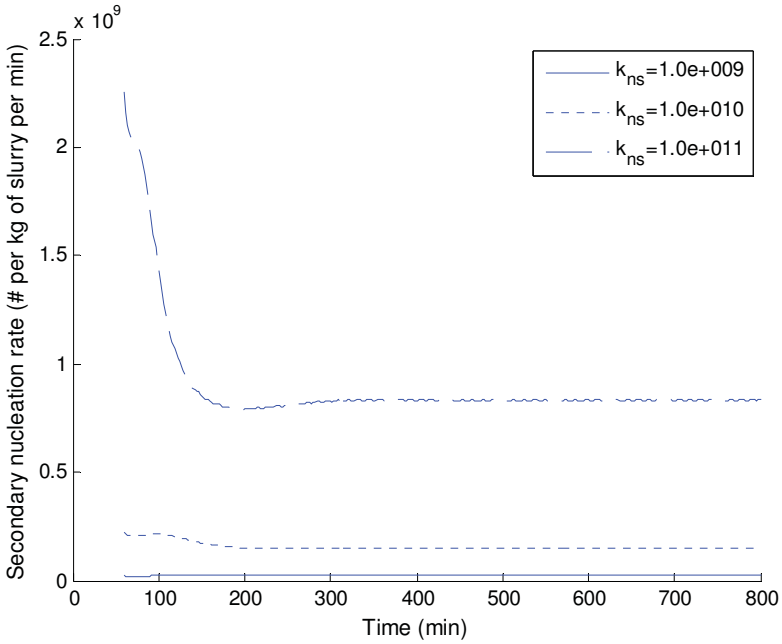
(b)


Slurry density (kgm-3)
Time (min)
k_ns=1.0e+009
k_ns=1.0e+010
k_ns=1.0e+011

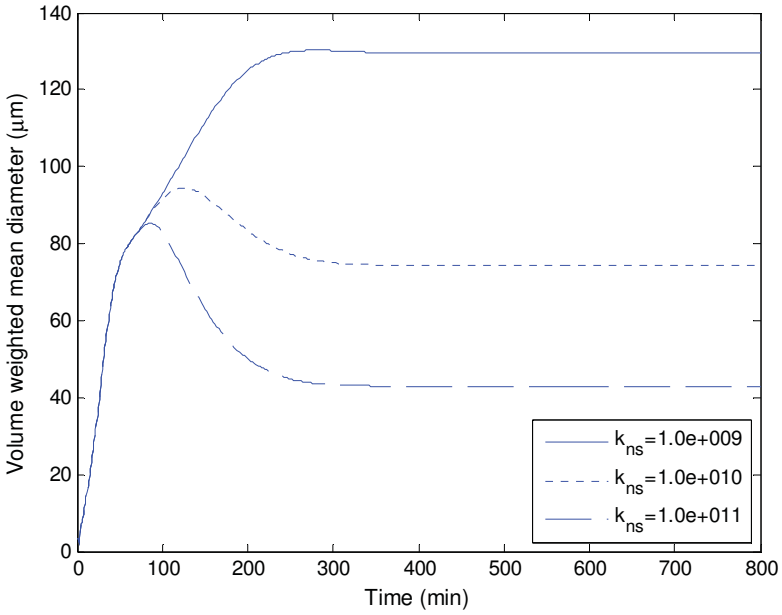
(c)


Crystal content (kg of crystal per kg of slurry)
Time (min)
0
0.1
0.2
0.3
0.4
0.5
0.6
0.7
0
100
200
300
400
500
600
700
800
k_ns=1.0e+009
k_ns=1.0e+010
k_ns=1.0e+011

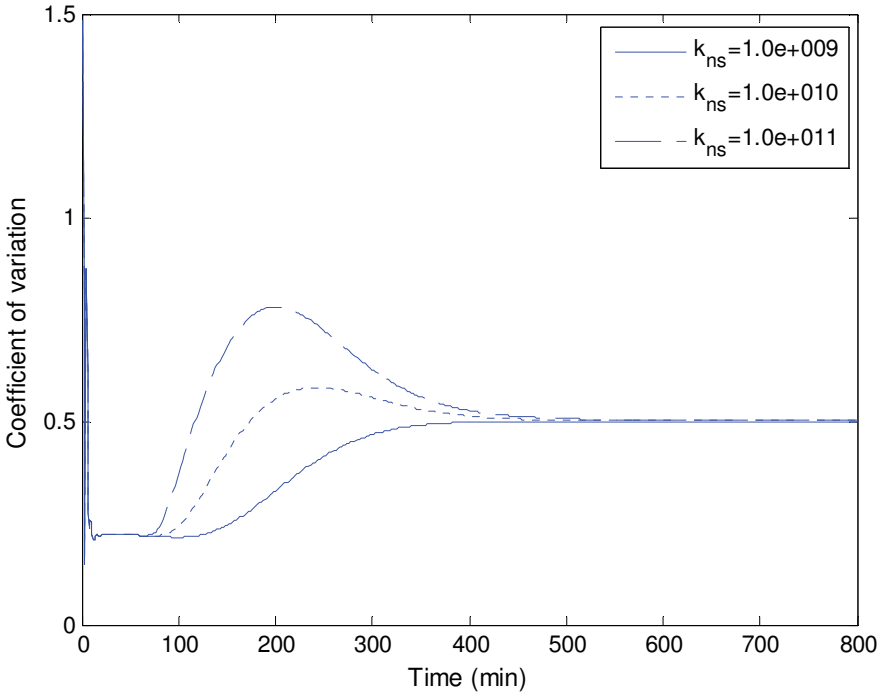
(d)


x 10^9
Secondary nucleation rate (# per kg of slurry per min)
Time (min)
0
0.5
1
1.5
2
2.5
0
100
200
300
400
500
600
700
800
k_ns=1.0e+009
k_ns=1.0e+010
k_ns=1.0e+011

(e)



(f)

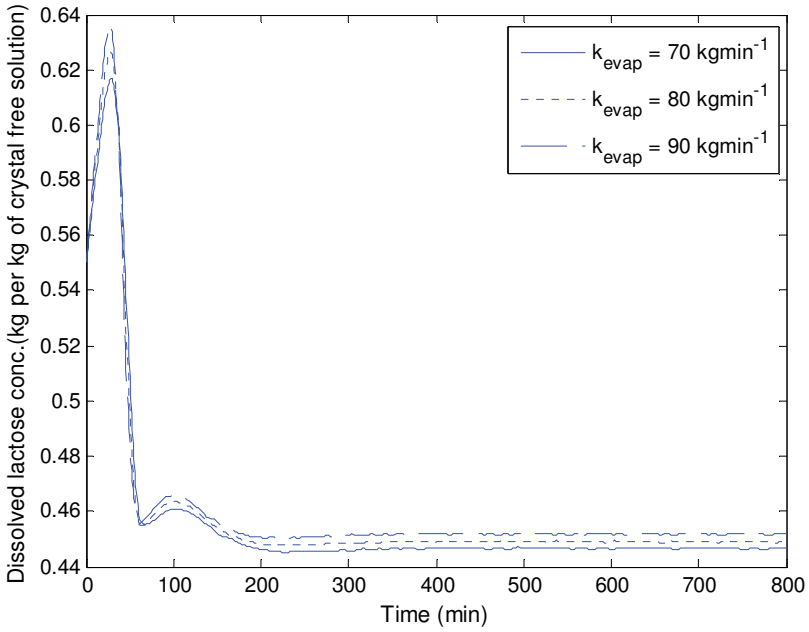


(g)

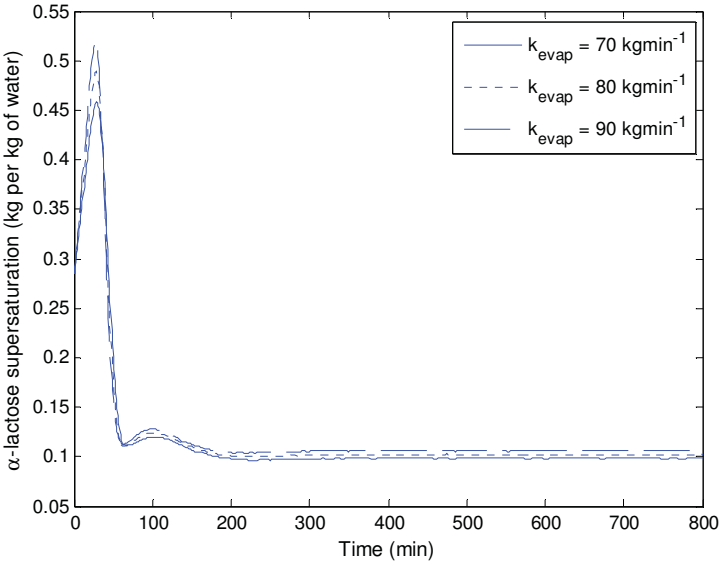
Figure 5-7. Effect of secondary nucleation rate constant on a), dissolved lactose; b), supersaturation; c), slurry density; d), crystal concentration; e), instantaneous secondary nucleation rate; f), mean diameter; and g), coefficient of variation.

5.3.4 Effect of Evaporation Rate

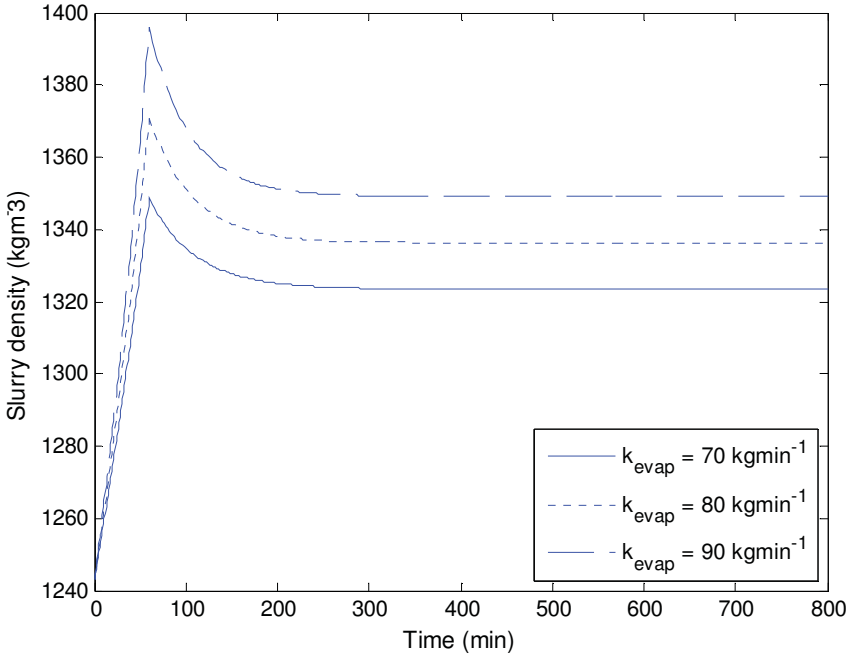
The results in Figure 5-8 show evaporation rate does not have any major effect on the steady state lactose concentration, supersaturation and mean particle size. Crystal content and the slurry density increased with an increase in the evaporation rate.



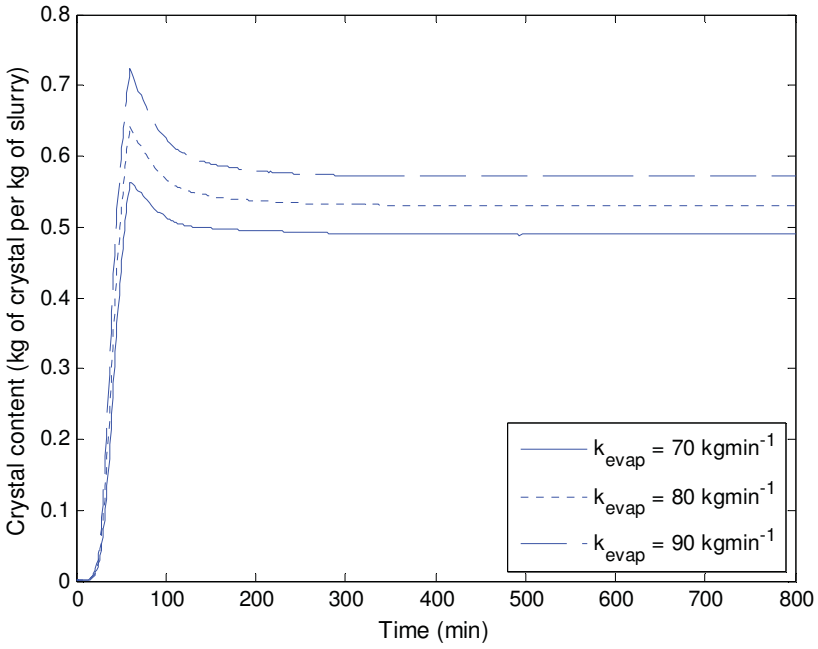
(a)



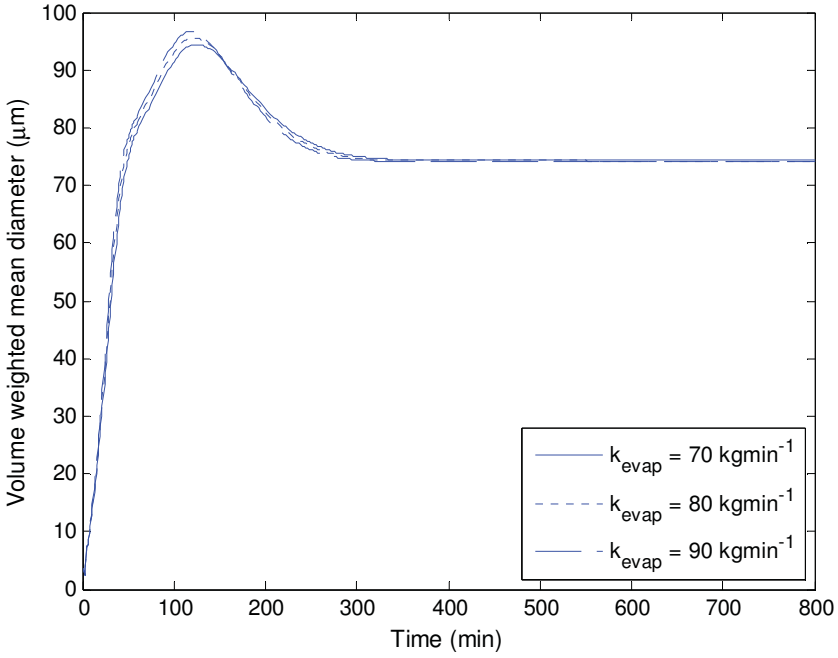
(b)


Slurry density (kgm^3)
Time (min)
1400
1380
1360
1340
1320
1300
1280
1260
1240
0
100
200
300
400
500
600
700
800
k_evap = 70 kgmin^-1
k_evap = 80 kgmin^-1
k_evap = 90 kgmin^-1

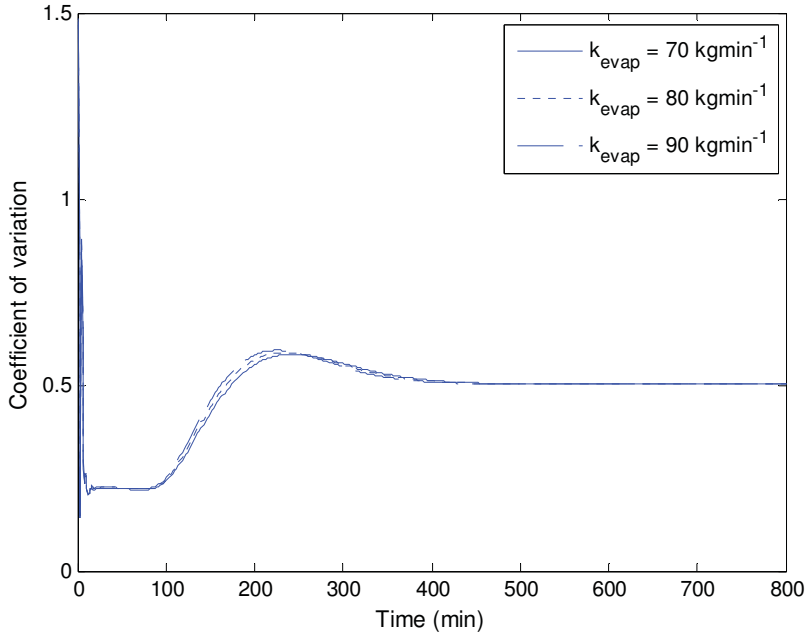
(c)


Crystal content (kg of crystal per kg of slurry)
Time (min)
0.8
0.7
0.6
0.5
0.4
0.3
0.2
0.1
0
0
100
200
300
400
500
600
700
800
k_evap = 70 kgmin^-1
k_evap = 80 kgmin^-1
k_evap = 90 kgmin^-1

(d)



(e)



(f)

Figure 5-8. Effect of evaporation rate on a), dissolved lactose; b), supersaturation; c), slurry density; d), crystal concentration; e), mean diameter; and f), coefficient of variation.

5.3.5 Effect of Residence Time

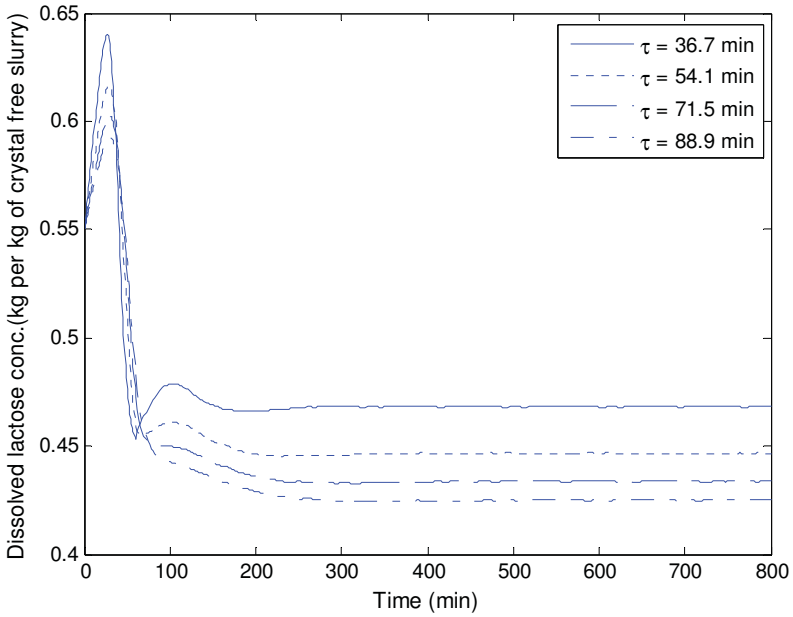
There are two ways of manipulating the residence time. One is altering the input and the output flow rate keeping the active crystallizer volume constant. The other approach is to alter the active crystallizer volume, keeping the input/output flow rates constant. Industrial crystallizers are normally operated at the highest possible throughput rates, fixed by the handling capacity of the downstream equipment. Hence, altering the crystallizer active volume is a more practical and desirable way of manipulating the residence time.

The results in Figure 5-9 show that a longer residence time creates a longer transition time to reach the steady state. A longer residence time results in a lower steady state dissolved lactose concentration and supersaturation as shown in Figure 5-9 (a) & (b), as crystals get more time to grow and remove lactose from the solution. The order of dependence on supersaturation for growth (g=1.3) is just slightly smaller that of secondary nucleation (b=1.5). Therefore, the decrease in secondary nucleation rate is relatively more than the growth rate with the decrease in supersaturation. Thus, a small increase in mean crystal size is observed with an increase in residence time. This is shown by the relationship between residence time and mean particle (Jones, 2002)

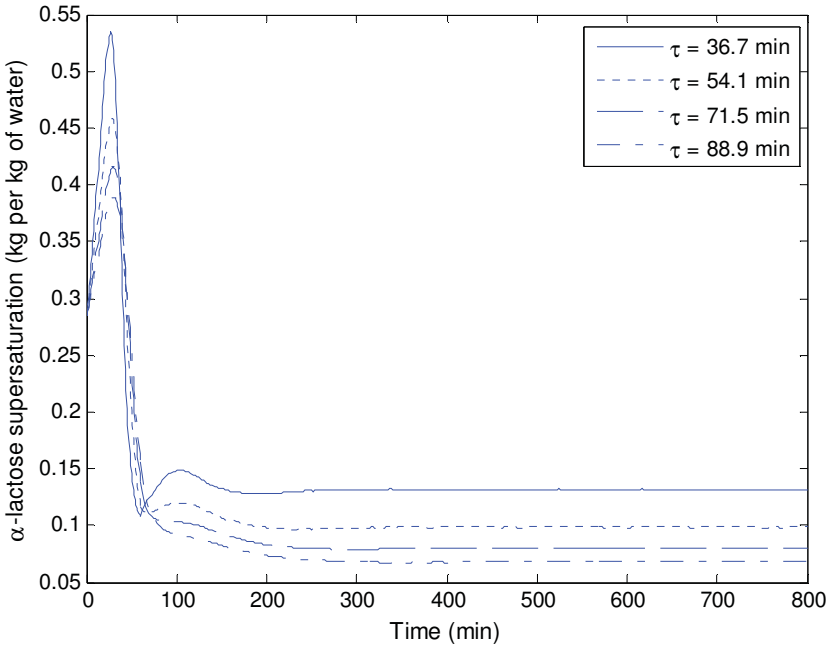
$$L \propto \tau^{\frac{w-1}{w+3}},$$

Equation 5-30 Relationship between residence time and mean particle size

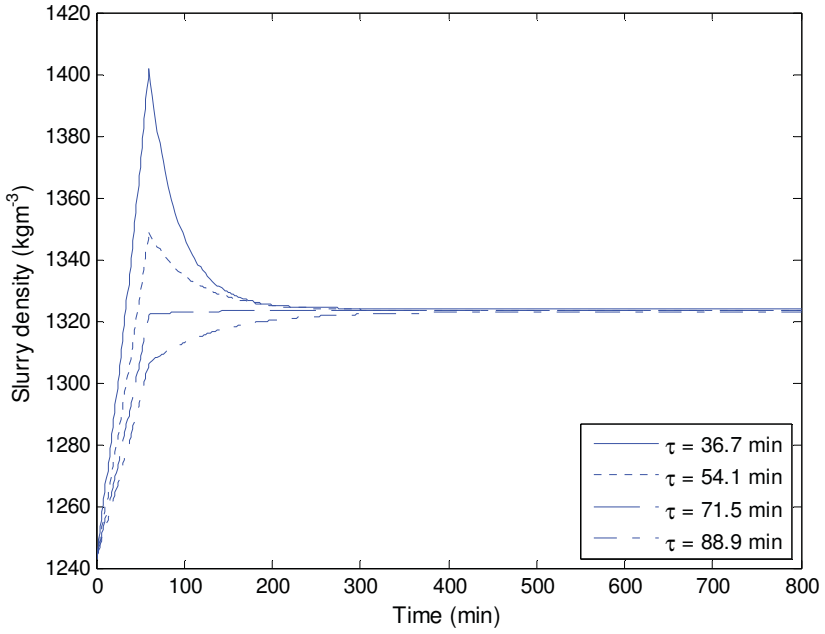
where w is the ratio of nucleation and the growth rate order, (b/g) and L, is the mean particle size. In general w>1 and hence the mean particle size increases with mean residence time, τ but usually only weakly (Jones, 2002). If the literature kinetic parameters for lactose can be applied at the industrial scale, then increasing the residence time brings no appreciable benefits in the mean particle size. This has implications to the design of evaporative crystallizers; as it means that relatively small gains in particle size are seen with increase in the holdup volume. Increase in the holdup volume however; add significantly to the size of the crystallizer and the capital investment required.


Dissolved lactose conc.(kg per kg of crystal free slurry)
Time (min)
τ = 36.7 min
τ = 54.1 min
τ = 71.5 min
τ = 88.9 min
0.65
0.6
0.55
0.5
0.45
0.4
0
100
200
300
400
500
600
700
800

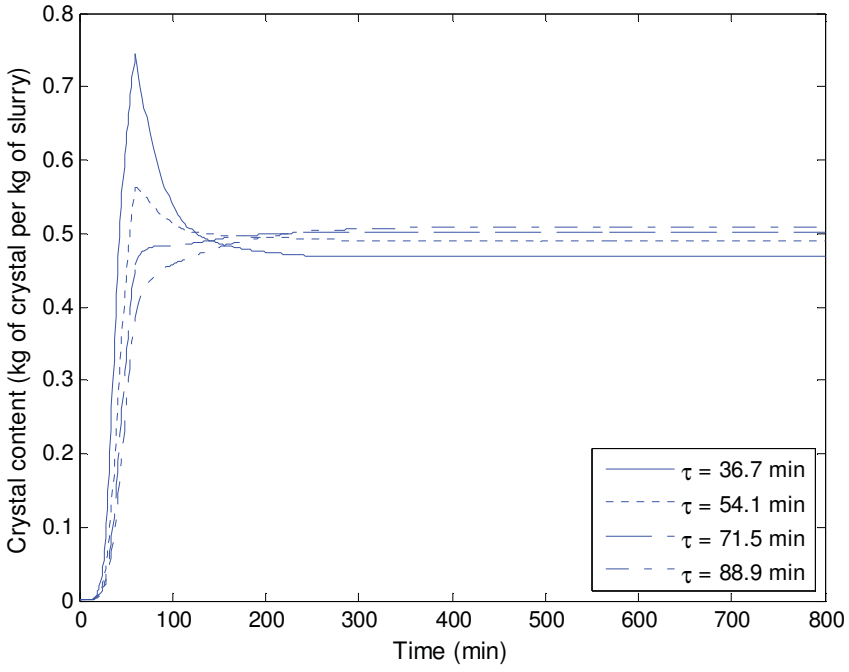
(a)


α-lactose supersaturation (kg per kg of water)
Time (min)
τ = 36.7 min
τ = 54.1 min
τ = 71.5 min
τ = 88.9 min
0.55
0.5
0.45
0.4
0.35
0.3
0.25
0.2
0.15
0.1
0.05
0
100
200
300
400
500
600
700
800

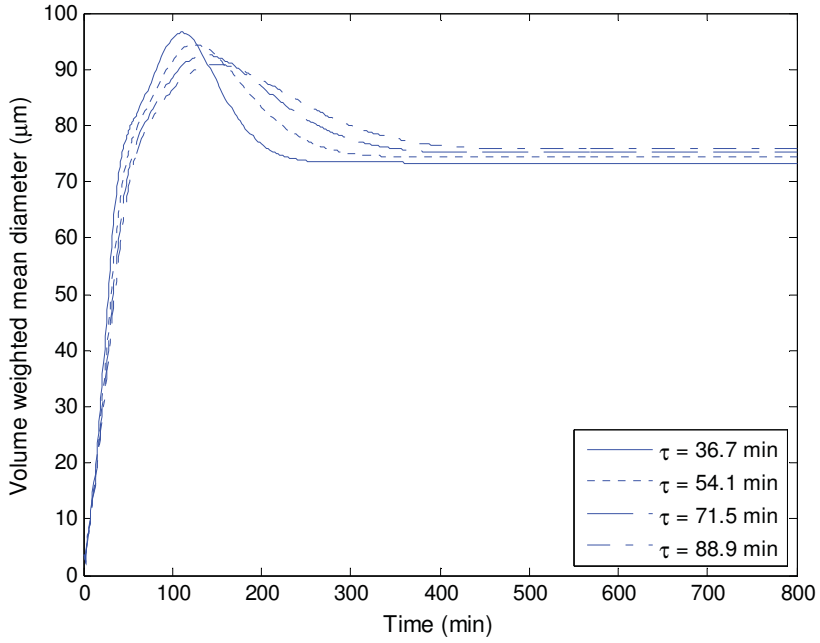
(b)


Slurry density (kgm-3)
Time (min)
τ = 36.7 min
τ = 54.1 min
τ = 71.5 min
τ = 88.9 min

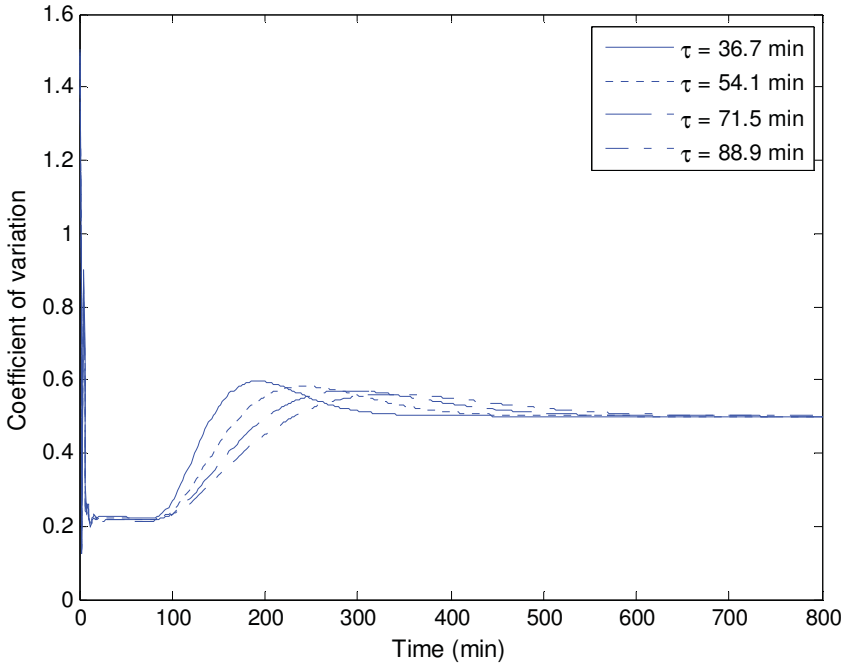
(c)


Crystal content (kg of crystal per kg of slurry)
Time (min)
τ = 36.7 min
τ = 54.1 min
τ = 71.5 min
τ = 88.9 min

(d)



(e)

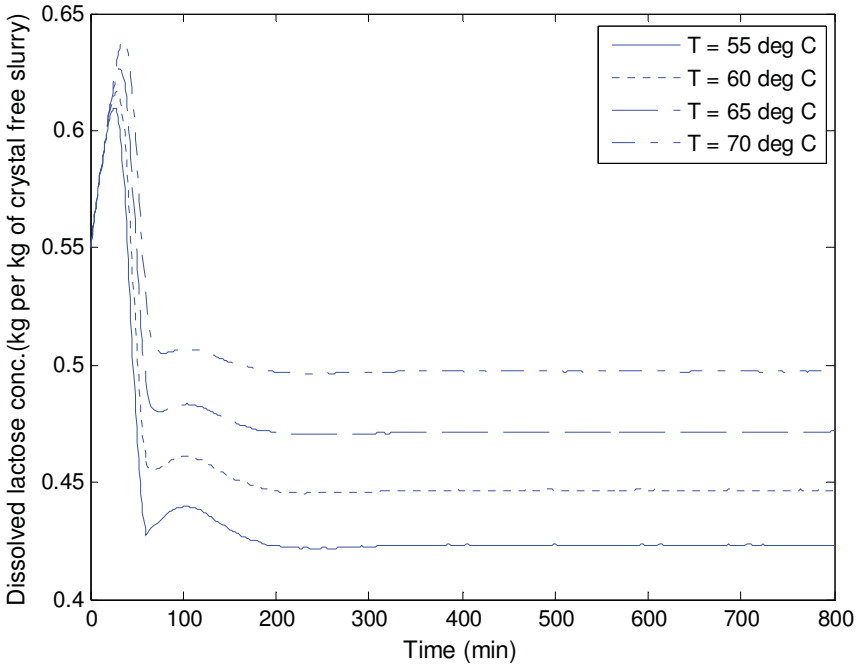


(f)

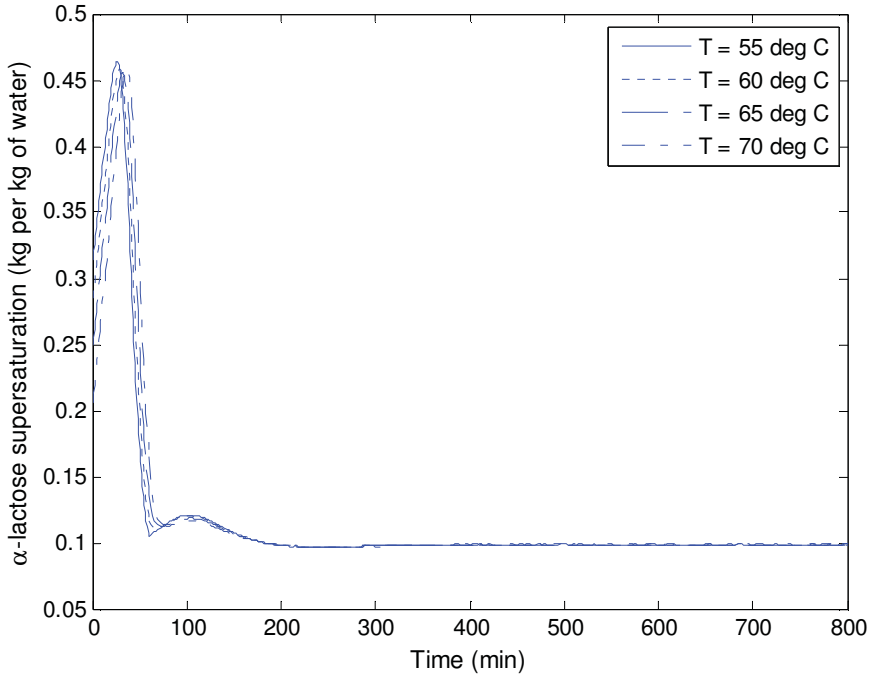
Figure 5-9. Effect of residence time on a), dissolved lactose; b), supersaturation; c), slurry density; d), crystal concentration; e), mean diameter; and f), coefficient of variation.

5.3.6 Effect of Temperature

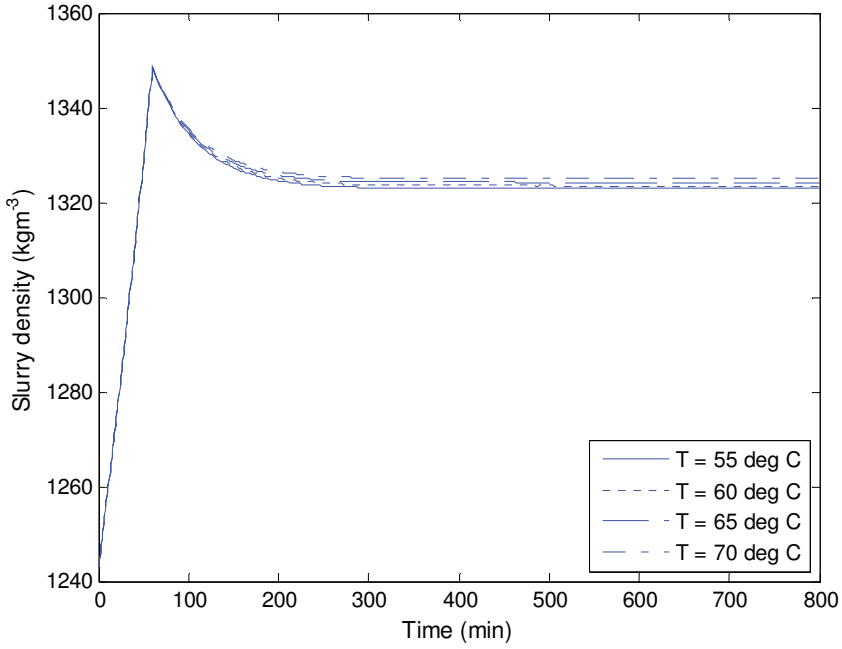
Evaporative crystallizers are generally operated under isothermal conditions. Simulations at different evaporator temperatures showed that the dissolved lactose content at the steady state increased as the temperature increased due to increased solubility of lactose at higher temperatures (Figure 5-10a). However, α-LMH supersaturation did not change with temperature (Figure 5-10b) and hence no increase in the crystal size was observed (Figure 5-10e). The crystal content of the slurry dropped with an increase in temperature (Figure 5-10d). This was because; for the same slurry density (which is controlled by evaporation rate and is constant for all simulated temperatures), more lactose remained in the dissolved state at higher temperatures.



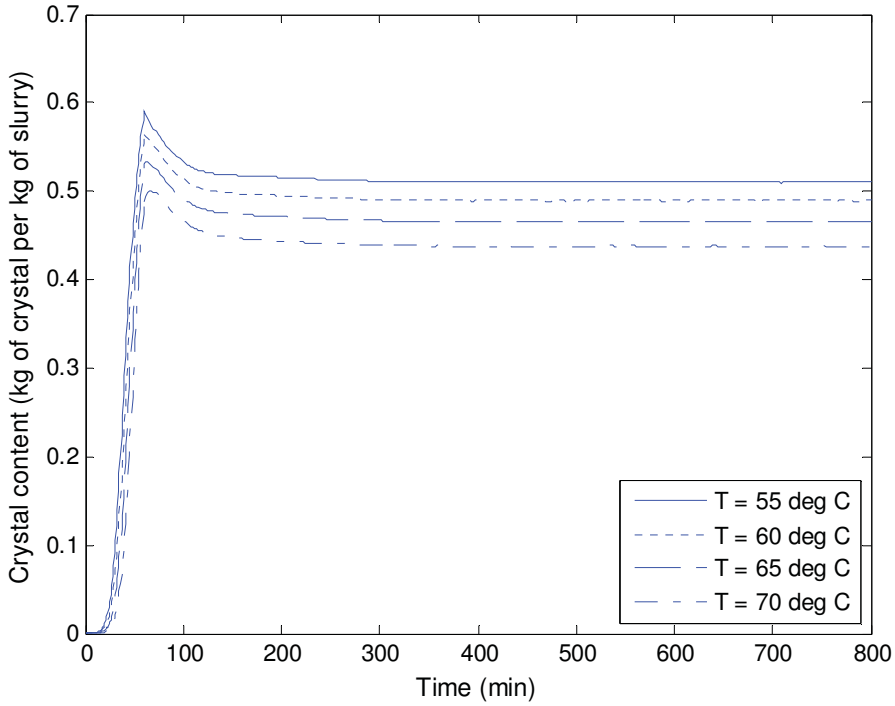
(a)


α-lactose supersaturation (kg per kg of water)
Time (min)
T = 55 deg C
T = 60 deg C
T = 65 deg C
T = 70 deg C

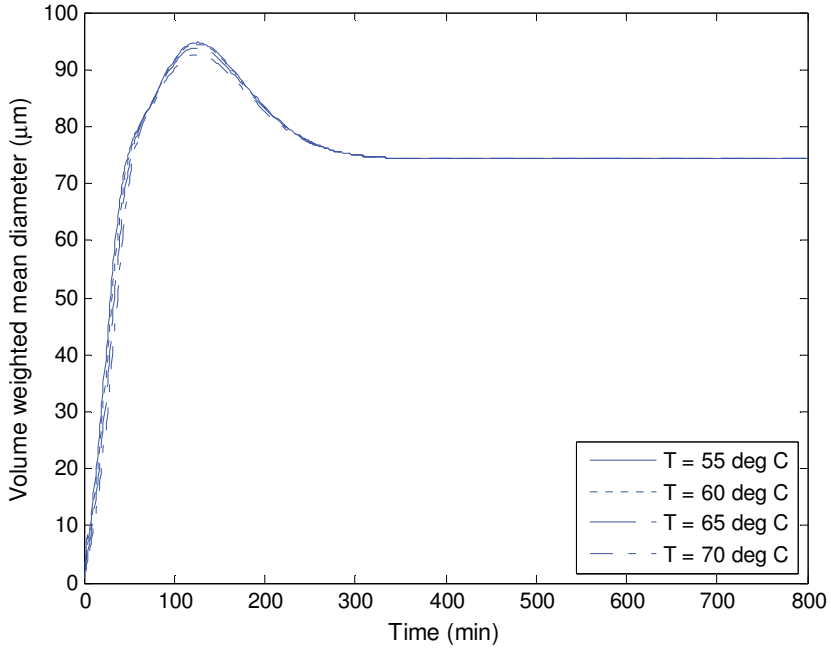
(b)


Slurry density (kgm-3)
Time (min)
T = 55 deg C
T = 60 deg C
T = 65 deg C
T = 70 deg C

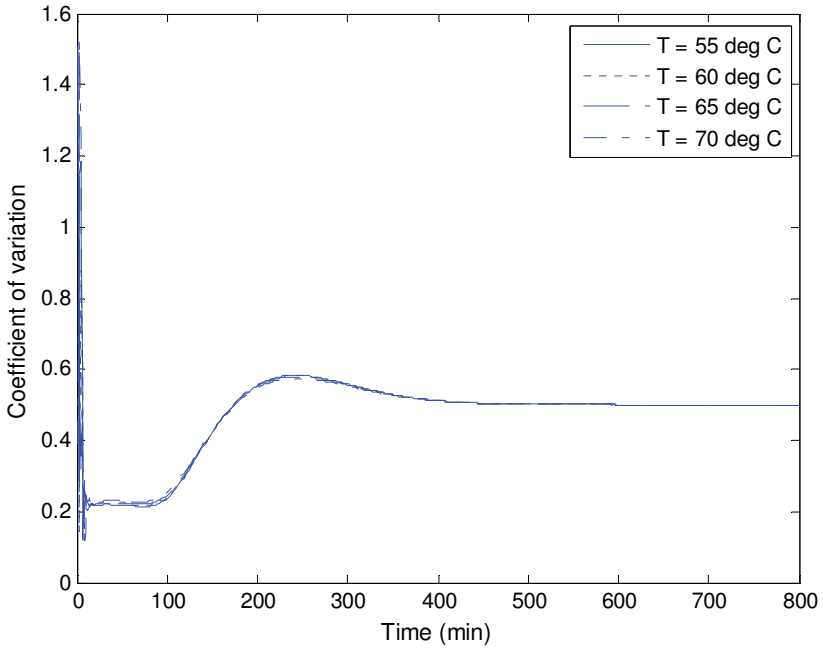
(c)


Crystal content (kg of crystal per kg of slurry)
Time (min)
T = 55 deg C
T = 60 deg C
T = 65 deg C
T = 70 deg C

(d)


Volume weighted mean diameter (μm)
Time (min)
T = 55 deg C
T = 60 deg C
T = 65 deg C
T = 70 deg C

(e)



(f)

Figure 5-10. Effect of temperature of operation (constant for an evaporative crystallizer) on a), dissolved lactose; b), supersaturation; c), slurry density; d), crystal concentration; e), mean diameter; and f), coefficient of variation.

5.4 Summary and Conclusions

The simulation results showed that the coefficient of variation followed by the particle size is the slowest output parameters to reach steady state, in spite of a seemingly thermodynamically (supersaturation) steady state being reached by the crystallizer. It generally took six to seven residence times for the mean crystal size to stabilize. This is typical of crystallizers due to the complex feedback interaction of the crystal size distribution (CSD) with the same parameters (growth and nucleation rates, supersaturation, and residence time) that govern the formation of CSD. The simulation studies provide a tool to compare the influence of various parameters (kinetic and operational) on crystallizer dynamics as shown in Table 5-3.

It was found that, to increase the slurry density, increasing the evaporation rate was the only feasible option. The changes in crystallization kinetic parameters (growth and nucleation rates) only resulted in a different redistribution of lactose in dissolved and crystalline form, the total solids or slurry density remaining the same. The secondary

nucleation rate impacted most the output crystal size. It needs to be stated here that the current model presents only preliminary results and is not validated. The understanding gained in this chapter is used for model parameter estimation in the next chapter.

Table 5-3 *Values of the Crystallizer Outputs at Steady State at the Maximum and Minimum Values of the Various Kinetic and Operation Parameters Simulated*

Kinetic and operational parameters		Particle size (μm)	Supersaturation [kg of α-LMH per kg of water]	Crystal content of the slurry [(kg of crystal) (kg of slurry)$^{-1}$]	Slurry density (kg m^{-3})
Growth rate	(McLeod, 2007)	75	0.1	0.49	1323
	(Shi, et al., 1990)	87	0.075	0.51	1323
Primary nucleation rate constant	3.1E7	75	0.1	0.49	1323
	3.1E9	75	0.1	0.49	1323
Secondary nucleation rate constant	1.0E9	130	0.15	0.45	1323
	1.0E11	43	0.1	0.51	1323
Evaporation rate (kg min^{-1})	70	75	0.1	0.49	1323
	90	75	0.1	0.57	1350
Residence time (min)	37	74	0.13	0.47	1323
	89	77	0.07	0.51	1323
Temperature (^{o}C)	55	75	0.1	0.51	1323
	70	75	0.1	0.44	1323

Chapter 6 Industrial Crystallizer

The biggest challenge in the field of crystallization is scaling up the findings from the laboratory scale to industrial crystallizers. This is because of the extensive dependence of crystallization kinetics on the hydrodynamics of the system. Hydrodynamics change dramatically on scaling up and from one configuration to another. Thus, the operation and design of industrial crystallizers is still based on experience rather than on sound mechanistic principles. With the understanding gained in the preceding chapters, together with the existing body of knowledge on industrial crystallizers, an attempt is made in this chapter to characterize the current evaporative crystallizer.

6.1 Hydrodynamics

Previous studies have reported that the hydrodynamics inside an industrial crystallizer are far from uniform, leading to the formation of supersaturation, crystal distribution and energy dissipation gradients (Bermingham, et al., 1998a). In an evaporative crystallizer, supersaturation is generated by taking the thermal energy transferred to the fluid in the calandria and using it to generate vapour in the boiling zone. As a result supersaturation will be at maximum in the boiling zone and at minimum in the heat exchanger/calandria. Large volume areas, like the crystallizer main body, can see big drops in supersaturation due to the residence time they provide for growth. The introduction of hot feed to the cooler circulating slurry can also lead to localised extremes of supersaturation and thus leading to a primary nucleation event if mixing is not instantaneous. This distribution of supersaturation means that nucleation cannot be considered to be occurring at an equal rate throughout the vessel.

The location in the crystalliser also has an impact on the hydrodynamic conditions. The mixing intensity in the vicinity of the pump will be orders of magnitude higher than that in the bulk (Rielly & Marquis, 2001). In the main crystallizer body, where there is no provision for external agitation, larger crystals can settle down if the fluid velocity is lower than the particle settling velocities. This will result in preferential removal of larger crystals leading to fines build up in the system.

The hydrodynamics and the crystallization kinetics are intricately linked, as shown in Figure 6-1 and hence it is necessary to predict kinetics at the local hydrodynamic conditions. One tool used to do this is compartmental modelling (Bermingham, et al., 1998a; Bermingham, Neumann, Muusze, Kramer, & Verheijen, 1998b; Kramer, Bermingham, & van Rosmalen, 1999; Kramer, Dijkstra, Neumann, Ó Meadhra, & van Rosmalen, 1996; Kramer, Dijkstra, Verheijen, & Van Rosmalen, 2000). In this approach the crystallizer is divided into compartments, selected using the hydrodynamic conditions prevailing in them such that considerable energy dissipation gradients are not present within the chosen compartment. Secondly, the compartments are checked for the presence of significant supersaturation gradients. A good estimation for this is the supersaturation half life time $t_{\Delta C,1/2}$, introduced by Garside (1985), which is a measure of the time taken for the supersaturation to deplete to half its initial value. This value can be compared to the circulation time (t_s) of the slurry, given by the ratio of total slurry volume to the circulation rate. Finally, a classification function is introduced to account for non-uniform distribution of the solid phase.

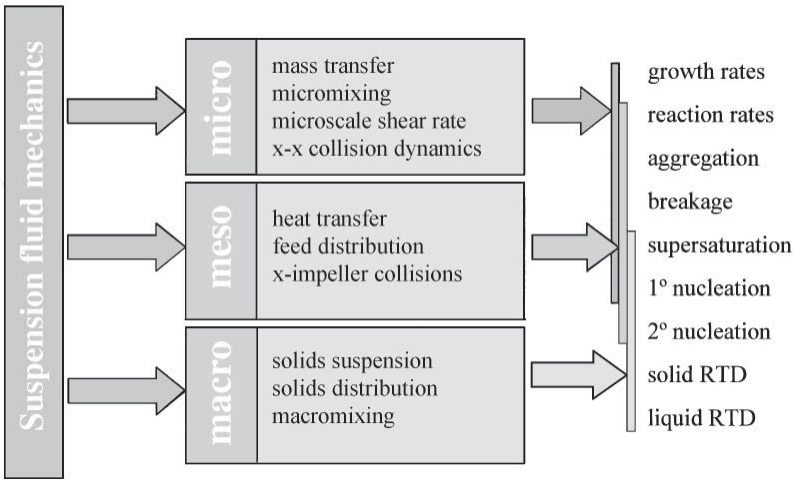


Figure 6-1. Fluid dynamics scale in a crystallizer, x represents crystal (reproduced from Rielly & Marquis (2001)).

Using the above guidelines and computational fluid dynamics (CFD), Kramer, et al. (2000) proposed a compartmental model for a forced circulation, submerged tube,

evaporative crystallizer (Figure 6-2). Five compartments were determined to be necessary.

1. The main vessel which accounts for the bulk of the residence time
2. The point of entry of the slurry into the main vessel was (based on CFD modelling) treated as a separate mixing compartment.
3. The boiling zone because of the high supersaturation.
4. The pump due to the high energy dissipation rates.
5. The heat exchanger because of the heat input leading to a temperature rise and hence lowering of supersaturation.

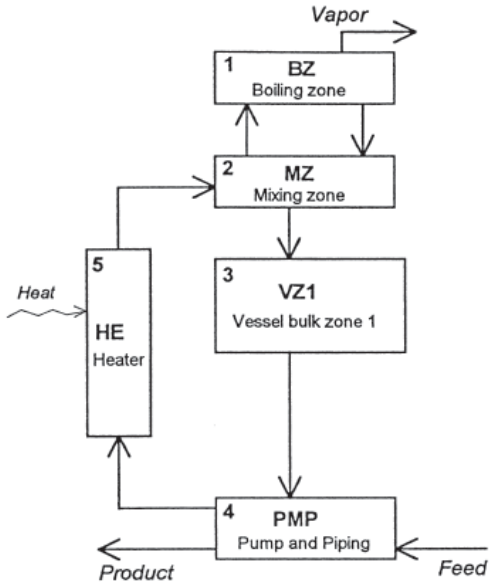


Figure 6-2. Compartment model for a forced circulation evaporative crystallizer (reproduced from Kramer, et al. (2000)).

The crystallizer being investigated in this work is a boiling in tube type so it requires a different compartmental model to that described above. The boiling zone shifts to the heat exchanger and the mixing zone no longer exists as a separate compartment. The main body of the crystallizer provides the means to separate the vapour from the slurry bulk and hence is termed a separator.

As part of determining the number of compartments necessary, single and boiling two phase flow through the heat exchanger were modelled. The detailed formulation of the model is explained in Appendix III. Results of the modelling are now discussed.

The point of intersection between the temperature/pressure saturation curve and the slurry temperature gives the height in the tube at which boiling starts, 1.32 m (Figure 6-3). The high velocities in the boiling zone due to formation of vapour phase result in turbulence at the exit of the tubes compared to laminar flow prior to boiling (Figure 6-4) and hence merit a separate compartment as shown in Figure 6-5.

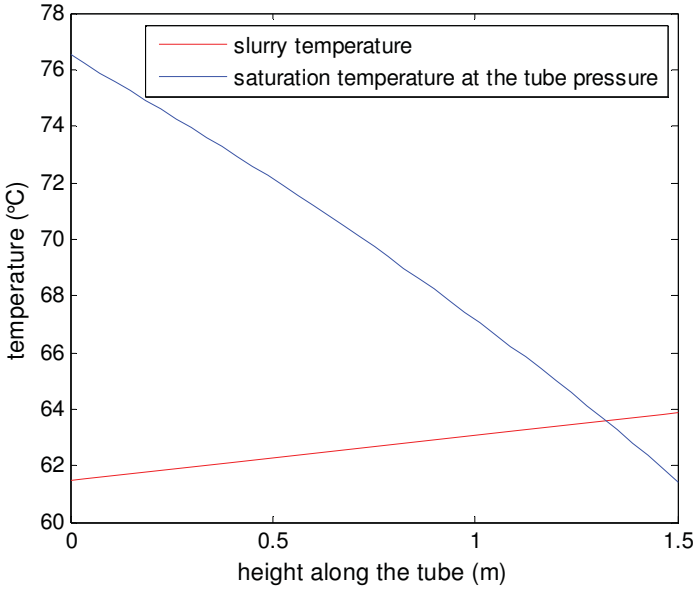


Figure 6-3. Prediction of the height at which boiling starts inside the calandria tubes of the Kapuni FC evaporative crystallizer.

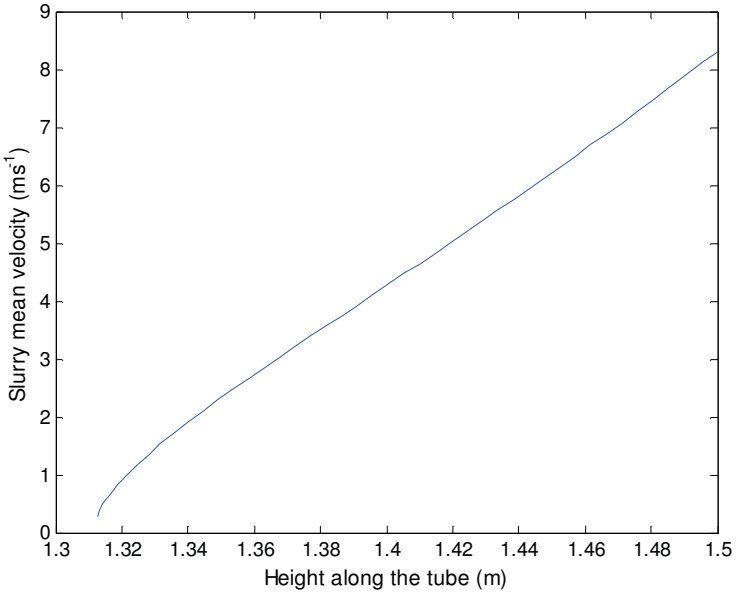


Figure 6-4. Slurry velocity in the boiling zone in the calandria tubes of the Kapuni FC evaporative crystallizer.

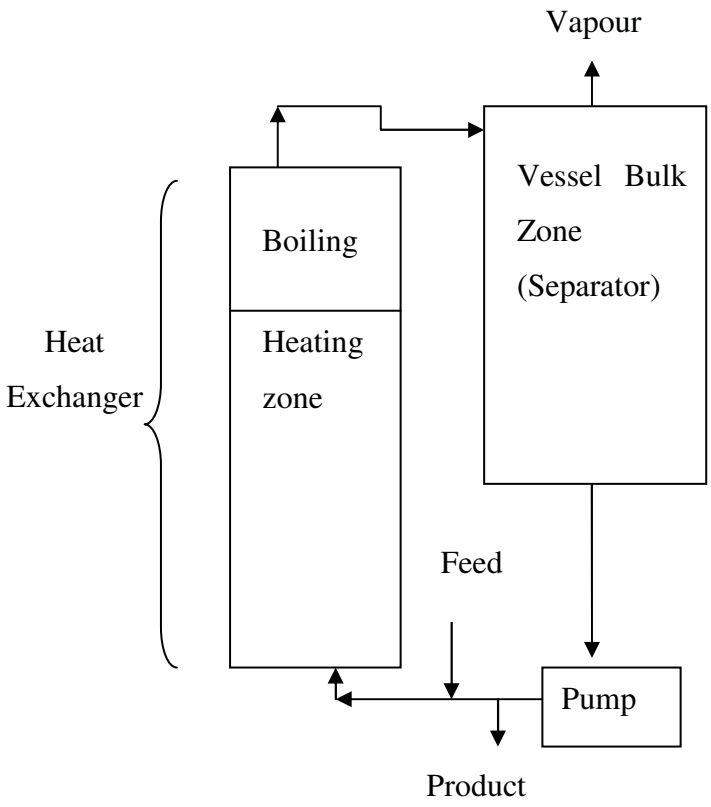


Figure 6-5. Compartmental model for the Kapuni FC evaporative crystallizer.

The slurry volume and the circulation velocity inside the crystallizer were calculated to be 9 m^3 and 0.328 $m^3\ s^{-1}$, which gives a circulation time (t_s) of 27.4 s. The supersaturation half life time ($t_{\Delta C,1/2}$) was estimated by performing a batch simulation at steady state values without supersaturation generation using the method of moments discussed in Chapter 5. From the supersaturation profiles (Figure 6-6), $t_{\Delta C,1/2}$ can be determined. For a measured average steady state supersaturation of 8.8 g per 100 g of water, $t_{\Delta C,1/2}$ works out to be 5 min. Since the $t_s \ll t_{\Delta c,1/2}$ no significant desupersaturation will occur in any part of the crystallizer. The high slurry density (1320 kg m^{-3}), viscosity (0.02 kg $m^{-1}\ s^{-1}$), small average crystal size (300 μm) and high solid content (40% v/v) results in a very low crystal settling velocity (0.05 cm s^{-1}). This combined with the high circulation velocities, mean that no crystal segregation will occur. The rise in the slurry temperature inside the calandria is only two degrees (Figure 6-3) and hence no significant changes in the supersaturation will take place in the calandria compared to the bulk. Based on the above analysis the following conclusions can be drawn:

i) Supersaturation remains constant throughout the crystallizer.

ii) The crystal mass is in uniform suspension.

iii) Two areas of relatively high turbulence compared to the bulk, the pump and the boiling zone exists. These will be the main sources of secondary nuclei in the crystallizer.

The first two points satisfy the conditions for a crystallizer to be regarded as mixed suspension mixed product removal (MSMPR). Also, the growth rate for lactose crystals, under constant supersaturation is independent of the hydrodynamics as long as the crystals are maintained in a suspension (McLeod, 2007). This suggests that growth rate is going to be constant in the studied crystallizer (from *a* and *b*) and cannot be altered. Primary nucleation can be neglected at the operational supersaturation other than during the start up (which constitutes only 2-3% of the total runtime). Thus, because of its dependence on the local hydrodynamics, secondary nucleation should become the most important handle for controlling the crystal size distribution in the crystallizer.

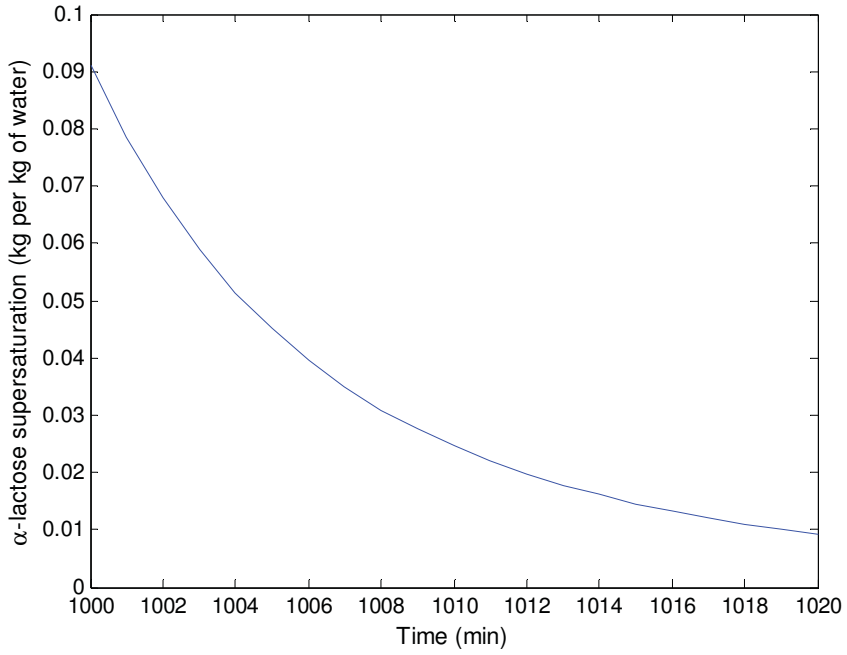


Figure 6-6. Supersaturation decay transient profile in absence of evaporation i.e. no supersaturation generation, for prediction of $t_{\Delta c,1/2}$.

6.2 Plant Data and Parameter Estimation

It is possible to ascertain crystallization kinetics in an evaporative crystallizer using the steady state mixed suspension mixed product removal (MSMPR) criterion, which was established in the last section. Under these conditions a plot of the natural log of the population density and crystal size results in a straight line. From the slope and the intercept of the line, growth and nucleation rate respectively can then be calculated.

The crystallizer being studied in this work operates in two modes: semi batch and continuous. Sampling was conducted during the continuous state in order to meet the MSMPR requirements. In an MSMPR operation, conditions inside the crystallizer will be the same as that of the outlet stream. This means that analysis of the crystallizer operation can be made by taking samples from the crystallizer discharge stream. The outlet product from the crystallizer was sampled and analyzed for dissolved solids, total solids and particle size distribution. Temperature and residence time in the crystallizer were recorded directly from the control room HMI (Human Machine Interface) consoles. Residence time was calculated using the separator level (mass of the crystallizer) and the product outlet flow rate and is presented in Figure 6-7. These parameters provide the necessary data to evaluate and further refine the model developed in previous chapter.

6.2.1 Sampling and analysis

For steady state operation to be assumed, Randolph & Larson (1988) state that approximately eight residence times are required. To ensure steady state for the crystallizer being studied, sampling was started at least 15 hours after the crystallizer was switched to continuous mode. Once this state was achieved in the crystallizer samples of the slurry were collected every 30-40 minutes for 210 minutes. Where a stoppage occurred sampling was abandoned because the steady state was disturbed. Ongoing issues in plant operations and the fact that the crystallizers underwent cleaning twice a week, three non-stop sampling replicates under steady state were achieved over a period of month. Measurements were also conducted during the transient regime of the crystallizer immediately after it moves from the semi-batch to continuous mode for approximately 8 hours.

At each sampling time slurry was collected in sealed plastic 125 ml sampling containers. The sample was split and a portion transferred into a separate sealed sample tube, cooled under running water and stored for total solids determination. The cooling was done to reduce evaporative losses. The remaining slurry was allowed to stand for up to two minutes to get a top crystal free liquid layer. The liquid layer free of bigger crystals was siphoned off with a help of a 10 ml syringe. 1-1.5 g of liquor was filtered with a 0.44 micron filter on to the pan of the halogen moisture analyzer (HB43, Mettler Toledo). The total dissolved solids were also measured using a handheld digital refractometer (Atago, PAL-1) as a quick estimate of the dissolved solids values. Moisture anaylzer readings were considered more reliable and accurate because of the dependence of refractive index on temperature and the composition of the dissolved solids. Comparison of the two values obtained by the two techniques is shown in Figure 6-8. Following this the total solids of the sample was determined (Figure 6-9). The slurry was well mixed with a help of a spatula and 0.8-1.2 g of sample was smeared over the moisture metre pan. The analyzer quickly heats up to 155 °C and it takes 6-10 minutes for the analysis to be complete, depending on the mass of sample. Knowing the total solids and dissolved solids, the crystalline content of the slurry was determined by mass balance (Figure 6-10).

The slurry sample was also used for crystal size determination (Figure 6-11). The slurry was diluted with slightly supersaturated lactose solution at 25 °C (~20% w/w) to reduce the viscosity of the slurry so that a homogenous suspension of the crystal mass could be obtained. The Malvern cell was flushed twice with water and once with the dispersant lactose solution before each analysis. Fresh dispersant (lactose solution) was then introduced and stirring started and the background measurement was allowed to stabilize. The slurry sample was shaken manually to ensure uniform suspension of the crystals and introduced into the Malvern cell using a transfer pipette. Since the particle concentration of the slurry was high, 5-10 drops of sample were enough to get to the desired obscuration levels in the Malvern cell (10-20%). The volume weighted mean diameter for the three runs is plotted in Figure 6-12.

6.2.2 Results

The measured parameters vary within a narrow range and can be considered fairly stable over the three hour period. The only exception is for the volume weighted mean diameter profile in trial 1, Figure 6-12, where the first three points for the volume weighted mean diameter profile are considerably lower than the average size of around 320 µm. The probable reason for the lower particle size will be discussed later in the chapter. Using these results it can be concluded that the crystallizer generally operates with the following steady state parameters in continuous mode: residence time: 1 hour; dissolved solids (mass fraction): 0.45- 0.46; total solids (mass fraction): 0.72-0.73; crystalline content (mass fraction): 0.49-0.52; D[4,3]: 300-340 µm.

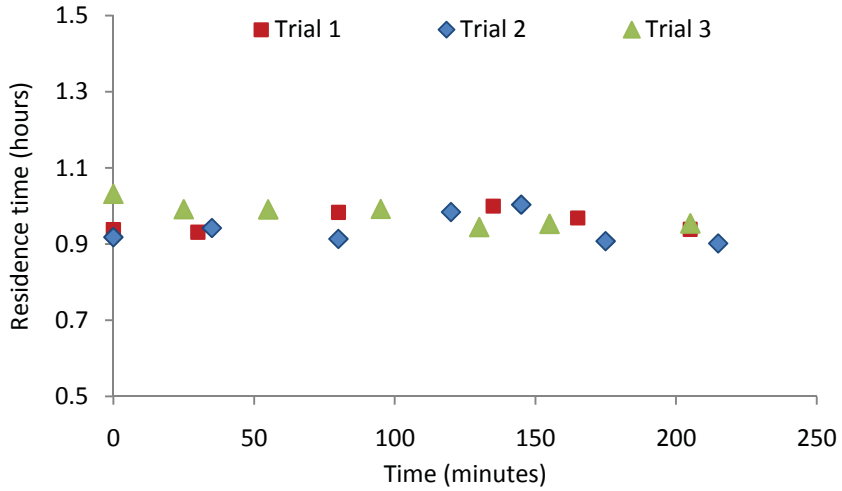


Figure 6-7. Residence time profile of the Kapuni FC evaporative crystallizer during the three sampling trials.

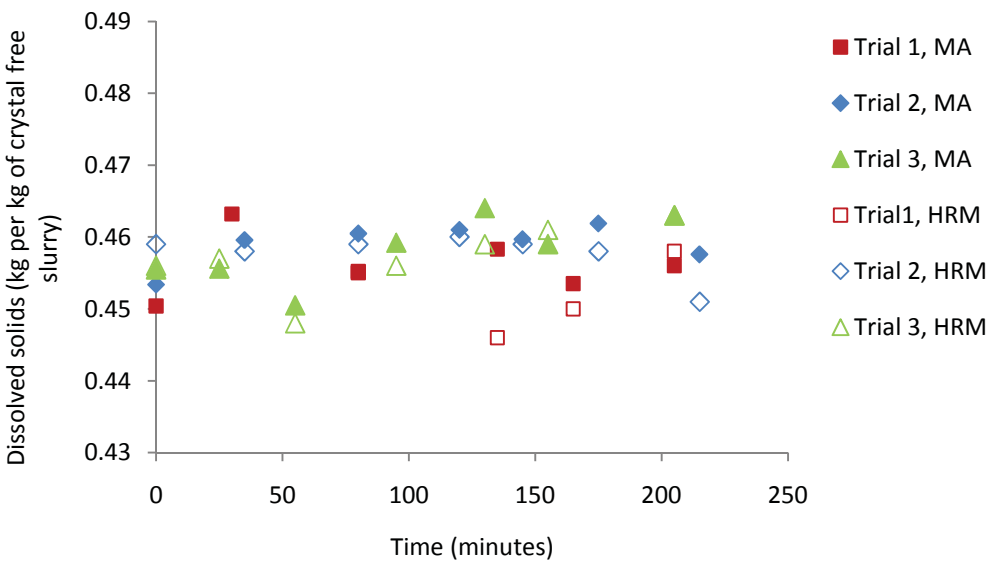


Figure 6-8. Dissolved solids profile of the Kapuni FC evaporative crystallizer for the three sampling runs (MA: Moisture Analyzer and HRM: Handheld Refractometer).

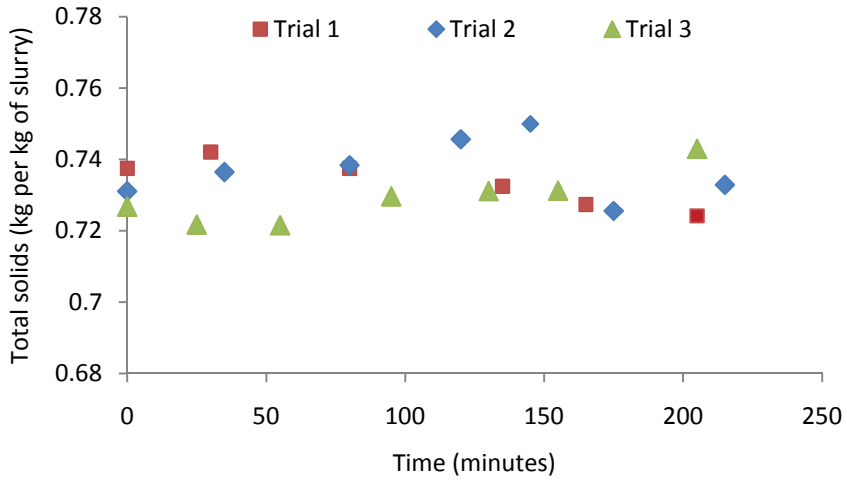


Figure 6-9. Total solids profile of the Kapuni FC evaporative crystallizer for the three sampling runs (measured using the Metler Toledo moisture analyzer).

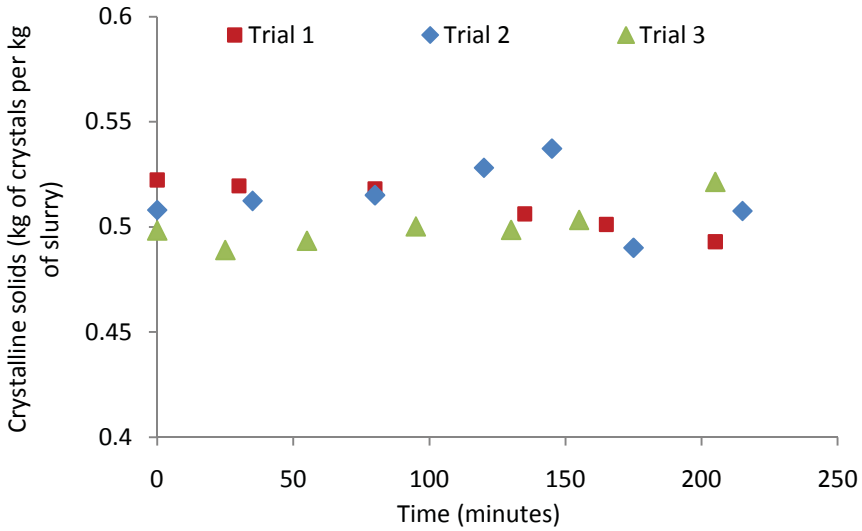
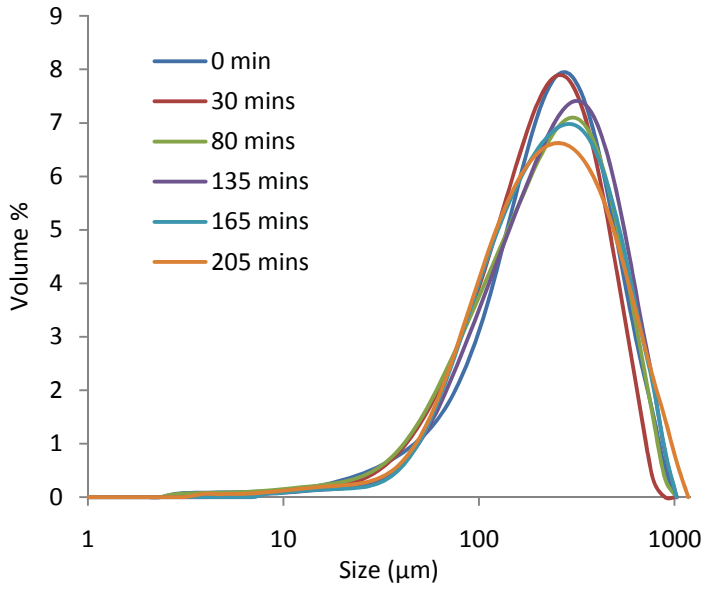
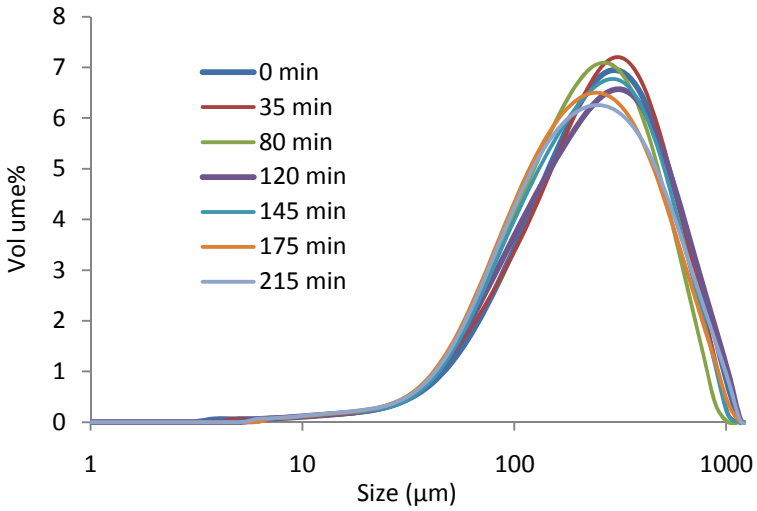


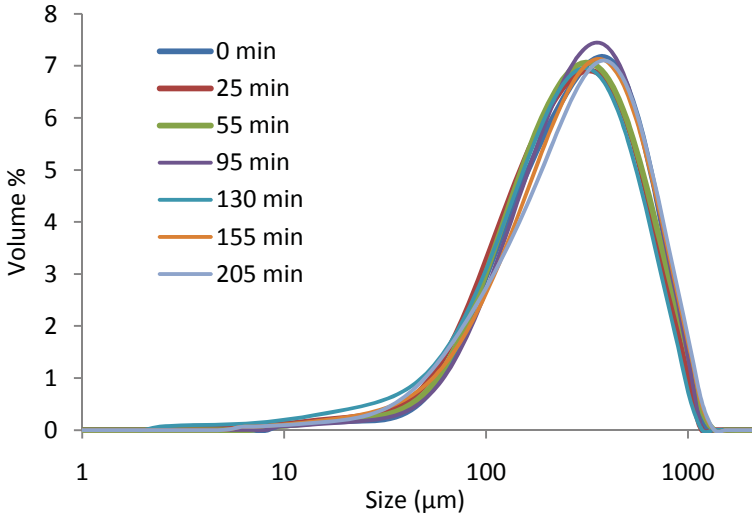
Figure 6-10. Crystalline solids content profile of the Kapuni FC evaporative crystallizer for the three sampling runs (calculated from mass balance using total solids and dissolved solids).



a)



b)



c)

Figure 6-11. Crystal size distribution profile of the Kapuni FC evaporative crystallizer for the three sampling runs a) Trial 1 b) Trial 2 c) Trial 3 during the steady state operation. 0 minute indicates the time of first sample.

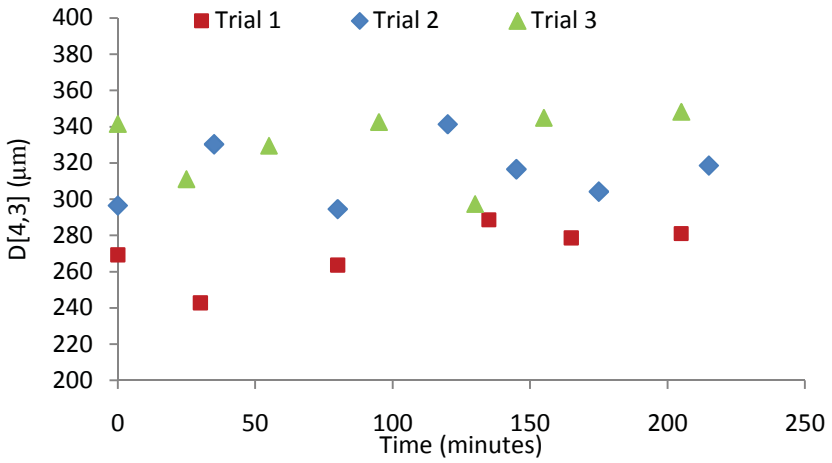


Figure 6-12. Volume weighted mean diameter profiles of the Kapuni FC evaporative crystallizer for the three sampling runs.

6.2.3 MSMPR Analysis

To estimate the crystallization kinetics from steady state operation, the volumetric distribution needs to be converted to a number density distribution. This can be done using the following formula:

$$n(L) = \frac{6C_c v}{100\pi\rho_c L^3(\Delta L)10^{-18}}$$

Equation 6-1 Converting volumetric distribution to population density distribution

where,

n, is the population density of crystal of size L [#(kg of slurry)$^{-1}$µm^{-1}]

v, is the mass percent occupied by crystal of size L (Malvern output)

L, is the geometric mean size of the two consecutive size bins used in Malvern output [µm]

ΔL, is the difference between the two consecutive size bins used in Malvern output [µm]

ρ_c, is the density of α-lactose monohydrate crystal [kg m^{-3}]

C_c, is the crystal content in terms of weight fraction of the slurry [(kg of crystal) (kg of slurry)$^{-1}$]

The plot of *ln(n(L))* verus *L* for the CSD measured under steady state for trial 2 is shown in Figure 6-13.

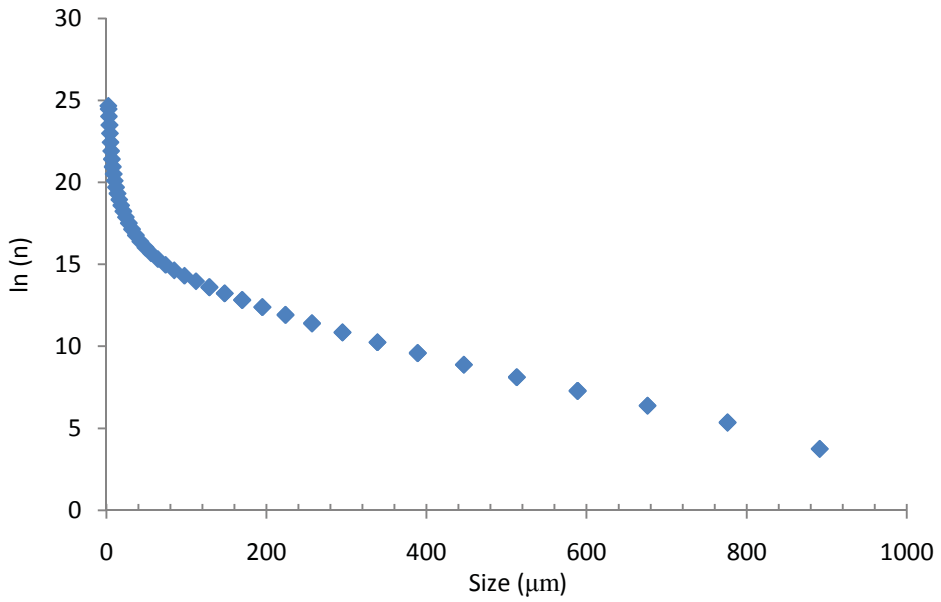


Figure 6-13. Population density curve for lactose crystals obtained from the Kapuni FC evaporative crystallizer under steady state.

The plot is not a straight line. It has a strong upward curvature at about 40 micron. The upward curvature makes it difficult to calculate accurate crystallization kinetics from the MSMPR model. A linear extrapolation leads to an under estimation of nucleation rate while over estimating the growth rates (Liang, et al., 1991). This deviation from the MSMPR model can be explained by growth rate dispersion (GRD) or size dependent growth rate (SDG) (Liang, et al., 1991). GRD dispersion refers to a distribution of growth rates experienced by a crystal population; due to either different conditions they experience in a crystallizer or due to some inherent structural conditions that differ from crystal to crystal (Randolph & Larson, 1988). SDG refers to the dependence of growth rate on the crystal size with growth increasing with size. A comprehensive review by Garside (1980) discusses SDG and GRD in light of various theories like mass transfer effects, growth mechanisms, Ostwald ripening and the presence of impurities in reference with the experimental findings. However, it is

not possible to distinguish between the two phenomena by MSMPR size analysis alone (Randolph & Larson, 1988).

There are numerous GRD and SDG models in the literature. Mydlarz (1996) fitted many of these various GRD and SDG models to the population density curve. He concluded that the SDG models do a better job of predicting the population density curves and suggested further development of GRD models as there is experimental evidence to support GRD phenomenon.

For α-lactose monohydrate (α-LMH) there are various studies which used different GRD models: Weibull (McLeod, 2007) , Log normal (Butler, 1998), Gamma, Inverse Gamma and Sum of two constant growth rates (Liang, et al., 1991). No study using size dependent model has been found for modelling lactose crystallization. Size dependent growth rate for the generated contact nuclei was discarded by Shi, et al. (1989) on the basis that no correlation existed between crystal size and growth rate. Dincer, et al., (2009a) found that the larger α-LMH crystals (>300 μm) have rough surfaces with macrosteps and a greater number of spirals compared to smaller crystals that usually have one spiral originating from the centre of the face. This suggests the possibility of bigger crystals growing faster or SDG (Dincer, et al., 2009b). Since both mechanisms find mention in the literature, their fit to the measured population density curve will now be compared.

6.2.3.1 Size Dependent Growth Rate

The size dependent model used was proposed by Mydlarz (1993) as follows:

$$G(L) = G_e\{1 - \exp[-a(L + c)]\}$$

Equation 6-2 Size dependent growth rate

When substituted in the population balance equation for an ideal MSMPR system, the population density equation takes the following form:

$$n(L) = n_o \exp(aL)\left(\frac{\exp[a(L + c)]}{\exp(ac) - 1}\right)^{-1-(a\tau G_e)/(a\tau G_e)}$$

Equation 6-3 Population density with size dependent growth rate

where,

G_e , is the effective size independent growth rate [μm min^{-1}]

n_o, is the 'zero-size' population density [# μm^{-1} (kg of slurry)$^{-1}$]

τ, is the residence time [min]

L, is the crystal size

a and c are the model parameters

DataFit (Oakdale Engineering, trial version 9) was used to fit the Equation 6-3 to the plant data Figure 6-14 to estimate the parameters for the SDG model. The growth rate as a function of crystal size is shown in Figure 6-15.

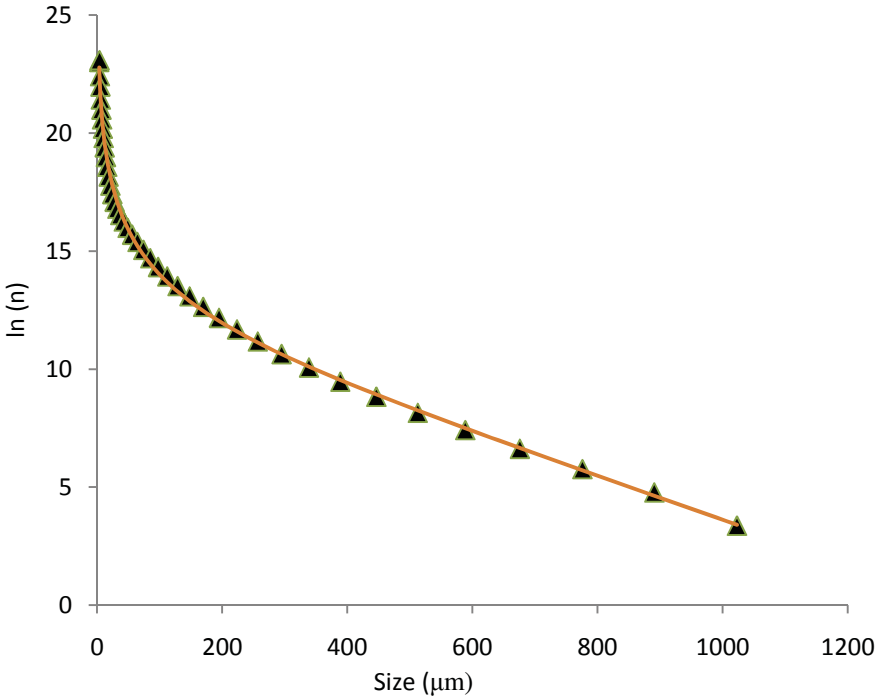


Figure 6-14. Size dependent growth rate fitted to the population density curve in Figure 6-13.

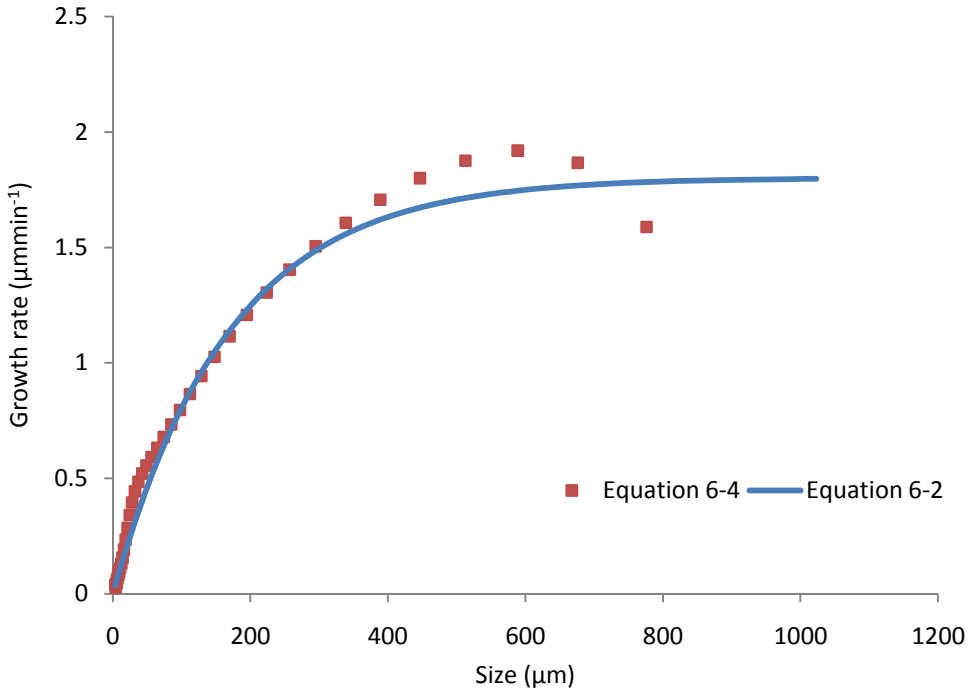


Figure 6-15. Size dependent growth rate versus crystal size. Fitted values of the parameters a, c and G_e for the Mydlarz model are 0.0059, 0.0091 and 1.82 µm min^{-1}, respectively.

White, Bending, & Larson (1976) cited in Mydlarz & Briedis (1992) proposed Equation 6-4 to calculate growth rate directly from the population density distribution and has been included in Figure 6-15 for comparison. It is to be noted that this equation holds whether growth rate varies with size or not (Mydlarz & Briedis, 1992). The growth rate predicted by SDG rate model (Equation 6-2) is fairly in agreement with that predicted by Equation 6-4 up until 400 µm. Equation 6-2 predicts that growth rate becomes size independent at crystal sizes of greater than approximately 700 µm, while Equation 6-4 predicts a falling off of the growth rate at these sizes.

$$G(L) = \frac{L_{i-1} - L_i}{\tau ln\left(\frac{N(L_i)}{N(L_{i-1})}\right)}$$

Equation 6-4 Growth rate from population density distribution

6.2.3.2 Growth Rate Dispersion

Different GRD models were tried as shown in Table 6-1.

.

Table 6-1 *Growth Rate Dispersion Models*

Distribution	Probability density function	Parameter constraints	Parameter fitted value	Mean value of the distribution ($\mu m\ min^{-1}$)	
Gamma	$\frac{1}{\beta^{\alpha}\Gamma\alpha} g^{\alpha-1}\exp\ \frac{-g}{\beta}$	α >0 β>0	0.35 0.31	αβ	0.11
Inverse gamma	$\frac{\alpha^{\beta-1}}{\Gamma(\beta-1)} g^{-\beta} exp\left(\frac{-\alpha}{g}\right)$	α>0 β>3	0.21 3.88	$\alpha/(\beta-2)$	0.11
Log normal	$\frac{1}{\beta\sqrt{2\pi}g} exp\left[-\frac{(\ln(g)-\alpha)^2}{2\beta^2}\right]$	α β>0	-2.69 1.03	$exp\left(\frac{\beta^2}{2}+\alpha\right)$	0.11
Weibull	$\alpha\beta g^{\beta-1}\exp\ (-\alpha g)^{\beta}$	α>0 β>0	117.6 0.44	$\frac{\Gamma\left(1+\frac{1}{\beta}\right)}{\alpha}$	0.02
Sum of two constant growth rates	$\frac{1}{\alpha}$ $when\ g = G_1$ $(\alpha-1)$ $when\ g = G_2$ 0 $when\ g \neq G_1\ and\ g \neq G_2$	G_1 >0 G_2 >0 α>1	0.99 0.14 82.9		

The number of crystals greater than size *L* (cumulative number distribution) with all possible growth rates is given by Larson, White, Ramanarayanan, & Berglund (1985):

$$N(L) = \int_0^{\infty} N_T \exp\left(-\frac{L}{G\tau}\right) f(G) dG\ ,$$

Equation 6-5 Cumulative size distribution with growth rate distribution

where, N_T is the total number of crystals per kg of slurry present in the crystallizer

f(G) is the growth rate distribution function

N(L) from the above equation can be changed to population density frequency distribution by:

$$n(L) = \frac{N(L_{i-1}) - N(L_i)}{L_i - L_{i-1}}$$

Equation 6-6 Converting cumulative number distribution to frequency distribution

An analytical solution is available only for the inverse gamma function (Larson, et al., 1985):

$$n(L) = \frac{(\beta - 1)(\alpha\tau)^{\beta-1}}{(L + \alpha\tau)^{\beta}}$$

Equation 6-7 Analytical solution for inverse gamma distribution function

The remaining distributions were solved numerically using the trapezoidal rule. The theoretical calculated population densities for the various distributions were fitted to the plant density distribution data using the solver function in Excel. The fits of the various distributions are shown in Figure 6-16 and the probability densities in Figure 6-17.

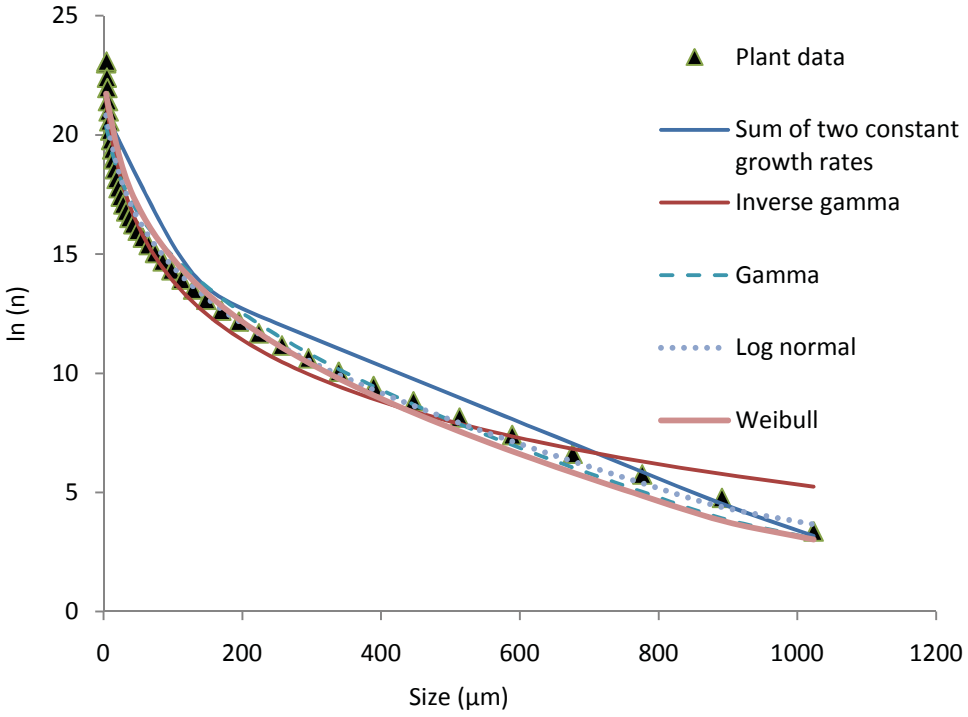


Figure 6-16. Various growth rate dispersion models fitted to plant population density.

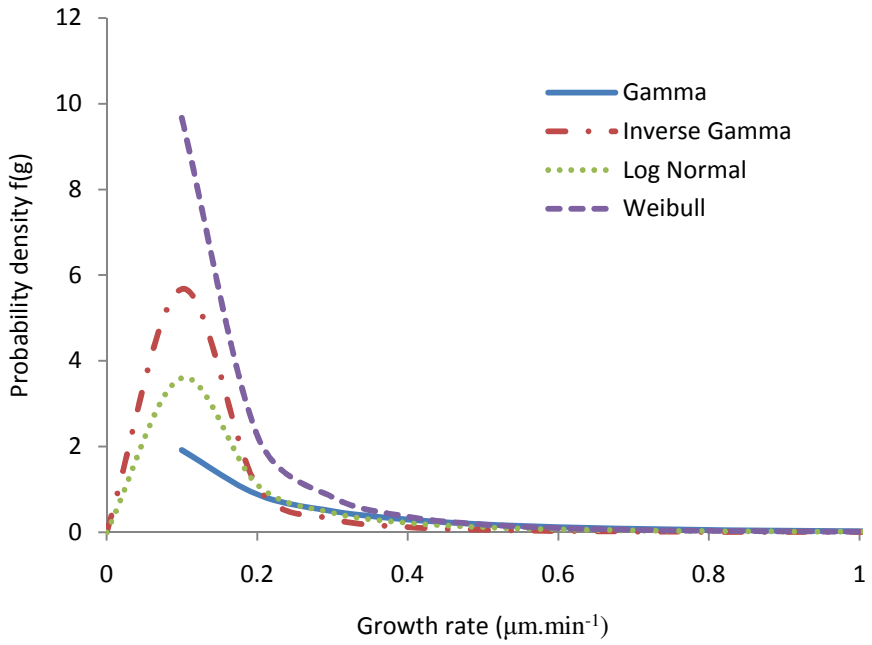


Figure 6-17. Probability density distribution for various growth rate dispersion models (value of the fitted parameters is listed in Table 6-1)**.**

.

In comparing all the models, SDG gave the best fit. The log normal distribution had the closest fit among the growth rate distribution models. The numbers of parameters in the SDG model give it more flexibility when making a fit. Since the main aim of this study is to predict most accurately the size distribution from the crystallizer, SDG model is being used in further analysis. Selection of this approach does not however suggest that the α-LMH crystals exhibit size dependent growth rate. Experimental data is still inconclusive regarding SDG in lactose and needs further examination.

6.2.4 Simulation and Parameter Estimation

To implement a size dependent growth rate model, it is necessary to further develop the crystallizer model of Chapter 5 to simulate a complete population density distribution. The previous model, based on moments does not give the complete crystal size distribution and calculates only mean volume weighted mean diameter. The discretization technique for solving the population balance to obtain the complete distribution is discussed in Chapter 2. The effective size independent growth rate (G_e) in the SDG model (Equation 6-2) was expressed similar to the normal growth rate equation of Chapter 5 (as a function of supersaturation). For the boundary conditions

it is assumed that all nuclei are formed at a size of 1 micron. This assumption appears to be valid in the light of data presented by (Shi, et al., 1989). They followed the growth of the secondary nuclei formed and then extrapolated the time versus nuclei size plot to time zero to determine an initial nuclei size distribution. The nuclei birth size varied from 1-13 μm. The lower limit of this range was taken as the size at which all nuclei are formed. It also becomes the lower limit of the particle size distribution (as the size of any crystal cannot be lower than the size of the nuclei).

The population balance was solved using the method of lines (MOL) as described in Chapter 2. In MOL, the size domain is discretized into p number of grid points. Accuracy of the solution of the resulting ODEs increases with the increase in the number of grid points or in other words, with decrease in the grid size. However, a greater number of grid points also increases the computational time. Hence a balance needs to be achieved between the desired accuracy and the computational time. In order to determine the optimum number of grid points, simulation runs were conducted at 100, 200, 500, 1000, 2000 and 4000 grid points. The maximum crystal size was chosen as 1000 μm based on the actual crystal size distribution measured from the plant. Hence the grid sizes corresponded to 10, 5, 2, 1, 0.5 and 0.25 μm, respectively for the number of grid points used. The results for simulated D[4,3] at various grid lengths are shown in Figure 6-18. It can be seen that for a decrease in the grid size below 1 μm there was no significant improvement in the simulation results. Therefore a grid size of 1 μm and L_{max} = 1000 μm were used during the simulations.

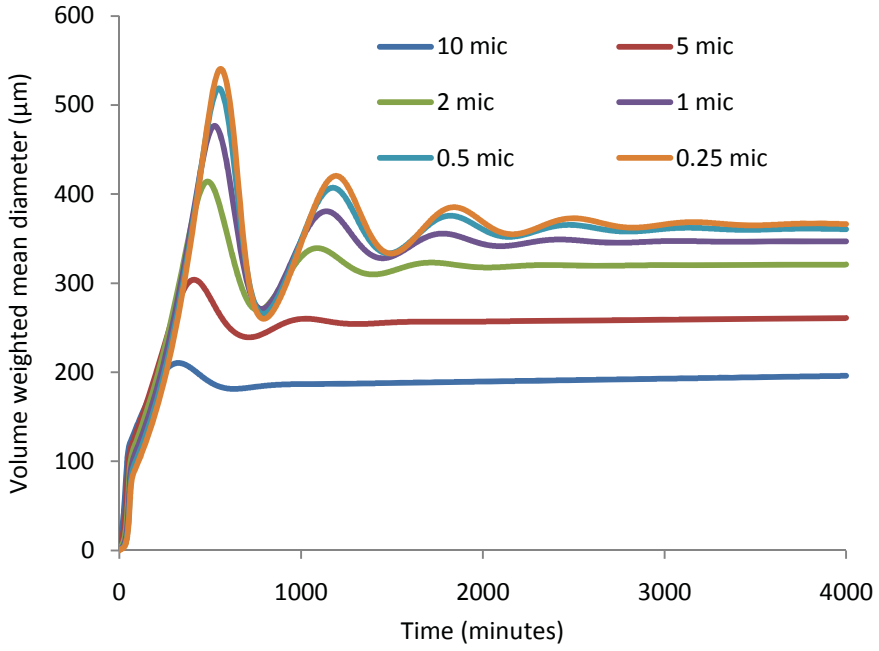


Figure 6-18. Effect of grid size on simulation results.

The understanding gained in Chapter 5 by the sensitivity analysis was used to optimize the various kinetic parameters to match the model predictions with the measured data. The supersaturation exponents for growth, primary and secondary nucleation were kept constant at 1.3, 1.5 and 2.5 respectively from the different literature sources cited in Chapter 5. The rate constants were manipulated by trial and error to achieve the best fit by the following considerations. The total solids value depends on the evaporation rate and hence was the first parameter to be set based on total solids measurements. The secondary nucleation rate constant drove the particle size and the dissolved solids concentration (supersaturation). It was thus optimized to approximately predict the measured steady state mean particle size (~ 325 µm) and dissolved lactose (~0.435 mass fraction). The growth rate constant was then tuned to get a closer fit to the measured points. The first measurements at the start of the continuous stage provided the crystal size at the end of the batch process (crystal size of around ~100-130 µm) and were used to fix the primary nucleation rate constant.

The measured data points during the transient regime (period between the start of continuous phase and achievement of steady state) as well as the steady state operation are shown along with the simulation results in Figure 6-19-Figure 6-23. The discontinuous line denotes the profile during the batch process. No sampling

during the batch stage was possible and hence this could not be validated. The mother liquor was found to contain 95% (by mass) dissolved lactose by HPLC analysis. Since the model predicts the pure lactose dissolved content, the measured dissolved solids values were multiplied by 0.95 to obtain the dissolved lactose concentration.

The dissolved lactose and the mean particle size profiles exhibited dampening oscillatory behaviour. Sampling for 8 hours was insufficient to cover the entire transient stage as the model shows that the crystal size requires approximately 25 hours to stabilize. The other parameters are stable long before this. The decaying transient dynamics of the crystal size cannot be validated by direct measurements as it was not possible to sample continuously for 25 hours. However, an alternative way to confirm whether such dynamics are exhibited by the crystallizer was established.

Normal plant operation procedures require the operators to sample the dried lactose crystals and perform a sieve test using an 80 and 200 mesh sieve every two of hours. The sieve test data was collected from the operator log books after three different start ups. The results are shown in Figure 6-24. The increase in the mass fraction of crystals retained on the 80 mesh (170 μm) sieve indicates an increase in the mean crystal size and vice a versa. It is clear that the crystal size shows oscillatory dynamics. The first cycle of increasing particle size, reaching a maxima and then dropping to a minimum size is easily distinguishable. Although exact crystal sizes were not measured, the trends support the model findings. Such dynamics have also been reported by numerous previous simulation and experimental studies of evaporative industrial crystallizers (Bermingham, et al., 1998a; Kramer, et al., 1996; Kramer, et al., 2000). These dynamics also probably explain the reason for the smaller mean particle size measurement in trial 1 as they may have been measured during the time when the crystal size was passing through the lower point of the oscillation cycle. The measured crystal size cycle is out of sync with the model predictions but follows the trend accurately. The final steady state crystal density distribution was very well predicted by the model using the optimized parameters as is shown in Figure 6-23**.** It is to be noted that the parameters were not optimized to fit the population density curve. A good fit proves the validity of the model.

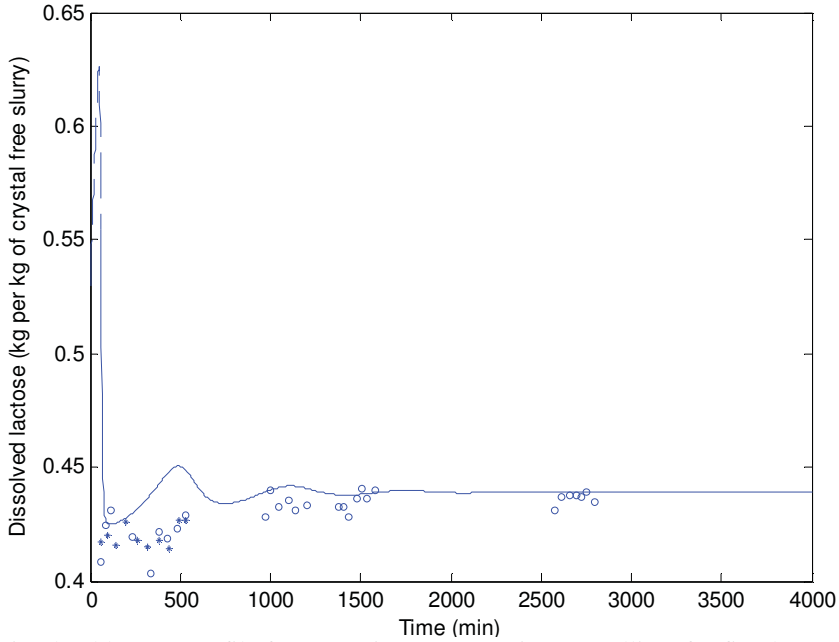


Figure 6-19. Dissolved lactose profile for Kapuni FC evaporative crystallizer for fitted growth, primary nucleation and secondary nucleation rate constants. The broken and continuous lines represent the model prediction during the semi-batch and the continuous mode respectively.

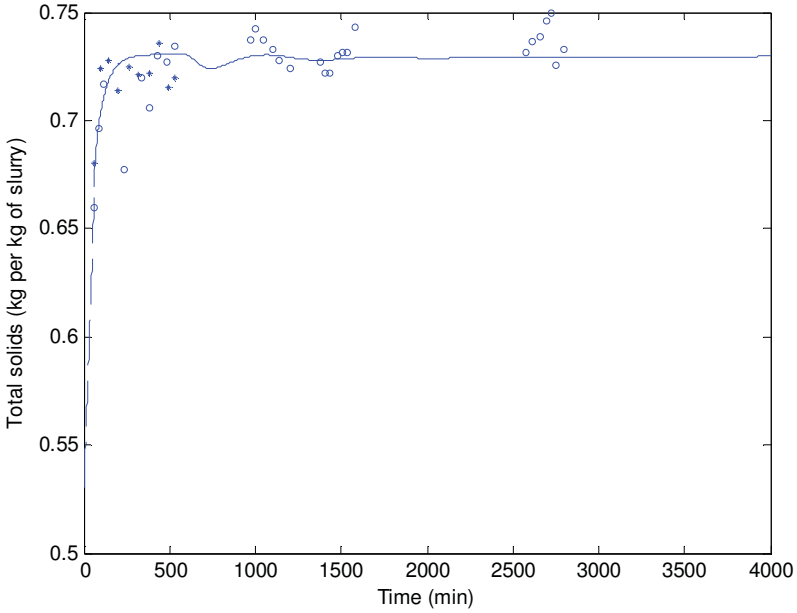


Figure 6-20. Total solids profile for Kapuni FC evaporative crystallizer for fitted growth, primary nucleation and secondary nucleation rate constants. The broken and continuous lines represent the model prediction during the semi-batch and the continuous mode respectively.

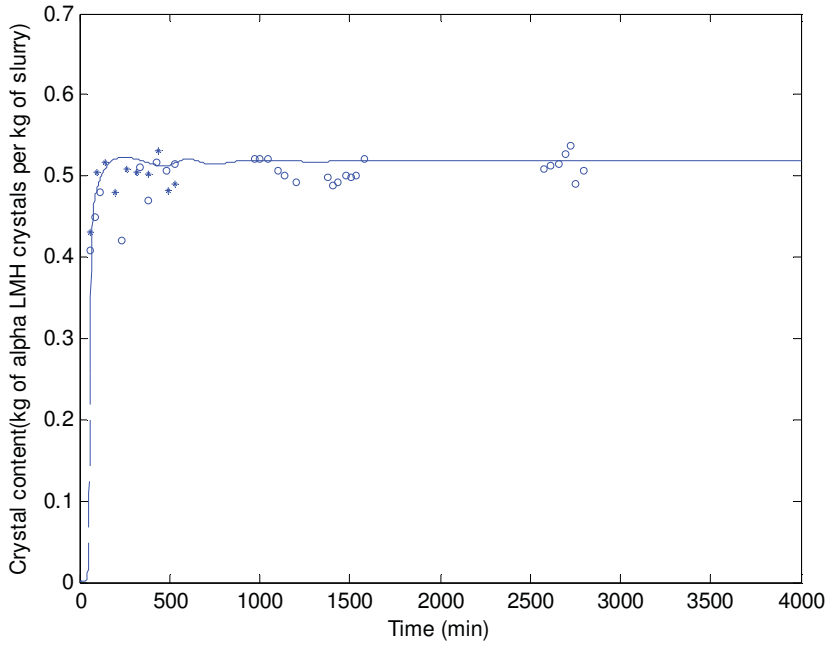


Figure 6-21. Crystal concentration profile for Kapuni FC evaporative crystallizer for fitted growth, primary nucleation and secondary nucleation rate constants. The broken and continuous lines represent the model prediction during the semi-batch and the continuous mode respectively.

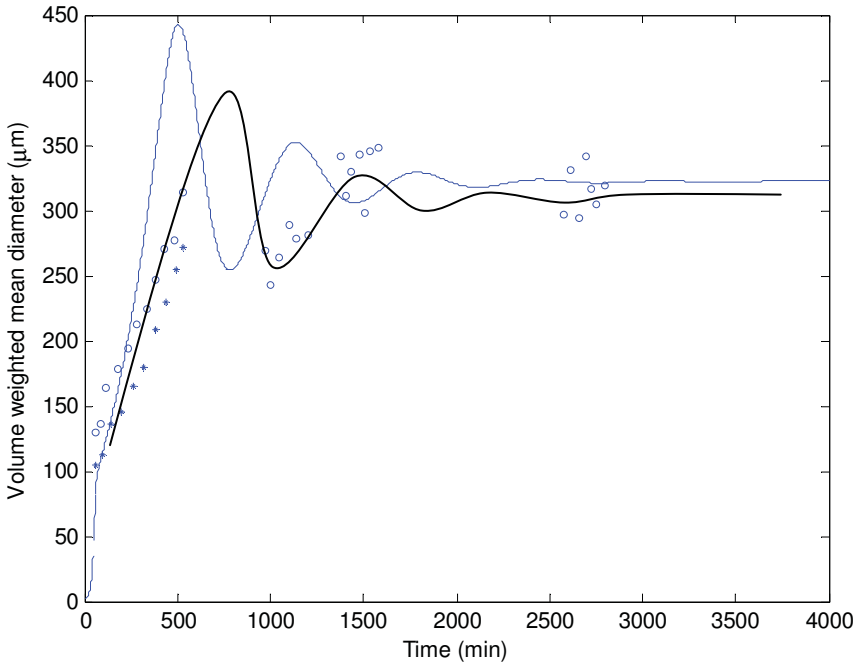


Figure 6-22. Volume weighted mean diameter profile for Kapuni FC evaporative crystallizer for fitted growth, primary nucleation and secondary nucleation rate constants. The broken and continuous lines represent the model prediction during the semi-batch and the continuous mode respectively. The line through the measured data points is drawn as a visual guide to compare with the model prediction.

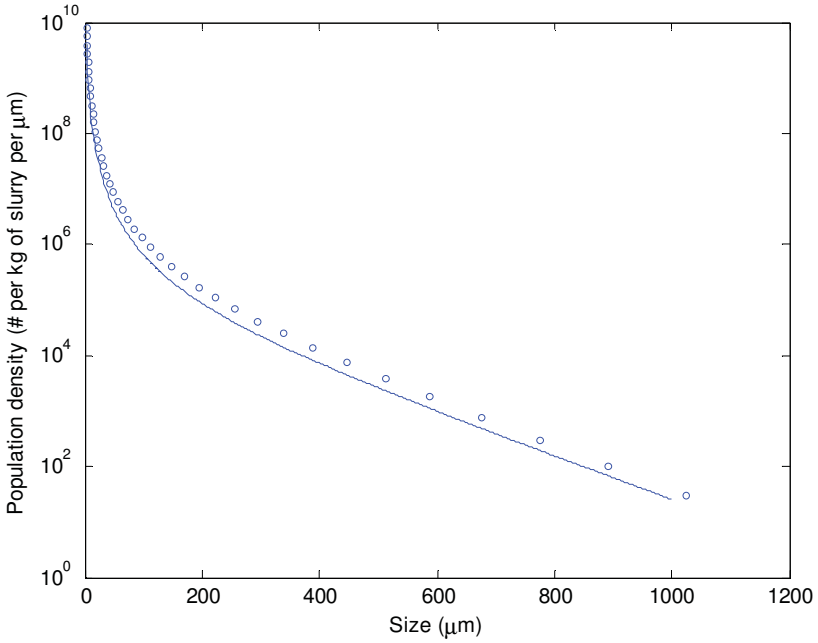


Figure 6-23. Steady state population density distribution for Kapuni FC evaporative crystallizer predicted by the model using optimized fitted parameters**.**

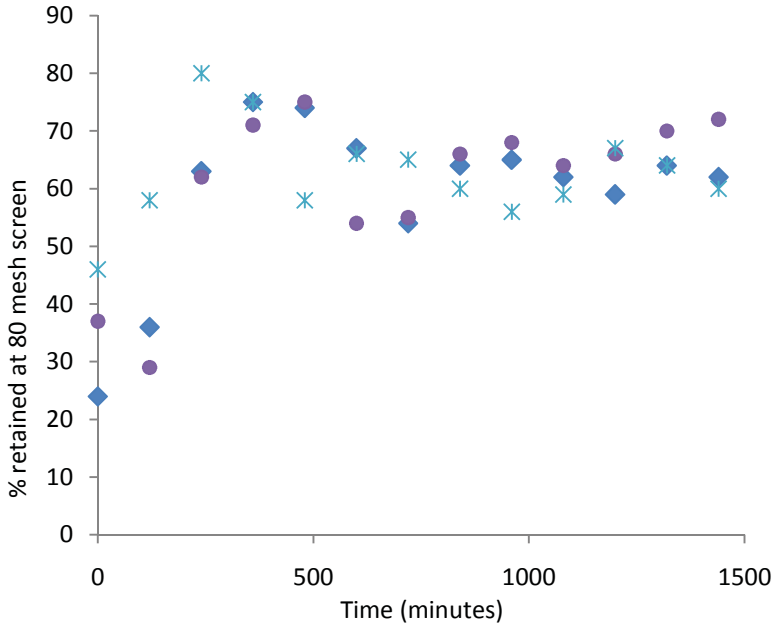


Figure 6-24. Dry crystal sieve analysis representative of the CSD dynamics of the Kapuni FC evaporative crystallizer.

Such dynamics can be caused by numerous factors such as fines destruction, classified product removal, size dependent growth rate, kinetics of nucleation rate and external

modulation of parameters (Lakatos, Sapundzhiev, & Garside, 2007). Thus it is difficult, if not impossible, to exactly figure out the source of instability (Randolph & Larson, 1988). In the present study, no fines destruction or classified product removal occurred and therefore size dependent growth rate could be one of the reasons for the observed dynamic behaviour. In order to confirm this, simulations with size independent growth (SIG) rate were conducted and some of the results are shown in Figure 6-25-Figure 6-27. The kinetic parameters needed to be adjusted to make the simulation results match with the measured data.

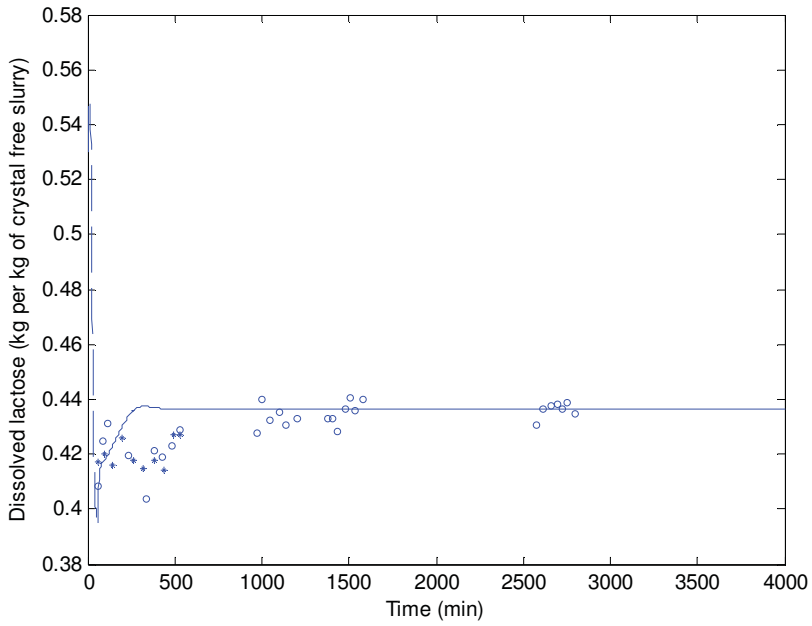


Figure 6-25. Dissolved lactose profile for size independent growth.

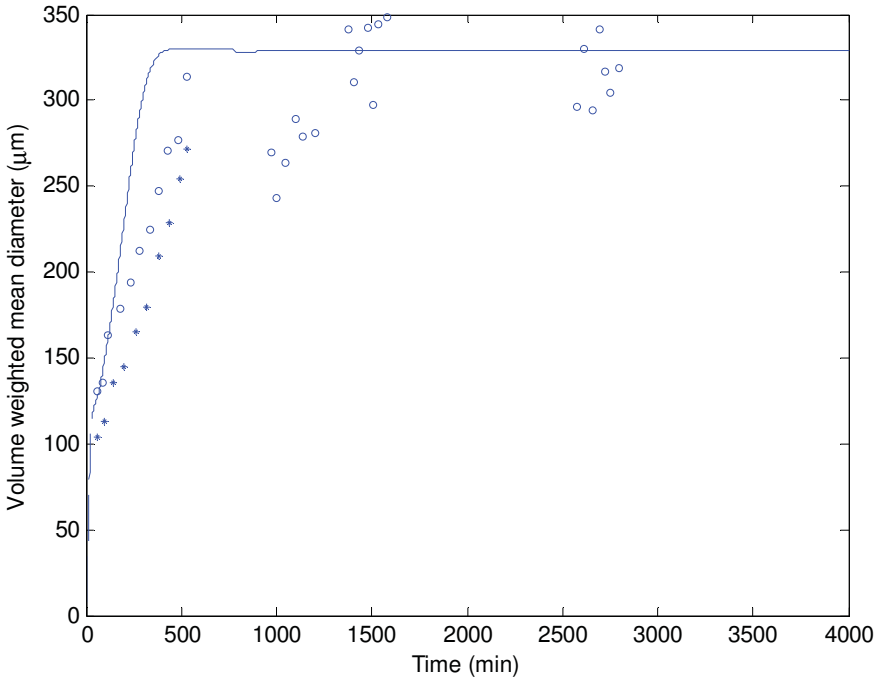


Figure 6-26. Volume weighted mean diameter profile for size independent growth.

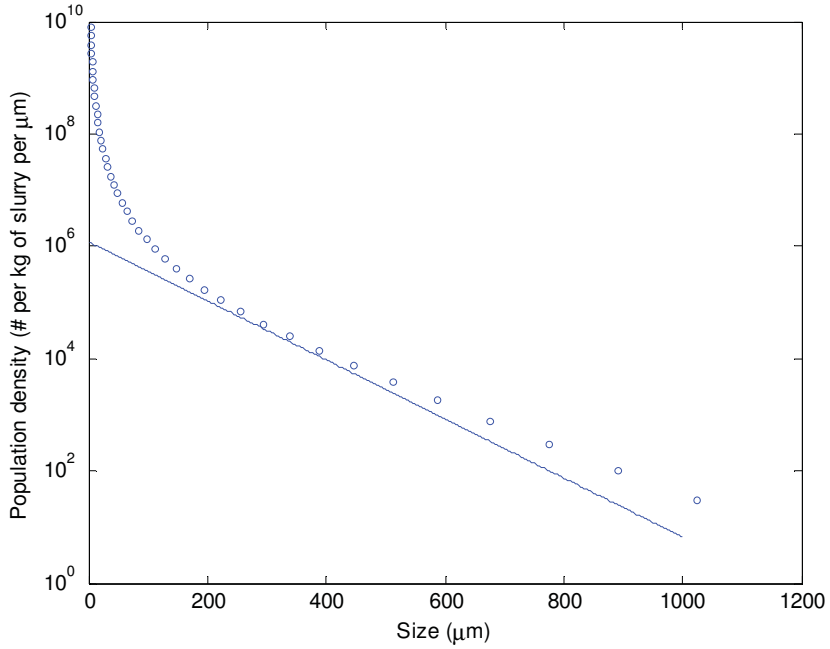


Figure 6-27. Population density curve for size independent growth.

It can be seen that the decaying transient disappears when the growth becomes size independent and the model failed to predict the fluctuations in the crystal size

observed in the plant. Therefore, SDG captures the plant dynamics more precisely than SIG. An expected straight line is obtained on a population density versus crystal size plot for SIG. The estimated values of the kinetic parameters for both size independent and dependent growth rate are shown in Table 6-2.

Simulations were also conducted using the MOMs, with the same parameters as those fitted for SIG. The simulation results shown in Figure 6-28 and Figure 6-29 closely matched the measured values and to that of SIG predictions. Thus, the discretized population balance is similar to the MOMs for solving a crystallization system when the growth kinetic is size independent.

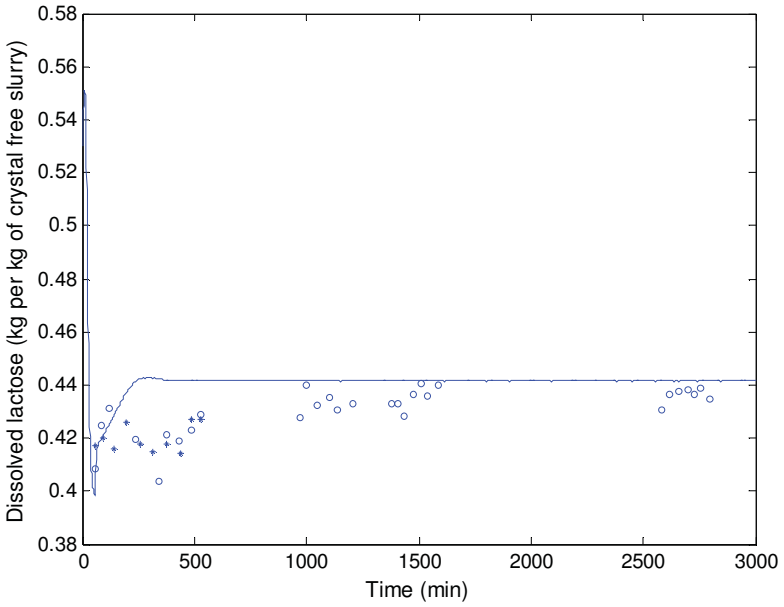


Figure 6-28. Dissolved lactose profile using method of moments and parameters estimated by SIG (size independent growth).

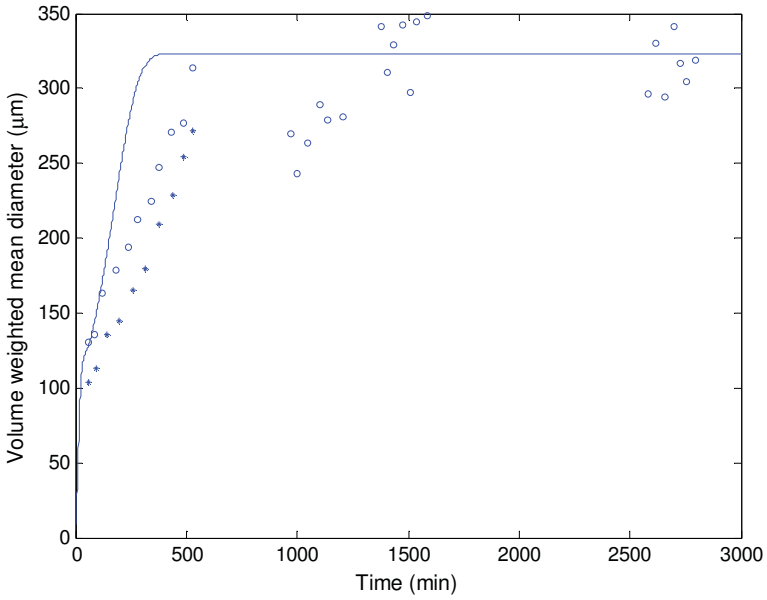


Figure 6-29. Volume weighted mean diameter profile calculated using the method of moments.

Table 6-2 *Kinetic Parameters Estimated from Size Dependent and Size Independent Growth Models*

Kinetic parameter → / Model ↓	k_g [m min^{-1}((kg of α-LMH) (kg of water)$^{-1}$)$^{-1.3}$]	$k_{n,p}$ [# min^{-1} (kg of slurry)$^{-1}$((kg of α-LMH) (kg of water)$^{-1}$)$^{-2.5}$]	$k_{n,s}$ [# min^{-1} (kg of slurry)$^{-1}$ ((kg of α-LMH) (kg of water)$^{-1}$)$^{-1.5}$]
SDG	42	8E8	4E10
SIG	32	3E8	1.3E8

6.3 Simulations using Mechanistic Models for Secondary Nucleation

In this section various mechanistic models available for secondary nucleation rate will be used in the simulation runs and compared to the measured values. For growth and primary nucleation, the optimized parameters for size dependent growth, as shown in Table 6-2, will be used.

6.3.1 Attrition

Attrition occupies the bulk of the literature as the assumed source of contact secondary nucleation. The experimental work on lactose attrition in this study showed that lactose is susceptible to attrition (Chapter 4). However, it is difficult to estimate the exact magnitude of attrition at the industrial scale based on the laboratory scale study. A lot of work in understanding and developing a mechanistic model for

attrition due to crystal-impeller impacts was reported by Mersmann and his group in a series of publications (Gahn & Mersmann, 1995, 1997, 1999a, 1999b; Mersmann, et al., 1988; Ploß & Mersmann, 1989; Pohlisch & Mersmann, 1988) which culminated in a detailed chapter in the handbook by Mersmann (2001b). Since it is a model derived from first principle, it can be used to predict secondary nucleation due to attrition independent of the scale of operation and the compound being crystallized. The model requires impeller geometric features, operational conditions and the mechanical properties of the crystal. The detailed mathematical treatment of the model is given in Appendix IV. Equation 6-8 gives the salient components of the model:

$$B_{attr} = K_{mech} E_k f_c \chi$$

Equation 6-8 Secondary nucleation rate due to attrition

where; B_{attr} is the nucleation rate [# min^{-1} (kg of slurry)$^{-1}$], K_{mech} is the nucleation constant [# J^{-1}] and signifies the number of secondary nuclei generated per unit of contact energy at the given supersaturation, $E_k$is the kinetic energy of contact [J], f_c is the contact frequency per unit mass of slurry [# min^{-1} (kg of slurry)$^{-1}$] and χ is the effective nucleation rate factor.

Equation 6-8 is in line with Equation 4-12 introduced in Chapter 4. The equation is re-introduced here for ease of comparison.

$$B_N = K_N E_k f_c \sigma^b$$

Equation 6-9 Collision secondary nucleation

As attrition is a mechanical process, Equation 6-8 does not contain a supersaturation dependency term. K_{mech} is a mechanistic attrition constant comprising of the mechanical properties of the crystal; fracture surface energy, hardness and shear modulus and was the main focus of Mersmann's work. The other feature of the model is the incorporation of the concepts of target and geometric efficiency in the frequency term (f_c). Collision probability determines the likelihood of the crystal of a given size to collide with the impeller blades. Geometric efficiency predicts the chance that crystal will be present in the given blade segment. χ is the ratio of the number of attrition fragments that grow (effective) to that total formed and is included

to account for non-growing or 'dead' nuclei and depends on supersaturation. This makes attrition indirectly dependent on supersaturation. Non-growing nuclei have been attributed to the additional strain energy incorporated into them during the process of attrition. χ needs to be determined experimentally. There are number of inbuilt assumptions in the model as summarised by Gahn & Mersmann, (1999a). The model also does not accurately predict the number of fragments in the 1 μm size range. It is valid only for compounds satisfying the condition E/H <100, where E is the Youngs modulus and H is hardness (Gahn & Mersmann, 1999a). Lactose satisfies this condition (Appendix I) and hence the model can be applied to the current system.

It was found during the simulation runs that the previous L_{max} value of 1000 μm was insufficient to accommodate the entire crystal population. This was due to the lower value of secondary nucleation due to attrition which drove the crystal size distribution over the set 1000 μm limit. This led to errors in the simulation results as a mass of crystals above 1000 μm was over looked. Therefore, the maximum crystal size was doubled to 2000 μm. In order to maintain the grid size to 1 micron the number of grid points was doubled to 2000.

The length of the impeller blade (0.175 m) was discretized into small segments to account for the variation of kinetic energy with the position of impact on the blade. Simulation runs were conducted at segment lengths of 0.05, 0.01 and 0.005 m to ascertain its effect on simulation results. Results are shown in Figure 6-30. Segment length less than 0.005 m does not give any improvement on the predicted results. Also discretization below 0.005 m segment length led to very long simulation time (greater than 60 minutes). Therefore, 0.005 m was chosen as the segment length for the impeller blade.

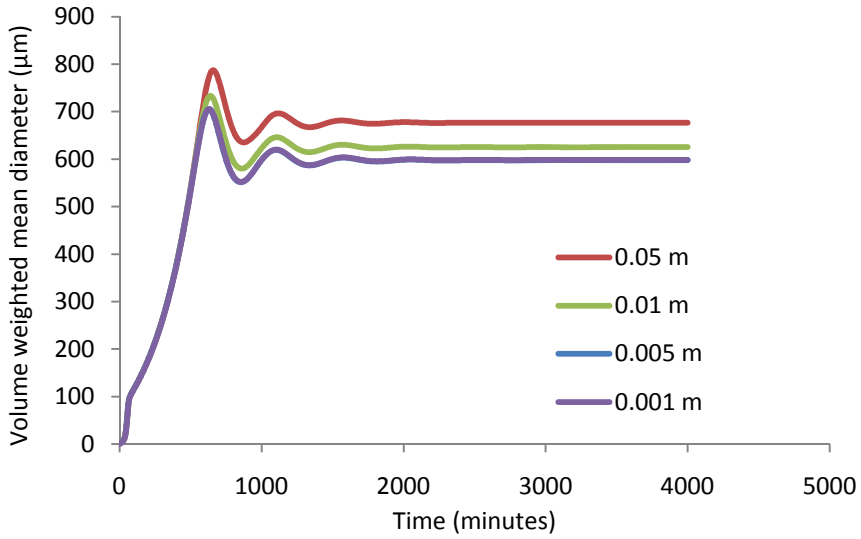


Figure 6-30. Effect of impeller blade discretization on simulation results.

The following assumptions were made during the simulation:

i) Due to the small blade angle of the pump, the majority of the collisions will occur on the edges perpendicular to the flow and not on the face. Hence, impacts only on the edge of the pump blades were considered.

ii) The effect of particle size on viscosity is neglected

iii) The blade angle is independent of the radial position

iv) The value of χ is taken as 1 in the absence of any experimental data for growth of lactose attrition fragments, which meant that all the attrition fragments grew, and hence calculated a very conservative figure for nucleation rate due to attrition. A value of 0.017 has been experimentally determined for KNO_3 (Mersmann, 2001b).

v) The mechanical properties of the crystal are independent of temperature

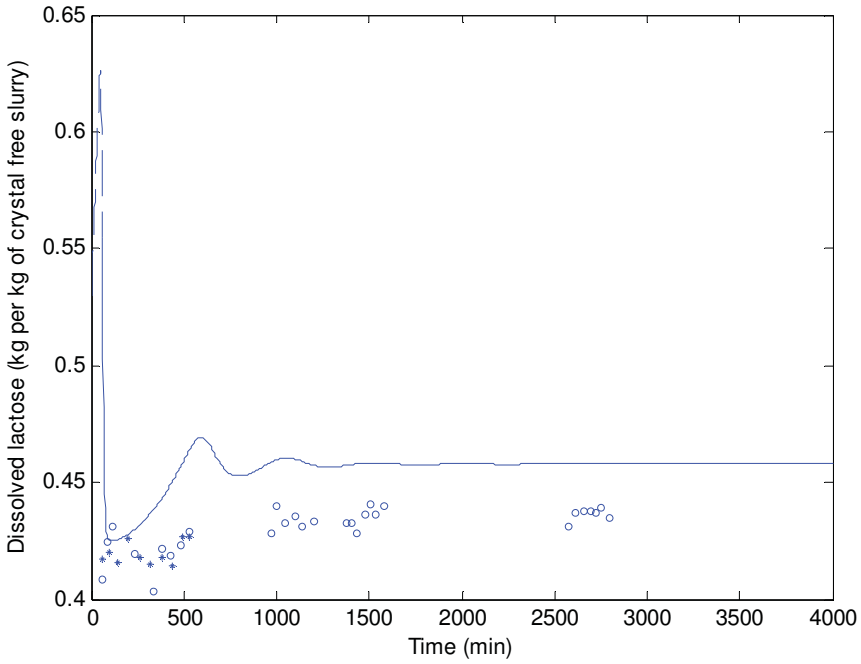


Figure 6-31. Dissolved lactose concentration profile with attrition (calculated by Mersmann model) as the source of secondary nucleation. Markers depict measured values.

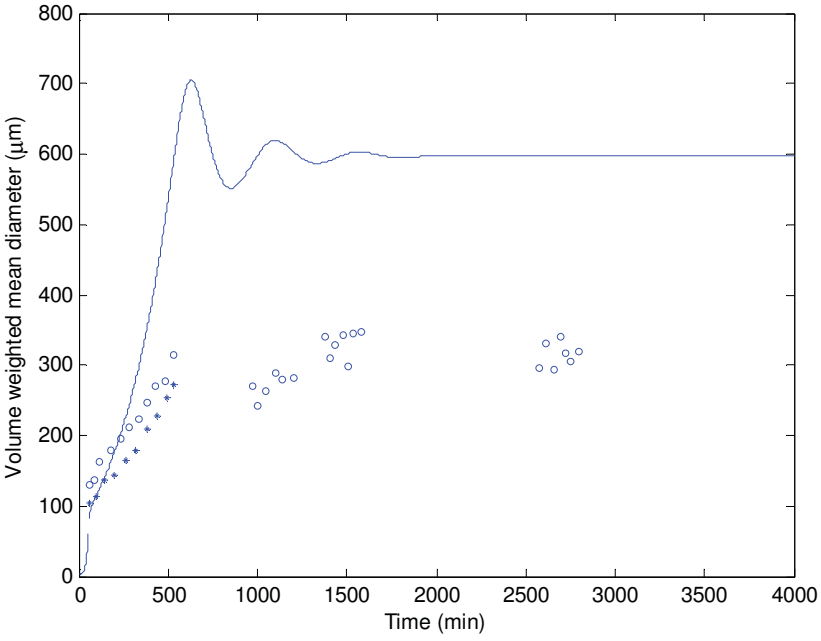


Figure 6-32. Volume weighted mean diameter profile with attrition (calculated by Mersmann model) as the only source of secondary nucleation. Markers depict measured values.

Simulation results for dissolved lactose concentration and volume weighted mean diameter with nucleation rate calculated by the Mersmann model are shown in Figure

6-31-Figure 6-32. The simulation predicts higher steady state dissolved lactose concentration and twice the crystal mean size compared to the measured values. Both of the above parameters increase with a decrease in secondary nucleation (from sensitivity analysis in Chapter 5). This indicates that the secondary nucleation rates calculated by the Mersamann model are lower than the actual rates. This shows that attrition, as predicted by the Mersmann model is not the main source of secondary nucleation in the evaporative lactose crystallizers. This is also evident from the photographs of the crystals drawn from the crystallizer. The crystals are largely intact and do not show any major evidence of attrition other at the edges and tips, as shown in Figure 6-33.

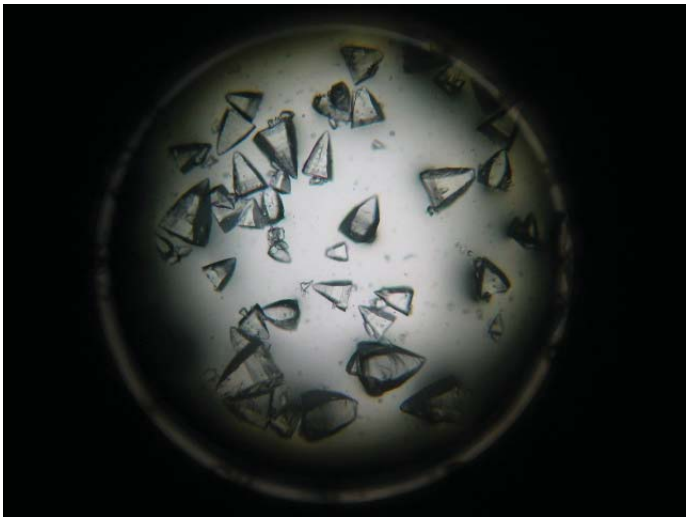


Figure 6-33. Crystals withdrawn from the crystallizer at steady state.

6.3.2 Contact Nucleation due to Crystal-Impeller Collisions

In order to determine non-attrition contact nucleation due to crystal impeller contacts, values of K_N and b in Equation 6-9 needs to be established. f_c and E_K terms are determined in the same way as that for attrition model. K_N physically signifies the number of nuclei generated per unit collision kinetic energy and is analogous to K_{mech}. b represent the nucleation rate order. K_N and b can be estimated from the fitted lines at different supersaturations in Figure 4-11 and is reproduced here in Figure 6-34 for convenience. The lines in Figure 6-34 were fitted to only 2% (w/w) seed loading data. However, it was found that the secondary nucleation rates for all the seed loadings (2, 5 and 10% w/w) fell on a single curve (Figure 4-10, Chapter 4) for one of the studied supersaturations, when considered from a kinetic energy and collision

frequency perspective. It is hence assumed that the study can be extrapolated to the industrial slurry of 50% w/w. Figure 6-34 was plotted between the nucleation rate (normalized by collision frequency) and the impeller-crystal kinetic energy. Equation 4-20 can be modified

$$\frac{B}{\eta n_c N_i} = K_N \sigma^b \frac{K_D d_i^3}{V_{sus}} E_{k,i-c}^S .$$

Equation 6-10 Modified Equation 4-20 for secondary nucleation due impeller-crystal collisions

Comparing Equation 6-10 with the fitted line, $y = Ix^S$,where I is the intercept and S is the slope; it can be worked out that $y = \frac{B}{\eta n_c N_i}$, $x = E_{k,i-c}$, and $I = K_N \sigma^b \frac{K_D d_i^3}{V_{sus}}$. The fitted value of *s* was close to 1. Taking the natural log on both sides for the intercept term gives

$$ln(I) = \ln\left(K_N \frac{K_D d_i^3}{V_{sus}}\right) + b ln\sigma$$

Equation 6-11 Determination of collision nucleation rate constant and supersaturation dependence

In order to estimate K_N and b, $ln(I)$ was plotted against $ln(\sigma)$, shown in Figure 6-35. Supersaturation units used are (kg of α-LMH per kg of water) to maintain consistency to that used in the model. The slope (8.18) and the exponential of the intercept (3.06E17) of the fitted line give the values of b and $K_N \frac{K_D d_i^3}{V_{sus}}$, respectively. In order to estimate K_N; K_D, d_i and V_{sus} needs to be known. The terms d_i and V_{sus} are know from the experimental details of section 4.2 as 0.05 m and ≈250 ml. The discharge coefficient (K_D) was taken as 0.4 for a 2 bladed, 45° blade angle impeller (Broz, Fort, Sperling, Heiser, & Rieger, 2004). Substituting these values in the intercept term $K_N \frac{K_D d_i^3}{V_{sus}}$, K_N value works out as 1.53E18 # J^{-1} (kg per kg of water)$^{-8.2}$ from the calculated value of intercept from the plot. The value of K_N is independent of scale of operation and the mode of collision (crystal-crystal or crystal-impeller) and is used in simulation runs for estimating contact nucleation at industrial scale.

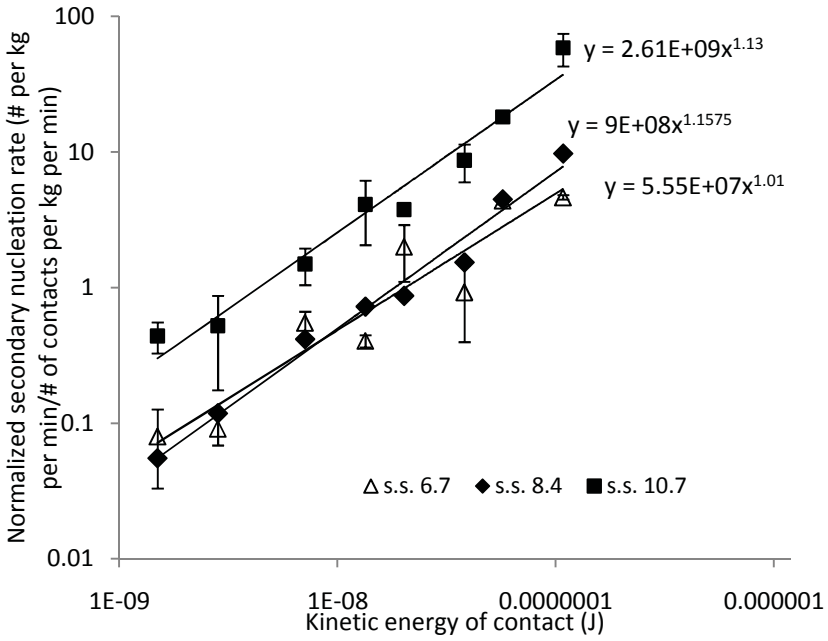


Figure 6-34. Secondary nucleation at constant seed loading of 2% (w/w) at 10.7 and 6.7 s.s. (g α-LMH per 100 g water) from a kinetic energy and frequency of contacts perspective.

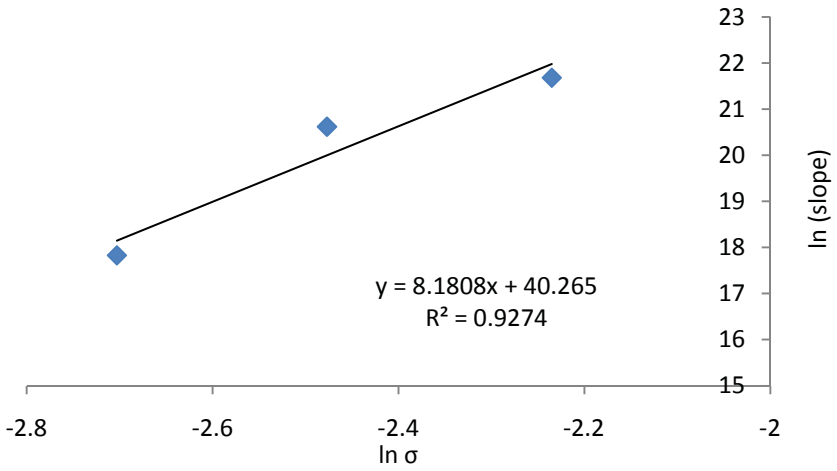


Figure 6-35. Plot of ln of the intercept of the lines fitted in Figure 4-11 versus the ln of the supersaturations to determine K_N and b in Equation 4-12.

Simulation runs were done with the above estimated values for impeller-crystal collision induced secondary nucleation model for a circulation pump speed of 720 rpm. The results are shown in Figure 6-36 and Figure 6-37. The dissolved lactose concentration prediction matches well with that of the measured values. The predicted mean crystal size is nearly half to that of the plant measurements. The D[4,3] shows a more intense dampening oscillation and requires a longer time to

reach the steady state, compared to the plant behaviour. This might be due to the very high dependence of nucleation rate on supersaturation (power of 8.2) combined with size dependent growth rate.

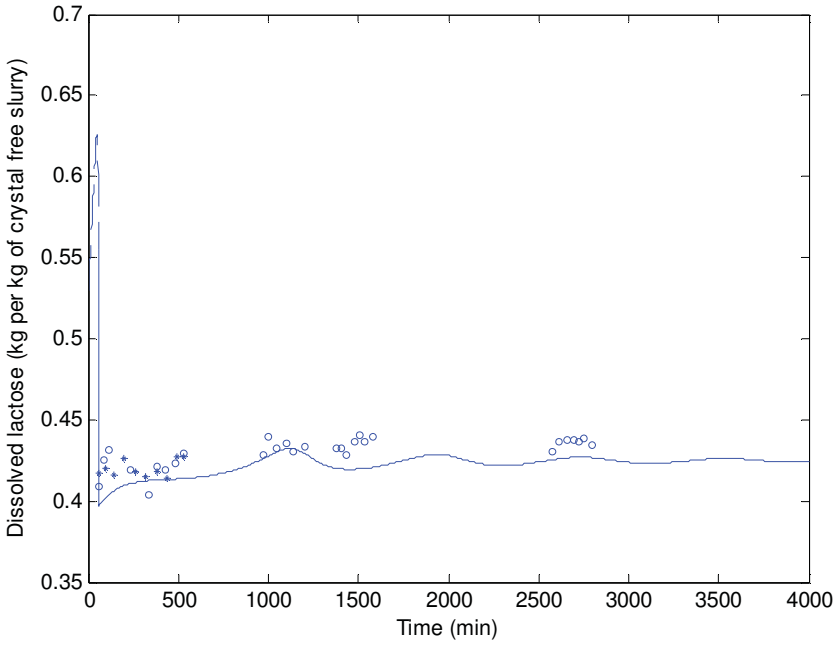


Figure 6-36. Dissolved lactose concentration profile with crystal-impeller contact nucleation at the operational circulation pump speed as the source of secondary nucleation. Markers depict measured values.

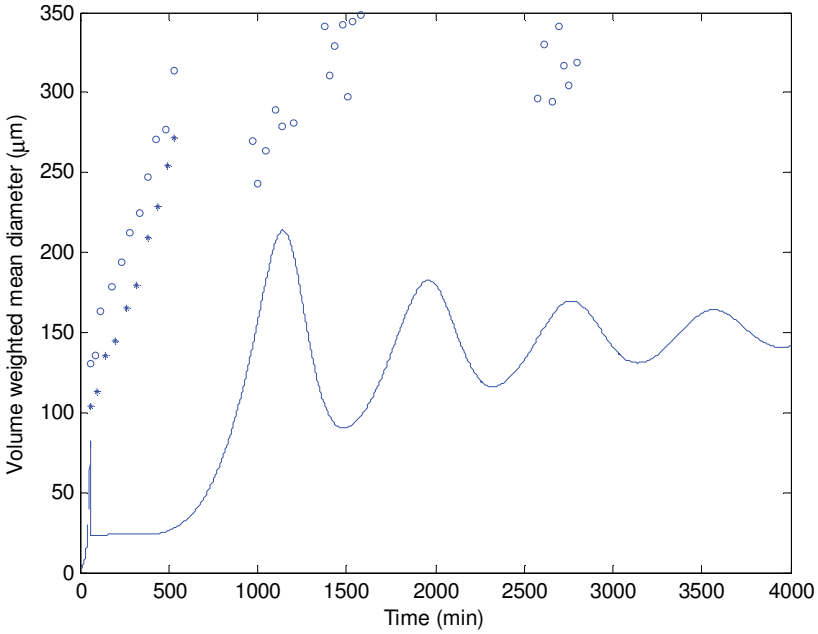


Figure 6-37. Volume weighted mean diameter profile with crystal-impeller contact nucleation at the standard operating circulation pump speed as the source of secondary nucleation. Markers depict measured values.

6.3.3 Contact Nucleation due to Crystal-crystal Collisions

A forced circulation evaporator contains flowing slurry; hence crystal-crystal interactions occur throughout the crystallizer. The intensity and frequency of such interactions will depend on the slurry properties and local hydrodynamic conditions. The slurry encountered in the system being investigated has a high solid to liquid ratio (volumetric crystalline hold up $\varphi \approx 0.4$). Eskin, Leonenko, & Vinogradov (2004a) presented following arguments to consider dense slurry ($\varphi > 0.18$) as a continuous liquid showing Newtonian behaviour to which classical turbulence model can be applied:

i) In this slurry the crystals have restricted freedom of movement, as the inter-crystal spaces are very small. The average clearance (δ) between the two crystals is given by Equation 4-22.

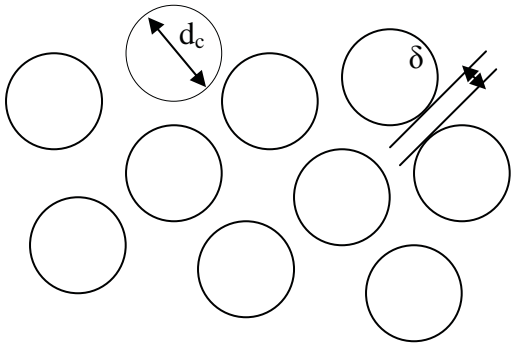


Figure 6-38. Solid liquid suspension (redrawn from (Eskin et al., 2004))

For lactose evaporative crystallizers, φ is around 0.4 and φ_{lim} for monodisperse spherical crystals is 0.6, the average clearance works out to be 43 μm for a mono-disperse suspension of 300 μm crystals. Hence, a dense slurry can be considered as a continuum as contrasted to dilute slurries where significant crystal-fluid lags can occur.

ii) The Prandtl mixing length, which characterizes the length of turbulent fluctuations transporting momentum between two adjacent layers, was shown to be independent of solids concentration of the slurry. Thus the turbulence models applicable to flow of pure fluid can be applied to dense slurry.

iii) Eskin, et al., (2004a) also presented experimental data demonstrating Newtonian behaviour of dense slurries. They calculated and found that the

Bagnold number, *Ba* (ratio of inertial to shear forces in the slurry) satisfied the condition for Newtonian behaviour of slurries (*Ba*<40) for particles of size range 150-300 micron, φ>0.18, relatively large pipe diameters (>0.05-0.1 m) and average velocities 3-5 $m.s^{-1}$.

Crystal-crystal collisions occur due to generation of relative velocity between the crystals by either turbulent shear or different particle inertia. The inertial effect is gauged by the tendency of the particle to follow a fluid streamline and is characterized by the Stokes number, the ratio of particle relaxation time to the characteristic time scale of the flow (Rielly & Marquis, 2001). The macro level time scale is in the order of the slurry circulation time. Macro flow results in a bulk movement of the particles and will result in low inter-particle velocities and will contribute very little to crystal-crystal collisions (ten Cate, et al., 2001). Hence, the micro level time scale characterized by the turbulent eddy life is used to define the Stokes number (Rielly & Marquis, 2001). For ψ<<1, the crystals will follow the fluid flow, hence very few collisions will occur. However, for $\psi \geq 1$ the particles will lag behind the fluid flow due to their inertia, leading to a more random movement of the crystals and resulting in increased collisions.

$$\psi = \frac{t_c}{t_e}$$

Equation 6-12 Stokes number

where, t_c the crystal relaxation time [s] is defined as (ten Cate, et al., 2001)

$$t_c = {d_c^2(2\rho_c + \rho_s)}\Big/{36\mu_s}$$

Equation 6-13 Particle relaxation time

and t_e, the turbulent eddy life time [s] is given as (ten Cate, et al., 2001)

$$t_e = \frac{k}{\varepsilon},$$

Equation 6-14 Turbulent eddy life time

where k is the specific turbulent kinetic energy [$m^2\ s^{-2}$] defined as (ten Cate, et al., 2001)

$$k = \frac{3}{2} v'^2$$

Equation 6-15 Turbulent kinetic energy

and ε is the energy dissipation rate [$m^2\ s^{-3}$], for a pipe flow can be calculated as (Eskin, et al., 2004a)

$$\varepsilon = \frac{1}{\rho_s} \frac{dP}{dl} v\,.$$

Equation 6-16 Energy dissipation rate in a pipe flow

v' is the root mean square (rms) velocity [ms^{-1}] of turbulent eddy in the flow and is of the same order as the shear velocity for a turbulent pipe flow (Oroskar & Turian, 1980) given by

$$v' = v_* = \sqrt{\frac{\tau_w}{\rho_S}}.$$

Equation 6-17 Shear velocity

τ_w , wall shear stress [$kg\ s^{-2}\ m^{-1}$] is defined as

$$\tau_w = f \frac{\rho_S v^2}{2},$$

Equation 6-18 Wall shear stress

where *f* is the friction factor and *v* is the mean velocity [ms^{-1}] of the flow. The RMS velocity of the crystal ($v'_{c\text{-}c}$) is related to the RMS velocity of an eddy as (Abrahamson, 1975)

$$\frac{v'^2_{c-c}}{v'^2} = \frac{\frac{t_e}{t_c} + q^2}{\frac{t_e}{t_c} + 1},$$

Equation 6-19 Crystal RMS velocity

where *q* is given as

$$q = \frac{3\rho_S}{2\rho_c + \rho_S}.$$

Equation 6-20 Constant in Equation 6-19

The collision frequency [# min^{-1}(kg of slurry)$^{-1}$] of mono disperse particles of diameter d_c can be predicted, as suggested by ten Cate, et al., (2001) as

$$f_{c,c-c} = 4\sqrt{\pi} n_c^2 d_c^2 \sqrt{v'^2_{c-c}}\,.$$

Equation 6-21 Crystal-crystal collision frequency

n_c is the concentration of the crystals [# (kg of slurry)$^{-1}$]. The equation for collision frequency needs to be multiplied by slurry density term to convert the unit from per unit volume to per unit mass of slurry. The kinetic energy for crystal-crystal collisions can be calculated as:

$$E_{k,c-c} = \frac{1}{2} m v'^2_{c-c}$$

Equation 6-22 Kinetic energy of crystal-crystal contact

Simulating all the possible collisions in a dense slurry is computationally demanding. Hence, no simulations were carried out. Instead parameters were evaluated assuming that the slurry contains mono dispersed particles of size 300 μm. This value represents the volume weighted mean crystal size produced in the crystallizer. Values of different parameters for the flow in the external loop pipe are presented in Table 6-3. The kinetic energy of contact is more than an order of magnitude lower than the threshold kinetic energy (1.5E-9 J) estimated in Chapter 4. It was concluded by the experimental studies on contact nucleation that kinetic energy is the most important parameter governing secondary nucleation. Hence, secondary nucleation due to crystal-crystal contacts can be discarded in the circulation loop pipe in spite of the high number of contacts. A crystal size of around 1000 μm is required to cross the threshold kinetic energy at the estimated contact velocity. This represents the maximum size of the crystal produced in the current crystallizer (Figure 6-11) and they will not be present in large enough numbers to influence the secondary nucleation rate.

Table 6-3 *Values of Critical Parameters for Crystal-Crystal Contacts in the Circulation Loop Pipe*

Pipe diameter [d_p]	0.5	m
Volumetric flow rate	0.39	$m^3 s^{-1}$
Slurry mean velocity through pipe [v]	1.67	$m s^{-1}$
Slurry density [ρ_S]	1320	$kg m^{-3}$
Slurry viscosity [μ_S]	0.02	$kg s^{-1} m^{-1}$
Reynolds number	55000	
Pipe roughness ratio [e/d_p]	1.0E-4	
Friction factor [f]	0.005	
Shear/Collision velocity [v_*]	0.083	$m s^{-1}$
Energy dissipation rate [ε]	0.093	$m^2 s^{-3}$
Turbulent kinetic energy [k]	0.011	$m^2 s^{-2}$
Eddy life time [t_e]	0.12	s
Crystal relaxation time [t_c]	5.5E-4	s
Stokes number [ψ]	5E-3	
Kinetic energy of collision [E_k]	7.64E-11	J
Particle concentration [n_c]	2.3E7	$\# kg^{-1}$
Frequency of collision [$f_{c,c\text{-}c}$]	6.1E8	$\# kg^{-1} min^{-1}$
Kolmogorov eddy length	440	μm

The boiling compartment in the calandria (heat exchanger) in the evaporator was established as a zone with high turbulence. High turbulence is caused either due to high flow velocities or due to steam bubble formation and subsequent bursting. The flow becomes two phase (the slurry of mother liquor and crystals is treated as single phase) once boiling starts. The change in flow quality (kg of steam per kg of steam-slurry mixture) along the length of pipe after the onset of boiling can be predicted using the model developed in Appendix III and is shown in Figure 6-39. The density, viscosity and two phase friction factor for the steam-slurry mixture were calculated using the correlations given in Appendix III (Equation III-2, III-24 and III-26). The calculated values of the various parameters for selected velocities in the boiling zone (from Figure 6-4) are shown in Table 6-4.

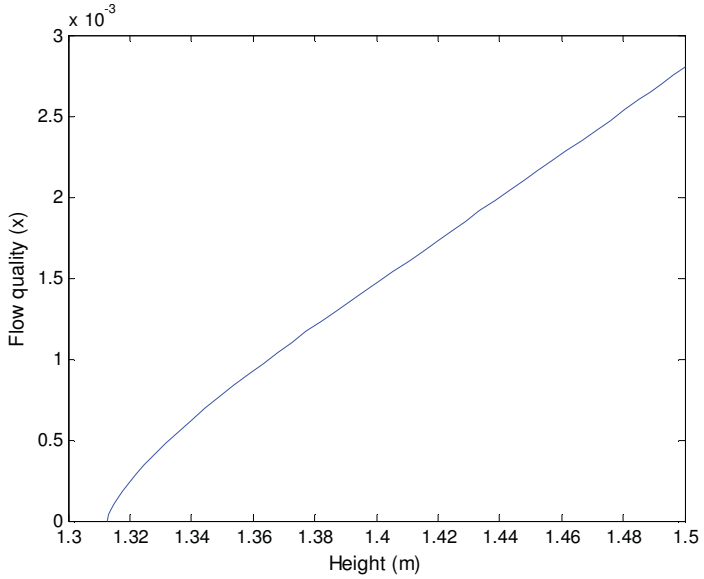


Figure 6-39. Variation of flow quality with the tube height in the calandria of the Kapuni FC evaporative crystallizer.

Table 6-4 *Values of Critical Parameters for Crystal-Crystal Contacts in the Calandria Pipes*

Slurry mean velocity through pipe [v]	5	6	7	8	m s^{-1}
Flow quality through the tube	0.0017	0.002	0.00225	0.0025	
Steam-slurry density mixture	73	62	56	50	kg m^{-3}
Steam-slurry mixture viscosity	5E-3	4.4E-3	4E-3	3.7E-3	kg s^{-1} m^{-1}
Reynolds number	3.64E3	4.25E3	4.88E3	5.49E3	
Friction factor [f]	1.05E-2	1.00E-2	9.68E-3	9.38E-3	
Wall shear stress [τ_w]	9.54	11.3	13.2	15.1	kg s^{-2} m^{-1}
Shear velocity [v_*]	0.36	0.43	0.49	0.59	m s^{-1}
Specific energy dissipation rate [ε]	52.4	86.8	133	193	m^2 s^{-3}
Specific turbulent kinetic energy [k]	0.2	0.27	0.36	0.45	m^2 s^{-2}
Eddy life time [t_e]	3.75E-3	3.13E-3	2.68E-3	2.34E-3	s
Crystal relaxation time [t_c]	1.59E-3	1.80E-3	1.97E-3	2.15E-3	s
Stokes number [ψ]	0.42	0.58	0.74	0.93	
$\frac{v\prime_c^2}{v\prime^2}$	0.94	0.93	0.92	0.91	
Crystal rms velocity [$v'_{c\text{-}c}$]	0.34	0.41	0.45	0.5	m s^{-1}
Kinetic energy of collision [$E_{k,c\text{-}c}$]	1.28E-9	1.71E-9	2.20E-9	2.72E-9	J
Collision frequency [$f_{c,c\text{-}c}$]	1.97E10	1.98E10	2.03E10	2.06E10	# kg^{-1} min^{-1}
Kolmogorov eddy length	281	252	230	212	μm
Nucleation rate	5.80E10	7.84E10	1.03E11	1.29E11	# kg^{-1} min^{-1}

The Stokes number is <1. This shows that the crystals will follow the flow fluctuations and the chance of collisions occurring due to inertia effect are very low. The Kolmogorov length, which represents the length of the smallest eddy in a system, are larger than the inter crystal space present in the slurry. Hence, these eddies at which the viscous dissipation of the turbulent energy occurs in pure fluid, cannot exist in the dense slurries. The kinetic energy of the turbulence is therefore dissipated in the form of crystal-crystal collisions (Eskin, Leonenko, & Vinogradov, 2004b). The kinetic energy of collision just exceeds the threshold level of 1.5E-9 J at the exit velocity of 6 m s^{-1}. Hence contact nucleation can occur in the boiling zone. A mass average crystal size (300 μm) was taken for calculation of kinetic energy. Any crystals below this size will not possess critical threshold kinetic energy and hence will not contribute to nucleation. Since the smaller size crystals will dominate the numbers, for better estimation of effective collision frequency, only the numbers of crystals greater than 300 μm are only considered.

Since no simulation runs were performed for crystal-crystal collisions, a direct comparison with other models is not possible. However, for the sake of evaluation, secondary nucleation rates due to crystal-crystal collisions were estimated from Equation 6-9 at the measured steady state supersaturation (8.4 g α-LMH per 100 g of water). Kinetic energy and frequency for crystal-crystal collisions in the calandria pipe are known from Table 6-4. Using the estimated value of K_N and b in the previously, calculated secondary nucleation rates are presented in Table 6-4.

In order to tie together all the findings of the thesis, the nucleation rates in the different zones of the crystallizer as identified in Figure 6-5 are discussed:

i) Nucleation rates in the main body of the calandria and the separator can be assumed to be negligible. The only feasible mechanism in these compartments is through crystal-crystal contact. It has been shown previously in this section that the collision energy is unlikely to reach the critical level required for secondary nucleation in the pipeline connecting the two zones. The average slurry velocity in the separator and the calandria will be smaller (due to their larger cross section areas) than the connecting pipe. Hence it is

improbable that the critical collision velocities will be reached in these compartments.

ii) Shear stresses during bubble rupture in the boiling zone can reach between 95-200 Nm^{-2} (corresponding shear rates of 95000-200000 s^{-1} for water). These are an order of magnitude higher than the shear rate of 10000 s^{-1}, above which the nucleation rate was observed to be independent in the shear nucleation study (Figure 4-13) at the supersaturation of 8.4 g of α-LMH per 100 g of water. However, it needs to be pointed that nucleation rates in the boiling zone can be much higher due to the presence of higher supersaturations at the liquid vapour interface than that in the bulk. An order of magnitude higher nucleation rates were observed at the higher supersaturation studied (Figure 4-13). The shear levels at the pump blade surface are orders of magnitude higher than those at the impeller outlet and can reach up to 1000000 s^{-1} (Wu, Graham, & Mehidi, 2006). Shear nucleation is therefore likely to occur in pump zone.

iii) Attrition will occur only in the pump zone and were estimated by the Mersmann model. Secondary nucleation rate due to attrition is not enough to account for the observed crystal size distribution and hence other nucleation mechanism are dominant. However, the Mersmann model has inherent assumptions as discussed previously. Lactose mechanical properties were calculated indirectly and it was assumed that all the generated fragments grew.

iv) The crystal-crystal contact nucleation values were completely based on theoretical analysis and needs to be considered with caution. If the reported crystal collision velocities have been overestimated by even 30%, the kinetic energy of collisions will drop below the kinetic energy threshold limit, ruling out any secondary nucleation. If the kinetic energy values do stand, then more accurate determination of collision frequency needs to be done for more precise estimation of nucleation rates due to crystal-crystal collisions.

The observations made during the few off plant trials are now explained in the light of above findings.

6.3.4 Plant trials

A couple of plant trials were conducted to quantify the effect of change of operational parameters on the crystal size. The hydrodynamic and the thermodynamic state of the system were altered by changing the circulation pump speed and the crystallizer temperature respectively. These trials were conducted on a different newly commissioned, evaporative crystallizer producing edible grade lactose.

The speed of the centrifugal pump was reduced by 50% and the evaporator set temperature incremented by 5 °C (compared to the normal operation) during the start up. In both cases no changes in the mean crystal size was observed. The refractive index (dissolved solids) trend for the trials at the two temperatures is shown in Figure 6-40. It can be seen that the refractive index increases during the batch mode, reaches a maxima and then decreases as nucleation and growth occurs. It then settles down to a constant steady state value. The steady state refractive index value (~ 61.3%) for the higher temperature trial was greater than that at the lower temperature (~ 59%). This is in agreement with the trends shown in the Figure 5-10 (a), which shows the effect of temperature on dissolved lactose concentration. No change in crystal size can be understood from the fact that supersaturation was found to be independent of temperature, as shown in Figure 5-10 (b). With no apparent change in the other parameter affecting nucleation rate, the hydrodynamics, the crystal size remained unchanged.

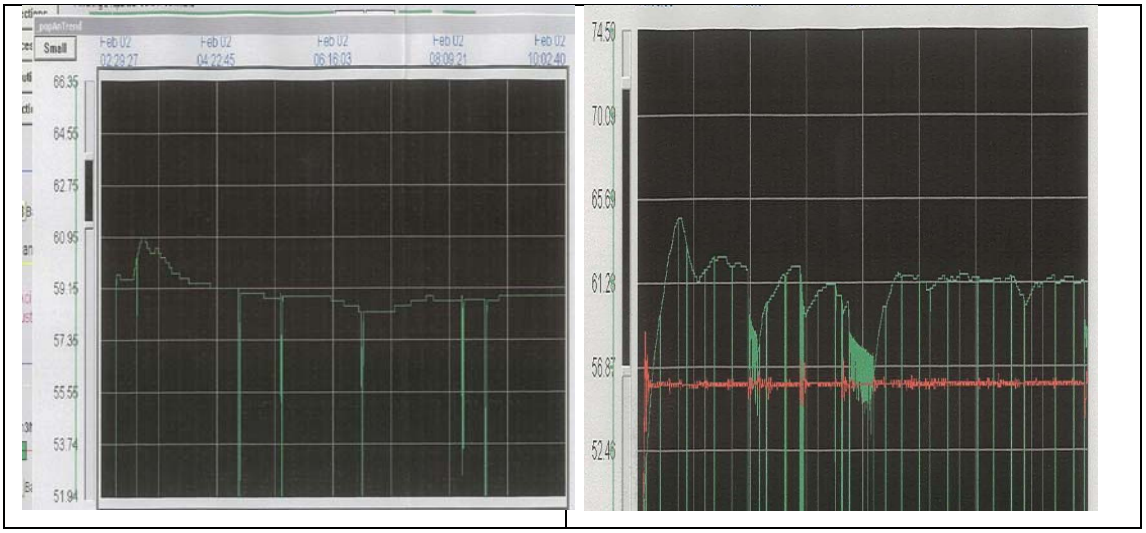


Figure 6-40. The refractive index (dissolved solids in wt %) trends for the plant trial conducted at two temperatures. The figure on the left gives trend for the lower temperature (standard operating temperature) and to the right is for the higher temperature used during the trial.

One off trial at reduced speed (50% of the normal) was also conducted on the Kapuni FC evaporative crystallizer. No change in crystal size was observed. Absence of the impact of pump speed on crystal size can be explained in two possible ways:

i) The crystal-impeller contact nucleation is not the controlling nucleation mechanism. Attrition has also been shown not to be a significant contributor. The boiling zone in the crystallizer provided conditions conducive for shear nucleation; high shear rates (bubble bursting) and high supersaturation (liquid-vapour interface). An order of magnitude higher nucleation rates were observed at the higher supersaturation as shown in Figure 4-13 and thus it is possible that shear nucleation becomes the leading source of nucleation. Hydrodynamics of the boiling zone should be independent of the pump speed. This suggests that manipulating the nucleation rates and hence the crystal size is not possible by changing the pump speed.

ii) In the second scenario, crystal-impeller contact nucleation still remains the dominant mechanism. However, it is likely that at a certain kinetic energy of contact all the clusters at the crystal surface are cleaved off and above which no increase in contact nucleation will be observed. In other words, contact nucleation will become independent of collision energy. It is thus possible that even at the reduced speed the operation of the crystallizer remains in the realm where contact nucleation rate is independent of the pump speed. This needs to be further looked into.

It is clear that the chances of manipulating the secondary nucleation rate through hydrodynamics are limited. Thermodynamics however seems to provide a window of opportunity. It needs to be clarified that this trial was not planned. The trends were observed during the collection of data for the one off circulation pump speed reduction trial at Kapuni site. It was found that the FC crystallizer was producing larger crystals (shown by the blue line in the Figure 6-41); D[4,3] of 470 μm compared to ~320 μm produced on a regular basis. The temperature and the pump speed were the same as during normal operation. The only aberration was a lower concentration feed (50% lower than that during normal operation) being fed to the evaporative crystallizer for the last few hours due to some operational issues. After

the normal feed resumed, samples were drawn and analyzed after approximately three and four hours (the green and the red line, respectively in the Figure 6-41). It can be seen that the bigger sized particles progressively diminished (being washed out of the system) whereas smaller ones formed (more nucleation) and then grew.

This showed that resorting to the normal feed induced higher nucleation levels (normal in terms of crystallizer operation). Primary nucleation can be ruled out as the feed is unsaturated when entering the crystallizer under normal conditions. It is thought that the mixing between the circulating slurry and the feed is not instantaneous, leading to localized dilution of the bulk supersaturation level in the slurry prior to reaching the pump. When the lower concentration feed was fed, the dilution would have been greater than that during normal operation, locally reducing the supersaturation. A very high order of dependence of supersaturation (8.4) on secondary nucleation rate was observed in the current study. This means a small drop in the supersaturation will lead to a big drop in secondary nucleation rate due to crystal-impeller collisions at the pump.

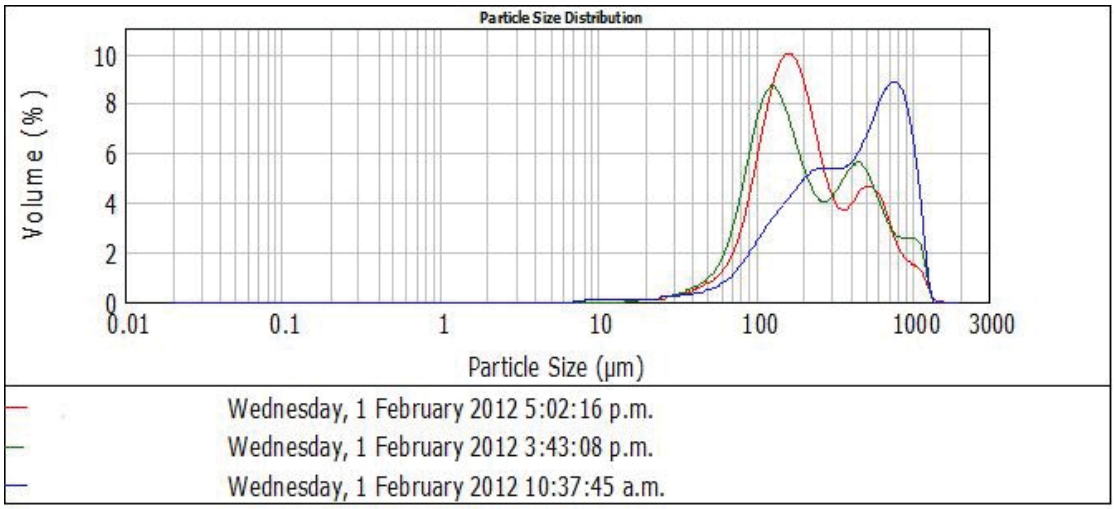


Figure 6-41. Observed crystal size distribution during unplanned one off trial. Blue line depicts the CSD with the lower feed concentration. Normal feed resumed around midday. Green and red lines depict CSD after approximately 3 and 4 hours of resumption of normal feed.

6.4 Conclusions

This chapter dealt with quantification of the hydrodynamics of industrial crystallizers. It was found that the current crystallizer fulfils criteria to be a mixed suspension crystallizer with two zones of high turbulence: calandria tubes and the circulation pump; where bulk of the secondary nucleation can be expected to occur.

The mathematical model in Chapter 5 was further developed to predict the complete crystal size distribution. A SDG model was implemented to account for the upward curvature in the population density curve and was found to be the reason for the transient decay dynamics exhibited by the crystallizer. SIG simulations showed no dampening oscillatory behaviour. The crystallizer model parameters were obtained by fitting the plant data to the model predictions using the learning from the sensitivity analysis of Chapter 5. The model based on optimized parameters correctly predicted the steady state crystal size distribution. The mean crystal size predictions, although relatively poorly matched compared to other parameters, followed the measured trends.

Simulations using the mechanistic model for attrition induced nucleation were performed. Values of the parameters in the mechanistic contact nucleation model were determined from the experimental work described in section 4.2. Simulations were also performed using these values. It was found that attrition, based on the estimated lactose mechanical properties, is unlikely to be the only source of secondary nucleation in lactose crystallization. The impeller-crystal contact model predicted closely the dissolved lactose profile. However, it under estimated the mean crystal size and showed more intense oscillatory dynamics than that of the plant. Nucleation due to crystal-crystal collisions can occur in the boiling zone of the calandria tubes. However, their exact magnitude is not certain and needs further study with advanced simulation tools. Shear nucleation can be an important source of nuclei in the boiling zone and needs further investigation.

Chapter 7 Project Review

This chapter reviews the contribution of this work to the current body of knowledge on crystallization in general and nucleation in particular of lactose. Recommendations for future work are included wherever appropriate.

The main highlights of the research are:

I. This is the first investigation looking into evaporative lactose crystallization on an industrial scale.

II. The research focused on the secondary nucleation aspect of the crystallization process as it is known to be the dominant source of new nuclei in industrial crystallizers (Chapter 3 and Chapter 4). Based on the critical review (Chapter 3) of the existing literature on secondary nucleation, the following three mechanisms relevant to the current system were identified; (i), attrition (ii), contact/collision nucleation (iii), shear nucleation. The experimental section (Chapter 4) studied each mechanism independently with no interference or pollution by the others.

III. Attrition studies were conducted in a non-solvent for solute (methanol) i.e. in absence of any supersaturation to prevent the other two mechanisms from occurring simultaneously. Attrition was found to be most affected by kinetic energy of collision, manifesting itself in the form of impeller speed and the crystal size. Contact nucleation trials were conducted under mild stirring conditions to minimize attrition and shear nucleation. It was found that there exists a lower value of kinetic energy below which no nucleation is expected to occur. When expressed in terms of kinetic energy and collision frequency all the data points for different crystal sizes, concentrations and impeller speeds collapsed onto a single curve. This is the first time that has been shown to be the case. No measurable levels of attrition or primary nucleation occurred showing that contact nucleation was the dominant mechanism at play. A preliminary investigation on shear nucleation was undertaken. Crystals were in an immobilized state during the trials to prevent the above two mechanisms, promoted by crystal collisions. The magnitude of shear

nucleation was an order of magnitude lower than contact nucleation at the same supersaturations. For the bulk supersaturation at which the studied crystallizer operates, shear nucleation can be neglected. Contact nucleation is thus likely to become the dominant mechanism due to its occurrence at much milder conditions than those required for attrition.

IV. A model describing the operation of the studied crystallizer was developed. The model development was done in two stages. The first stage involved the development of the model using the method of moments (Chapter 5). In spite of the limitations posed by the MOM, it provides desired information for the current system and was used in conducting a sensitivity analysis of the different operating parameters. In the second stage, the method of lines (MOL), which involves discretization of the size domain, was used. This allowed incorporating size dependent growth rate into the model and replicating the exact CSD from the crystallizer (Chapter 6). The discretized model was also able to closely follow the decaying oscillation trend shown by the industrial crystallizer.

V. Hydrodynamic analysis of the crystallizer was undertaken based on available literature. Simulations based on mechanistic secondary nucleation models for attrition and contact mechanisms were conducted and compared to the fitted value. Few plant trials were also conducted and the results were explained on the basis of the findings in this study. It was concluded that the majority of secondary nucleation would occur in the boiling zone and the circulating pump.

Recommended research areas arising from this work are:

I. The hydrodynamics of the system are the critical factor controlling nucleation and thus the CSD. Development of hydrodynamic models was out of scope of this work. Only the existing model for predicting attrition due to crystal-impeller collisions was used in the simulation runs. An accurate prediction of crystal-crystal collision velocity and frequency in high solid laden slurry is very difficult. This is required for correct estimation of collision nucleation. Further research is required in this field. This also includes computational

fluid dynamic study of the industrial crystallizer to determine the hydrodynamic conditions prevailing in the various parts of the crystallizer.

II. It is likely that at a certain maximum kinetic energy of contact all the clusters at the surface will be cleaved off and above which no increase in contact nucleation will be observed. In other words, contact nucleation will become independent of collision energy. This is postulated based on trials at the end of the study in which reducing the pump speed did not bring any increase in crystal size. It is possible that the operation of the crystallizer is in the realm where contact nucleation rate is independent of the pump speed. This needs to be further looked into.

III. The boiling interface was identified as a potential dominant nuclei producing zone. High supersaturation together with high shear rates provides a conducive environment for nuclei generation and thus requires separate investigation.

Nomenclature

B	Secondary nucleation rate	[# min^{-1} (kg of slurry)$^{-1}$]
B_p	Primary nucleation rate	[# min^{-1} (kg of slurry)$^{-1}$]
C_α	Dissolved α- lactose concentration	[kg (kg of solution)$^{-1}$]
C_β	Dissolved β-lactose concentration	[kg (kg of solution)$^{-1}$]
$C_{\alpha s}$	Equilibrium solubility of α-lactose	[kg (kg of solution)$^{-1}$]
C_{LS}	Equilibrium solubility of lactose	[kg (kg of water)$^{-1}$]
C	Total dissolved lactose concentration	[kg (kg of solution)$^{-1}$]
C_c	Crystal content of slurry	[kg (kg of slurry)$^{-1}$]
D	Tube diameter	[m]
D[4,3]	Volumetric weighted mean diameter	[μm]
E_k	Kinetic energy	[kg m^2 s^{-2}]
F	Correction factor for α-LMH solubility	
G	Growth rate	[m min^{-1}] or [μm min^{-1}]
G_e	Effective size independent growth rate	[μm min^{-1}]
ΔH	Height difference	[m]
K_m	Mutarotation rate constant	
K_D	Impeller discharge coefficient	
K_N	Collision nucleation rate constant	[J^{-1} ((g of α-LMH) (100 g of water)$^{-1}$)$^{-b}$]
L	Bin size / Crystal size	μm
K_{mech}	Attrition rate constant	[# J^{-1}]
L_e	Smallest eddy length	[μm] / [m]
$L_{inertial}$	Inertial subrange eddy length	[μm] / [m]
M	Mass of slurry in the crystallizer	[(kg of slurry)]
N_i	Impeller speed	[min^{-1}] or [s^{-1}]
N_T	Total number of crystals per unit of slurry	[# (kg of slurry)$^{-1}$]
ΔP	Pressure drop	[kg m^{-1} s^{-2}]
Q	Slurry flow rate	[(kg of slurry) min^{-1}]
T	Crystallizer temperature	[° C]
T_L	Target length in Stokes number definition	[m]

a,c	Parameters in size dependent growth rate model	
b	Secondary nucleation rate order	
d_p	Pipe diameter	[m]
d_i	Impeller diameter	[m]
d_c	Mean crystal size/ diameter	[m] or [μm]
f	Fanning friction factor	
f_c	Collision frequency	[# min^{-1} (kg of slurry)$^{-1}$]
$f_{c,i-c}$	Impeller-crystal collision frequency	[# min^{-1} (kg of slurry)$^{-1}$]
$f_{c,c-c}$	Crystal-crystal collision frequency	[# min^{-1} (kg of slurry)$^{-1}$]
g	Growth rate order	
w	Relative kinetic order	
j	Crystal content exponential dependence	
k	Specific turbulent kinetic energy	[kg m^2 s^{-2}]
l	Tube or pipe length	[m]
k_{evap}	Evaporation rate	[kg min^{-1}]
$k_{n,p}$	Primary nucleation rate constant	[# min^{-1} (kg of slurry)$^{-1}$((kg of α-LMH) (kg of water)$^{-1}$)$^{-b}$]
$k_{n,s}$	Empirical secondary nucleation rate constant	[# min^{-1} (kg of crystal)$^{-1}$((kg of α-LMH) (kg of water)$^{-1}$)$^{-b}$]
k_g	Growth rate constant	[μm min^{-1} ((kg of α-LMH)(kg of water)$^{-1}$)$^{-g}$]
m	Mass of single crystal	[kg]
m_0	0th moment of CSD	[# (kg of slurry)$^{-1}$]
m_1	1st moment of CSD	[m (kg of slurry)$^{-1}$]
m_2	2nd moment of CSD	[m^2 (kg of slurry)$^{-1}$]
m_3	3rd moment of CSD	[m^3 (kg of slurry)$^{-1}$]
m_4	4th moment of CSD	[m^4 (kg of slurry)$^{-1}$]
n(L)	Population density of crystal size *L*	[# (kg of slurry)$^{-1}$ $μm^{-1}$]
n_B	Number of blades	
n_o	Population density of zero sized crystals	[# $μm^{-1}$ (kg of slurry)$^{-1}$]
n_p	Primary nucleation rate order	
n_c	Crystal concentration	[# (kg of slurry)$^{-1}$]
t	Time	[min] or [s]

t_e	Turbulent eddy life time	
v	Velocity	[m s^{-1}]
v_e	Smallest eddy velocity	[m s^{-1}]
v'	Root mean square velocity	[m s^{-1}]
v_*	Friction velocity	[m s^{-1}]
$v_{inertial}$	Velocity scale of inertial subrange eddy	[m s^{-1}]
v_{i-c}	Impeller-crystal collision velocity	[m s^{-1}]
v_{c-c}	Crystal-crystal collision velocity	[m s^{-1}]
v_{rel}	Relative velocity between the impeller and the crystal	[m s^{-1}]
v_s	Solution velocity	[m s^{-1}]

Greek Symbols

α	Volume of crystals per unit mass of slurry	[(m^3 of crystal) (kg of slurry)$^{-1}$]
μ_S	Slurry dynamic viscosity	[kg m^{-1} s^{-1}]
μ_s	Lactose solution viscosity	[kg m^{-1} s^{-1}]
ν_S	Slurry kinematic viscosity	[m^2 s^{-1}]
η	Target efficiency for crystal-impeller collisions	
ε	Energy dissipation rate per unit mass	[m^2 s^{-3}]
ρ_c	Crystal density	[kg m^{-3}]
ρ_s	Lactose solution density	[kg m^{-3}]
ρ_S	Slurry density	[kg m^{-3}]
φ	Void fraction of slurry	[(kg of lactose solution) (kg of slurry)$^{-1}$]
1- φ	Crystal content of slurry	[(kg of crystalline lactose) (kg of slurry)$^{-1}$]
τ	Residence time	[min]
τ_w	Wall shear stress	[kg m^{-1} s^{-2}]
σ	supersaturation	[(g of α-LMH) (100 g of water)$^{-1}$] or [(kg of α-LMH) (kg of water)$^{-1}$]
χ	Effective nucleation factor in secondary nucleation due to attrition	
ψ	Stokes number	
γ	Shear rate	[s^{-1}]

δ	Inter-particle space in a slurry	[μm]

Subscripts

f	Inlet/Feed stream
o	Outlet/Product stream
i-c	Impeller-crystal
c-c	Crystal-crystal
c	Crystal
s	Lactose solution
S	Slurry

Abbreviations

CSD	Crystal Size Distribution
CV	Coefficient of Variation of a CSD
MOL	Method of Lines
MOM	Method of Moments
MSMPR	Mixed Suspension Mixed Product Removal crystallizer
ODEs	Ordinary Differential Equations
PDEs	Partial Differential Equations
DAI	Differential Attrition Index
GRD	Growth Rate Dispersion
SDG	Size dependent Growth
VAR	Volumetric Attrition Rate
Re	Reynolds number
N_p	Power number
α-LMH	α-Lactose Monohydrate
nCSD	Normalized Crystal Size Distribution
TS	Total Solids

References

Abbas, A., & Romagnoli, J. A. (2007). Multiscale modeling, simulation and validation of batch cooling crystallization. *Separation and Purification Technology, 53*(2), 153-163.

Abrahamson, J. (1975). Collision rates of small particles in a vigorously turbulent fluid. *Chemical Engineering Science, 30*(11), 1371-1379.

Abulnaga, B. E. (2002). Slurry systems handbook (pp. 1.22): McGraw-Hill.

Arellano, M. P., Aguilera, J. M., & Bouchon, P. (2004). Development of a digital video-microscopy technique to study lactose crystallisation kinetics in situ. *Carbohydrate Research, 339*(16), 2721-2730.

Arneth, S., & Stichlmair, J. (2001). Characteristics of thermosiphon reboilers. *International Journal of Thermal Sciences, 40*(4), 385-391.

Awad, M. M., & Muzychka, Y. S. (2008). Effective property models for homogeneous two-phase flows. *Experimental Thermal and Fluid Science, 33*(1), 106-113.

Barbosa-Cánovas, G. V., Ortega-Rivas, E., Juliano, P., & Yan, H. (2005). *Food powders : Physical properties, processing, and functionality*. New York London: Kluwer Academic/Plenum.

Bemrose, C. R., & Bridgwater, J. (1987). A review of attrition and attrition test methods. *Powder Technology, 49*(2), 97-126.

Bennet, R. C. (2002). Crystallizer selection and design. In A. S. Myerson (Ed.), *Handbook of industrial crystallization*: Butterworth-Heinemann.

Bennett, R. C., Fiedelman, H., & Randolph, A. D. (1973). Crystallizer influenced nucleation. *Chemical engineering Progress, 69*(7), 86-93.

Bermingham, S. K., Kramer, H. J. M., & van Rosmalen, G. M. (1998a). Towards on-scale crystalliser design using compartmental models. *Computers & Chemical Engineering, 22*(Supplement 1), S355-S362.

Bermingham, S. K., Neumann, A. M., Muusze, J. P., Kramer, H. J. M., & Verheijen, P. J. T. (1998b). Modelling the settling, dissolution and non-uniform nucleation kinetics in a 150-litre forced circulation crystallizer. *Particle & Particle Systems Characterization, 15*(1), 56-61.

Bhat, H. L., Sherwood, J. N., & Shripathi, T. (1987). The influence of stress, strain and fracture of crystals on the crystal growth process. *Chemical Engineering Science, 42*(4), 609-618.

Biscans, B. (2004). Impact attrition in crystallization processes. Analysis of repeated impacts events of individual crystals. *Powder Technology, 143-144*, 264-272.

Biscans, B., Chemini, R., Guiraud, P., & Laguerie, C. (1996a). Design of an attrition experiment to simulate the effects of crystal-wall or crystal-stirrer impacts occurring in a crystallizer. *Powder Technology, 86*(2), 155-161.

Biscans, B., Guiraud, P., Laguérie, C., Massarelli, A., & Mazzarotta, B. (1996b). Abrasion and breakage phenomena in mechanically stirred crystallizers. *The Chemical Engineering Journal and the Biochemical Engineering Journal, 63*(2), 85-91.

Blem, K. E., & Ramanarayanan, K. A. (1987). Generation and growth of secondary ammonium dihydrogen phosphate nuclei. *AIChE Journal, 33*(4), 677-680.

Botsaris, G. D., Qian, R.-Y., & Barrett, A. (1999). New insights into nucleation through chiral crystallization. *AIChE Journal, 45*(1), 201-203.

Bravi, M., Di Cave, S., Mazzarotta, B., & Verdone, N. (2003). Relating the attrition behaviour of crystals in a stirred vessel to their mechanical properties. *Chemical Engineering Journal, 94*(3), 223-229.

Broz, J., Fort, I., Sperling, R., Heiser, M., & Rieger, F. (2004). Pumping capacity of pitched blade impellers in a tall vessel with a draught tube. *Acta Polytechnica 44*(4), 48-53.

Bubnik, Z., Kadlec, P., Urban, D., & Bruhns, M. (1995). *Sugar technologists manual. Chemical and physical data for sugar manufacturers and users*. Berlin: Bartens Pub. Co.

Buma, T. J. (1980). Viscosity and density of concentrated lactose solutions and of concentrated cheese whey. *Netherland Milk and Dairy Journal, 34*, 65-68.

Butler, B. K. (1998). *Modelling industrial lactose crystallization.* PhD, The University of Queensland, Brisbane.

Chalmers, J. J., & Bavarian, F. (1991). Microscopic visualization of insect cell-bubble interactions. II: The bubble film and bubble rupture. *Biotechnology Progress, 7*(2), 151-158.

Chen, N. H. (1979). An explicit equation for friction factor in pipe. *Industrial & Engineering Chemistry Fundamentals, 18*(3), 296-297.

Cherry, R. S., & Hulle, C. T. (1992). Cell death in the thin films of bursting bubbles. *Biotechnology Progress, 8*(1), 11-18.

Cherry, R. S., & Papoutsakis, E. T. (1986). Hydrodynamic effects on cells in agitated tissue culture reactors. *Bioprocess and Biosystems Engineering, 1*(1), 29-41.

Clontz, N. A., & McCabe, W. L. (1971). Contact nucleation of magnesium sulphate heptahydrate. *Chemical Engineering Symposium Series No. 110, 67*, 6-17.

Crawley, G. M., Gruy, F., & Cournil, M. (1996). In-line study of crystal fragmentation in a stirred reactor. *Chemical Engineering Science, 51*(20), 4537-4550.

Dincer, T. D., Ogden, M. I., & Parkinson, G. M. (2009a). Crystal growth mechanisms of the (0 1 0) face of [alpha]-lactose monohydrate crystals. *Journal of Crystal Growth, 311*(8), 2427-2432.

Dincer, T. D., Ogden, M. I., & Parkinson, G. M. (2009b). In situ investigation of growth rates and growth rate dispersion of [alpha]-lactose monohydrate crystals. *Journal of Crystal Growth, 311*(5), 1352-1358.

Dorofeeva, M., Kol'tsova, E., & Gordeev, L. (2006). Investigation and mathematical modeling of attrition. *Theoretical Foundations of Chemical Engineering, 40*(4), 372-378.

Elankovan, P., & Berglund, K. A. (1987). Contact nucleation from aqueous dextrose solutions. *AIChE Journal, 33*(11), 1844-1849.

Eskin, D., Leonenko, Y., & Vinogradov, O. (2004a). On a turbulence model for slurry flow in pipelines. *Chemical Engineering Science, 59*(3), 557-565.

Eskin, D., Leonenko, Y., & Vinogradov, O. (2004b). Theoretical estimates of air bubble behavior in dense pipeline slurry flows. *Chemical Engineering and Processing, 43*(6), 727-737.

Estrin, J., Wang, M. L., & Youngquist, G. R. (1975). Secondary nucleation due to fluid forces upon a polycrystalline mass of ice. *AIChE Journal, 21*(2), 392-395.

Farshad, F., Rieke, H., & Garber, J. (2001). New developments in surface roughness measurements, characterization, and modeling fluid flow in pipe. *Journal of Petroleum Science and Engineering, 29*(2), 139-150.

Friej, S., Reyhani, M. M., & Parkinson, G. M. (1998). An AFM investigation of the mechanism of secondary nucleation induced by contact. *Applied Physics A: Materials Science & Processing, 66*, S507.

Gahn, C., & Mersmann, A. (1995). The brittleness of substances crystallized in industrial processes. *Powder Technology, 85*(1), 71-81.

Gahn, C., & Mersmann, A. (1997). Theoretical prediction and experimental determination of attrition rates. *Chemical Engineering Research and Design, 75*(2), 125-131.

Gahn, C., & Mersmann, A. (1999a). Brittle fracture in crystallization processes part a. Attrition and abrasion of brittle solids. *Chemical Engineering Science, 54*(9), 1273-1282.

Gahn, C., & Mersmann, A. (1999b). Brittle fracture in crystallization processes part b. Growth of fragments and scale-up of suspension crystallizers. *Chemical Engineering Science, 54*(9), 1283-1292.

Garside, J. (1985). Industrial crystallization from solution. *Chemical Engineering Science, 40*(1), 3-26.

Garside, J., & Davey, R. J. (1980). Invited review secondary contact nucleation: Kinetics, growth and scale-up. *Chemical Engineering Communications, 4*(4), 393 - 424.

Garside, J., Rusli, I. T., & Larson, M. A. (1979). Origin and size distribution of secondary nuclei. *AIChE Journal, 25*(1), 57-64.

Geankoplis, C. J. (2004) *Transport processes and unit operations*
New Delhi: Prentice Hall of India.

Genck, W. J. (2003, June). Optimizing crystallizer scaleup. *Chemical Engineering Progress,* 36-44.

Green, D. (2002). Crystallizer mixing: Understanding and modelling crystallizer mixing and suspension flow. In A. S. Myerson (Ed.), *Handbook of industrial crystallization*: Butterworth-Heinemann.

Griffin, D. W., Mellichamp, D. A., & Doherty, M. F. (2010). Reducing the mean size of API crystals by continuous manufacturing with product classification and recycle. *Chemical Engineering Science, 65*(21), 5770-5780.

Griffiths, R. C., Paramo, G., & Merson, R. L. (1982). Preliminary investigation of lactose crystallization using the population balance technique. *AIChE Symposium Series No. 218, 718*, 118-128.

Hunziker, O. F. (1949). *Condensed milk and milk powder* (7th ed.). La Grange, Illinois: Hunziker.

Jagannathan, R., Sung, C. Y., Youngquist, G. R., & Estrin, J. (1980). Fluid shear secondary nucleation of magnesium sulfate and potassium aluminium sulfate. *AIChE Symposium Series, 76*, 90.

Jelen, P., & Coulter, S. T. (1973). Effects of supersaturation and temperature on the growth of lactose crystals. *Journal of Food Science, 38*(7), 1182-1185.

Johnson, R. T., Rosseau, R. W., & McCabe, W. L. (1972). Factors affecting contact nucleation. *AIChE Symposium Series No. 121, 68*, 31.

Jones, A. G. (2002). Crystallization process systems: Butterworth Heinemann.

Kauter, M. D. (2003). *The effect of impurities on lactose crystallization.* PhD, University of Queensland, St. Lucia.

Kramer, H. J. M., Bermingham, S. K., & van Rosmalen, G. M. (1999). Design of industrial crystallisers for a given product quality. *Journal of Crystal Growth, 198-199*(Part 1), 729-737.

Kramer, H. J. M., Dijkstra, J. W., Neumann, A. M., Ó Meadhra, R., & van Rosmalen, G. M. (1996). Modelling of industrial crystallizers, a compartmental approach using a dynamic flow-sheeting tool. *Journal of Crystal Growth, 166*(1-4), 1084-1088.

Kramer, H. J. M., Dijkstra, J. W., Verheijen, P. J. T., & Van Rosmalen, G. M. (2000). Modeling of industrial crystallizers for control and design purposes. *Powder Technology, 108*(2-3), 185-191.

Kubota, N., & Kubota, K. (1982). Contact nucleation of MgSO4 · 7H2O at low impact energy levels. *Journal of Crystal Growth, 57*(2), 211-215.

Lakatos, B. l. G., Sapundzhiev, T. J., & Garside, J. (2007). Stability and dynamics of isothermal CMSMPR crystallizers. *Chemical Engineering Science, 62*(16), 4348-4364.

Larson, M. A., White, E. T., Ramanarayanan, K. A., & Berglund, K. A. (1985). Growth rate dispersion in MSMPR crystallizers. *AIChE Journal, 31*(1), 90-94.

Liang, B., Hartel, R. W., & Berglund, K. A. (1987). Growth rate dispersion in seeded batch sucrose crystallization. *AIChE Journal, 33*(12), 2077-2079.

Liang, B., Shi, Y., & Hartel, R. W. (1991). Growth rate dispersion effects on lactose crystal size distributions from a continuous cooling crystallizer. *Journal of Food Science, 56*(3), 848-854.

Lifran, E. V., Vu, T. T. L., Durham, R. J., Hourigan, J. A., & Sleigh, R. W. (2007). Crystallisation kinetics of lactose in the presence of lactose phosphate. *Powder Technology, 179*(1-2), 43-54.

Lim, S. G., & Nickerson, T. A. (1973). Effect of methanol on the various forms of lactose. *J. Dairy Sci., 56*(7), 843-848.

Malave-Lopez, J., & Peleg, M. (1986). Patterns of size distribution changes during the attrition of instant coffees. *Journal of Food Science, 51*(3), 691-694.

Markande, A., Nezzal, A., Fitzpatrick, J. J., & Aerts, L. (2009). Investigation of the crystallization kinetics of dextrose monohydrate using in situ particle size and supersaturation monitoring. *Particulate Science and Technology, 27*(4), 373-388.

McBride, J. M., & Carter, R. L. (1991). Spontaneous resolution by stirred crystallization. *Angewandte Chemie, 103*(3), 298-300.

McLeod, J. (2007). *Nucleation and growth of alpha lactose monohydrate.* PhD Thesis, Massey University.

Meier, M., John, E., Wieckhusen, D., Wirth, W., & Peukert, W. (2009). Influence of mechanical properties on impact fracture: Prediction of the milling behaviour of pharmaceutical powders by nanoindentation. *Powder Technology, 188*(3), 301-313.

Menacho, J. M. (1986). Some solutions for the kinetics of combined fracture and abrasion breakage. *Powder Technology, 49*(1), 87-95.

Mersmann, A. (2001a). Attrition and attrition controlled secondary nucleation. In A. Mersmann (Ed.), *Crystallization technology handbook* (Second ed.). New York: Marcel Dekker.

Mersmann, A. (Ed.). (2001b). *Crystallization technology handbook* (2nd ed.): CRC Press.

Mersmann, A., Sangl, R., Kind, M., & Pohlisch, J. (1988). Attrition and secondary nucleation in crystallizers. *Chemical Engineering & Technology 11*(1), 80-88.

Mimouni, A., Schuck, P., & Bouhallab, S. (2009). Isothermal batch crystallization of alpha-lactose: A kinetic model combining mutarotation, nucleation and growth steps. *International Dairy Journal, 19*(3), 129-136.

Mydlarz, J. (1996). Modelling of growth rate for MSMPR crystallizer data. *Crystal Research and Technology, 31*(5), 541-565.

Mydlarz, J., & Briedis, D. (1992). Growth rate dispersion vs size-dependent growth rate for MSMPR crystallizer data. *Computers & Chemical Engineering, 16*(9), 917-922.

Mydlarz, J., & Jones, A. G. (1993). On the estimation of size-dependent crystal growth rate functions in MSMPR crystallizers. *The Chemical Engineering Journal and the Biochemical Engineering Journal, 53*(2), 125-135.

Myerson, A. S., & Ginde, R. (2001). Crystals, crystal growth, and nucleation. In A. S. Myerson (Ed.), *Handbook of industrial crystallization* (Second ed., pp. 47): Butterworth-Heinemann.

Nagata, S. (1975). *Mixing - pinciples and applications*. New York: Halsted Press.

Neumann, A. M. (2001). *Characterizing industrial crystallizers of different scale and type.* PhD, Delft University of Technology, Delft, Netherland.

Ó Meadhra, R., Kramer, H. J. M., & van Rosmalen, G. M. (1995). Size dependent growth behaviour related to the mosaic spread in ammonium sulphate crystals. *Journal of Crystal Growth, 152*(4), 314-320.

Oroskar, A. R., & Turian, R. M. (1980). The critical velocity in pipeline flow of slurries. *AIChE Journal, 26*(4), 550-558.

Ostwald, W. (1897). Studien uber die bildung und umwandlung fester korper. *Zeitschrift fur Physilische Chemie 22*, 289-330.

Ottens, E. P. K., & de Jong, E. J. (1973). A model for secondary nucleation in a stirred vessel cooling crystallizer. *Industrial & Engineering Chemistry Fundamentals, 12*(2), 179-184.

Perkins, M., Ebbens, S. J., Hayes, S., Roberts, C. J., Madden, C. E., Luk, S. Y., et al. (2007). Elastic modulus measurements from individual lactose particles using atomic force microscopy. *International Journal of Pharmaceutics, 332*(1-2), 168-175.

Ploß, R., & Mersmann, A. (1989). A new model of the effect of stirring intensity on the rate of secondary nucleation. *Chemical Engineering & Technology 12*(1), 137-146.

Pohlisch, J., & Mersmann, A. (1988). The influence of stress and attrition on crystal size distribution. *Chemical Engineering & Technology 11*(1), 40-49.

Pope, S. B. (2000). *Turbulent flows*. Cambridge: Cambridge University Press.

Qian, R.-Y., & Botsaris, G. D. (1996). Laboratory simulation of industrial crystallizer cycling. *Industrial & Engineering Chemistry Research, 35*(4), 1163-1172.

Qian, R.-Y., & Botsaris, G. D. (1997). A new mechanism for nuclei formation in suspension crystallizers: The role of interparticle forces. *Chemical Engineering Science, 52*(20), 3429-3440.

Qian, R.-Y., & Botsaris, G. D. (1998). Nuclei breeding from a chiral crystal seed of $NaClO_3$. *Chemical Engineering Science, 53*(9), 1745-1756.

Quintana-Hernández, P., Bolaños-Reynoso, E., Miranda-Castro, B., & Salcedo-Estrada, L. (2004). Mathematical modeling and kinetic parameter estimation in batch crystallization. *AIChE Journal, 50*(7), 1407-1417.

Randolph, A. D., & Larson, M. A. (1988). *Theory of particulate processes*. San Diego: Academic Press.

Reyhani, M. M., Freij, S., & Parkinson, G. M. (1999). In situ atomic force microscopy investigation of the growth of secondary nuclei produced by contact of different growth faces of potash alum crystals under supersaturated solutions. *Journal of Crystal Growth, 198-199*(Part 1), 258-263.

Reyhani, M. M., & Parkinson, G. M. (1996). A comparison of secondary nuclei produced by contact of different growth faces of potash alum crystals under supersaturated solutions. *Journal of Crystal Growth, 166*(1-4), 1068-1073.

Rielly, C. D., & Marquis, A. J. (2001). A particle's eye view of crystallizer fluid mechanics. *Chemical Engineering Science, 56*, 2475-2493.

Ristic, R. I., Sherwood, J. N., & Wojciechowski, K. (1988). Assessment of the strain in small sodium chlorate crystals and its relation to growth rate dispersion. *Journal of Crystal Growth, 91*(1-2), 163-168.

Roetman, K., & Buma, T. J. (1974). Temperature dependence of the equilibrium β/α ratio of lactose in aqueous solution. *Netherland Milk and Dairy Journal, 28*, 155-165.

Rusli, I. T., Larson, M. A., & Garside, J. (1980). Initial growth of secondary nuclei produced by contact nucleation. *AIChE Symposium Series, 76*(193), 52-58.

Serra, T., Colomer, J., & Casamitjana, X. (1997). Aggregation and breakup of particles in a shear flow. *Journal of Colloid and Interface Science, 187*(2), 466-473.

Shah, N. O., & Nickerson, T. A. (1978). Functional properties of hydrolyzed lactose: Solubility, viscosity and humectant properties. *Journal of Food Science, 43*(4), 1081-1084.

Shi, Y., Hartel, R. W., & Liang, B. (1989). Formation and growth phenomena of lactose nuclei under contact nucleation conditions. *J. Dairy Sci., 72*(11), 2906-2915.

Shi, Y., Liang, B., & Hartel, R. W. (1990). Crystallization kinetics of alpha-lactose monohydrate in a continuous cooling crystallizer. *Journal of Food Science, 55*(3), 817-820.

Shiau, L.-D. (2003). The distribution of dislocation activities among crystals in sucrose crystallization. *Chemical Engineering Science, 58*(23-24), 5299-5304.

Sung, C. Y., Estrin, J., & Youngquist, G. R. (1973). Secondary nucleation of magnesium sulfate by fluid shear. *AIChE Journal, 19*(5), 957-962.

Synowiec, P., Jones, A. G., & Ayazi Shamlou, P. (1993). Crystal break-up in dilute turbulently agitated suspensions. *Chemical Engineering Science, 48*(20), 3485-3495.

Tai, C. Y., McCabe, W. L., & Rousseau, R. W. (1975). Contact nucleation of various crystal types. *AIChE Journal, 21*(2), 351-358.

Tai, C. Y., Tai, C. D., & Chang, M. H. (2009). Effect of interfacial supersaturation on secondary nucleation. *Journal of the Taiwan Institute of Chemical Engineers, 40*(4), 439-442.

Tai, C. Y., Wu, J.-F., & Rousseau, R. W. (1992). Interfacial supersaturation, secondary nucleation, and crystal growth. *Journal of Crystal Growth, 116*(3-4), 294-306.

Tait, S., White, E. T., & Litster, J. D. (2009). A study on nucleation for protein crystallization in mixed vessels. *Crystal Growth & Design, 9*(5), 2198-2206.

Tavare, N. S. (1995). *Industrial crystallization: Process simulation analysis and design*. New York: Plenum Press.

Tavare, N. S., & Chivate, M. R. (1977). Analysis of batch evaporative crystallizers. *The Chemical Engineering Journal, 14*, 175-180.

ten Cate, A., Derksen, J. J., Kramer, H. J. M., van Rosmalen, G. M., & Van den Akker, H. E. A. (2001). The microscopic modelling of hydrodynamics in industrial crystallisers. *Chemical Engineering Science, 56*(7), 2495-2509.

Thurlby, J. A. (1976). Crystallization kinetics of alpha lactose. *Journal of Food Science, 41*(1), 38-42.

Troy, H. C., & Sharp, P. F. (1930). α and β lactose in some milk products. *Journal of Dairy Science, 13*(2), 140-157.

van der Heijden, A. E. D. M., Elwenspoek, M., & van der Eerden, J. P. (1989). Size distribution of embryos produced by crystal-rod contacts. *Journal of Crystal Growth, 98*(3), 398-410.

van Kreveld, A., & Michaels, A. S. (1965). Measurement of crystal growth of alpha-lactose. *Journal of Dairy Science, 48*(3), 259-265.

Virone, C., ter Horst, J. H., Kramer, H. J. M., & Jansens, P. J. (2005). Growth rate dispersion of ammonium sulphate attrition fragments. *Journal of Crystal Growth, 275*(1-2), e1397-e1401.

Visser, R. A. (1982). Supersaturation of alpha-lactose in aqueous solutions in mutarotation equilibrium. *Netherlands Milk and Dairy Journal, 36*, 89-101.

Wang, J., & Estrin, J. (1996). Secondary nucleation of sucrose by fluid shear in aqueous solutions. *Chemical Engineering Communications, 152*(1), 275-287.

Wang, M. L., Huang, H. T., & Estrin, J. (1981). Secondary nucleation of citric acid due to fluid forces in a couette flow crystallizer. *AIChE Journal, 27*(2), 312-315.

Wang, M. L., & Yang, H. M. (1981). Secondary nucleation of caprolactum in toluene solution by fluid shear forces. *Chemical Engineering Communications, 12*(4), 241 - 251.

Ward, J. D., & Yu, C.-C. (2008). Population balance modeling in simulink: PCSS. *Computers & Chemical Engineering, 32*(10), 2233-2242.

White, E. T., Bending, L. L., & Larson, M. A. (1976). The effect of size on the growth rate of potassium sulfate crystals. *AIChE journal Symposium Series No. 153, 72*(41).

Williams, A. M., Jones, J. R., Paterson, A. H. J., & Pearce, D. L. (2009). Effect of fines on agglomeration in spray dryers: An experimental study. *International Journal of Food Engineering, 5*(2), Article 7.

Wohlgemuth, K., Kordylla, A., Ruether, F., & Schembecker, G. (2009). Experimental study of the effect of bubbles on nucleation during batch cooling crystallization. *Chemical Engineering Science, 64*(19), 4155-4163.

Wöhlk, W., Hofmann, G., & de Jong, E. J. (1991). Die kristallisationstheorie in der praxis. *Chemie Ingenieur Technik, 63*(4), 293-297.

Wong, S. Y., Bund, R. K., Connelly, R. K., & Hartel, R. W. (2011). Determination of the dynamic metastable limit for alpha-lactose monohydrate crystallization. *International Dairy Journal, 21*(11), 839-847.

Wu, J., Graham, L. J., & Mehidi, N. N. (2006). Estimation of agitator flow shear rate. *AIChE Journal, 52*(7), 2323-2332.

Appendix I

Physical properties of lactose: crystal, solution and slurry

Density

The density of α-lactose monohydrate (α-LMH) crystals, lactose solution and slurry (suspension of lactose solution and (α-LMH) crystals) is required during the simulation as well as experimental runs. The density of α-LMH crystals used is 1550 kg m^{-3}.

To check if the density of the solution changes when lactose is present in either dissolved or crystalline form, the following experiments were done. 20, 30 and 40 g of lactose powder were weighed in three different volumetric flasks. Preheated water at 40 °C was introduced into the flasks. The contents were shaken while filling the flask to ensure removal of air bubbles and complete wetting of the solids. Preheated water was used to reduce the error due to a change in volume of water with temperature. The volume was gradually made up to 100 ml and the flasks were sealed with a stopper to reduce evaporation losses and then introduced into the constant temperature bath maintained at 40 °C. The contents were intermittently shaken to ensure faster dissolution. The meniscus level in the volumetric flask was closely monitored as dissolution happened. Complete dissolution occurred in the flask containing 20 g of lactose over a period of two hours while the other two flasks had undissolved lactose in them. No measurable change in the meniscus level occurred in any of the flasks. Similar experiments were performed at 65 °C with two flasks containing 40 and 45 g of lactose. When the flasks were introduced in the water bath the meniscus level increased within the first few minutes. This was due to thermal expansion of water in the flask which would have cooled to below 65 °C while preparing the slurry. The meniscus then stabilized to a steady level. Complete dissolution of lactose took place in the first flask over 45 minutes. No measurable change in the meniscus level was observed indicating that the volume and hence the density (since mass was constant in a given flask) remain unchanged, irrespective of the state of the solute in the slurry. Thus a relationship between dissolved lactose

concentration and density can be used if the total solid (dissolved plus crystalline) in the slurry is known. For example, density of a 70% (w/w) lactose solution will be same as the slurry containing 70% total solid.

Due to a lack of data on lactose solution density at higher concentrations, sucrose (a similar disaccharide sugar having the same solid density) solution density data from Bubnik, Kadlec, Urban, & Bruhns (1995) was used to correlate density to total solids at the crystallizer temperature. The sucrose solution density matched very closely (a maximum error of 1%) with the limited density data available for lactose solutions from Buma (1980).

$$\rho_s = 983.2e^{0.0042(T.S.)}$$

Equation I- 1 Denisty as a function of total solids

Viscosity

The viscosity of a slurry (μ_S) depends on the volumetric concentration of the particles suspended (ϕ)and the viscosity of the fluid media (μ_s) as given by Abulnaga (2002):

$$\mu_S = \mu_s\left[1 + 2.5\phi + 10.05\phi^2 + 0.00273\exp(16.6\phi)\right]$$

Equation I- 2 Slurry viscosity in terms of volumetric concentration of the particles

The viscosity of the mother lactose solution (μ_s) as a function of concentration at the crystallizer temperature was plotted for the combined data from Buma (1980) and Shah & Nickerson (1978) as shown in Figure I-1. The lactose solution viscosity at the temperature and concentrations used in the contact and shear nucleation trials were estimated from the values reported by Buma (1980).

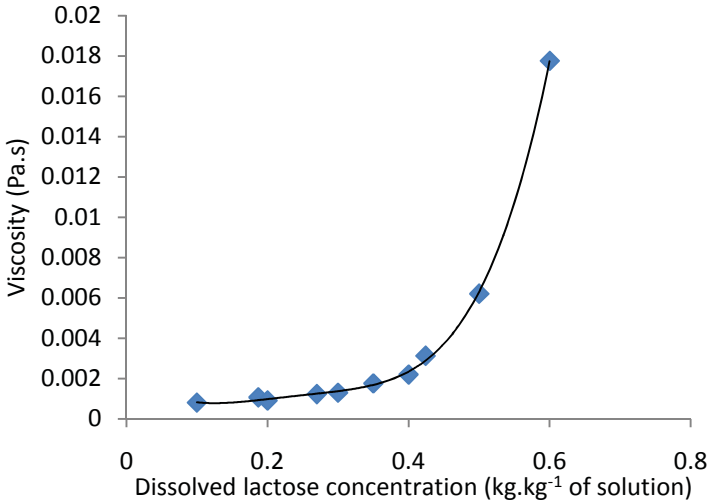


Figure I-1. Viscosity versus concentration for lactose solution at the crystallizer temperature.

A fourth order polynomial was fitted to the above data as:

$$\mu_s = 0.87C^4 - 0.81C^3 + 0.28C^2 - 0.04C + 0.0026$$

Equation I- 3 Viscosity as a function of dissolved lactose concentration at the crystallizer temperature

Specific heat

The specific heat of lactose, $C_{p,L}$ was taken as 1250 J kg^{-1} $°C^{-1}$. The slurry specific heat was determined using the following relationship:

$$C_{p,s} = XC_{p,L} + (1 - X)C_{p,w}$$

Equation I- 4 Specific heat of slurry

where X is the mass fraction of lactose in the slurry and $C_{p,w}$ is the specific heat of water.

Mechanical properties of α-LMH crystal

The Mersmann model requires mechanical properties of lactose monohydrate crystals. Hardness value (H) and Youngs modulus (E) were available in the literature (Table I-1). Shear modulus (S) can be predicted from Young's modulus and the Poisson ratio (P) values by the following relationship:

$$S = \frac{E}{2(1+P)}$$

Equation I- 5 Shear modulus in terms of Young's modulus and Poisson ratio

No literature citing directly the value of fracture surface energy could be found for lactose. It is the most uncertain property in the model. It can be estimated from the relationships given by Gahn & Mersmann (1999a):

$$\frac{\Gamma}{K_r} = \frac{0.1 W_C^{1/3} H^{5/3}}{S}$$

Equation I- 7 Fracture surface energy

W_c in simplistic terms can be defined as the critical work to form cracks and is given by

$$W_C \approx 0.05\sqrt{\frac{F^3}{H}}$$

Equation I- 8 Critical work to form a crack

where, F is the indentation force applied on the crystal. The value of F was taken from a study on milling behaviour of lactose by nanoindentation (Meier, John, Wieckhusen, Wirth, & Peukert, 2009). A graph relating the applied load and the crack radius was presented to measure the fracture toughness. The lowest force magnitude studied (~0.21 N) which produced a crack length of ~ 60 micron was taken as the value of F. The mechanical properties used in the model are summarized in Table I-1.

Table I- 1 *Mechanical Properties of Lactose Monohydrate*

Property	Value	units	Reference
Hardness [H]	0.869E9	Nm^{-2}	(Meier, et al., 2009)
Youngs moduls [E]	21.44E9	Nm^{-2}	(Meier, et al., 2009)
Poisson ratio [P]	0.31	--	(Perkins, et al., 2007)
Shear modulus [S]	8.2E9	Nm^{-2}	Equation I-6
Force required to form crack [F]	0.21	N	(Meier, et al., 2009)
Fracture surface energy [$\frac{\Gamma}{K_r}$]	58.34	Jm^{-2}	Equation I-6 and Equation I-7

Appendix II

Kapuni Crystallizer: Dimensions and Operational Specifications

Table II- 1 *Crystallizer Flow Pump Dimensions*

Axial Flow Pump			
Diameter [d_{pump}]	Outside $d_{pump,O.D.}$	Inside $d_{pump,I.D.}$	m
	0.35	0.175	
Number of blades [n_B]	6		
Pitch	0.06		m
Blade Angle [β]	17.2		deg
Width of edge [$L_{a,edge}$]	0.005		m
Breadth of face [$L_{a,face}$]	0.187		m
Pump discharge coefficient [K_D]	0.6		

The slurry circulation rate by the axial flow pump is given by

$$Q_{circ} = pitch * n_B * N_{pump} * \pi(d^2_{pump,O.D.} - d^2_{pump,I.D.}) /(4 * 60)$$

Equation II- 1 Slurry circulation rate

The discharge coefficient of the pump is given by:

$$K_D = Q/(N_{pump} d^3_{pump,O.D.})$$

Equation II- 2 Discharge coefficient of the pump

The effective volume of the crystallizer was determined using the equation used in the plant control systems for calculating the residence time. The expression used to calculate the volume of the crystallizer is:

$$V_{sus} = 5.69 + 0.17 * level(\%)$$

Equation II- 3 Effective crystallizer volume

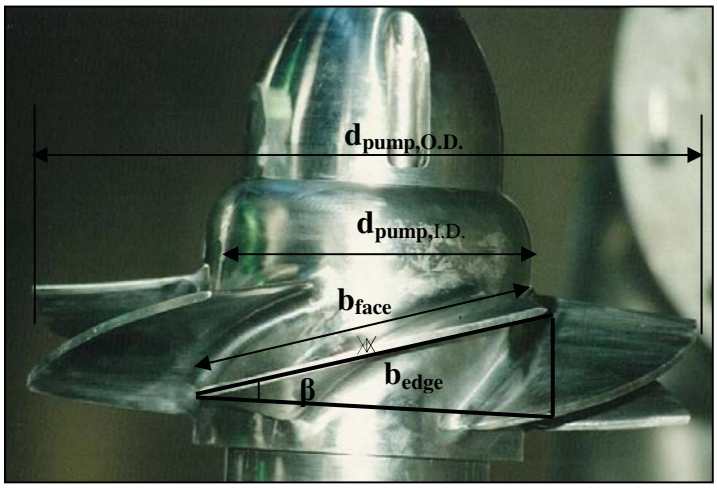


Figure II-1. Axial flow pump used for slurry circulation in the Kapuni FC evaporative crystallizer.

Table II- 2 *Crystallizer Operating Conditions*

Pump speed [N_{pump}]	12.66	s^{-1}
Circulation rate [Q_{circ}]	0.328	$m^3 s^{-1}$
Effective crystallizer volume [V_{sus}]	9	m^3

Operating pressure and temperature cannot be disclosed for commercial reasons

Appendix III

Model for the flow through the calandria

The evaporator in Kapuni is a boiling in tube type. Thus the calandria can be divided into two zones: a) subcooled zone, where the liquid is heated up to its boiling point and above that, b) an evaporation zone where the liquid is partially evaporated by further heating as well as by pressure drop (flashing). The fluid entering the calandria is subcooled due to the liquid head above it. As the fluid rises, its temperature increases (due to heat input) and the pressure decreases (due to reduced liquid head). At a given height of the tube, where the temperature corresponding to the saturation pressure is reached, boiling of the fluid starts. Here the heating zone ends and the evaporation zone starts. Arneth & Stichlmair, (2001) approximate the heating zone as 20-50% of the total tube length for operation under atmospheric pressure and around 90% or more for high vacuum services as in the present evaporator. Since the evaporation zone lengths are very small, it becomes very important to include the effect of flashing, especially in cases with high mass flux rates and low evaporation rates (low exit mass flow quality). Although the actual rise in temperature inside the calandria is only two of degrees, the high mass flux rates results in a considerable amount of heat energy getting stored in the fluid as sensible heat. This large quantity of sensible heat then gets converted to the latent heat of vaporization during the flashing process contributing significantly to the overall evaporation process.

To simplify the model the following assumption were made:

a. the system operates under steady state
b. flow through the tubes is one dimensional, homogenous and in equilibrium. There are no gradients in the radial direction of the tubes
c. some suitable average properties are considered for the slurry-vapor mixture
d. the slurry was considered as an incompressible pseudo single phase liquid with the effect of the solid phase accounted for in the physical properties of viscosity and density
e. Latent heat (h_{fg}) was considered to be constant for the pressure range
f. instantaneous transfer of heat occurs from the wall to the bulk mixture flowing up the tube

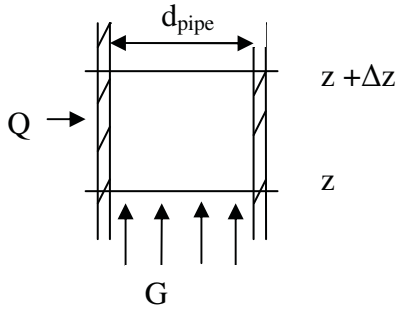


Figure III-1. Schematic of the flow through a calandria pipe section

Continuity

From continuity balance, $mass\ flux = G = const$ [kg s^{-1} m^{-2}]

The velocity, v_m [m s^{-1}] of the slurry-vapour mixture is given as:

$$v_m = GV_m$$

Equation III-1

where V_m [m^3 kg^{-1}] is the specific volume of the mixture given by:

$$V_m = V_l + (V_v - V_l)x$$

Equation III-2 Specific volume of the mixture

x is the flow quality given by the ratio of mass of vapour to the total mass of mixture, V_l and V_v are specific volume of pure liquid and vapour phase [m^3 kg^{-1}]

Momentum Balance

The momentum balance across a control volume $A\Delta z$ is given by:

$rate\ of\ momentum\ in - rate\ of\ momentum\ out + forces\ acting\ within\ the\ system = rate\ of\ momentum\ accumulation$

Convective momentum at z $\left[\frac{Av_m v_m}{V_m}\right]_z$

Convective momentum at $z+\Delta z$ $\left[\frac{Av_m v_m}{V_m}\right]_{z+\Delta z}$

Forces acting on the element Δz :

Pressure force at z $[PA]_z$

Pressure force at $z+\Delta z$ $[PA]_{z+\Delta z}$

Shear force at the tube wall $[\zeta_w p \Delta z]$

Gravitational force $\left[\frac{A \Delta z g}{V_m}\right]$

where P is the absolute pressure [Nm^{-2}], A is the cross sectional area [m^2], ζ_w is the wall shear stress [Nm^{-2}], p is the perimeter [m], g is the gravitational constant [ms^{-2}]. At steady state the accumulation term becomes zero and substituting the different forces, the momentum balance equation takes the form:

$$[\frac{A v_m v_m}{V_m}]_{z+\Delta z} - [\frac{A v_m v_m}{V_m}]_z + [PA]_{z+\Delta z} - [PA]_z + [\zeta_w p \Delta z] + \left[\frac{A \Delta z g}{V_m}\right] = 0$$

Equation III-3 Force balance over the pipe element

Substituting for v_m and dividing throughout by $A\Delta z$ and under conditions of constant cross sectional area and mass flux rate, Equation III-3 takes the form:

$$\frac{dP}{dz} + \frac{\zeta_w p}{A} + \frac{g}{V_m} + G^2 \frac{dV_m}{dz} = 0$$

Equation III-4 Differential momentum balance

The shear wall stress can be expressed in terms of friction coefficient as:

$$\zeta_w = \frac{f}{2V_m} v_m^2$$

Equation III-5 Wall shear stress

$$p = \pi d_{pipe}$$

Equation III-6 Pipe perimeter

$$A = \frac{\pi d_{pipe}^2}{4}$$

Equation III-7 Pipe cross section area

Combining Equation III-4 to Equation III-7 gives the expression for pressure gradient along the tube height:

$$-\frac{dP}{dz} = \frac{2 f V_m G^2}{d_{pipe}} + \frac{g}{V_m} + G^2 \frac{dV_m}{dz}$$

Equation III-8 Pressure gradient along the tube height

Energy Balance

The continuous flow specific energy balance [J kg^{-1}] between vertical positions z and $z+\Delta z$ in a tube is

$$H_z + E_{kz} + E_{p\,z} + Q = H_{z+\Delta z} + E_{k\,z+\Delta z} + E_{p\,z+\Delta z} + F$$

Equation III-9 Energy balance over the pipe element Δz

where, H is the specific enthalpy of the mixture, E_k is the kinetic energy, E_p is the potential energy, Q is the specific heat input to the system between z and $z+\Delta z$ and F is the specific work required to overcome friction .The thermodynamic relation $H = U + PV$ means that enthalpy includes the work of expansion that occurs when the liquid reaches it boiling point and begins to change phase.

$$H = h_f + xh_{fg} = C_p T + xh_{fg}$$

Equation III-10 Specific enthalpy of the slurry flowing through the pipe

where, the first term on the right hand side (RHS) is the specific enthalpy of the liquid phase and the second term represents the enthalpy of the vapour phase.

$$E_k = \frac{1}{2} v_m^2$$

Equation III-11 Specific kinetic energy

$$E_p = gz$$

Equation III-12 Specific potential energy

$$Q = \frac{m_s h_{fg} \Delta z}{GANl}$$

Equation III-13 Specific heat input

where, m_s is the steam feed rate to the calandria [kg s^{-1}], h_{fg} is the specific phase change liquid-vapour enthalpy [J kg^{-1}], N is the number of tube and L is the length of the tube [m]:

$$F = \frac{2 f \Delta z v_m^2}{d_{pipe}}$$

Equation III-14 Specific frictional work

Combining Equation III-9 to Equation III-14 yields:

$$(C_p T)_z + (h_{fg} x)_z + \left(\frac{1}{2} * G^2 V_m^2\right)_z + gz + \frac{m_s h_{fg} \Delta z}{GANL} = (CpT)_{z+\Delta z} + (h_{fg} x)_{z+\Delta z} + \left(\frac{1}{2} G^2 V_m^2\right)_{z+\Delta z} + g(z+\Delta z) + \frac{2 f \Delta z G^2 V_m^2}{D_{pipe}}$$

Equation III-15 Macroscopic energy balance over the pipe segment

Dividing throughout by Δz and taking the limit $\Delta z \rightarrow 0$, and neglecting variation of C_p and h_{fg} with height (and hence with temperature and pressure) and by continuity, having mass flux G constant throughout the length of flow for a constant diameter tube,

$$C_p \frac{dT}{dz} + h_{fg} \frac{dx}{dz} + V_m G^2 \frac{dV_m}{dz} + g - \frac{m_s h_{fg}}{GANL} + \frac{2 f G^2 V_m^2}{d_{pipe}} = 0$$

Equation III-16 Differential energy balance over the pipe segment

The frictional energy is required to overcome the frictional drag with the walls of the tube. Over time this friction energy should degrade as heat, but it does not within the context of this balance equation. Therefore, we assume that this energy remains stored in the fluid, for example in turbulent eddies, over the limited timeframe that the fluid travels up the tube. Further development of the momentum and energy balance equations is possible when considering the periods prior to and after the onset of boiling. This is discussed below.

Prior to boiling

Before boiling starts there is no vapour generation $x = 0$ and $dx/dz = 0$. Also the mixture specific volume equals that of the liquid phase, $V_m = V_l$ and the condition of incompressibility leads to $dV_l/dz = 0$.

Under these conditions, the pressure gradient reduces to

$$-\frac{dp}{dz} = \frac{2 f G^2 V_l}{d_{pipe}} + \frac{g}{V_l}$$

Equation III-17 Single phase pressure gradient

And the energy balance in reduces to

$$-\frac{dT}{dz}=\frac{g-\frac{m_s h_{fg}}{GANL}+\frac{2fG^2V_l^2}{D}}{C_p}$$

Equation III-18 Single phase temperature gradient

f, the single phase fanning friction factor under laminar flow conditions is calculated as

$$f = 16/Re$$

Equation III-19 Single phase friction factor

Equation III-17 and Equation III-18 can be solved simultaneously to get the temperature rise of the slurry and the pressure drop, respectively for the single phase flow.

After the onset of boiling

But once boiling starts, the vapour-liquid saturation line can be specified by either pressure or temperature. Thus, the specific volume of the mixture as per Equation III-2 becomes a function of vapour fraction and pressure only, $V_m = f(x, P)$

Hence the variation of specific volume with height can be written as:

$$\frac{dV_m}{dz}=\left(\frac{dV_m}{dx}\right)_P\frac{dx}{dz}+\left(\frac{dV_m}{dP}\right)_x\frac{dP}{dz}$$

Equation III-20

The first and second terms on the RHS are given by Equation III-21 and Equation III-22, respectively:

$$\left(\frac{dV_m}{dx}\right)_P\frac{dx}{dz}=(V_v-V_l)\frac{dx}{dz}$$

Equation III-21

$$\left(\frac{dV_m}{dP}\right)_x\frac{dP}{dz}=\left[\frac{dV_l}{dP}+x\left(\frac{dV_v}{dP}-\frac{dV_l}{dP}\right)\right]\frac{dP}{dz}$$

Equation III-22

Here, it is reasonable to assume that the liquid phase specific volume changes negligibly with pressure and so $dV_l/dP = 0$

$$\frac{dV_m}{dz} = (V_v - V_l)\frac{dx}{dz} + x\left(\frac{dV_v}{dP}\frac{dP}{dz}\right)$$

Equation III-23 Specific volume gradient

The two phase Darcy's friction factor was calculated from the explicit equation (Chen, 1979)

$$\frac{1}{\sqrt{f_{2p}}} = -2\log\left[\frac{1}{3.7065}\frac{e}{d_{pipe}} - \frac{5.0452}{\mathrm{Re}_{2p}}\log\left(\frac{1}{2.8257}\left(\frac{e}{d_{pipe}}\right)^{1.1098} + \frac{5.8506}{\mathrm{Re}_{2p}^{\,0.8981}}\right)\right]$$

Equation III-24 Two phase friction factor

e/d_{pipe} was taken as 0.001 (for commercial steel $e = 5*10^{-5}$ (Geankoplis, 2004).
Two phase Reynolds number was defined as :

$$\mathrm{Re}_{2p} = \frac{GV_m}{\mu_m}$$

Equation III-25 Two phase Reynolds number

where, μ_m is the viscosity of the mixture. Multiple empirical relationships are available in the literature to predict the same (Awad & Muzychka, 2008). However the following definition is the most commonly used:

$$\mu_m = \left(\frac{x}{\mu_v} + \frac{1-x}{\mu_l}\right)^{-1}$$

Equation III-26 Two phase viscosity for slurry-vapour mixture

μ_v and μ_l are the viscosities of the vapour and the liquid phase respectively. The viscosity of the vapour phase was taken as 0.000011 Nsm^{-2} (independent of pressure in the range considered) and the slurry viscosity was estimated from relationships given in Appendix I. Substituting Equation III-23 into Equation III-8 and rearranging gives the two phase pressure gradient.

$$-\frac{dP}{dz}=\frac{\frac{f_{2p}G^2V_m}{2d_{pipe}}+G^2(V_v-V_l)\frac{dx}{dz}+\frac{g}{V_m}}{1+G^2x\frac{dV_v}{dP}}$$

Equation III-27 Two phase pressure gradient

The specific volume of water vapour can be related to pressure, using standard steam table data as:

$$V_v = 82748P^{-0.9378}$$

Equation III-28 Specific volume –pressure relationship

On differentiating, dV_v/dP is obtained as:

$$\frac{dV_v}{dP} = -77617P^{-1.9378}$$

Equation III-29

After boiling starts the system is at saturation and one state variable, temperature or pressure, is sufficient to describe the system. Choosing pressure, we can say that temperature is dependent on the pressure which is solely a function of height. This allows us to write:

$$\frac{dT}{dz}=\frac{dT}{dP}\frac{dP}{dz}$$

Equation III-30

Substituting Equation III-23 and Equation III-30 in Equation III-6 yields:

$$C_p\frac{dT}{dP}\frac{dP}{dz}+h_{fg}\frac{dx}{dz}+V_mG^2\left((V_v-V_l)\frac{dx}{dz}+x\frac{dV_v}{dp}\frac{dP}{dz}\right)+g-\frac{m_sh_{fg}}{GANL}+\frac{2f_{2p}G^2V_m^2}{D_{pipe}}=0$$

Equation III-31 Two phase energy balance

Solving the above equation for dx/dz gives:

$$\frac{dx}{dz}=\frac{\frac{m_sh_{fg}}{GANL}-g-\frac{f_{2p}G^2V_m^2}{2d_{pipe}}-\frac{dP}{dz}\left(C_P\frac{dT}{dP}+G^2V_mx\frac{dV_v}{dP}\right)}{h_{fg}+G^2V_m(V_v-V_l)}$$

Equation III-32 Flow quality gradient

The saturation temperature and pressure were related using steam table data as follows:

$$T = 1.85P^{0.349} + 0.8$$

Equation III-33 Temperature pressure saturation curve

In the absence of data for boiling point elevation (BPE) of lactose, the BPE of sucrose was used. For a 42% concentration (calculated mother liquor concentration) and 100% purity, BPE works out to be 0.8 °C (Bubnik, et al., 1995).

dT/dP is given by:

$$\frac{dT}{dP} = 0.64P^{-0.65}$$

Equation III-34

Equation III-27 and Equation III-32 can be solved simultaneously to give the corresponding pressure and flow quality profile from which can then be used to calculate the slurry velocity profile.

Solution scheme

To solve the above ODEs the initial conditions must be known. Only one initial condition for the single phase flow (inlet temperature) and one boundary condition (exit pressure) for the two phase flow is known from the plant operation:

$T\ (x=0) = 61.5$ °C

$P\ (x=L) = 20000$ Nm^{-2}

To solve the single phase flow equations a second initial condition is required i.e. the pressure at the tube bottom. In order to overcome this, the solution scheme was set such that the exit conditions at the single phase flow become the initial conditions for the two phase flow. The boundary conditions for the single phase flow corresponded to the one present at tube height at which boiling starts. This was determined as the height at which the saturation temperature curve as per Equation III-33 (corresponding to the pressure calculated from Equation III-17) intersected with the temperature curve of the slurry (Equation III-18). The set of equations for the two phases were then solved simultaneously using MATLAB. The inlet pressure at the tube bottom was arrived at by trial to achieve the known exit pressure at the tube end.

Appendix IV

Mersmann model for secondary nucleation induced by attrition due to crystal impeller contacts

The Mersmann model can be expressed as a function of mechanical property of the crystals (K_{mech}), collision frequency (f_c), collision energy (E_k) and an effective nucleation factor (χ).

$$B_{attr} = K_{mech} f_{c\,i,j} E_{k\,i,j} \chi$$

Equation IV-1 Secondary nucleation due to attrition by crystal impeller contacts

K_{mech} is given by:

$$K_{mech} = 7 * 10^{-4} \frac{H^5}{S^3} \left(\frac{K_r}{\Gamma} \right)^3$$

Equation IV-2 Mechanical properties constant

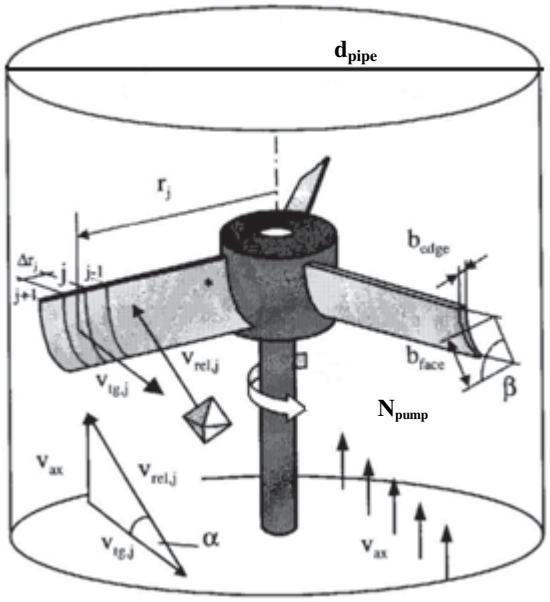


Figure IV-1. Relative motion of the crystal and the pump blades (reproduced from Neumann (2001))

Figure IV-1 shows the relative motion of the particle and the propeller blades. The crystal can collide either with the edge or the face of the impeller blades. However, the contribution of the edge to the impeller-crystal collisions is much greater than the

face when the blade angle (β) is less than 25° (Mersmann, 2001a). Since the blade angle of the axial flow pump used in the present crystallizer is 17° (Appendix II), collisions only with the edge have been considered.

$f_{ci,j}$ is the collision frequency of crystals in size class i with the segment j of the impeller blade with either the face or the edge. It is given by

$$f_{ci,j} = n_{c,i} \frac{Q_{circ}}{V_{sus}} \eta_{w,i,j} \eta_{g,j}$$

Equation IV-3 Collision frequency

n_c is the crystal number density of size class i. η_w is the target efficiency and depends on the hydrodynamics and the propeller geometry. It quantifies the probability that a crystal moving on a streamline towards the impeller collides with this target. It is also used as a damping factor in the calculation of the collision velocity. It is expressed as a function of Stokes number (ψ) as:

$$\eta_{w,edge,i,j} = \left(\frac{\psi_{edge,i,j}}{0.32 + \psi_{edge,i,j}} \right)^{2.1}$$

Equation IV-4 Target efficiency

$$\psi_{edge,i,j} = \frac{(\rho_c - \rho_s) v_{rel} d_{c,i}^2}{18 \mu_s T_{edge}}$$

Equation IV-5 Stokes Number

$$v_{rel,j} = \sqrt{v_{ax}^2 + v_{tg,j}^2}$$

Equation IV-6 Relative velocity between the crystal and the pump blades

where, v_{ax} and v_{tg} are defined as:

$$v_{ax} = \frac{4\phi_{circ}}{\pi d_{pipe}^2}$$

Equation IV-7 Axial velocity

$$v_{tg,j} = \pi N d_{pump,j}$$

Equation IV-8 Tangential velocity

η_g is the geometric efficiency and depends on the geometry of the impeller and quantifies the probability of the crystals being present in the projection plane of the impeller.

$$\eta_{g,edge} = \frac{4 b_{e,edge} n_B \Delta r_j}{\pi d_{pipe}^2 \sin(\alpha_j)}$$

Equation IV-9 Geometric efficiency

where,

$$\alpha_j = \arctan\left(\frac{v_{ax}}{v_{tg,j}}\right)$$

Equation IV-10 Angle of approach

Since the impact velocity changes along the radius of impeller blade, the blade radius needs to be discretized into small fragments (Δr_j). $b_{e,edge}$ is the effective target length given by:

$$b_{e,edge} = b_{edge} \cos(\beta - \alpha_j)$$

Equation IV-11 Effective edge length

$E_{ki,j}$ is the collision kinetic energy given by

$$E_{k\,i,j} = \frac{1}{2} \rho_c k_v d_{c,i}^3 v_{coll,i,j}^2$$

Equation IV-12 Collision kinetic energy

$w_{coll,i,j}$ is the collision or impact velocity of crystal in size class $\underline{i}$ with the j^{th} segment of the impeller :

$$v_{coll,i,j} = \eta_{w,edge,i,j} v_{rel,edge,\perp}$$

Equation IV-13 Collision velocity

where,

$$v_{rel,edge,\perp,j} = v_{rel,j} \left|\cos(\beta - \alpha_j)\right|$$

Equation IV-14 Perpendicular component of the collision velocity

χ is the ratio of the number of attrition fragments that grow (effective) to that total formed. It is an intrinsic thermodynamic property of the attrition fragments which results in dissolution of small attrition fragments due to additional strain energy incorporated into them during the process of attrition. χ needs to be determined experimentally as there exists no simple relationship to predict it.